Synthesis of ZnO nanoparticles and its characterization

A thesis submitted in fulfillment of the degree of

DOCTOR OF PHILOSOPHY

IN

BIOTECHNOLOGY

THAPAR INSTITUTE
OF ENGINEERING & TECHNOLOGY
(Deemed to be University)

Submitted by

Prerna
(Reg. No. 901300005)

Under the Guidance of

Dr. Dinesh Goyal
Professor

Department of Biotechnology

THAPAR INSTITUTE OF ENGINEERING AND TECHNOLOGY
(Deemed to be University)

Patiala – 147004, Punjab, India

May, 2023

CERTIFICATE

Certified that the thesis **"Synthesis of ZnO nanoparticles and its characterization"**which is submitted by **Ms. Prerna**, in fulfillment of the requirement for the award of the degree of **Doctor of Philosophy** in the Department of Biotechnology, Thapar Institute of Engineering and Technology, Patiala,Punjab, India is a record of the candidate's own independent and original research work carried out by her under my supervision and guidance. The matter embodied in this thesis has not been submitted in part or full to any other University or Institute for the award of any degree.

Place: Patiala
Date: May 25, 2023

Supervisor
(Dr. Dinesh Goyal)
Professor,
Department of Biotechnology,
Thapar Institute of Engineering and Technology,
Patiala- 147004
Punjab, India

DECLARATION

I hereby declare that the work which is being presented in this thesis **"Synthesis of ZnO nanoparticles and its characterization"** submitted by me for the award of the degree of **Doctor of Philosophy**in the Department of Biotechnology, Thapar Institute of Engineering and Technology, Patiala, is true and original record of my own independent and original research work carried out under the supervision of **Dr. Dinesh Goyal**, Professor, Department of Biotechnology, Thapar Institute of Engineering and Technology, Patiala, Punjab, India. The matter embodied in this thesis has not been submitted in part or full to any other university or institute for the award of any degree in India or abroad.

Prerna

(Prerna)

Place: Patiala
Date: May 25, 2023

Dedicated to my

Supervisor

Dr Dinesh Goyal

Special Remembrance

To the memory of my grandfather ***Daaji (Dr. Sohan Lal Vasant)*** *and my mamaji* ***Sh. Mukesh Ahuja****, who today would have been the proudest on earth. Gone too soon.*

I wish they could have been with me for some more time. Their absence has left a great void in my life. I feel blessed to have received their love and support. I would like to recompense my veneration to them for giving me strength and patience to work through all these years so that today I can stand proud with my head held high.

In my thoughts and heart they will live on forever…

Acknowledgements

"Independent will is our capacity to act. It gives us the power to transcend our paradigms, to swim upstream, to rewrite our scripts, to act based on principle rather than reacting based on emotion or circumstance." ~ Stephen Covey

Penning down my thesis has not been just a documentation/ demonstration work but has been like writing a script which could make sense out of my Ph.D. journey. The accomplishment of this work could never be achieved without punctilious efforts, constructive discussions, collaborations, persistent encouragement, love and care of accompanying supportive people during various phases of this long tumultuous journey.

I feel very blessed and privileged to acknowledge and thank them all who became a contributor in the accomplishment of my work in any direct or indirect manner and in making me who I am today.

At the outset, I express my gratitude to my Mentor and Supervisor, ***Dr. Dinesh Goyal****, Professor, Department of Biotechnology, Thapar Institute of Engineering and Technology, Patiala whose encouragement, guidance and support from the initial to the final level enabled me to develop an understanding of the subject. His perceptive knowledge and benevolent attention enabled me to pursue the work presented in this dissertation. I am indebted to him for the dexterous guidance, untiring efforts, constructive criticism and providing continuous enthusiasm during the entire tenure of my research work. His passion for research, unending zeal, exceptional ideas and creative criticism always encouraged me to face insurmountable challenge. Being always empowered by his graceful and friendly behavior, I enjoyed every moment of my research period. His vast experience generated an aura around to exercise freedom of working at an independent level. His academic brilliance clubbed with practical insights enabled me to grapple with the problem thought.*

During moments of struggle and mental fatigue, there were instances when I felt stuck, and my resolve weakened. However, he remained steadfast by my side, infusing me with renewed energy and illuminating the path towards finding solutions. I am fortunate enough to be able to work with an encouraging professor like him. Not only he has been a brilliant scientist, but at the same time he is a thorough gentleman who taught me honor, determination, humility, and respect.

I greatly value the close personal rapport that we have forged over the years. I quite simply cannot imagine a better adviser and will forever cherish. He made me realise what I had only heard, "When the going gets tough, the tough gets going". I will never find words to tell what I owe to him, and if I start doing it, I would not know where to stop…thanks for everything Sir…. I really feel privileged to be associated with a genius like him during my life. His association with this endeavor of mine will remain a beacon light to me throughout my life. He would remain my role model and source of inspiration in my future professional life.

I would also fondly cherish the unconditional and warm care bestowed by Madam ***Mrs. Seema Goyal*** *for the rest of my life.*

I need to specially acknowledge here, the galaxy of knowledge contributors to my research, who may remain incognito, as only a fraction of them get mentioned in the bibliographical citations; for their enlightening and thought provoking studies and research, into the myriad aspects of the nebulous field of Nano-biotechnology and beyond, and for widening my horizons.

I express my immense gratitude to ***Dr. P.K. Nair****,* ***Director,*** *Thapar Institute of Engineering and Technology, Patiala, for providing me with the infrastructure that was instrumental in steamrolling my research work.*

I owe my profound thanks to ***Dr. N.Tejo Prakarsh****,* ***Dean*** *(Research and Sponsored Projects), Thapar Institute of Engineering and Technology, Patiala, for his understanding, encouragement and providing all the necessary facilities which paved smooth completion of my dissertation.*

My special word of thanks should also go to ***Dr. M.S. Reddy****, Head, Department of Biotechnology and members of my doctoral committee,* ***Dr. N. Das, Dr. Sanjai Saxena****, Department of Biotechnology, TIET and* ***Dr. B.N. Chudasama****, School of Physics and Material Science, TIET for the technical discussions, critical inputs and encouragement they offered me during the course of the study.*

I extend my sincere word of thanks to ***Dr. Bonamali Pal****, School of Chemistry and Biochemistry, TIET for their valuable suggestions, encouragement and support facilitating quality research work.*

I acknowledge the TEQIP-II, Government of India for providing me with the necessary fellowship which buttressed me to perform my work comfortably.

It is my privilege to express heartfelt thanks and sincere gratitude to ***Late Dr. O.N. Srivastava****, Professor, Department of Physics, Banaras Hindu University, Varanasi for his counsel and scholarly insights that have been a source of unending inspiration.*

No research is possible without collaboration. Quality research cannot be attained without collaboration. The results compiled in the thesis could not have been obtained without timely technological assistance from few laboratories. I extend my thanks to Sophisticated Analytical Instrument Facility at Punjab University, Chandigarh, Central Instrumentation Facility, Punjab University, Chandigarh, Central Research Facility, IIT Delhi, Institute Instrumentation Centre, IIT Roorkee, Material Analysis and Research Centre, Bengaluru, Advanced Instrumentation Research Facility, Jawaharlal Nehru University, New Delhi, Department of Physics, Banaras Hindu University, Varanasi, and Sophisticated Analytical Instruments Laboratories Thapar Institute of Engineering and Technology, Patiala, India for providing necessary instrumentation facilities to carry out my research work.

I remain grateful to ***Science & Technology Entrepreneur's Park (STEP)****, Thapar Institute of Engineering and Technology for necessitating equipment and facilities to carry out work.*

One more chapter played by Lab assistant ***Mr. Ram Newal (Babban Ji)*** *for his unconditional support and timely help.*

Special thanks to ***Mr. Lallan Yadav, Mr. Surinder, Mr. Mahinder, Mr. Phoolchand*** *and all the* ***non-teaching staff*** *for helping and their ungrudging assistance.*

I extend my profuse thanks to ***Mr. Vijay*** *(Accountant),* ***Mrs. Rachna*** *(Accountant) and* ***Mrs. Nisha*** *for their timely help and cooperation.*

Some contributing people ***Mrs. Ruchi Gupta*** *and* ***Mrs. Manjula Kamra*** *who were the hidden sources of energy that boosted my output. I appreciate their love, care and support. Thank You so much.*

My special thanks to ***Mrs. Renu Bala*** *(Mess Manager) for her moral support, motivation, laughter in our togetherness which drives me to give my best.*

I owe my thanks to my former senior fellow colleagues ***Dr. Sumit Jaiswal, Dr. Santosh*** *and* ***Dr. Charu*** *for their problem-solving attitude and healthy discussions during the course of my research work. Their constant guidance, cooperation and support, has always kept me going*

ahead. I owe a lot of gratitude for always being there for me and I feel privileged to be associated with them during my life.

I wish to extend my thanks to my colleagues ***Dr. Ravneet Kaur, Dr. Vagish, Dr. Devinder Sillu*** *and* ***Dr. Samriti*** *for providing a harmonious atmosphere. Their scientific inputs, personal helps and friendly nature has always made me feel at ease and I could always look back on them for any support during my course of Ph.D.*

I cannot forget to acknowledge the unforgettable workshops and the numerous discussions with my junior fellow workmates ***Simarpreet, Harmeet, Nirmalya, Pawandeep Dr. Ishtpreet, Jyotika****,* ***Amrit, Drishti*** *and* ***Kashmi*** *throughout this tenure that was like a necessary fuel to move on.*

There are friends, there is family and then there are friends that become family. I am fortunate to live uncountable beautiful memories with my dearest friends ***Dr. Nadeem Akhtar, Akashdeep, Aniee, Komal*** *and* ***Pratik****. Even the most difficult times passed with ease just because of the support and care from such friends. I want to make a special mention for them who showed faith in me and my intellect even when I felt like digging hole and crawling into one because I didn't have faith in myself. I could not have asked for more than what I got from you all. I express my sincere love and affection towards all those benevolent souls and true friends.*

Some friends are never too busy to give us a hand whenever they are needed. I humbly thank them all whether they were shaping my life only in a non-academic aspect or also contributing to the academic part as well. I acknowledge my friends ***Sahil Rana, Gerij Sharma, Kriti Dhingra, Sunny Bhardwaj, Vikaran Goyal, Dr. Animesh, Rajesh, Navneet Gill, Vivek, Sanjeev, Dr. Harshit*** *and* ***Kanishq*** *for their love and support during various stages of this journey. Also, countless interactions and chilling moments with them on diversified topics always influenced my perspective to understand nature positively.*

These were Here, I would also like to thank all those who said a clear 'No' to me in any situation because that enormously helped me a lot in my growth.

Words are too meagre a medium to express my feelings of deep gratitude for my father ***Mr. Shashi Kant*** *and mother* ***Mrs. Renuka****. I don't imagine a life without their love and blessings. Without their unwavering support, I would have never found the mental strength to take the initial step towards embarking on my PhD journey. Thank you mummy and papa for unstinted, unflinching support, believing in me, encouraging me to pursue my dreams, standing*

by me, and providing unconditional support through the various ups and downs during this phase. I owe respect for all the sacrifices that they have made on my behalf. Without their love and belief, I may not have embarked on this journey. I consider myself the luckiest in the world to have such a supportive family, standing behind me with their love and support.

A special thanks and a huge token of love for my sister ***Dr. Nidhi****. "Thanks for being brutally honest with me, especially when I was the most ridiculous." My sister has been there throughout, in both my highs and lows, each day of my life as a friend, as a mother and as a confidant. Her presence means the world to me and I am definitely fortunate to have her in my life.*

I highly appreciate unsolicited cooperation and cheery assistance of my uncle ***Divya Kant (Nikku Chachaji),*** *jiju* ***Varun Sethi*** *loving brother* ***Dr. Pranav Kant*** *and most respectable uncle* ***Praful Chander Nagpal (Chachaji)*** *and* ***Subodh Chander Nagpal (Chachaji)*** *as their abundant affection, unflagging love and support were the constant source of inspiration for me.*

I consider it a tremendous privilege to have spent numerous years in the ***Department of Biotechnology*** *at TIET, Patiala, and its members will always hold a special place in my heart. I am grateful to* ***Thapar Institute of Engineering and Technology, Patiala****, for granting me the opportunity to engage in research activities and for fostering an environment that facilitated my holistic development.*

One of the joys of completion is to look over the journey past and remember all the friends and family who have helped and supported along this long but fulfilling road.

All may not be mentioned but no one is forgotten. Thank you everyone for helping me to complete this research work.

Date: May 25, 2023

Place: Patiala ***(Prerna)***

ABSTRACT

Nanomaterials (NMs) tailored *via* conventional physicochemical routes play havoc with the environment which has led to the evolution of competent green routes for the actualization of a circular economy on an industrial scale. “Green route” of synthesis of nanoparticles has emerged as a revolutionary approach. The current study aimed to exploit plant and algal-mediated synthesis of ZnO nanoparticles (ZnO NPs), optimize the process for gram scale synthesis and use the ZnO NPs for the photocatalytic degradation of textile dyes (brilliant green and indigo caramine) and organic pollutants (bisphenol-A).

One-step biosynthesis of ZnO NPs from biomolecules in lemon grass extract was carried out. The main objective was to investigate the role of aqueous extract of lemon grass in the production of ZnO nanoparticles. Different molecules were present in the crude extract of Lemon grass were identified by GC-MS and NMR (^{13}C and ^{1}H NMR) spectroscopy and observed 23 bioactive compounds in the extract rich in various forms of terpenoids, monoterpenes, keto-enol compounds, fatty acids, palmitic acid, and phytol along with some other ancillary phytochemicals which could be potential candidates for capping agents. The abundant presence of citral and photocitral-B in lemon grass extract acted as a coating and provides stability to ZnO NPs. Eco-friendly lemon grass capped ZnO NPs were synthesized using lemon grass extract and confirmed using different characterization techniques like UV- Vis spectroscopy, XRD, SEM and HR-TEM analysis. We found the size of the lemon grass capped ZnO NPs as 43.58± 3.2 nm and the shape of the particles as hexagonal through the HR-TEM analysis

Phycosynthesis of ZnO NPs using a single-step process, from biomolecules present in the cyanobacterial extracts of *Anabaena variabilis* ARM 441 was carried out and analyzed for photocatalytic degradation of textile dyes. The primary focus was to explore the role of aqueous cellular extract of diazotrophic cyanobacterium *A. variabilis* ARM 441 in the fabrication of ZnO NPs. Bioactive components of algal extracts identified by GC-MS and NMR (^{13}C and ^{1}H NMR) spectroscopy, reveals 21 different compounds, among which n-hexadecanoic acid and 13 tetradecenal had properties of reducing and capping agent required in the synthesis of ZnO NPs. Microscopic investigation of particle size and zeta potential confirmed the formation of hexagonal ZnO NPs with an average size of 33.31 nm. The EDX and XPS analyses established

the chemical composition and high purity of ZnO NPs. The rietveld refinement studies of X-ray diffraction studies elucidated crystalline and wurtzite phase of ZnO NPs. Pore size (11.551 nm), surface area (38.718 m^2/g) and pore volume (0.1633 cc/g) were studied by BET analysis.

In order to optimize the synthesis process response surface methodology (RSM) was applied. To get gram scale yield, BBD (Box-Behnken Design) at different parameters was employed to both lemon grass and *A.variabilis* ARM 441 mediated synthesis of ZnO NPs. Impact of three crucial paramters, *i.e.* zinc concentration (mM), reaction time (h) and extract concentration (%) was investigated in both the cases. In case of gram scale synthesis for lemon grass mediated ZnO NPs, numerical optimization result revealed that the hydrothermally green synthesis of ZnO NPs using 550 mM zinc salt concentration, 45% lemon grass extract for 8 h could yield 1857.2 mg ZnO NPs.

Similarly, in case of *A.variabilis* ARM 441 capped ZnO NPs in co-precipitation method, the production was most affected by extract concentration with the highest F-value (369.96). Zinc ion concentration had the second-highest F-value (244.78), whereas reaction time had the lowest (9.69). The overall nanoparticle yield of 1565.26 mg was reported at optimized conditions of 250 mM (Zn^{2+}), 30% algal extract for 6 h. The nanoparticle yield was dependent on the extract's reducing ability (%), which affects zinc ion availability. The rapid interaction between zinc ions and bioactive compounds in the extract reduced the reaction time.

Further, the photocatalytic behavior of Lemon grass *(Cymbopogon citrates)* synthesized ZnO NPs was estimated by the photodegradation of Bisphenol-A (BPA) under UV illumination. After 45 min of exposure of BPA to UV light, about 97.41 % of BPA was degraded with a rate constant 5.15×10^{-2} min^{-1}. The photodegradation of BPA followed pseudo first-order kinetics with catalytic dosage (50mg/100mL), BPA concentration (0.5 mM); pH (6). Further, in the reusability experiments, it was observed that after 5 cycles, the degradation efficiency of ZnO NPs for BPA was 86.9%. Photodegradation was also observed, and its degradation products were analyzed by LC-MS analysis and a metabolic pathway was inferred.

The photocatalytic behaviour of *A.variabilis* ARM 441 synthesized ZnO NPs was estimated by the photodegradation of Brilliant green (BG) and Indigo caramine (IC) under UV illumination. A comparative study was performed to test the photocatalytic efficiency of ZnO NPs with cationic

and anionic dyes. The photodegradation of BG dye followed first-order kinetics with catalytic dosage (50 mg/100 mL), dye concentration (30 mM); pH 7.0. However, in the case of IC, after the exposure of 130 minutes, about 80.8% of the dye was degraded, and it also followed first-order kinetics with catalytic dosage (50 mg/100 ml), dye concentration (30 mM, and pH 5.0. The decolouration reusability experiments for BG and IC were performed. It was observed that after 5 cycles, the degradation efficiency of ZnO NPs for BG and IC was 88% and 69%, respectively. The degradation products were studied *via* LC-MS analysis and identified by interpretation of their *m/z* value. Various by-products of lower masses (*m/z*) at different degradation stages were observed. The opening of the aromatic rings occurred and aliphatic compounds were converted into oxalic acid, which ultimately oxidized into CO_2 and H_2O. Based on the produced metabolites, a degradation pathway was proposed.

The ability of as-prepared ZnO NPs to produce an extensive amount of reactive radicals (such as superoxides, hydroxides and peroxides) owing to their large surface area makes it an eligible photocatalyst. Biosynthesized ZnO NPs showed evidence to act as an effective photocatalyst, which is appropriate for industrial wastewater treatment, especially to degrade harmful and toxic pollutants that persist in aquatic environment.

TABLE OF CONTENT

	Page No.
Acknowledgement	**iii-vii**
Abstract	**viii-x**
Content	**xi-xiv**
List of Figures	**xv-xviii**
List of Tables	**xix-xx**
List of Abbreviations	**xxi-xxiv**
List of Symbols	**xxv-xxvi**
CHAPTER-I Introduction	**1-4**
CHAPTER-II Review of Literature	**5-46**
2.1 Categories of nanomaterials	**5**
2.2 Classification of nanoparticles	**6**
2.3 Synthesis of Nanoparticles	**6**
2.4 Characterization of Nanoparticles	**9**
2.4.1 Spectroscopic and diffractographic techniques	9
2.4.2 Advanced microscopic techniques	10
2.5 Limitations of physicochemical methods	**11**
2.6 Green synthesis of nanoparticles	**12-40**
2.6.1 Plants as a source for bionanomaterial	16
2.6.2 Biosynthesis of ZnO NPs via plants and their possible cause	19
2.6.3 Algae as a source for bionanomaterial	25
Gold nanoparticles from algae	25
Silver nanoparticles from algae	26
Algae-mediated synthesis of other nanomaterials	26
Algae-mediated synthesis of bimetallic nanoparticles	27
2.6.4 Mechanism of synthesis of nanoparticles from algae	**38**
2.6.4.1 Intracellular mode of synthesis of nanoparticles	38
2.6.4.2 Extracellular mode of synthesis of nanoparticles	39
2.7 Zinc oxide nanoparticle	**40-45**
2.7.1 Properties of ZnO	41
2.7.2 Crystal structure of ZnO	42
2.7.3 Lattice Parameters	43
2.7.4 Mechanical Properties	44
2.7.5 Electronic Properties	44
2.7.6 Optical Properties	45
2.8 Application of zinc oxide nanoparticles	**45-46**
2.9 Concluding remarks	**46**
CHAPTER-III Material and Methods	**47-54**

3.1 Material Required **47**
3.1.1 Chemicals and Glassware **47**
General (analytical) chemicals 47
Plants 47
Algal Strains 47
Glassware and plastic ware 47
3.1.2 Sterilization Techniques **47**
3.2 Preparation of extracts **48**
Preparation of Plant extracts 48
Preparation of cyanobacterial cell extracts 48
3.3 GC-MS analysis, ^{1}H NMR, and ^{13}C NMR spectroscopy of extract **49**
3.4 Green synthesis of ZnO Nanoparticles **49-50**
Plant-mediated synthesis of ZnO NPs 49
Phycosynthesis of ZnO NPs 49
3.5 Analytical Characterization of ZnO Nanoparticles **50-52**
3.5.1 UV-Visible spectroscopy 50
3.5.2 Particle size, polydispersity index (PDI), and zeta potential 50
3.5.3 Fourier transform spectroscopy (FT-IR) analysis 50
3.5.4 Brunauer–Emmett–Teller (BET) 50
3.5.5 X-ray powder diffraction (XRD) analysis 51
3.5.6 X-ray Photoelectron Spectroscopy (XPS) 51
3.5.7 Field emission scanning electron microscopy (FE-SEM) and energy-dispersive X-ray spectroscopy (EDX), High-resolution transmission electron microscopy (HR-TEM), and Selected area diffraction (SAED) analysis 51
3.5.8 Thermogravimetric analysis (TGA) 52
3.6 Optimization of nanoparticle synthesis using Response surface methodology (RSM) **52-53**
3.7 Photocatalytic degradation **53-54**
3.7.1 Photocatalytic degradation of Brilliant green and Indigo carmine by ZnO synthesized by *A. variabilis* ARM 441 53
3.7.2 Photocatalytic degradation of Bisphenol- A by ZnO synthesized by Lemon grass 53
3.7.3 Degradation kinetics 54
3.8 Liquid chromatography mass spectroscopy (LC-MS) analysis of by-products **54**
CHAPTER-IV Results and Discussion **55-111**
4.1 Green Synthesis of ZnO nanoparticles **55-69**
4.1.1 Synthesis of ZnO nanoparticles using Lemon grass extract **55**
4.1.1.1 Determination of the content of Lemon grass bio-active compounds 55
GC-MS analysis of extract from Lemon grass 55
^{1}H and ^{13}C NMR Spectroscopic analysis Lemon grass extract 55

4.1.1.2 Biosynthesis of ZnO NPs using extracts from Lemon grass 56
4.1.1.3 Mechanism of Synthesis of ZnO NPs from Lemon grass extract 60
4.1.2 Synthesis of ZnO nanoparticles using *A.variabilis* ARM 441 extract 61
4.1.2.1 Determination of the content of *A. variabilis* ARM 441 bio-active compounds 61
GC-MS analysis of extract from A.variabilis ARM 441 61
^{1}H and ^{13}C NMR Spectroscopic analysis A. variabilis ARM 441 extract 62
4.1.2.2 Biosynthesis of ZnO NPs using extracts from *A.variabilis* ARM 441 66
4.1.2.3 Mechanism of synthesis of ZnO NPs from *A.variabilis* ARM 441 extract 68
4.2 Characterization of ZnO nanoparticles 70-87
4.2.1 Characterization of ZnO NPs synthesized using Lemon grass 70
4.2.1.1 UV-Vis of ZnO NPs synthesized using Lemon grass 70
4.2.1.2 Particle size, polydispersity index (PDI), and Zeta potential of ZnO NPs synthesized using Lemon grass 71
4.2.1.3 Fourier transform spectroscopy (FT-IR) analysis of ZnO NPs synthesized using Lemon grass 71
4.2.1.4 Thermal behaviour of ZnO NPs synthesized using Lemon grass 73
4.2.1.5 Nitrogen adsorption-desorption isotherms analysis (BET analysis) of ZnO NPs synthesized using Lemon grass 73
4.2.1.6 Crystallinity Study of ZnO NPs synthesized using Lemon grass 74
4.2.1.7 Structural and chemical nature of ZnO NPs synthesized using Lemon grass 75
4.2.1.8 Microstructural features of ZnO NPs synthesized using Lemon grass 76
4.2.2 Characterization of ZnO NPs synthesized using *A.variabilis* ARM 441 78
4.2.2.1 UV-Vis Spectroscopy of ZnO NPs synthesized using *A.variabilis* ARM 441 78
4.2.2.2 Particle size, polydispersity index (PDI), and Zeta potential of ZnO NPs synthesized using *A.variabilis* ARM 441 79
4.2.2.3 Fourier transform spectroscopy (FT-IR) analysis of ZnO NPs synthesized using *A.variabilis* ARM 441 80
4.2.2.4 Thermal behaviour of ZnO NPs synthesized using *A.variabilis* ARM 441 81
4.2.2.5 Nitrogen adsorption-desorption isotherms analysis (BET analysis) of ZnO NPs synthesized using *A.variabilis* ARM 441 82
4.2.2.6 Crystallinity Study of ZnO NPs synthesized using *A.variabilis* ARM 441 83
4.2.2.7 Structural and chemical nature of ZnO NPs synthesized using *A.variabilis* ARM 441 84
4.2.2.8 Microstructural features of ZnO NPs synthesized using *A.variabilis* 86

ARM 441
4.3 Process optimization for gram scale synthesis of ZnO nanoparticles **88-95**
4.3.1 Gram scale synthesis of Lemon grass mediated ZnO NPs using Response Surface Methodology (RSM) **88**
4.3.2 Gram scale synthesis of *A.variabilis* ARM 441 mediated ZnO NPs using Response Surface Methodology (RSM) **92**
4.4 Photocatalytic activity of ZnO NPs **96-112**
4.4.1 Photocatalytic activity of Bisphenol A using ZnO NPs synthesized from Lemon grass **96**
4.4.1.1 Mechanism of photodegradation of Bisphenol A 99
4.4.2 Photocatalytic activity of BG and IC using ZnO NPs synthesized from *A.variabilis* ARM441 **101**
4.4.2.1 Mechanism of photodegradation of brilliant green dye 106
Salient Findings **113**
Future scope of work **114**
Bibliography **115-145**
Publications **146**
Conferences and Symposia **147**

LIST OF FIGURES

Figure	Description	Page No
2.1	Classification of Nanomaterials	6
2.2	Synthesis of nanoparticles *via* top down and bottom up approach	8
2.3	Different types of metallic nanomaterials	8
2.4	Advantages of green methods and disadvantages of physicochemical methods	12
2.5	Scheme representing generalized flow of nanoparticle synthesis via green route	13
2.6	ZnO crystal structure (a) rock salt, (b) Zinc blende and (c) Wurtzite	43
3.1	Schematic flow illustrating the preparation of Lemon grass extract	48
4.1	GCMS of Lemon grass extract	57
4.2	^{1}H NMR analysis Lemon grass extract	59
4.3	^{13}C NMR analysis Lemon grass extract	60
4.4	Schematic presentation of synthesis of ZnO NPs from Lemon grass extract	61
4.5	GCMS of *A.varaibilis* ARM 441 extract	64
4.6	^{1}H NMR analysis *A. variabilis* extract	65
4.7	^{13}C NMR analysis *A. variabilis* extract	66
4.8	Schematic flow illustrating the preparation of *A. variabilis* ARM441 extract and formation-mechanism of the ZnO NPs	67
4.9	Schematic diagram of interaction of Zn^{2+} ions with main compounds found in *A.variabilis* ARM 441 to produce ZnO NPs	69
4.10	Plot of $(\alpha h\upsilon)^2$ vs $h\upsilon$ inset UV–vis spectra of the ZnO NPs synthesized using Lemon grass extract	70
4.11	Particle size distribution (DLS histogram) of the ZnO NPs synthesized using Lemon grass extract	72
4.12	FTIR spectra *of A.variabilis* ARM 441 extract and ZnO NPs	72
4.13	TG thermogram of the ZnO NPs synthesized using Lemon grass extract	73
4.14	(a) Nitrogen adsorption-desorption isotherm (b) Pore size distribution curve	74
4.15	(a) Crystallographic (XRD) pattern (b) Reitveild refinement (c,d) Wurzite hexagonal structure of ZnO NPs of the ZnO NPs synthesized using Lemon grass extract	75
4.16	(a) XPS survey scan Deconvolution spectra of	76

	(b) Zn 2p (c) O1s of the ZnO NPs synthesized using Lemon grass extract	
4.17	Micrographs of ZnO NPs synthesized using Lemon grass extract (a, b) FESEM image (c) EDX Spectra	77
4.18	HRTEM image of ZnO NPs synthesized using Lemon grass extract	78
4.19	Plot of $(\alpha h\upsilon)^2$ vs $h\upsilon$ inset UV–vis spectra of the ZnO NPs synthesized using *A.variabilis* ARM 441 extract	79
4.20	Particle size distribution (DLS histogram) of the ZnO NPs synthesized using *A.variabilis* ARM 441 extract	80
4.21	FTIR spectra of *A.variabilis* ARM 441 extract and ZnO NPs	81
4.22	TG thermogram ZnO NPs synthesized using *A.variabilis* ARM 441 extract	82
4.23	(a) Nitrogen adsorption-desorption isotherm (b) Pore size distribution curve	83
4.24	(a) Crystallographic (XRD) pattern (b) Reitveild refinement (c,d) Wurzite hexagonal structure of ZnO NPs synthesized using *A.variabilis* ARM 441 extract	84
4.25	(a) XPS survey scan Deconvolution spectra of (b) Zn 2p (c) O1s using *A.variabilis* ARM 441 extract	85
4.26	Micrographs of ZnO NPs synthesized using *A.variabilis* ARM 441 extract (a, b) FESEM image (c) EDX Spectra	87
4.27	(a,b) HRTEM image; (c) SAED pattern of ZnO NPs synthesized using A.variabilis ARM 441 extract	87
4.28	2D contour and 3D response surface plots for analyzing the interaction effects between (a) Zinc concentration and reaction time, (b) Zinc concentration and Lemon grass extract concentration and (c) Reaction time and Lemon grass extract concentration	91
4.29	2D contour and 3D response surface plots for analyzing the interaction effects between (a) Zinc concentration and reaction time, (b) Zinc concentration and *A.variabilis* ARM 441 extract concentration (c) Reaction time and *A.variabilis* ARM 441 extract concentration	95
4.30	(a) Time dependent photocatalytic degradation studies by ZnO NPs, absorption spectra of BPA samples	97

	(b) Reusability Efficiency of ZnO NPs for BPA	
4.31	Effect of operational parameters on degradation efficiency of ZnO NPs on BPA (a) pH (b) dye concentration (c) catalyst dosage and (d) time	97
4.32	Plots of BPA (a) Time dependent degradation (b) First order kinetics (c) Pseudo first order kinetics (d) Second order kinetics (e) Pseudo second order	98
4.33	Mass spectra of BPA (a) Before irradiation (b) after UV irradiation in the presence of ZnO NPs for 20 and 45 min	100
4.34	Detailed photocatalytic degradation mechanism of BPA by ZnO NPs under UV irradiation	101
4.35	Effect of operational parameters on degradation efficiency of ZnO NPs on BG and IC dyes (a) pH (b) dye concentration (c) catalyst dosage and (d) time	103
4.36	Time dependent photocatalytic degradation studies by ZnO NPs (a) Absorption spectra of BG dye samples (b) Absorption spectra of IC dye samples	103
4.37	Plots of BG and IC dyes (a) Time dependent degradation (b) First order kinetics (c) Pseudo first order kinetics (d) Second order kinetics (e) Pseudo second order	104
4.38	Degradation of IC and BG (a) in presence ZnO NPs and absence of UV light (b) in absence of ZnO NPs and presence of UV light	105
4.39	Reusability Efficiency of ZnO NPs for BG and IC	105
4.40	Mass spectra of BG Dye (a) Before irradiation (b) after UV irradiation in the presence of ZnO NPs for 60 and 130 min	109

4.41	Mass spectra of IC Dye (a) Before irradiation (b) after UV irradiation in the presence of ZnO NPs for 130 min	110
4.42	Detailed photocatalytic degradation mechanism of BG dye by ZnO NPs under UV irradiation	111

LIST OF TABLES

Table	Description	Page No
2.1	Comparison between physicochemical and green methods	11
2.2	Green synthesis of metallic NPs from various plant extracts	17
2.3	Synthesis of ZnO NPs from various plant extracts and their application	20
2.4	Algae mediated synthesis of gold nanoparticles (Au-NPs)	29
2.5	Algae mediated synthesis of silver nanoparticles (Ag-NPs)	31
2.6	Algae mediated synthesis of other nanomaterials (NMs)	36
2.7	Physical properties of ZnO	42
3.1	The ranges and levels of variables in Box–Behnken statistical experimental design for Lemon grass	52
3.2	The ranges and levels of variables in Box–Behnken statistical experimental design for *A. variabilis* ARM 441	52
4.1	Bioactive compounds of Lemon grass extract identified through GC–MS analysis	58
4.2	Characteristic peaks of Lemon grass extract identified through of ^{1}H and ^{13}C NMR	59
4.3	Bioactive compounds of *A. variabilis* ARM 441 extract identified through GC–MS analysis	63
4.4	Characteristic peaks of *A. variabilis* ARM 441 extract identified through of ^{1}H and ^{13}C NMR	65
4.5	Refined Parameters and phase data of ZnO NPs synthesized using Lemon grass	74
4.6	Refined Parameters and phase data of ZnO NPs synthesized using *A.variabilis* ARM 441	84
4.7	RSM based Box-Behnken Design for the independent variables and their corresponding response for nanoparticle synthesis using Lemon grass extract	89
4.8	ANOVA results of response surface quadratic model for nanoparticle yield (mg) using Lemon grass extract	89
4.9	ANOVA results for the coefficients of response surface quadratic model for nanoparticles yield (mg) using Lemon grass extract	90
4.10	RSM based Box-Behnken Design for the independent variables and their corresponding response for nanoparticle synthesis using *A.variabilis* ARM 441 extract	92
4.11	ANOVA results of response surface quadratic model for nanoparticle yield (mg) using *A.variabilis* ARM 441 extract	93
4.12	ANOVA results for the coefficients of response surface quadratic model	94

for nanoparticles yield (mg) using *A.variabilis* ARM 441 extract

4.13	Kinetic parameters for degradation of BPA via ZnO NPs under UV-illumination	96
4.14	Kinetic parameters for degradation of BG and IC via ZnO NPs under UV-illumination	102
4.15	Comparison of photocatalytic performance of green synthesized ZnO NPs with other green synthesized ZnO nanomaterials on degradation of different organic pollutants	112

LIST OF ABBREVATIONS

^{13}C NMR	Carbon 13 nuclear magnetic resonance
^{1}H NMR	Proton nuclear magnetic resonance
Å	Angstrom
AAS	Atomic absorption spectroscopy
Ag NP	Silver nanoparticle
AgCl	Silver chloride
$AgNO_3$	Silver nitrate
ANOVA	Analysis of Variance
Au NP	Gold nanoparticle
BBD	Box-Behnken Design
BET	Brunauer-Emmett-Teller
BG	Brilliant green
BPA	Bisphenol-A
cc g^{-1}	cubic centimeters per gram
CdS	Cadmium sulphide
cm	centimeters
CO_2	Carbon dioxide
CuO	Copper oxide
DLS	Dynamic light scattering
DNA	Deoxyribonucleic acid
DRS	Diffuse reflectance spectroscopy
DSC	Differential scanning calorimetry
EDS/EDX	Energy dispersive x-ray spectroscopy
ESI	Electrospray ionization
et al	And others
etc	And other things
FCC	Face centered cubic
FE-SEM	Field emission scanning electron microscopy
$FeSO_4.7H_2O$	Ferrous sulphate heptahydrate

FT-IR	Fourier transform infrared spectroscopy
g	Gram
g cm^{-1}	Gram per centimeter
g kg^{-1}	Gram per kilogram
g L^{-1}	Gram per liter
g mol^{-1}	Gram per mole
GC-MS	Gas chromatography–mass spectrometry
GLC	Gas–liquid chromatography
h	Hour
H_2O	Water
H_2O_2	Hydrogen peroxide
H_2SO_4	Sulfuric acid
HCl	Hydrochloric acid
HPLC	High-performance liquid chromatography
HR-TEM	High resolution-transmission electron microscopy
Hz	Hertz
I_2O_3	Indium Oxide
IC	Indigo carmine
ICP-AES	Inductively coupled plasma atomic emission spectroscopy
JCPDS	Joint Committee on Powder Diffraction Standards
k	Rate constant
kb	Kilo base
kDa	Kilodalton
kg	Kilogram
L	Liter
L h-1	Liter per hour
LC-ESI-Q-TOF-MS	Liquid chromatography-electrospray ionization quadrupole time-of-flight mass spectrometry
M	Molar
m/z	Mass by charge
mA	Milliampere

MALDI-TOF	Matrix-assisted laser desorption ionization–time-of-flight
MB	Methylene blue
mg	Milligram
MG	Malachite green
mg g^{-1}	Milligram per gram
mg kg^{-1}	Milligram per kilogram
mg L^{-1}	Milligram per litre
MHz	Mega hertz
min	Minute
mL	Milliliter
mM	Millimolar
mm	Millimeter
MO	Methyl orange
N	Normal
NaOH	Sodium hydroxide
ng	Nanogram
ng g^{-1}	Nanogram per gram
ng mL^{-1}	Nanogram per milliter
NIST	National Institute of Standards and Technology
nm	Nanometer
NM	Nanomaterial
NPs	Nanoparticles
O_2	Oxygen
OD	Optical Density
Pa	Pascal
PDI	Polydispersity index
ppm	Parts per million
PZC	Point of zero charge
R^2	Regression coefficient
R^2adj	Adjusted R-squared
RB	Rhodamine B

RNA	Ribonucleic acid
rpm	Revolution per minute
RSM	Response surface methodology
s	Second
SAED	Selected area diffraction
SDS	Sodium dodecyl sulphate
SEM	Scanning electron microscopy
SiO_2 NP	Silica nanoparticle
STEM	Scanning transmission electron microscopy
TEM	Transmission electron microscopy
TGA	Thermo gravimetric analysis
TiO_2	Titanium oxide
UV	Ultra violet
VB	Valence band
viz.	As follows
VSM	Vibrating-sample magnetometer
W	Watt
WD-XRF	Wavelength dispersive X-ray fluorescence
XANES	X-ray absorption near edge strucure
XPS	X-ray photoelectron spectroscopy
XRD	X-ray diffraction
$Zn(CH_3COO)_2$	Zinc acetate
ZnO	Zinc oxide
µg	Microgram
µg g^{-1}	Microgram per gram
µg kg^{-1}	Microgram per kilogram
µg L^{-1}	Microgram per liter
µg mL^{-1}	Microgram per milliliter
µL	Microliter
µm	Micrometer
χ^2	Reduced Chi-square

LIST OF SYMBOLS

%	Percentage
θ	Angle
®	Registered
°C	Degree Celsius
µ	Micron
Ag	Silver
Au	Gold
C	Carbon
Cu	Copper
Da	Dalton
Fe	Iron
H	Hydrogen
h	Hours
Hg	Mercury
K	Kelvin
kDa	Kilo Dalton
L	Liter
M	Molar
Mg	Magnesium
N	Nitrogen
Ni	Nickel
O	Oxygen
P	Phosphorus
Pd	Palladium
Pt	Platinum
S	Sulfur
™	Trademark
U	Unit
V	Volt

v/v	Volume by volume
w/v	Weight by volume
Zn	Zinc
α	Alpha
β	Beta
γ	Gamma
λ	Lambda
π	pi

CHAPTER-I Introduction

Nanotechnology has allured tremendous attention due to parallel augmentation in experimental techniques for the development of sustainable materials and resources. It is a diverse and contemporary field of research, stimulating the development of nanoscale systems and analysing their assets *via* size, shape, and morphology. Nanoparticles bridge the gap between bulk materials and atomic or molecular structures. Generally, nanomaterials possess a high surface area to volume ratio with improved surface functionalization, making nanoparticles exhibit pharmacological activity, thermal conductivity, optoelectronic properties, chemical steadiness, and catalytic reactivity (Borah *et al.*, 2020). Such widespread applications of nanomaterials have opened novel frontiers in innovating protocols for the synthesis of nanoparticles.

The existing physicochemical methods are often complicated as they may involve toxic reducing and stabilizing agents, non-biodegradable organic and inorganic chemicals, have high-energy consumption with relatively low yield (He *et al.*, 2017; (Agarwal, Venkat Kumar and Rajeshkumar, 2017). The resulting nanomaterials retain the capping of hazardous chemical reagents involved in the conventional synthetic process, resulting in diminished therapeutic applications of nanoparticles (Borah *et al.*, 2020). However, there are many reports in the existing literature indicate that the biological synthesis of metallic and metal oxides nanoparticles is more environmentally friendly than the conventional chemical or physical methods (Kharissova *et al.*, 2013; Makarov, Love and Sinitsyna, 2014; Bandeira *et al.*, 2020). Thus, a crucial need for the development of green strategies has emerged.

A wide array of plants, bacteria, fungi, lichens, virus, algae etc. have been employed for the synthesis of nanoparticles as a bio-compatible alternative which is a harmless and environment-friendly approach (Parveen *et al.*, 2022). The extracts of these bio-moieties have a cocktail of natural compounds such as phenolics, terpenoids, flavonones, amines, amides, proteins, pigments, alkaloids etc., which assists in both metal reduction and their stabilization at ambient temperature with controlled pH for the desired size, shape and composition of nanoparticles (Asmathunisha and Kathiresan, 2013). Noteworthy, such green approaches have advantages include large-scale, cost-effective nanoparticles free from noxious chemicals (impurities) and easy accessibility of raw materials from natural surroundings. Although greener technologies would not be an alternative to physico-chemical methods, lesser damage to the ecosystem could

be definitely assured. The existing literature on green approaches for the synthesis of nanoparticles using phyto-ingredients is voluminous.

Biosynthesis of ZnO nanoparticles has been documented using a wide variety of plant species, with the Fabaceae family (including *Aspalathus linearis, Cassia fistula)* and the Rutaceae family (including *Citrus limon*, *Limonia acidissima*) being the most frequently used followed by Apocynaceae, Solanaceae and Lamiaceae (Basnet *et al.*, 2018). Amongst the different plants used for the fabrication of various types of nanoparticles, lemon grass chosen due to easily availability and cultivability. The *Cymbopogon citrate* (lemon grass) is a member of the family of Gramineae, and is a herb that is known worldwide for its high essential oil content. Traditional applications of lemon grass in different countries show its diversity as a common tea, medicinal supplement, insect repellent, insecticide, and as anti-inflammatory and analgesic. Although several works have extensively reported on lemon grass, using various nanoparticles synthesised from its different types of solvent extracts, there is a deficiency of information regarding the synthesis of ZnO NPs from aqueous extract of lemon grass (Riyanto *et al.*, 2022).

Algae, the largest photoautotrophic group of microorganisms, are the storehouse of secondary metabolites, pigments, and proteins. Algae belonging to different classes such as *Cyanophyceae, Chlorophyceae, Phaeophyceae,* and *Rhodophyceae* have been widely exploited for intracellular and extracellular synthesis of metallic nanoparticles (Ag, Au, Pt, Ni, etc.) and metal oxide nanoparticles (CuO, ZnO, MnO_2, TiO_2, Fe_3O_4, etc.) (Suresh *et al.*, 2015). However, in contrast to other microorganisms, very few algae have been screened for their ability to promote the biogenic synthesis of ZnO NPs. *Anabaena variabilis* ARM 441 was chosen because it grows luxuriantly in paddy fields and it can be easily cultivated in inorganic media (Chittora *et al.*, 2020). The present research was focused to explore the role of aqueous cellular extract of diazotrophic cyanobacterium *A. variabilis* ARM 441 in the fabrication of ZnO NPs (Malek Shahkouhi and Motamedian, 2020).

ZnO is essentially a multifaceted semiconductor with some exciting characteristic properties such as non-toxicity, wide band gap (~3.37 eV), excitation energy (60 meV) (Aminuzzaman *et al.*, 2018), high electron mobility, broad absorption range, high thermal and chemical stability, large binding energy, excellent transparency in the visible range, photostability, oxidation resistivity, high piezoelectric features, biocompatibility and biodegradability (Ebadi *et al.*, 2019). ZnO NPs are exceptionally advantageous, as they have exhibited outstanding

performances in various fields such as cosmetics, food packaging, anti-corrosives, sensors, electronics, communication, agriculture, environmental remediation, and medicinal therapeutics and photo-catalysis (Chauhan, Kataria and Garg, 2020; Rafique *et al.*, 2022).

Green synthesis of NPs is impacted by various factors such as solution pH, synthesis temperature and time, extract concentration, and synthesis process. The effect of these individual parameters on green synthesis of NPs has been studied extensively (Nayak *et al.*, 2020). Response surface methodology (RSM) is a robust analytical tool that enables the prediction of the correlation between independent parameters and system responses, including their interactions. It additionally delineates the impact of individual and interactive factors on the process under consideration (Surendra *et al.*, 2016). The utilization of RSM has been prevalent in the design of experiments and optimization procedures through the amalgamation of mathematical modelling and statistical techniques (Perez *et al.*, 2017).

Brilliant green (BG) (4-{[4-(diethylamino)phenyl](phenyl)methylidene}-N,N-diethylcyclohexa -2,5-dien-1-iminium) is triphenylmethane based cationic dye (Alderman, 1985) which has insightful applications as a biological stain (Zhang *et al.*, 2019), as a dermatological agent, as a veterinary medicine, an additive to poultry feed to inhibit propagation of mould, intestinal parasites and fungus (Demirbas, 2009). It has extensive usage in the leather, textile and paper industry (Bhattacharya *et al.*, 2019). Time bound exposure of hazardous BG dye causes gastrointestinal and respiratory tract irritation in humans. Rarely, exposure of this perilous dye to skin may lead to dermatitis.

Indigo carmine (IC) (3,3’-dioxo-2,2’-bisindolyden-5,5’-disulfonic acid sodium salt) is an anionic dye belonging to the highly toxic indigoid class of dye (Ryali and Sanasi, 2018). It is widely used as a colorant in the textile industry and as an additive in pharmaceutical capsules and food items (Lakshmi *et al.*, 2009). It has widespread application in the health industry (Almoisheer *et al.*, 2018); however, prolonged consumption of IC tainted water can cause mild to severe hypertension, cardiovascular and respiratory disorders (Subramani *et al.*, 2007). It may have deleterious carcinogenic impact on reproductive, developmental, and neuronal health (Yazdi *et al.*, 2018). Moreover, the presence of these hazardous dye molecules in the industrial effluent streams that mixes with river and domestic water sources leads to a polluted water ecosystem (Ali *et al.*, 2019; Chauhan, Kataria and Garg, 2020). Hence, effective treatment of these dye polluted aqueous streams by a simple, effective and low-cost methodology is needed (Aminuzzaman *et al.*, 2021; Rambabu *et al.*, 2021).

Bisphenol-A (BPA) sourced from biomass is commonly employed as a stabilizer during the production of plastics and epoxy resins. It was reported that global consumption of BPA reached approximately 7.7 million metric tonnes in 2015, with an anticipated annual growth rate of nearly 5% (Wang *et al.*, 2020). Bisphenol-A is widely known as an endocrine disruptor compound (EDC) and possess carcinogenic and genotoxic properties. A substantial amount of BPA was detected in surface water (193 ng/L) and subsurface and bottom water (39 ng/L) (Rachna, Rani and Shanker, 2019). The release of BPA into the ecosystem poses a potential risk to human well-being, even at the minimum levels of exposure. It has been established that BPA exhibits stability in an aqueous solution and demonstrates resistance to degradation due to its symmetrical structure comprising two benzene rings. Therefore, the imperative and pressing need lies in the advancement of effective techniques for the elimination of BPA from aqueous systems (Ye *et al.*, 2019; Wang *et al.*, 2020)

The rationale of the current study was the synthesis of ZnO NPs *via* green routes by exploiting the extracts of plants and algae. ZnO NPs were synthesized using aqueous extracts of Lemon grass and *A. variabilis* ARM 441 and were characterized using various spectroscopic and microstructural techniques. Gram scale synthesis of ZnO NPs using both the extracts was optimized using response surface methodology. Photocatalytic degradation of organic pollutants (Bisphenol A) and textile dyes (Brilliant green and Indigo caramine) by synthesized ZnO NPs was studied and metabolites of degradation were analysed and plausible degradation pathway is proposed.

Objectives

1. Green synthesis of ZnO nanoparticles
2. Characterization of ZnO nanoparticles
3. Process optimization for gram scale synthesis of ZnO nanoparticles

CHAPTER-II Review of Literature

Nanotechnology is the design, characterization, and application of structures, systems and devices by controlled manipulation of size and shape of particles at the nanometric scale (10^{-9} m) (Basnet *et al.*, 2018). The particles are reduced down to the nano-regime because of their superior characteristics compared to the bulk particles. Due to the vastly superior properties of nanoparticles compared to their bulk counterparts (such as greater chemical reactivity), there has been extensive research into synthesizing and optimizing nanoparticles (Mittal, Chisti and Banerjee, 2013; Vinotha *et al.*, 2019). In addition, the fabrication of nanoparticles is cheaper, easier, and requires a much smaller quantity per application. It is well established in the scientific literature that the properties of nanoparticles depend on their morphology and size (Vinotha *et al.*, 2019; Borah *et al.*, 2020).

2.1 Categories of nanomaterials

Metal oxides – The majority of commercial nanomaterials are ceramics made from oxides of zinc, iron, cerium, silicon, and zirconium. These materials are utilised in chemical polishing agents for scratch-resistant coatings, cosmetics, and sunscreens (Shanmugapriya, Thanuja and Anusuya, 2013).

Nanoclays – These plate-shaped clay particles exist naturally and are employed to boost a material's tensile strength, flexural rigidity, thermal stability, and flammability. They are utilized in the manufacturing of tennis balls, plastic water bottles, paper juice boxes, and other barrier films (Espitia *et al.*, 2012).

Nanotubes and spheres – These are particularly utilized in coatings to decrease static electricity in hard disc handling trays and fuel lines. It can also be found in field emitter sources in flat panel displays, flame-retardant fillers for polymers, and electrostatically paintable exterior automobile parts (Nath and Sahajwalla, 2012)

Quantum dots – These are exploited in the investigative fields of medical diagnostics and therapies, as well as in the self-assembly of nanoelectronic structures.

A wide range of nanoparticles (NPs) exists naturally in the environment or can be fabricated artificially; the latter is sometimes called anthropogenic NPs. Despite the presence of natural NPs in living organisms, their existence is assumed in the biosphere since the genesis of the earth. Natural NPs can be obtained as a result of forest fires, volcanic eruptions, weathering of rocks, explosion of clay minerals, soil erosions, and sandstorms (Baker *et al.*, 2013).

2.2 Classification of nanoparticles

Nanoparticles bridge the gap between bulk materials and atomic or molecular structures. Physicochemical synthesis of NPs is often cumbersome and costly with the release of harmful by-products posing a high risk to living systems (Borah *et al.*, 2020). NPs are classified in different categories based on shape and dimension, phase composition and nature of the material (Fig: 2.1).

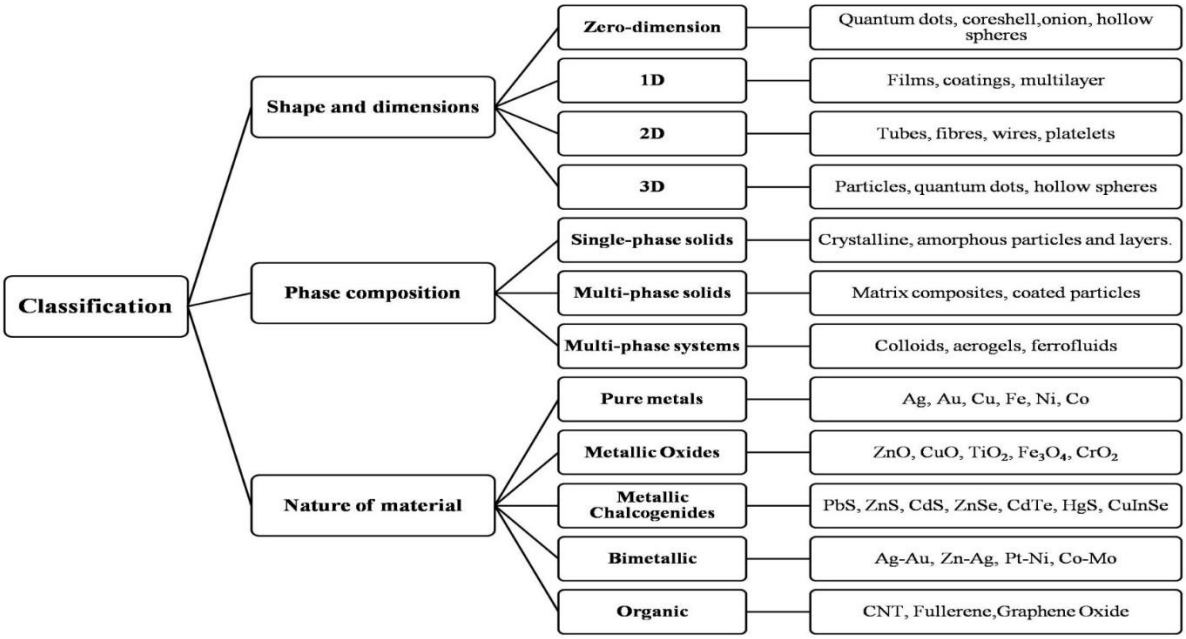

Fig. 2.1: Classification of Nanomaterials

2.3 Synthesis of nanoparticles

Fundamentally there are two approaches for the synthesis of NPs, the top-down approach and the bottom-up approach). The top-down approach involves slicing of bulk materials into reduced size self-assembled nanoscale objects. It often uses microfabrication techniques, where externally controlled tools are used to cut, mill, and shape materials into the desired size and shape (Debjani

Nath and Banerjee, 2013; Khan, Saeed and Khan, 2017). A variety of metallic NPs were fabricated by top-down approaches like mechanical milling (Arbain, Othman and Palaniandy, 2011), etching (Cheng *et al.*, 2016), laser ablation (Amendola and Meneghetti, 2009), sputtering (Matsumura and Tarin, 2020) and electro-explosion (Ghorbani, 2014).

Whereas the bottom-up approach is reversed altogether therefore referred to as molecular nanotechnology involving assembly of a defined structure by joining atom by atom, molecule by molecule, cluster by cluster or self-organization (Thakkar, Mhatre and Parikh, 2010). In this mode, self-assembled properties of single molecules are exploited to build up complex conformations at the nanoscale (D. Nath and Banerjee, 2013). Nanoscale structures that have been reported to be synthesised by bottom up approaches are supercritical fluid synthesis (Türk and Erkey, 2018), use of templates (Apolinário *et al.*, 2014), plasma or frame spraying synthesis (Tanaka, 2018) sol-gel process (Sekine *et al.*, 2009), laser pyrolysis (D'Amato *et al.*, 2013), chemical vapour deposition (Bhaviripudi *et al.*, 2010), molecular condensation (Gurentsov, Eremin and Schulz, 2007), chemical reduction (Guzmán, Dille and Godet, 2009) and most significantly green synthesis (González-Ballesteros *et al.*, 2017) (Fig. 2.2). The main focus is inclined towards the synthesis of NPs of different chemical composition, sizes, morphologies and monodispersity (Sastry *et al.*, 2003; Iravani, 2011).

In top-down approaches, physicochemical processes are involved which may lead to surface imperfections that affect the NPs properties. Similarly, in bottom-up approaches, NPs are clustered from smaller units. So in both cases, the growth of the NPs is controlled *via* kinetic processes which determine the shape and size of the NPs. The energy and growth rate of crystals are monitored by introducing compatible templates or surfactants which can curtail the interfacial energy (Khan, Saeed and Khan, 2017; Khan *et al.*, 2018).

There is an array of various kinds of metallic NPs depending on their metallic behaviour, magnetic properties etc. (Fig. 2.3). Up until now, various commercial surfactants such as cetyl trimethyl ammonium bromide (CTAB), polyvinylpyrrolidone (PVP), sodium dodecyl sulfate (SDS), thioglycerol (TG), mercaptoethanol (ME), sodium hexametaphosphate (SHMP) (Rahdar 2013) have been used as capping agents, which could directly modify the surface morphology of NPs during their synthesis. Usually, a colour change is the convenient visible signature and the

qualitative indication for any reaction to take place in the biological/chemical synthetic process. Most of the NPs are fabricated in a colloidal solution which can be detected easily (Poinern, 2014; Khan, Saeed and Khan, 2017). After completion of the reaction, the NPs are subjected to simple downstream processing such as high-speed centrifugation for their recovery (Poinern, 2014).

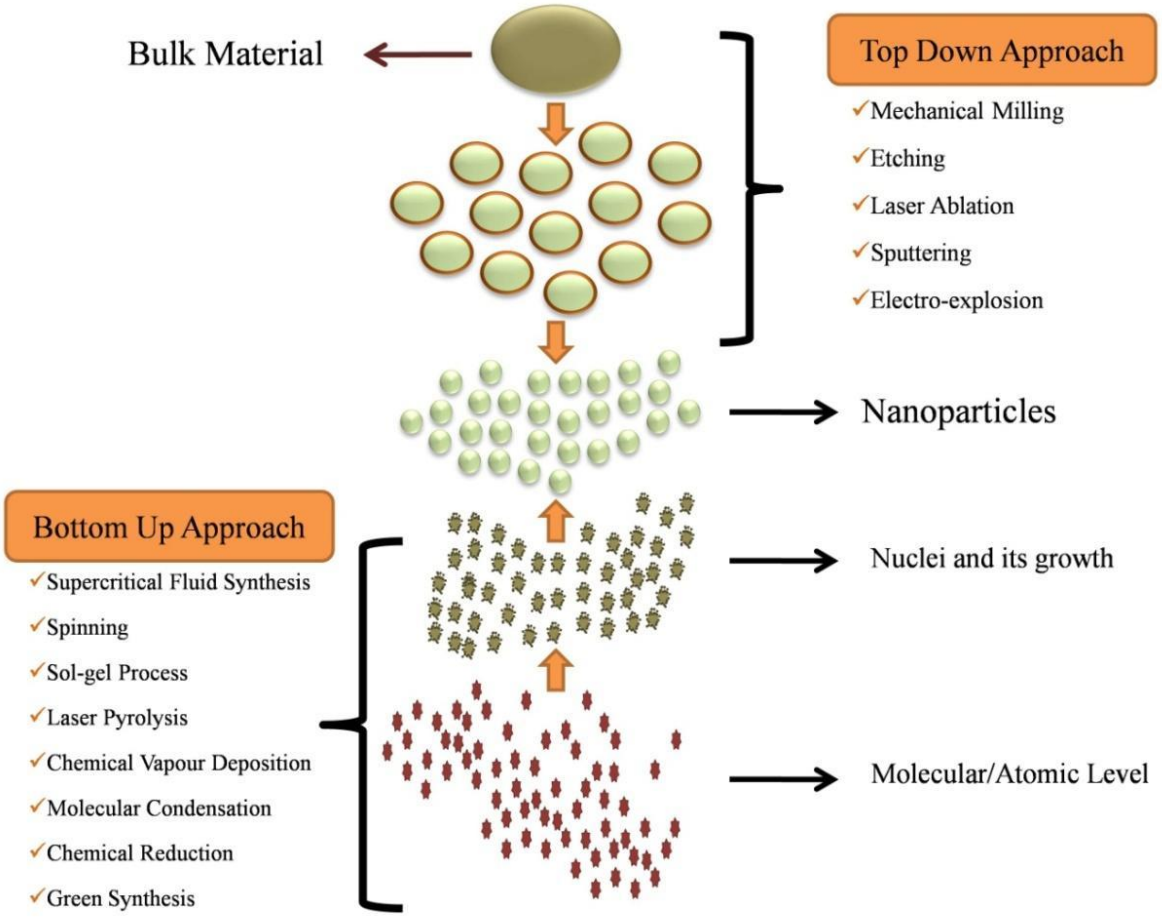

Fig. 2.2: Synthesis of nanoparticles *via* top down and bottom up approach

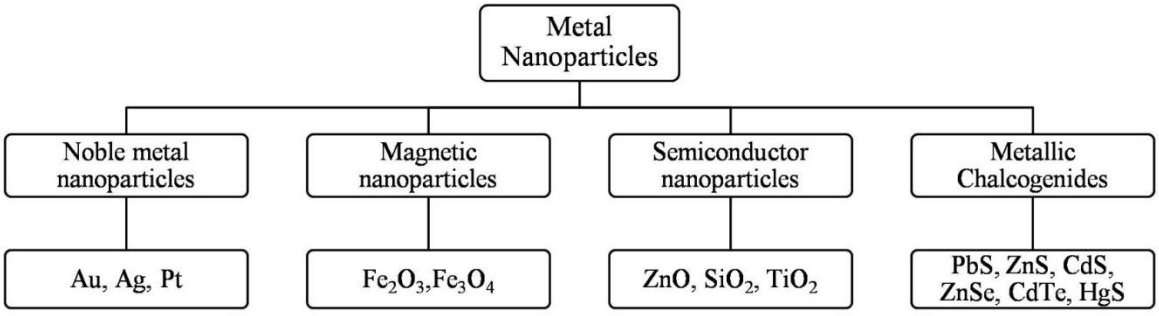

Fig. 2.3: Different types of metallic nanomaterials

2.4 Characterization of nanoparticles

Nanoparticles are subjected to various characterization techniques to ascertain their size, shape, distribution, surface morphology, and surface area. Spectroscopic and diffractographic techniques involved in the characterization include UV-visible spectroscopy (UV-vis), dynamic lights scattering (DLS), energy dispersive spectroscopy (EDS), X-ray diffraction (XRD), Fourier transform infrared spectroscopy (FT-IR), X-ray photo-electron spectroscopy (XPS) and Raman spectroscopy (Shah *et al.*, 2015; Menon, S. and S., 2017). These are the indirect methods used to analyse composition, structure, and crystal phase. Whereas scanning electron microscopy (SEM), transmission electron microscopy (TEM), high-resolution transmission electron microscopy (HR-TEM), and atomic force microscopy (AFM) are employed to determine the size and morphological features of NPs (Quester, Avalos-Borja and Castro-Longoria, 2013; Hulkoti and Taranath, 2014).

2.4.1 Spectroscopic and diffractographic techniques

Generally, metallic NPs have striking optical properties due to surface plasmon resonance (SPR), which is monitored by UV-Vis spectroscopy within the range of 190-1100 nm (Sharma *et al.*, 2016). These radiations interact with the metals and promote the electronic transition from ground to higher energy state and a specific SPR band is obtained which may help to obtain the size and shape of NPs up to a certain limit (2-100 nm) (Poinern, 2014). The absorption spectra for different materials is different e.g. for Ag-NPs it is 400-450 nm (Aboelfetoh, El-Shenody and Ghobara, 2017), for Au-NPs it falls in between 500-550 nm and for ZnO-NPs it is between 350-390 nm (Poinern, 2014; Shukla and Iravani, 2017).

It has been suggested that the broadening of the SPR band width, which illustrates a shift toward the red or blue end is considered as an index of size, state of aggregation, shape, the type of capping or binding agents, polydispersity, and the surrounding dielectric medium (Govindaraju et al., 2008; Jena et al., 2013, Mahmudin et al., 2015). Furthermore, an increase in particle size in the aqueous solution is depicted by an increase in band intensity. UV/Vis- diffuse reflectance spectrometer (DRS) is a fully equipped device, which can be used to measure the optical absorption, transmittance and reflectance. DRS is an exceptional technique to calculate the bandgaps of NMs which is important for determining the photoactivity and conductance of the material (Khan, Saeed and Khan, 2017; Shukla and Iravani, 2017).

To investigate the underlying mechanism of synthesis and surface chemistry, FT-IR spectroscopy is done to identify the functional groups attached to the NPs. Usually, it ranges between 4000 and 400 cm^{-1}, and a resolution of 4 cm^{-1} gives a clear idea about the reducing agents responsible for capping, reduction and stabilization. The comparison between the transmittance spectra of aqueous native extract and reaction medium gives an idea of the biomolecules involved in the process (Dahoumane *et al.*, 2016). Most common functional groups, which adhere to the NPs are −C=O−, $-NH_2-$ and −SH− (Jena *et al.*, 2015). However, FT-IR has limitations because of the high degree of overlapping of IR absorption bands in the complex biological matrix. Additionally, other characterization techniques, such as XPS, could shed light on the interaction between the produced NPs and their surrounding biomolecules (Dahoumane *et al.*, 2016).

Surface charge, hydrodynamic diameter and distribution of NPs in liquid form is measured by DLS spectroscopy and particle stability is determined by zeta potential (Poinern, 2014). Whereas the purity, crystalline size, geometry, orientation and phases can be determined by XRD data, generally the diffraction patterns are compared with the standard crystallographic database like JCPDS to have the structural information (Shah *et al.*, 2015). It gives a rough idea about the particle size determined by Debye Scherer formula (Shah *et al.*, 2015). XRD works well with both single and multiphase identification of NPs. Moreover, XRD diffractogram gets influenced with amorphous NMs having varied inter-atomic lengths (Ingham, 2015).

2.4.2 Advanced microscopic techniques

Properties of NPs are greatly influenced by their morphology which is studied by advanced microscopic techniques such as SEM, TEM, AFM and HR-TEM. SEM provides information about particles at the nanoscale and assists in determining the surface morphology and dispersion of NPs in bulk or matrix. TEM is most commonly used for size and shape, and it can also provide information about the number of material layers as it varies from low to high magnification. However when both are combined with EDAX or EDS, information is given about the metals present (Oza *et al.*, 2012). In some cases of intracellular synthesis of NPs, localization of synthesized NPs is explored by SEM and TEM. However, in order to determine the exact shape, size and crystalline structure HR-TEM is absolutely required. AFM on the other hand provides information on surface topography. While TEM images mainly represent a two-dimensional image

of three-dimensional nanoparticles, AFM can be used to obtain three-dimensional information of synthesized particles (Quester, Avalos-Borja and Castro-Longoria, 2013; Khan, Saeed and Khan, 2017).

2.5 Limitations of physicochemical methods

Physical and chemical approaches have been mostly relied upon to confirm the synthesis of metal nanoparticles because of their consistency in yielding highly pure and well defined nanoparticles (Sailaja, Amareshwar and P.Chakravarty, 2011). Unfortunately, these techniques are extremely costly, poisonous, time-consuming, heat-intensive, chemically damaging, non-sustainable, and inefficient. These procedures necessitate the utilization of strong and weak chemical reducing agents and protecting agents, such as sodium borohydride alcohols, phenyl hydrazine, sodium citrate, etc., which are poisonous, combustible, and unsafe for direct exposure in the natural environment (Borah *et al.*, 2020). Therefore, it is essential to use environmentally friendly strategies for nanoparticle synthesis (Table 2.1, Fig. 2.4).

Table 2.1: Comparison between physicochemical and green methods

Property	**Physicochemical method**	**Green method**
Particle size	Smaller	Larger
Cost	Higher experimental duration	Lower experimental duration
Toxicity	Toxic, involves the use of noxious chemicals	Non-toxic, involves the use of extracts of biological moieties
Stability	Unstable (without capping agents) or stable (with capping agents)	Stable (As the extracts act as both reducing as well as capping agent)
Application		
a) Photocatalytic efficiency b) Anti-microbial activity	a) Higher photocatalytic efficiency b) Lower anti-microbial activity	a) Lower photocatalytic efficiency b) Higher anti-microbial activity

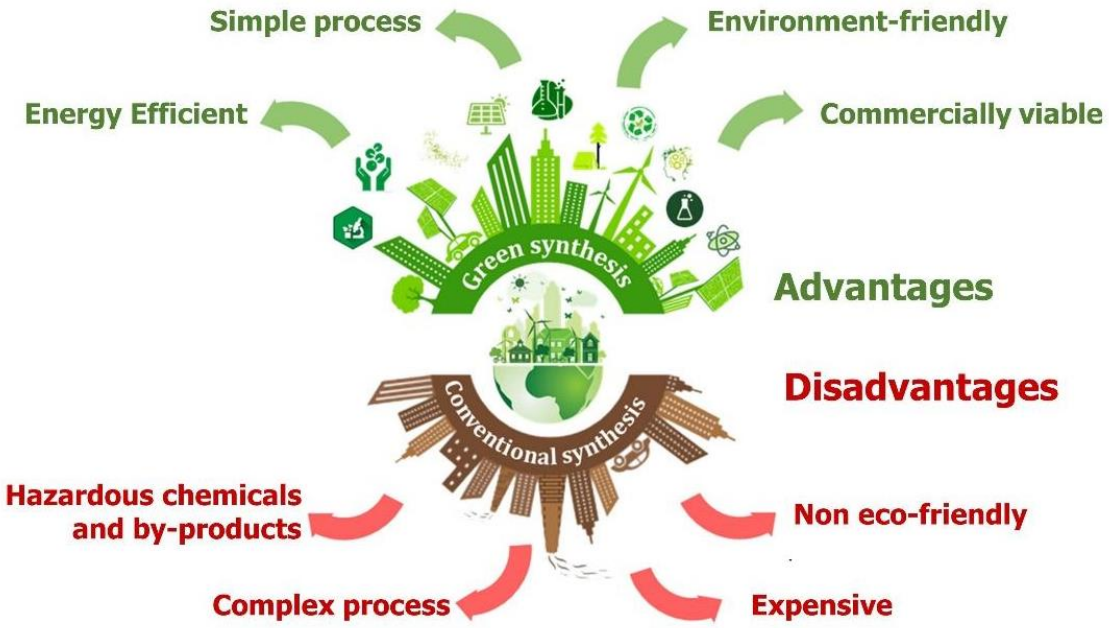

Fig. 2.4: Advantages of green methods and disadvantages of physicochemical methods (Duvauchelle, Meffre and Benfodda, 2023)

2.6 Green synthesis of nanoparticles

Producing and stabilizing nanoparticles via chemical processes necessitates the use of potentially dangerous compounds, which represent a significant risk to both humans and animals. On the other hand, components that are biologically produced can be employed to create nanoparticles because they are chemically and environmentally safe. As a result, nanoparticles can be synthesized using a single-step, pollution-free technique that requires less energy to initiate the reaction and has a shorter production time as compared to conventional methods. The key asset of this green synthesis is its affordability and cost-effectiveness. As the reducing agents involved in this process are readily accessible biological species or plants, there is no need to dispose of any hazardous and usually poisonous wastes associated with these procedures (Kumar *et al.*, 2021). In addition, the green synthesis method can be applicable for large scale, and their prospective uses are vast due to the abundance of plant species and related substances (Zeghoud *et al.*, 2022).

Synergy between engineering and medical sciences has opened novel frontiers in the ever-growing new domain of nanotechnology aimed at genesis, implementation and use of nanomaterials (NMs) to integrate with biological research. The fountainhead of nano-biotechnology is the fabrication of

nanoscale particles by virtue of biological moieties that influence the characteristics of nanoparticles (NPs). Synthesis of NMs of diverse sizes and shapes has underpinned great interest due to their novel properties as compared to their bulk counterparts. Consistency in the chemical, biochemical and physicochemical properties of materials varies immensely at the nanoscale mainly due to the high aspect ratio of surface area to volume. This leads to considerable differences in biological and catalytic activity, mechanical properties, melting point, optical absorption, thermal and electrical conductivity (Shah *et al.*, 2015). Biological synthesis of NPs using microbes, enzymes, plants, and algae has been proposed as an alternative to chemical and physical modes of synthesis. The prime focus is on selecting the compounds which are competent, harmless, eco-friendly and commercially viable. For the green synthesis, the following factors must be considered in order to produce highly stable and well-characterized nanoparticles (Iravani, 2011) (Fig. 2.5)

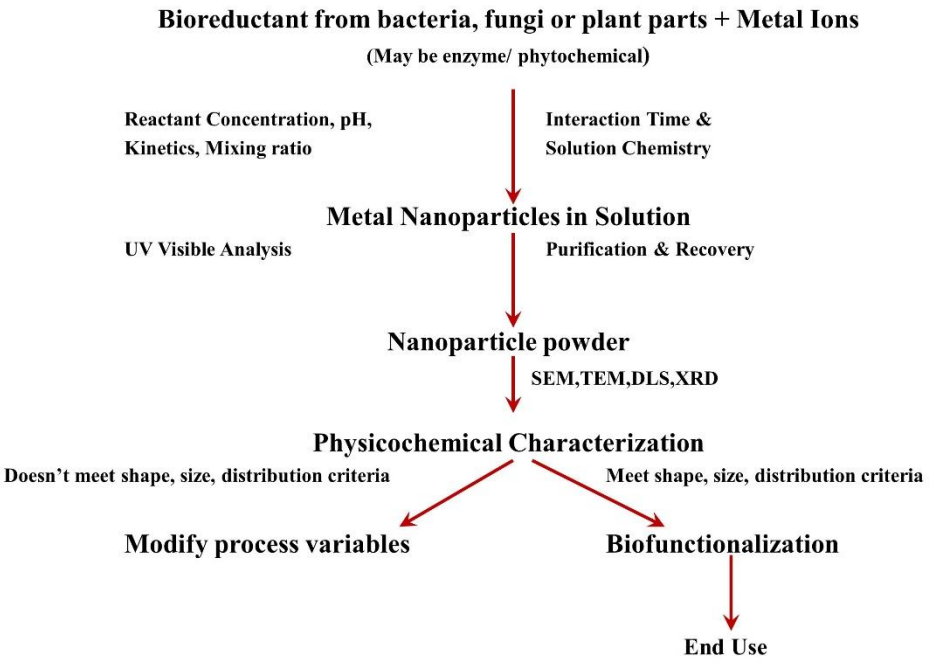

Fig. 2.5: Scheme representing generalized flow of nanoparticle synthesis *via* green route

Selection of the organism

In order to synthesize metal nanoparticles, it is important to acknowledge the inherent characteristics of organisms, including their enzyme activity and metabolic pathways. These biological features play a crucial role in the synthesis process.

Optimal conditions for cell growth and enzyme activity

To achieve optimal growth and synthesis of metal nanoparticles, various growth conditions need to be carefully optimized. Factors such as nutrients, inoculum size, light intensity, temperature, pH, mixing speed, and buffer strength should be adjusted accordingly. Additionally, it is beneficial to ensure the presence of substrates or related compounds at sub toxic levels right from the start of the growth process, as this can enhance the activity of the enzymes involved in the nanoparticle synthesis. Paying close attention to these conditions and factors is essential for obtaining successful and efficient metal nanoparticle synthesis

Optimal reaction conditions

In order to achieve higher yield and quality in the synthesis of nanoparticles using bioreduction, it is crucial to optimize the reaction conditions. Factors such as substrate, biocatalyst concentration, electron donor concentration, pH, exposure time, temperature, buffer strength, mixing speed, and light conditions need to be carefully optimized. These variables can significantly influence the size, morphology, and reaction rate of the nanoparticles. It has been emphasized that the optimization of these bioreduction conditions is essential for achieving desired outcomes in terms of yield and quality of the synthesized nanoparticles (Korbekandi, Iravani and Abbasi, 2009).

The utilization of in-vivo techniques in the production of nanoparticles via green nanotechnology involves the utilization of living cells as self-replicating bioreactors (Iravani, 2011). There exist two methods for the reduction of metal ions to metal nanoparticles, which serve to transform toxic ions into benign substances that can be safely discharged into the environment.

Intracellular synthesis – In this method, nanoparticle synthesis occurs via the utilization of intracellular enzymes, which are retained within the cell until extraction. The nanoparticles manufactured through this approach are stabilized by cellular constituents, predominantly enzymes, and concurrently exhibit distinct morphologies. The size range of nanoparticles is restricted in accordance with the organism's spatial limitations, which are determined by the cell wall and pre-existing cellular components (Shah *et al.*, 2015; Khan, Saeed and Khan, 2017; Basnet *et al.*, 2018).

Extracellular synthesis – In this method, nanoparticles are generated using enzymes that are located outside the cell, primarily enzymes secreted by the cell wall. The process involves the trapping of metal ions on the surface of the cells, followed by their reduction in the presence of these enzymes. The enzymes facilitate the conversion of the trapped metal ions into nanoparticles, leading to the formation of the desired nanoparticles. This approach allows for efficient and controlled synthesis of nanoparticles utilizing the enzymatic activity present in the external environment of the cells (Shah *et al.*, 2015; Khan, Saeed and Khan, 2017; Basnet *et al.*, 2018).

Simple methods have been developed comprising of extracellular or intracellular reduction of metal ions by biological extracts (Li *et al.*, 2011; Roychoudhury and Pal, 2014; Parial and Pal, 2015). Extracts from plants (Sangeetha, Rajeshwari and Venckatesh, 2011), bacteria (Li *et al.*, 2011), fungi (Mukherjee *et al.*, 2002; Mukherji, Ruparelia and Agnihotri, 2012), human cells (Anshup and Venkataraman, 2005; El-Said *et al.*, 2014) and diatoms (Schröfel *et al.*, 2011) have successfully transformed metal precursors to their corresponding NPs. The synthesis of these NPs has been facilitated by a soup of compounds such as terpenoids, phenolics, flavonones, amines, amides, proteins, pigments, alkaloids etc., present in the extracts, which assists in metal reduction and their stabilization (Asmathunisha and Kathiresan, 2013). The high metal uptake potential of algae and their predominance makes them a low-cost raw material (Kannan *et al.*, 2013). The interaction and biochemical activities of every microbe and the internal factors such as pH and temperature eventually play a crucial role in the size and morphology of the NPs (Makarov, Love and Sinitsyna, 2014; Shah *et al.*, 2015; Pathak *et al.*, 2019). The high surface area to volume ratio justifies their versatile applicability together with their ability to withstand harsh conditions (Dahoumane, Wujcik and Jeffryes, 2016). Their synthesis plays a vital role due to their broad spectrum applications, which diverge from medical, industrial, electronic devices, sensors, cosmetics, pharmaceutical, agriculture and bioremediation.

Bacteria, as prokaryotic microorganisms, are widely favoured for the synthesis of metallic nanoparticles due to their ability to multiply easily. One notable advantage is their capacity to produce nanoparticles intracellularly while maintaining their viability even after crystal growth (Mukherji, Ruparelia and Agnihotri, 2012). Various bacterial species have demonstrated the capability to synthesize metal nanoparticles intracellularly and extracellularly and even form nanoparticle alloys (Shankar *et al.*, 2016).

In the same line of trend, Fungi, a diverse group of eukaryotic organisms, offer advantages for nanoparticle synthesis, including scalability through thin solid substrate fermentation, economic viability, and ease of biomass handling. One significant advantage is their ability as eukaryotes to overexpress specific enzymes, which can be utilized for nanoparticle synthesis (Ganesan *et al.*, 2020). Fungi can serve as effective reducing agents for the conversion of metal ions into corresponding nanometals, either intracellularly or extracellularly, depending on the location of their reduction enzymes. In cases where the reduction enzymes responsible for the conversion of metal ions into nanometals are produced extracellularly (often secreted by the cell walls), the nanoparticle synthesis occurs outside the fungal cells (Mukherjee *et al.*, 2002).

2.6.1 Plants as a source for bionanomaterial

It has been recognized that plant extracts can reduce metal ions, but the nature of the reducing chemicals involved has not been well understood. Due to its apparent ease of use, the reduction of metal salts to nanoparticles using living plants or complete plant extract has garnered a lot of attention in the last 30 years. It is easier to use plant extracts to synthesize nanoparticles than it is to use complete plant extracts or plant tissue. The role of plant extracts as mediators of synthesis is gaining greater attention. In a one-step green manufacturing procedure, biomolecules found in plant extracts can be employed to reduce metal ions to nanoparticles. Rapid, room-temperature, pressure-free, and scalable, this bioreduction of metal ions to metal produces metals with few impurities. The environmental impact of synthesis mediated by plant extracts is minimal (Mittal, Chisti and Banerjee, 2013). Various water-soluble plant metabolites (e.g., alkaloids, phenolic compounds, and terpenoids) and coenzymes serve as reducing agents. It's also known that the origin of the plant extract impacts the characteristics of the nanoparticles (Singh, Dutta, *et al.*, 2018). This is because different extracts include organic reducing agents in varying quantities and combinations. Typically, a bioreduction mediated by a plant extract entails combining the aqueous extract with an aqueous solution of the relevant metal salt (Singh, Dutta, *et al.*, 2018). The reaction takes place at room temperature and concludes in minutes. The bioreduction process is relatively complex due to many different chemicals involved. Various plant parts reported for the synthesis of different types of nanoparticles are summarized in Table 2.2.

Table 2.2: Green synthesis of metallic NPs from various plant extracts

Plant	Nanoparticles	Size (nm)	Morphology	Application	References
Aloe barbadensis Miller	Au and Ag	10-30 nm	Spherical, triangular	Cancer hyperthermia	(Chandran *et al.*, 2006)
Aloe barbadensis Miller	In_2O_3	5-50 nm	Spherical	Solar cells, gas sensors	(Maensiri *et al.*, 2008)
Acalypha indica	Ag	20-30 nm	Spherical	Antibacterial activity	(Krishnaraj *et al.*, 2010)
Henna	Ag and Au	39 nm	Spherical, triangular, and quasi-spherical	Hyperthermia of cancer cells	(Kasthuri, Veerapandian and Rajendiran, 2009)
Avena sativa	Au	5-20 nm	Rod-shaped	-	(Armendariz *et al.*, 2004)
Azadirachta indica	Au, Ag and Ag-Au alloys	5-35, 50-100 nm	Spherical, triangular, hexagonal	Remediation of heavy metals	(Shankar *et al.*, 2004)
Camellia sinensis	Au and Ag	20 nm	Spherical, prism	Catalysts, sensors	(Mondal *et al.*, 2011)
Brassica juncea	Ag	2-35 nm	Spherical	-	(Haverkamp and Marshall, 2009)
Cinnamomum camphora	Au and Ag	55-80 nm	Triangular, spherical (Au), quasi-spherical (Ag)	-	(Huang *et al.*, 2007)
Carica papaya	Ag	60-80 nm	Spherical	-	(Mude *et al.*, 2009)
Citrus limon	Ag	< 50 nm	Spherical, spheroidal	-	(Prathna *et al.*, 2011)
Coriandrum sativum	Au	6.75-57.91nm	Spherical, triangular, truncated triangular, decahedral	Drug delivery, photo-thermal therapy	(Narayanan and Sakthivel, 2008)
Cymbopogon flexuosus	Au	200-500	Spherical, triangular	Infrared-absorbing optical coatings	(Shankar *et al.*, 2005)
Cycas sp.	Ag	2-6 nm	Spherical	-	(Jha and Prasad, 2010)
Diospyros kaki	Bimetallic Au-Ag	50-500 nm	Cubic	-	(Song and Kim, 2008)
Emblica officinalis	Au and Ag	10-20nm, 15-25 nm	-	-	(Ankamwar, Chaudhary and Sastry, 2005)

Eucalyptus citriodora	Ag	20 nm	Spherical	Antibacterial	(Ravindra *et al.*, 2010)
Eucalyptus hybrida	Ag	50-150 nm	Crystalline, spherical	-	(Dubey, Bhadauria and Kushwah, 2009)
Garcinia mangostana	Ag	35 nm	Spherical	Antimicrobial activity against *E. coli* and *S. aureus*	(Veerasamy *et al.*, 2011)
Gardenia jasminoides Ellis	Pd	3-5 nm	-	Nanocatalysts for *p*-nitrotoluene hydrogenation	(Jia *et al.*, 2009)
Syzygium aromaticum	Au	5-100 nm	Irregular	Detection and destruction of cancer cells	(Raghunandan *et al.*, 2010)
Jatropha curcas	Ag	15-50 nm	Spherical	-	(Bar *et al.*, 2009)
Ludwigia adscendens	Ag	100-400 nm	Spherical	-	(Mochochoko *et al.*, 2013)
Mentha piperita	Ag	5-30 nm	Spherical	Against microbes	(Parashar and Saxena, 2009)
Medicago sativa	Fe_2O_3	2-10 nm	Crystalline	Cancer hyperthermia, drug delivery	(Herrera-Becerra *et al.*, 2008)
Morus	Ag	15-20 nm	Spherical	Antimicrobial activity against *E. coli, B. subtilis*	(Singh *et al.*, 2017)
Ocimum sanctum	Ag	10 nm	Spherical	Catalytic reduction	(Singh, Mehta, *et al.*, 2018)
Ocimum sanctum	Au and Ag	30, 10-20 nm	Crystalline, hexagonal, triangular and spherical	Biolabeling, biosensor	(Philip and Unni, 2011)
Pear	Au	200-500 nm	Triangular, hexagonal	Catalysis, biosensing	(Ghodake *et al.*, 2010)
Pelargonium roseum	Au	2.5-27.5 nm	Crystalline	-	(Shiv Shankar *et al.*, 2003)
Psidium guajava	Au	25-30 nm	Spherical	-	(Raghunandan *et al.*, 2009)
Sedum alfredii	ZnO	53.7 nm	Hexagonal and pseudo-spherical	Nanoelectronics	(Qu, Luo and Hou, 2011)
Tanacetum vulgare	Au and Ag	11, 16 nm	Triangular, spherical	Antibacterial, sensors	(Dubey, Lahtinen and Sillanpää, 2010)

2.6.2 Biosynthesis of ZnO NPs *via* plants and their possible cause

Different plant families (eight major taxonomic ranks) can be used to account for the relationship between diverse plant species, as the majority of plants belonging to the same family have similar patterns, compounds, and medicinal characteristics (for example, the members of the Rosa family have five petals, typically numerous stamens, and contain tannic acid, which is used as an astringent). Biosynthesis of ZnO nanoparticles has been documented using a wide variety of plant species, with the Fabaceae family (including *Aspalathus linearis, Cassia fistula, Pongamia pinnata,* and *Trifolium pratense*) and the Rutaceae family (including *Citrus aurantifolia, Agathosma betulina, Citrus limon,* and *Limonia acidissima*) being the most frequently used followed by Apocynaceae, Solanaceae and Lamiaceae (Basnet *et al.*, 2018) (Table 2.3).

The Fabaceae family of plants are rich in polyphenols, flavonoids, alkaloids, saponins, etc. These phytochemicals are primarily responsible for the formation of zinc metal salt complexes with themselves. In fact, these phytochemicals are the primary biochemicals responsible for the reduction of metal salts that results in the production of ZnO nanoparticles. Furthermore, these phytochemicals serve as capping agents, resulting in ZnO nanoparticles with a limited size distribution. Carotenoids, coumarins, limonoids, flavonoids, etc., are common phytochemicals found in plants belonging to the family Rutaceae. However, the biosynthesis of ZnO nanoparticles is not feasible with every plant in the environment. Using plants containing polyphenols (or flavonoids) increases the likelihood of success because they are excellent reducing and capping/stabilizing agents. In addition, they readily form complexes with zinc metal salts, enabling the synthesis of ZnO nanoparticles by hydrolysis followed by calcinations.

Table 2.3: Synthesis of ZnO NPs from various plant extracts and their application

Plant	**Part**	**Size & Morphology**	**Application**	**Bioreductant and Capping Agent**	**Reference**
Anisochilus carnosus	Leaves	56.14, 49.55 and 38.59 nm	Photocatalytic degradation of MB; Antibacterial activities against *S. para- typhi, V. cholerae, S. aureus, and E. coli*	Polyphenols, carboxylic acid, polysaccharide, amino acid and proteins	(Anbuvannan *et al.*, 2015a)
Phyllanthus niruri	Leaves	25.61 nm	Semiconducting, pyroelectric, piezo- electric, catalysis	Presence of aromatic aldehydes, capping agent is Starch	(Anbuvannan *et al.*, 2015b)
Palm	Pollen	18nm	Bio-hybrid nanocomposite for pharmaceutical and biomedical	Amino acid residues of the protein molecules	(Azizi *et al.*, 2015)
Anchusa italic	Flower	~8 and ~14 nm	Antibacterial activity	Fatty acids	(Azizi *et al.*, 2016)
Hibiscus subdariffa	Leaves		Anti-diabetic effect on streptozotocin	-	(Bala *et al.*, 2015)
Vaccinium arctostaphylos L.	Dried Fruit	15.5 and 13.9 nm	-	Organic molecules	(Bayrami *et al.*, 2018)
Nasturtium officinale	Leaves	21 nm, 14 nm	Antidiabetic and enhanced antibacterial activities	Aromatic compounds	(Bayrami, Ghorbani, *et al.*, 2019)
Vaccinium arctostaphylos L.	Leaves	27.9 nm and 21 nm	Bacterial decontamination, removal of organic compounds	Phenolic compounds	(Bayrami, Alioghli, *et al.*, 2019)
Eryngium foetidum L	Leaves	8 nm	Antibacterial agent against *E. coli, P. aeruginosa, S. aureus, S. pneumoniae*	-	(Begum, Ahmaruzzaman and Adhikari, 2018)
Potato	Potato Extract	20 nm	Attractive for biological and medical applications	Starch	(Buazar *et al.*, 2016)

Calotropis gigantea	Leaves	10 nm	Military camouflage package	-	(Chaudhuri and Malodia, 2017)
Eucalyptus spp	Leaves	20-40 nm	Removal of MG	-	(Chauhan, Kataria and Garg, 2020)
Laurus Nobilis	Leaves	20-35 nm	Antibacterial and Photocatalytic activity	Polyphenols and flavonoids	(Chemingui *et al.*, 2019)
Juglans regia L.	Leaves		Cytotoxicity and antimicrobial	Phenolic and aromatic compounds	(Darvishi, Kahrizi and Arkan, 2019)
Lemon	Juice	21.5 nm	Photocatalytic degradation of MO, MR, and MB	Sucrose as reducing agent	(Davar, Majedi and Mirzaei, 2015)
Jacaranda mimosifolia	Flowers	2-4 nm	Antibacerial activity Gram -ve: *E. coli*; Gram +ve: *E. faecium*	Oleic acid as a reducing and capping agent	(Sharma *et al.*, 2016)
Camellia sinensis	Leaves	54.84 nm	Super capacitor applications	Amino acid, protein and lipids	(Dhanemozhi, Rajeswari and Sathyajothi, 2017)
Chelidonium majus	Whole	10 nm	Antimicrobial agents, Anti-cancerous against human non-small cell lung cancer A549	Chelidonine, chelerythrine, sanguinarine, berberine, coptisine and stylopine.	(Dobrucka, Dlugaszewska and Kaczmarek, 2017)
Sechium edule	Leaves	30 to 70 nm	Antibacterial agents on *B. subtilis* and *K. pneumoniae*	-OH groups from the phenol and flavonoid compounds	(Elavarasan *et al.*, 2017)
Azadirachta indica	Leaves	18 nm	Antimicrobial activities	Water-soluble phenolic acid and flavonoid compounds	(Elumalai and Velmurugan, 2015)
Solanum torvum	Leaves	28.24 nm	-	Alkaloids and flavonoids	(Ezealisiji *et al.*, 2019)
Mimosa pudica	Leaves & Powder	27.14 Å and 46.94Å	Photocatalytic activity in MB photooxidation	-	(Fatimah, Pradita and Nurfalinda, 2016)

Carissa edulis	Fruits	50–55 nm	Dye degradation	Water soluble phenolic and flavonoids	(Fowsiya *et al.*, 2016)
Momordica charantia	Leaves	21.32 nm	Anti-parasitic activity against *R. microplus, P. humanus capitis, An. Stephensi, Cx. quinquefasciatus*	Vinyl ethers, aldehydes, beta lactones, and aliphatic amines	(Gandhi *et al.*, 2017)
Catharanthus roseus	Leaves	36.83 nm	Antibacterial against Gram +ve and Gram -ve pathogens	-	(Gupta *et al.*, 2018)
Silybum marianum	Whole Plant	31.20 nm	Antioxidant, Antimicrobial against fungal and bacterial strains	Phytochemicals	(Hameed *et al.*, 2019)
Olea europaea	Leaves	41nm	-	Flavonoids, glycosides, proteins and phenols	(Hashemi *et al.*, 2016)
Corriandrum sativum	Leaves	9–18 nm	Photocatalytic degradation of anthracene	-	(Hassan *et al.*, 2015)
Pandanus odorifer	Leaves	90 nm	Anticancer and antimicrobial agent	-	(Hussain *et al.*, 2019)
Rosa canina	Fruits	13.3 and 11.3 nm	Dose dependent toxicity to cells	Fruit acids	(Jafarirad *et al.*, 2016)
Prunus cerasifera	Leaves	12 nm	Photocatalytic and antimicrobial activity	Phenols, terpenoids, anthocyanins, carboxylic acids, aromatic amines, aliphatic amines and alkyl halides	(Jaffri and Ahmad, 2019)
Zingiber officinale	Rhibozome	23-26 nm	Antimicrobial activity- *K. pneumonia, S. aureus, C. albicans* and *P. notatum*	-	(Janaki, Sailatha and Gunasekaran, 2015)

Lawsonia inermis	Leaves	24nm	Eco-friendly green synthesis	Linalool α-terpineol, Eugenol, etherphenylvinyla 1,3-indandione, 2-hydroxy-1, 4-napthoquionone, Oxirane-tetradecyl, Hexadecanoic acid	(Jayarambabu, Rao and Rajendar, 2018)
Kalopanax septemlobus	Dried Barks	500nm	-	Alkane, alcohol, hydroxyl	(Lu *et al.*, 2019)
Echinacea purpurea	Callus	40 nm	Growth and physiological changes in tissue culture in the field of plant science	-	(Karimi *et al.*, 2018)
Acalypha indica	Leaves	39.34 and 43.63 nm	-	-	(Karthik *et al.*, 2017)
Andrographis paniculata	Leaves	20.23 nm	Drug delivery processes	Aromatic ring polyphenol	(Kavitha *et al.*, 2017)
Sageretia thea	Leaves	12.4 nm	Antifungal potential and antioxidant potential	-	(Khalil *et al.*, 2017)
Abutilon indicum, Clerodendrum infortunatum, Clerodendrum inerme	Leaves	17.49 nm	Antimicrobial, antioxidant, and antifungal potential.	-	(Khan *et al.*, 2018)
Trianthema portulacastrum	Plant Biomass	25-90 nm	Biological and photocatalytic applications	-	(Z. U. H. Khan *et al.*, 2019)
Costus woodsonii	Bulb Extract	30-40 nm	Alternate pathway	Terpenoids, phenolic acid, flavonoids, and proteins	(M. M. Khan *et al.*, 2019)
Aloe barbadensis	Leaves	15 nm	Antimicrobial and anti-biofilm activities	Phenolic compounds, terpenoids and proteins	(Ali *et al.*, 2016)
Arabica coffee	Coffee Powder	25-31 nm	Inhibition of proteinase K activity and the increase in the thermal stability	Carboxylic acid, phenol, functional groups	(Koupaei *et al.*, 2016)

Pithecellobium dulce	Peel	11.5 ± 2 nm	-	Phytochemicals	(Madhumitha *et al.*, 2019)
Sutherlandia frutescens	Whole Plant	13.3 nm	Antiproliferative activity against human lung cancer cells (A549); Gram -ve: *E. coli, P. aeruginosa*; Gram +ve: *S. aureus, E. faecalis*	-	(Mahlaule-Glory *et al.*, 2019)
Sageretia thea	Leaves	31.03 nm, 25.15 nm	Catalytic and conductivity Electrochemical activity	Glucopyranoside, Polyphenolic compound (myricetrin and syringic acid)	(Shinwari and Maaza, 2017)
Punica granatum	Fruit Peel	22.39, 30.08, 32.39 and 57.36 nm	Cytotoxicity against colorectal cancer cells (HCT116) and normal colon cells (CCD112)	-	(Mohamad Sukri *et al.*, 2019)
Accinium arctostaphylos	Fruits	Crystalline, 12nm	Anti-bacterial agent	-	(Mohammadi-Aloucheh *et al.*, 2018)
Silybum marianum	Dried Seeds	Hexagonal, >18-22nm	Treatment of diabetes mellitus	Organic compounds	(Mohammadi Arvanag *et al.*, 2019)
Ocimum basilicum	Leaves	10–25 nm	Anti-bacterial agent	Phytochemical compounds	(Abdelsattar *et al.*, 2022)
Ocimum basilicum L. var. *purpurascens*	Leaves	Hexagonal, 50nm	-	-	(Abdul Salam, Sivaraj and Venckatesh, 2014)
Nephelium lappaceum L	Peel	50.95 nm	Anti-bacterial agent	-	(Yuvakkumar *et al.*, 2014)
Vitex negundo	Dried Leaves	38.17 nm	Anti-bacterial agent Gram -ve: *E. coli* ; Gram +ve: *S. aureus*	Isoorientin (flavone)	(Ambika and Sundrarajan, 2015)

2.6.3 Algae as a source for bionanomaterial

Algae are known to be one of the most primitive and influential biological entities existing autotrophically performing more than 50% of photosynthesis on this planet (Barsanti and Gualtieri, 2014; Rakesh *et al.*, 2015). Being rich in biologically active compounds they are regarded as an appealing platform to serve as photosynthetic biorefineries capable of contriving a spectrum of high value-added products in addition to fuels (Jeffryes, Agathos and Rorrer, 2015). Besides that, they are reported as hyperaccumulators of heavy metals and their chemical transformation and are believed to produce metal NPs (Zinicovscaia, 2012). Some of the pragmatic properties of the algae that make them as remarkable 'nanobiofactories' are (i) faster doubling time (Chisti, 2007) (ii) easily scalable and well developed systems (Chisti, 2007, 2008), (iii) cells can be readily disrupted (Chisti and Moo-Young, 1986), (iv) easily harvested (Molina Grima *et al.*, 2003) (v) low cost large-scale synthesis (Sharma, Kanchi and Bisetty, 2015) and (vi) nucleation and crystal growth are accelerated due to the presence of negative charge on the surface of the cell (Sahoo *et al.*, 2014). The chronicle, chemistry and the biological benefits of algae have been thoroughly discussed and documented elsewhere (Ramakrishnan *et al.*, 2010, 2023; Chen and Jiang, 2013; Namvar *et al.*, 2015). More than a hundred different micro and macro algae have been reported that exhibit the ability to tailor NPs both intracellularly (Roychoudhury and Pal, 2014) and extracellularly (Mohseniazar *et al.*, 2011), which can be recovered during downstream processing (Dahoumane *et al.*, 2012).

Algae belonging to different classes such as *Cyanophyceae, Chlorophyceae, Phaeophyceae,* and *Rhodophyceae* have been widely exploited for intracellular and extracellular synthesis of metallic nanoparticles (Ag, Au, Pt, Ni, etc.) and metal oxide nanoparticles (CuO, ZnO, MnO_2, TiO_2, Fe_3O_4, etc.) (Suresh *et al.*, 2015).

Gold Nanoparticles from algae

Algae have been proven to be a boon with indefinite applications in numerous fields that have been employed as a substitute to chemical reductants for the tailoring of Au-NPs. Au-NPs have been synthesized from four different classes of algae such as *Cyanophyceae* (Blue-green algae), *Chlorophyceae* (Green algae), *Phaeophyceae* (Brown algae) and *Rhodophyceae* (Red algae) (Table 2.4). Material scientists have been consistently trying to fabricate Au-NPs by numerous methods with uniform size, shape, and monodispersity. It has been a challenging and vital mission to fabricate flexible and straightforward eco-friendly preparation methods to produce shape- and size-preferred Au-NPs (Namvar *et al.*, 2015).

Silver nanoparticles from algae

Silver is known to be a good conductor of heat and electricity, however, the high price limits its application in the electrical industry (Keat *et al.*, 2015). For some time, the antimicrobial potential of silver has been explored in many medical fields and has been successfully tested against 650 pathogenic microbes (Annamalai and Nallamuthu, 2016). Among the various noble metallic NPs known so far silver NPs (Ag-NPs) have gained the most attention, exhibiting the highest level of commercialization, accounting for 55.4% of the NMs based consumer products existing in the market (313 out of 565) (Agnihotri, Mukherji and Mukherji, 2014). Consequently, nanosilver is eventually becoming the nucleus of the nano-industry. Ag-NPs have been synthesised from different microalgae and macroalgae belonging to *Cyanophyceae*, *Chlorophyceae*, *Rhodophyceae* and *Phaeophyceae* (Table 2.5).

Algae-mediated synthesis of other nanomaterials

As discussed in the previous sections, different types of algal species were reported to synthesize gold and silver NPs. Synthesis of various other NPs such as ZnO-NPs, TiO_2, CdS, Pt, Pd, Fe_3O_4 have also been reported (Table 2.6). Lengke and colleagues (2006 b) for the first time developed an alternative method to abiotic chemical methods for the synthesis of platinum NPs and platinum (II) organics from *Plectonema boryanum UTEX 485*. They investigated the synthesis at temperatures ranging from 25-180 °C, and the optimal temperature was found to be 29°C. The resulting NPs were spherical, connected with bead-like organic moieties released from dead cyanobacterial cells. However, the size could not be systematically studied as the variation in temperature and time was large. Crystallization and re-crystallization were affected by temperature, at lower temperature amorphous behaviour was observed contrary to the crystalline structure at higher temperature (180°C) (Lengke *et al.*, 2006). *Phormidium* was found to be a suitable candidate for the extracellular synthesis of copper NPs. The reduction of cationic copper was believed to be done by a 25 kDa metal chelating protein moiety in aerobic conditions at neutral pH and room temperature. The role of proteins in the stabilization of NPs was confirmed by SDS- PAGE and FT-IR (Rahman *et al.*, 2010). The aqueous cellular extract of diazotrophic cyanobacterial strain *Anabaena* L31 was exercised for the synthesis of ZnO-NPs conjugated with shinorine, water-soluble UV-B absorbent. A sharp decline in the surface charge of the conjugate from +30.25 mV to 3.75 mV resulted from the changes in the surface functionalities after conjugation formation (Singh *et al.*, 2014; Pathak *et al.*, 2019).

Aqueous extract from *Sargassum plagiophyllum* was reported successfully for the fabrication of AgCl-NPs (Dhas *et al.*, 2014) (Table 2.6). Advanced characterization techniques like UV-Vis, FT-IR, FE-SEM, HR-TEM and XRD were employed to confirm the formation of AgCl-NPs which could be used as antimicrobial agents (Dhas *et al.*, 2014). While screening a candidate for the synthesis of ZnO-NPs, *Sargassum myriocystum* was found to be suitable and process optimization was done for its synthesis (Azizi *et al.*, 2014). To optimize parameters resulting in the synthesis of 36 nm sized ZnO-NPs extracellularly, pH, temperature, concentration of seaweed extract and metal concentration were studied. *Sargassum muticum* was also reported to biosynthesize hexagonal ZnO-NPs with an average size of 4 nm (Azizi *et al.*, 2014).

A rapid and simple method for complete reduction of Pd (II) ions to Pd NPs by aqueous extract *Chlorella vulgaris* was demonstrated by Arsiya and co workers (2017). Gradual colour change of the solution from yellow to dark brown indicated the formation of Pd-NPs. The reaction was completed in 10 min as the characteristic peak of Pd (II) ions at 410 and 420 nm disappeared. Furthermore, the formation of Pd-NPs was confirmed by SPR peak range at 370-440nm. Polyol and amide groups of the extract were assumed to be responsible for the reduction and stabilization as strong and intense peaks were observed at 1051 cm^{-1} (Carbohydrate v(C-O-C) of polysaccharides, Nucleic Acid (and other phosphate-containing compounds), 1641 cm^{-1} (amide or C=C stretching vibrations of aromatic rings), 2922 (C−H stretching of polyols) and 3417 cm^{-1} (O−H group of polyols) in the FT-IR spectrum (Arsiya, Sayadi and Sobhani, 2017).

Algae-mediated synthesis of bimetallic nanoparticles

Bimetallic NPs are composed of two different metals and they are combined in different ratios to show novel properties derived from the constituting metals. These NMs have drawn more interest than monometallic NMs due to the presence of an extra degree of freedom. Extracellular interaction of single-cell proteins of *Spirulina platensis* with aqueous $AgNO_3$ and $HAuCl_4$ was examined for the biosynthesis of Ag-NPs, Au- NPs and Ag-Au core shell NPs. The interaction of cyanobacterial biomass and the metal precursor solutions ($AgNO_3$ and $HAuCl_4$ each at 10^{-3} M) solely or in combination for 120 h at 37°C led to significant chromatic changes due to the excitation of surface plasmon vibrations in the metal NPs. The visual change in the colour of the reaction mixture to yellowish brown (Ag-NPs), ruby red (Au-NPs) and purple to brown (Ag-Au bimetallic) was noticed. SPR λ_{max} bands were observed at 424, 530 for Ag-NPs, Au-NPs. However, for bimetallic NPs absorption peaks were observed at 509, 486

and 464 nm for 75:25, 50:50 and 25:75 (Au:Ag) mol concentrations, respectively. The gradual shift from 530 to 424 nm was commensurate with the increased mole fraction of silver. The size of the NPs observed for Ag-NPs was 7-16 nm, Au-NPs was 6-10 nm and for bimetallic Au-Ag NPs it was 17-25 nm (Govindaraju *et al.*, 2008; Pathak *et al.*, 2019).

Table 2.4: Algae mediated synthesis of gold nanoparticles (Au-NPs)

Algae	Size & morphology	Application	Characterization	Bioreductant and capping agent	Reference
Blue green algae-mediated synthesis of gold nanoparticles (Au-NPs)					
Nostoc ellipsosporum	20–40 nm, decahedral, icosahedra rods	Uniform distribution of aspect ratio of monodispersity	UV-Vis, TEM, DLS, Zeta Potential, XRD	Intracellular biotransformation, sodium citrate for extraction of nanorods	(Parial *et al.*, 2012)
Spirulina platensis	20-30 nm; spherical	Pharmaceutical technological purpose	UV-Vis, FTIR, TEM, SEM-EDAX, XRD, NAA, AAS	Extracellular; biomolecules (amino, carboxylic, phosphate, thiol)	(Kalabegishvili and Kirkesali, 2012)
Spirulina platensis	5 nm, spherical	Gram +ve strains: *B. subtilis* and *S. aureus;* stable for 2 months	UV-Vis, FTIR, HRTEM, EDAX	Carboxylate group in the reduction, Carboxyl, hydroxyl and primary amine are involved in stabilization	(Suganya *et al.*, 2015)
Green algae mediated synthesis of gold nanoparticles (Au-NPs)					
Klebsormidium flaccidum	10-20 nm	Sol-gel methods for encapsulation of algal species within silica gels	UV-Vis, XRD, TEM, PAM, PEA, XPS, SERS	Insitu, gold reduction occurs in thylakoids where reducing enzymes	(Sicard *et al.*, 2010)
Chlorella vulgaris	40-60 nm; spheroidal, polyhedral	Potentially attractive route to commercial production	XRD, TEM,XAS, AAS, XANES	Intracellular	(Luangpipat *et al.*, 2011)
Klebsormidium flaccidum	9 ±3.4 nm	Development of cell-based bioreactors for the production of metal NPs	PAM, TEM, UV-Vis	Intracellular	(Dahoumane *et al.*, 2012)
Chlorella pyrenoidusa	25-30 nm; spherical, icosahedral, FCC	pH-dependent size controllable tuning of the synthesis of thermodynamically stable Au nanoparticle	UV-Vis, XRD, HRTEM	NADH-dependent enzyme	(Oza *et al.*, 2012)
Spirogyra submaxima	2-50 nm; spherical, triangular, hexagonal	Pure, easily extractable NPs are formed which can be used in biomedical applications	UV-Vis, DLS, XRD, TEM, Zeta Potential	Intracelluar synthesis at cell wall and the chloroplast	(Roychoudhury and Pal, 2014)
Prasiola crispa	5-25 nm, FCC, spherical	Facile, one step and eco-friendly for the large scale synthesis	UV-Vis, XRD, FTIR, DLS, HRTEM	Protein and other molecules, extracellular	(Sharma *et al.*, 2014)
Stoechospermum marginatum	18.7 to 93.7 nm; spherical, triangular and hexagonal	Antibacterial against Gram -ve *E. faecalis*	PL, SEM, TEM, XRD, FTIR, WD-XRF	Hydroxyl groups present in the diterpenoids	(Rajathi *et al.*, 2012)

Turbinaria conoides	6-10 nm; spherical	Antibacterial, biocompatible	UV-Vis, XRD, FTIR, TEM	Fucoidan and polyphenolic groups	(Shanmugam Rajeshkumar *et al.*, 2013)
Turbinaria conoides	60 nm, triangle, rectangle and square	High antibacterial activity against *Streptococcus* sp, and medium for *B. subtilis* and *Klebsiella pneumoniae*	SEM, EDS	Biochemical material	(S. Rajeshkumar *et al.*, 2013)
Padina gymnospora	8-21 nm; spherical	Antitumor on liver cancer (HepG2) cell line	UV-Vis, XRD, AFM, HRTEM, FTIR	Fucoxanthin or flavonoids	(M. Singh *et al.*, 2014)
Dictyota bartayresiana	Spherical, poly-dispersed NPs	Antifungal against *Humiclo insulans* and *Fusarium dimerum*	UV-Vis, FTIR, SEM	Carboxylic, amine and polyphenolic groups	(Varun, Sudha and Kumar, 2014)
Sargassum muticum	5.42 ± 1.18 nm, spherical, FCC	Biomedical and pharmaceutical	UV-Vis, TEM, Zeta Potential, XRD	Capping of anionic bio-compounds, Bio-organic compounds/proteins	(Namvar *et al.*, 2015)
Turbinaria conoides	12-57 nm, anistropic, poly-dispersed NPs	Higher catalytic activity for reduction of aromatic nitro compounds and organic dye molecules	UV-Vis, HRTEM, FTIR, DLS, Zeta potential	Polyphenolic substances, hydroxyl group may act as capping agent	(Ramakrishna *et al.*, 2016)
Cystoseira baccata	8.4 ± 2.2 nm, spherical, polycrystalline	Cytotoxic effect against human colon cancer cell lines HT-29 followed by Caco-2; biocompatibility with healthy cell line PCS-201-010	UV–Vis, TEM, HR-TEM, STEM, EELS, EDS, FT-IR, Zeta potential	Bioreduction by polyphenols and polysaccharides; Capping by proteins; Metal complexation by sulfonic groups from polysaccharides	(González-Ballesteros *et al.*, 2017)
Red algae mediated synthesis of gold nanoparticles (Au-NPs)					
Kappaphycus alvarezii	10-40 nm; polydisperse	Antibacterial against *Pseudomonas flouresences, S. aureus*	UV-Vis, XRD, TEM, FTIR,FAAS	Extracellular, polyphenol compounds	(Rajasulochana, Krishnamoorthy and Dhamotharan, 2012)
Galaxaura elongata	3.85–77.13 nm; rod, triangular, truncated, triangular, hexagonal	Antibacterial against *E. coli*, *Klebsiella pneumonia, S. aureus* and *Pseudomonas aeruginosa*	TEM, FTIR, Zeta Potential, GC-MS, HPLC	Palmitic acid acts as stabilizing agent. Epigallocatechin catechin and epicatechin gallate are polyphenol compound as capping agents	(Abdel-Raouf, Al-Enazi and Ibraheem, 2017)

Table 2.5: Algae mediated synthesis of silver nanoparticles (Ag-NPs)

Algae	Size & Morphology	Application	Characterization	Bioreductant and capping agent	Reference
Blue green algae mediated synthesis of silver nanoparticles (Ag-NPs)					
Plectonema boryanum UTEX 485	Intracellularly (<10 nm) and extracellularly (1-200 nm), octahedral	Temperature-dependent size control of NPs	TEM, XPS, TEM-EDS	Utilizing nitrate by reducing nitrate to nitrite and ammonium, which is fixed as glutamine before death	(Lengke, Fleet and Southam, 2007a)
Spirulina platensis	10-15 nm; FCC	Live algal mass can used for synthesis	UV-Vis, XRD, TEM	Cellular reductases	(Mahdieh *et al.*, 2012)
Cylindrospermum stagnale NCCU-104	38- 88 nm, pentagonal	Extracellular cell free biosynthesis	UV-Vis, SEM	Proteins in the cell extract	(Husain, Sardar and Fatma, 2015)
Microchaete NCCU-342	60-80 nm, spherical, polydisperesed	Degradation of azo dye methyl red.	UV-Vis, TEM, DLS, Zeta potential	Cellular metabolites	(Husain *et al.*, 2020)
Green algae mediated synthesis of silver nanoparticles (Ag-NPs)					
Chlamydomonas reinhardtii	Rounded/rectangular *in vitro* 5±1 to 15±2 nm *in vivo* 5±1 to 35±5 nm	Understanding the role of diverse cellular protein in the synthesis and capping	UV-Vis, ICP- MS, SEM, TEM, EDAX, MALDI-TOF, MS	Cellular proteins *viz* histone (H4), CA, FNR, SOD, SBPase, ATP synthase, RuBP carboxylase, and OEE.	(Barwal *et al.*, 2011)
Chlorella sp.	34 nm, spherical, FCC	Scale up method	UV-Vis, XRD, FTIR, SEM	Enzymes or Protein	(Elumalai, Santhose and Devika, 2013)
Chlorococcum humicola	16 nm; spherical	Gram -ve: *E.coli*	UV-Vis, XRD,SEM , EDX, TEM, FTIR	Intracellular and extracellular synthesis, protein molecules	(Jena *et al.*, 2012)
Scenedesmus sp.	36 nm; spherical, FCC	Biological synthesis	UV-Vis, XRD, FTIR, SEM	Enzymes or protein	(Elumalai, Santhose and Devika, 2013)
Scenedesmus	15-20 nm, spherical,	Gram +ve: *S. mutans* Gram -ve: *E. coli*	AAS, UV-Vis, TEM, XRD, FTIR, DLS, TGA	Intracellular, extracellular synthesis Biomolecules, proteins and peptides	(Jena *et al.*, 2014)
Chlorella vulgaris	8–20 nm, FCC	Cost effective bioreactor for the conversion of ionic form of metals to NMs	UV-Vis, XRD, FTIR, TEM, DLS, Zeta Potential, SEM-EDAX,	Extracellular, aromatic groups in the protein moiety	(Satapathy *et al.*, 2015)
Chlorella pyrenoidosa	5-20 nm with average 12 nm, FCC,	Gram -ve: *K. pneumoniae, A. hydrophila, Acenetobacter* sp.; Gram +ve: *S. aureus;*	UV-Vis, XRD, SEM EDS, TEM, XRD, FTIR,	(NH)C=O group within the cage of cyclic peptides	(Aziz *et al.*, 2015)

		Photocatalytic agent: Degradation of methylene blue			
Urospora sp	20-30nm , FCC, spherical	Gram +ve: *S. aureus, B. subtilis;* Gram -ve: *E.coli, P. aeruginosa, K. pneumonia,*	UV-Vis, XRD, FTIR, HRTEM	Hydrogen bonded hydroxyl group, carbonyl and alcoholic group	(Suriya *et al.*, 2012)
Ulva fasciata	28-41 nm, spherical,	*Xanthomonas campestris* pv. *Malvacearum*	UV-Vis, FTIR, XRD, SEM and EDX.	1-(Hydroxymethyl)–2, 5, 5, 8A-tetramethyl decahydro-2-napthalenol as reducing agent; Hexadecanoic acid as stabilizing agent	(Rajesh *et al.*, 2012)
Ulva lactuca	20-56nm; spherical	Anticancer: Hep2, MCF7 and HT29 cancer cell lines	UV-Vis, FTIR, XRD, SEM, TEM, EDAX,	Release of protein molecules	(Devi and Bhimba, 2012)
Ulva lactuca	48.9 nm, spherical	Photocatalytic degradation of methyl orange dye	U-Vis, FTIR, Zeta Potential, HRSEM, XRD,	phenolic compounds, amines and aromatic ring	(Kumar *et al.*, 2013)
Codium capitatum	3-44 nm, 30 avg.	First report on using seaweed from the widespread *Codium* genus, non toxic	UV-Vis, EDX, FTIR,	Amine, peptide and sulphate groups	(Kannan, Stirk and Van Staden, 2013)
Enteromorpha flexuosa (wulfen) J.Agardh	15 +1.5nm, circular	Gram +ve: *B. subtilis, S. aureus, E. faecalis, S. epidermidis;* Gram -ve: *E.coli, K. pneumonia;*Fungus: *C. albicans, S. cerevisiae*	UV-Vis, XRD, TEM, EDS	Amines, peptides and secondary metabolites	(Yousefzadi, Rahimi and Ghafori, 2014)
Ulva lactuca	20 nm, spherical	Gram +ve: *Bacillus* sp.; Gram -ve: *Pseudomonas* sp., *E.coli*	UV-Vis, XRD, TEM, SEM, FTIR	Aromatic compound or alkanes or amine	(Sangeetha. and Saravanan., 2014)
Caulerpa racemosa	5-25 nm, 10nm; FCC	Gram +ve: *S. aureus;* Gram -ve: *P. mirabilis*	UV-Vis, XRD, TEM, FTIR	Cyclic peptides in stabilization and reduction	(Kathiraven *et al.*, 2015)
Pithophora oedogonia	25-44 nm, cubical and hexagonal-shaped	Gram -ve: *E. coli, P. aeruginosa, V. Cholera, Shigella flexneri*; Gram +ve: *B. subtilis, S. aureus, Micrococcus luteus*	UV-Vis, EDS, SEM, DLS, FTIR	Phytochemicals as reducing agents and protein as capping agents	(Sinha *et al.*, 2015)
Spirogyra	40-80 nm, spherical	First report for using Ag_2SO_4 as a salt; Gram +ve: *S. aureus;* Gram -ve: *E. coli*	UV-Vis, FTIR, TEM and NTA	Proteins	(Pinjarkar *et al.*, 2016)
Spirogyra varians	17.6 nm; FCC structure, quasi-spheres	Gram +ve: *S. aureus, B. cereus, L. Monocytogenes*	UV-Vis, XRD, FTIR, SEM	Amino, carboxylic, hydroxyl and carbonyl groups, quinine	(Salari *et al.*, 2016)

		Gram -ve: *S. typhimurium, E. coli, P. aeruginosa, Klebsiella*			
Caulerpa serrulata	10 ± 2 nm, spherical, fcc structure	Catalytic reduction of Congo red; Antibacterial activity Gram +ve : *S. aureus;* Gram –ve: *Salmonella typhi, E. coli, P. aeruginosa, Shigella*	UV–Vis, FT-IR, XRD, HR-TEM, ^{1}H and ^{13}C NMR	Caulerpenyne and/or its derivatives	(Aboelfetoh, El-Shenody and Ghobara, 2017)
Red algae mediated synthesis of silver nanoparticles (Ag-NPs)					
Gelidiella acerosa	22 nm; spherical, FCC	Antifungal against *Humicola insolens, Fusarium dimerum, Mucor indicus, Trichoderma reesei*	UV-Vis, SEM, TEM, XRD, FTIR,	Aromatic compound or alkanes or amines	(Vivek *et al.*, 2011)
Gracilaria edulis	12.5-100 nm; spherical	Downstream processing	UV-Vis, SEM, TEM, XRD, FTIR,	Proteins while terpenoids are implicated in stabilization extra cellular synthesis	(Murugesan, Elumalai and Dhamotharan, 2011)
Acanthophora spicifera	48 nm, spherical	Antimicrobial against biofilm forming bacteria *S. typhii* and *S. flexneri*	UV-Vis, FTIR, TEM	Alcohols and phenols, carboxylic acids and its derivatives and chloroalkanes	(Kumar, Senthamilselvi, *et al.*, 2012)
Gelidiella sp.	40-50 nm; spherical	Anticancer against Hep 2 cell lines	UV-Vis, XRD, FTIR, SEM, EDS,	Protein molecules	(Devi, Bhimba and Ratnam, 2012)
Gracilaria dura	6.0 ± 2 nm, sphere	Antibacterial against *B.pumilus*, food preservation and wound dressing	EDX, SAED, XRD, TGA, DSC, TEM	Polymer	(Shukla *et al.*, 2012)
Gracilaria corticata	18-46 nm	Antifungal activity against *C. albicans* and *C. glabrata*	UV-Vis, FTIR, TEM, DLS, Zeta Potential	Phenolic compounds, amide I group and aromatic rings were responsible for stabilization	(Kumar, Senthamil Selvi and Govindaraju, 2013)
Pterocladia capillacae,	7 nm; spherical	Gram +ve: *S.aureus*; Gram -ve: *E.coli*	UV-Vis, TEM , FTIR, GLC	Reducing sugar, carbonyl groups and sulphated polysaccharides	(El-Rafie, El-Rafie and Zahran, 2013)
Jania rubins,	12 nm; spherical	Gram +ve: *S.aureus*; Gram -ve: *E.coli*	UV-Vis, TEM , FTIR, GLC	Carbonyl group from amino acid residues and proteins	(El-Rafie, El-Rafie and Zahran, 2013)
Gracilaria edulis	55-99 nm, FCC, spherical,	Anticancerous against Human PC3 cell lines and non-toxic to normal Vero cell lines	UV-Vis, EDX, FTIR, FESEM, XRD	Free and bound amide groups	(Priyadharshini, Prasannaraj and Geetha, 2014)
Gracilaria birdiae	20.3 nm, spherical	Gram -ve: *E.coli*	UV-Vis, TEM, FTIR, DLS, Zeta Potential,	Reduction of the silver ions is coupled to the oxidation of the hydroxyl and carbonyl group	(de Aragão *et al.*, 2016)

Acanthophora specifera	33-81 nm, cubic	Gram +ve: *S. aureus, B. subtillis*; Gram -ve: *Salmonella* sp., *E. coli;* Fngus: *Candida albicans*	XRD, FTIR	Monosaccharide, polysaccharide, uronic acids and secondary metabolites	(Ibraheem, AbdElaziz and Saad, 2016)
Brown algae mediated synthesis of silver nanoparticles (Ag-NPs)					
Sargassum wightii grevilli	8-27 nm, spherical,	Gram +ve :*S. aureus, B. rhizoids*; Gram -ve: *E. coli, P. aeruginosa*	UV-Vis, FTIR, XRD, HRTEM	Extracellular, oxidation of alcoholic group to aldehyde, carboxylate ions	(Govindaraju *et al.*, 2009)
Sargassum ilicifolium	33-40 nm, spherical	Gram +ve: *S. aureus* Gram -ve: *E. coli, Klebsiella pneumoniae, S. typhii, Vibrio cholera;* Cytotoxic against *Artemia salina*	UV-Vis, SEM, TEM	Biologically active compounds	(Kumar, Selvi, *et al.*, 2012)
Sargassum polycystum	5-7 nm, spherical, FCC	Gram +ve: *S. aureus;* Gram -ve: *E. coli, P. aeruginosa, K. pneumonia;* Anticancer against MCF-7 breast cancer cell lines	UV-Vis, FTIR, HRTEM, XRD, GC-MS	Hexadecane, hexadecanoicacid, cis -9- octadecanol, 1-eicosanol, octadecanoic acid	(Thangaraju *et al.*, 2012)
Padina pavonica	10-72 nm; spherical, polydisperse	Cotton pathogens: Fungus: *Fusarium oxysporum* Bacteria: *Xanthomonas campestris*	UV-Vis, FTIR, XRD, SEM, TEM.	Extracellular, terpenoids	(Sahayaraj, Rajesh and Rathi, 2012)
Padina tetrastromatica	14 nm, spherical	Gram +ve: *Bacillus* sps, *B. Subtilis;* Gram -ve: *Klebsiella planticola, Pseudomonas* sp	UV-Vis, XRD, TEM, FTIR	Broalkanes engage in recreation the foremost role in the NPs synthesis	(S. Rajeshkumar, Kannan and Annadurai, 2012)
Turbinaria conoides	96 nm; spherical	Gram +ve: *B. subtilis*; Gram -ve: *K. planticola*	XRD, SEM, FTIR, UV-Vis	Amines and polyphenols	(Shanmugam Rajeshkumar, Kannan and Annadurai, 2012)
Padina gymnospora	25-40 nm, spherical	Gram +ve: *B.cereus;* Gram -ve: *E. coli*	UV-Vis, TEM	Aqueous extract of *Padina gymnospora*	(Shiny, Mukherjee and Chandrasekaran, 2013)
Colpmenia sinusa	20 nm; spherical	Gram +ve: *S.aureus;* Gram -ve: *E.coli*	UV-Vis, TEM , FTIR, GLC	-C-O- groups of polyols of polysaccharides; -C-O-SO_4- of sulphated polysaccharides.	(El-Rafie, El-Rafie and Zahran, 2013)
Cystophora moniliformis	75 nm, FCC	Temperature-dependent variation of the size of NPs	XRD, UV-Vis, SEM, DLS EDAX, Zeta Potential	Metabolites, phenolic compounds	(Prasad, Kambala and Naidu, 2013)

Sargassum longifolium	40-85 nm; spherical, FCC	Antifungal: *Aspergillus fumigatus, C. albicans, Fusarium* sp. *S.longifolium*	SEM, XRD. TEM. FTIR, UV-Vis, EDX	Proteins for capping; carboxylic groups involved in stability	(Rajeshkumar *et al.*, 2014)
Sargassum polycystum C. Agardh		Antibacterial: *E. coli, Streptococcus pyogenes, P. aeruginosa, S. flexneri, Morengilla morrgani;* Cytotoxic: Dalton's lymphoma ascites (DLA)	UV-Vis, FTIR, XRD	Capped by proteins and metabolites such as phenolic acid, carboxylic acid and flavonoids	(Asha *et al.*, 2015)
Sargassum vulgare	10 nm, spherical	Anticancer: Human myeloblastic leukemic cells HL60, cervical cancer cells HeLa	TEM, FACS, XRD, HR-TEM, FTIR, EDX	Alginate moieties, secondary OH groups	(Govindaraju *et al.*, 2015)

Table 2.6: Algae mediated synthesis of other nanomaterials (NMs)

Algae	NP	Size	Applications	Characterization	Bioreductant and capping agent	Reference
Blue green algae						
Plectonema boryanum UTEX 485	Pt	30 nm- 0.3 µm, spherical	First study as an alternative method to abiotic chemical methods	SEM,TEM, XPS	Polysaccharides have abundant uronic acid subunits, which, through their carboxyl groups	(Lengke, Fleet and Southam, 2006)
Plectonema boryanum UTEX 485	Pd	>30nm, spherical, FCC	First viable alternative method	SEM, TEM, XPS, XRD	Organic materials	(Lengke, Fleet and Southam, 2007b)
Anabaena flos-aquae	β-FeOOH	-	-	XRD, HRTEM, SEM-EDS	Intracellular	(Brayner *et al.*, 2009)
Calothrix pulvinata	β-FeOOH	-	-	XRD, HRTEM, SEM-EDS	Intracellular	(Brayner *et al.*, 2009)
Phormidium cyanobacterium	CuO	10-40 nm quasi-spheres, crystalline	Proteins induced under metal stress play a dual role of hydrolysis of precursor salt to CONPs and stabilizing agent, as particle solution is stable at room temperature for more than a week	UV-Vis, TEM, SEM,EDAX, XRD, FTIR, SDS-PAGE	Extracellular , 25 kDa protein fraction as capping agent	(Rahman *et al.*, 2010)
Phormidium tenue NTDM05	CdS	5.1 ± 0.2 nm, spherical	Biolabelling	FTIR. EDAX, TEM, UV-Vis	C-phycoerythrin, thiol groups partial capping along with biological molecules	(MubarakAli *et al.*, 2012)
Anabaena strain L31	ZnO	80nm, hexagonal,	Environmental-friendly sunscreen filters	UV-Vis, XRD, SEM, TEM, FTIR, SAED, DLS	Phycobiliproteins	(G. Singh *et al.*, 2014)
Brown algae						
Sargassum muticum	Fe_3O_4	18± 4 nm, cubic shape	High functional bioactivity	UV-Vis, EDXRF, XRD, FESEM, VSM,FTIR, TEM	Sulphated polysaccharides in the reduction process and the stabilization, extracellular synthesis	(Mahdavi *et al.*, 2013)
Sargassum myriocystum	ZnO	36 nm spherical, triangle, radial, hexagonal, rod, rectangle size	Natural nanomedicine against microbial infection.	UV–visible, DLS, AFM, SEM, EDX, TEM, XRD, FTIR	Fucoidan water soluble pigments	(Nagarajan and Arumugam Kuppusamy, 2013)
Sargassum plagiophyllum	AgCl	18–42 nm, spherical	Antibacterial properties	UV-Vis, FTIR, EDAX, HRTEM, FESEM,XRD	Role of C=C in the reduction	(Dhas *et al.*, 2014)

Bifurcaria bifurcata	CuO	5 to 45 nm; spherical	Antibacterial	UV-Vis , FTIR, XRD, TEM	Water-soluble compounds such as diterpenoids	(Abboud *et al.*, 2014)
Sargassum ilicifolium	Pd	60-80 nm, spherical	-	SEM, UV-Vis	-	(Prasad and Padmesh, 2014)
Sargassum muticum	ZnO	3-57nm; hexagonal wurtzite structures	One pot method for synthesis	UV-Vis, XRD, FESEM	Sulfate and hydroxyl moieties of polysaccharide	(Azizi *et al.*, 2014)
Green algae						
Klebsormidium flaccidum	β-FeOOH			XRD, HRTEM, SEM-EDS	Intracellular	(Brayner *et al.*, 2009)
Chlorella vulgaris	Pd	7nm, spherical	Photosynthetically driven metal transformation	TEM, SEM, ICP-OES, XPS	NADPH	(Eroglu *et al.*, 2012)
Chlorococcum sp. MM11	Fe	20-50 nm, spherical	Remediation of toxic Cr(VI)	UV-Vis, TEM, DLS, FTIR, EDAX	Carbonyl and amine bonds from polysaccharides and glycoproteins present in the algal cell wall	(Subramaniyam *et al.*, 2015)
Scenedesmus-24	CdS	120-175 nm, oval shape	Environmental remediation-based application	FTIR, XRD, TEM	Hydroxly Group, N-H bond of amino group	(Jena *et al.*, 2015)
Red algae						
Gracilaria edulis	ZnO	66-95 nm, rod shaped,	Anticancerous against PC3 cell lines	UV-Vis, EDX, FTIR, FESEM, XRD	Quinines	(Priyadharshini, Prasannaraj and Geetha, 2014)

2.6.4 Mechanism of synthesis of nanoparticles from algae

Algae are known to hyper accumulate heavy metal ions and possess an exceptional capability to remodel them into more malleable forms (Fawcett, Verduin and Shah, 2017). Because of these alluring attributes, algae have been foreseen as model organisms for fabricating bio-nanomaterials. Algal extracts consist of carbohydrates, proteins, minerals, oil, fats, polyunsaturated fatty acids along with the soup of bioactive compounds such as antioxidants (polyphenols, tocopherols), and pigments such as carotenoids (carotene, xanthophyll), chlorophylls, and phycobilins (phycocyanin, phycoerythrin) ((Michalak and Chojnacka, 2015)). These potentially active compounds have been elucidated as reducing and stabilizing agents. From the available reports, algae-mediated synthesis of NMs involves preparation of (i) algal extract, (ii) metal precursor solution, and (iii) incubation of algal extract with metal precursor solution (Sharma *et al.*, 2016). The reaction is initiated by mixing the liquid algal extract with the molar solution of metal precursor. Typically, the colour change of the reaction mixture demarcates as a visible signature for the initiation of reaction illustrating nucleation, followed by growth of NPs in which the adjoining nucleonic particles club together, thus forming thermodynamically stable NPs of different size and shape (Prasad, Pandey and Barman, 2016; Sharma *et al.*, 2016; Fawcett, Verduin and Shah, 2017). The bioactive component of extract supports the cascade of nanoparticle synthesis and the controlling factors involved are pH, temperature, concentration and time. Keeping aside the controlling factors, there are two routes of synthesis i.e. extracellular and intracellular. Initially, the nanoparticle synthesis was reported to be intracellular (Lengke, Fleet and Southam, 2007)but later algae were exploited for an extracellular mode of synthesis (Dahoumane *et al.*, 2012; Aboelfetoh, El-Shenody and Ghobara, 2017; Fawcett, Verduin and Shah, 2017).

2.6.4.1 Intracellular mode of synthesis of nanoparticles

The term “intracellular” refers to the process which takes place inside the cell. There is no requirement for any pre-treatment of microalgae because the process relies on metabolic pathways likely to be responsible for synthesis such as photosynthesis, respiration and nitrogen fixation (Sharma *et al.*, 2016). The reducing agents may be NADPH or NADPH dependent reductase in the energy generating steps during photosynthesis *via* electron transport system (ETS) or may be respiratory ETS at thylakoid membranes (Sicard *et al.*, 2010) or at the cell wall (Senapati *et al.*, 2012).

An example is of *Rhizoclonium fontinale* and *Ulva intestinalis* when treated with chloroauric acid for 72 h at 20 °C; there was a visual change in the colour of thallus from green to purple confirming the fabrication of Au-NPs. This was supported by the fact when the gold solution was incubated with dried biomass there was no change in colour, which affirms that the bioreduction process is not associated with any of the metabolic pathways involving enzymes or other metabolites and the cells were poisoned by Au^{3+} when converted to Au^{0} (Parial *et al.*, 2012). Sicard et al (2010) encapsulated *Klebsormidium flaccidum* in silica gel suspension. The evident colour change of chloroplasts from green to purple inside the cells demonstrated the capacity of the entrapped cells to reduce gold salts. TEM images showed dark spots of reduced gold salts in the thylakoid membranes suggesting involvement of enzymes (NADPH and NADPH dependent reductase) in the synthesis of nanoparticles (Sicard *et al.*, 2010).

In line with this trend, Senapati and co-workers (2012) demonstrated the intracellular synthesis by the algal cell wall in *Tetraselmis kochinensis.* UV-visible spectroscopy clearly proved that there was no extracellular synthesis. The NPs were more densely present near the cell wall rather than the cytoplasmic area, which is most likely due to the presence of bioactive moieties responsible for bioreduction. Further XRD of gold nano-alga biofilm confirms the synthesis of NPs at the cell wall (Senapati *et al.*, 2012). Another chlorophycean alga *Spirogyra submaxima*, was also found to be efficient in bioconversion of Au^{3+} to Au^{0}. After exposure to gold solution, colour of the biomass turned pinkish purple and Au-NPs were extracted using sodium citrate solution as a capping agent. The intracellular synthesis of crystalline gold was further supported by Bragg reflections of purple coloured biomass (Roychoudhury and Pal, 2014).

2.6.4.2 Extracellular mode of synthesis of nanoparticles

The term "extracellular" refers to the process that takes place outside the cell mainly supported by the exudates of cell metabolism comprising of metabolites, ions, pigments, various proteins (enzymes) and non-protein entities such as DNA, RNA, microbial by-products (hormones, antioxidants) and lipids (Mata *et al.*, 2009; Vijayan *et al.*, 2016). The algal biomass is subjected to rudimentary pre-treatments such as washing and blending (Dahoumane, Wujcik and Jeffryes, 2016).

Kalabegishvili et al. (2012) hypothesized that the active moieties on the surface of cells are not solely responsible for the synthesis rather optimum concentration of metal precursor and a number of cells is essential. Gold NPs were customized by varying the cell number and dose

of Au (III) ions. The presence of gold peak at 530 nm affirmed the extracellular synthesis assisted by biomolecules/ proteins and enzymes on the cell surface of *Spirulina platensis*. In addition, gold uptake is time dependent which takes place in two phases i.e. rapid phase in which metal ions are taken up quickly on the cell surface because of the presence of active biomolecules (amino, carboxylic, phosphate, thiol), and the slow phase in which metal ions cross the cell membrane using transport mechanisms of the cell (Kalabegishvili and Kirkesali, 2012).

In another study, Parial and Pal (2015) reported the extracellular synthesis of Au-NPs from *Lyngbya majuscula* and *Spirulina subsalsa*, where the gradual development of colour was a time-dependent convenient visible signature indicating massive bioconversion of Au^{3+} to Au^{0} leading to a steady synthesis of Au-NPs (Parial and Pal, 2015). Shakibaie et al. (2010) were hesitant to confirm the exact mechanism involved in the synthesis of Au-NPs *via Tetraselmis suecica*. The gold NPs fabricated were not enzyme dependent as the organism is a non-thermophile since the clear band at 530 nm appeared after 90 ^{o}C. The formation and stabilization of Au-NPs at these conditions might be due to the presence of reducing agents such as polyols and water-soluble heterocyclic compounds respectively (Shakibaie *et al.*, 2010). The dried biomass of epilithic green alga, *Prasiola crispa* was exercised to tailor spherical Au-NPs (Sharma *et al.*, 2014). The FT-IR spectrum clearly illustrated the extracellular production of protein and organic moieties which might be responsible for preventing agglomeration and facilitating synthesis. The colour of the algal biomass remained intact after the completion of the process, thus ruling out the intracellular mode. The authors believed an extracellular pathway was responsible indicated by the purple colour and an absorption peak at 535 nm (Sharma *et al.*, 2014).

Apart from the intracellular and extracellular modes of synthesis of NPs, two research groups reported both the modes of synthesis simultaneously (Parial *et al.*, 2012; Jena *et al.*, 2015). Though many theories and hypotheses have been postulated to date, not one could clearly explain the exact mechanism for the synthesis of NPs.

2.7 Zinc oxide nanoparticle

ZnO possesses a wide band gap of 3.37eV and exhibits natural n-type electrical conductivity, while also being non-toxic and belonging to the II-VI group (Rao *et al.*, 2022). The term "II-VI semiconductor" is utilized in materials science to denote a class of materials that possess

notable characteristics including favourable transparency, elevated electron mobility, broad band gap, and luminescent properties (Morkoç and Özgür, 2008). ZnO exhibits a white powdery appearance and displays a high degree of insolubility in aqueous solutions (Bhunia *et al.*, 2016). ZnO is a highly sought-after additive in various materials and products, including ceramics, glass, cement, lubricants, paints, ointments, adhesives, plastics, sealants, pigments, foods (zinc nutrient), batteries, ferrites, and fire retardants (Chauhan, Kataria and Garg, 2020). This is due to its exceptional properties, such as high refractive index, high thermal conductivity, strong binding energy, antibacterial effects, and UV-protection (Aminuzzaman *et al.*, 2021). According to some studies reported in literature, ZnO exhibits superior durability, selectivity, and heat resistance compared to both organic and inorganic materials (Morkoç and Özgür, 2008; Rao *et al.*, 2022). ZnO possesses favourable attributes such as rapid electron transfer and a high level of biocompatibility. These characteristics make it a promising candidate for utilization as a bio-mimetic membrane for the purpose of immobilizing and altering bio-molecules (Anbuvannan *et al.*, 2015; Azizi *et al.*, 2015; Sharma *et al.*, 2016). ZnO stands out among other semiconducting materials due to its abundance of nanostructures and its capacity to undergo various morphological transformations (Morkoç and Özgür, 2008; Aspoukeh, Barzinjy and Hamad, 2022). These transformations include the formation of nanowires (Manzano, Philippe and Serrà, 2022), nanorods (Aspoukeh, Barzinjy and Hamad, 2022), nanocombs (Asiya and Pal, 2022), nanoflowers (Raj *et al.*, 2022) and nanosheet (Supraja *et al.*, 2022). Despite its lack of toxicity to humans, it is commonly consumed in the form of a daily supplement for its mineral element, which is essential to human health. According to Rahmah and coworkers (2022) , PVC films coated with ZnO powder exhibited antibacterial properties against foodborne pathogens (Rahmah, Sabry and Aziz, 2022).

2.7.1 Properties of ZnO

The following section provides a comprehensive analysis of crystal structures, including various aspects such as lattice parameters, electronic band structures, mechanical properties (elastic constants and piezoelectric constants), thermal properties, electrical properties, and low-field and high-field carrier transports (Table 2.7).

Table 2.7: Physical properties of ZnO

Molecular formula	ZnO
Molecular Weight	81.37 g/mol
Stable phase at 300 K	Wurtzite
Colour	Pure microcrystalline ZnO is white
Odour	Odourless
Relative Density	5.607g/cm^3
Sublimation Point	1200℃
Melting Point	1975℃
Boiling Point	2360℃
Vapor Pressure (1500℃)	12mm
Solubility in water	0.16 mg/100 mL (30 °C)
Band gap (RT)	3.370 eV
Band gap (4 K)	3.437 eV
Exciton binding energy (meV)	60
Electron effective mass	0.24
Refractive Index	w = 2.004, e = 2.020
Heat of Sublimation between 1350℃ and 1500℃	129 Kcal/mole (vapor not disassociated) and 193 Kcal/mole (vapor associated)
Heat Capacity	Cp = 9.62 cal/deg/mole at 25℃
Linear expansion coefficient	a_0 : 6.5 $cm^3 \times 10^{-6}$
	c_0: 3.0 $cm^3 \times 10^{-6}$
Thermal conductivity (Wm^{-1} $℃^{-1}$)	0.6, 1-1.2
Static dielectric constant	8.656
Electron Hall mobility at 300 K (cm^2 /Vs)	200
Hole effective mass	0.59
Hole Hall mobility at 300 K (cm^2 /Vs)	5-50

2.7.2 Crystal structure of ZnO

ZnO exhibits the wurtzite hexagonal crystal structure, which is considered the most stable configuration (Morkoç and Özgür, 2008). This crystal structure is observable exclusively under

an electron microscope. The precise formation method greatly influences the distinctive structure of the crystal. ZnO displays variations in morphology, with acicular needle-like shapes (Chen *et al.*, 2023) and plate-shaped crystals (Ashour, El-Awady and Tawfik, 2022) exhibiting contrasting characteristics. Presently, specific deposition methods are being actively researched and developed to induce the formation of a crystalline structure in ZnO. It is noteworthy that ZnO commonly crystallizes in three distinct forms: the hexagonal wurtzite structure, the cubic zinc blende structure, and the cubic rock salt structure (Fig. 2.6) (Morkoç and Özgür, 2008; Aspoukeh, Barzinjy and Hamad, 2022).

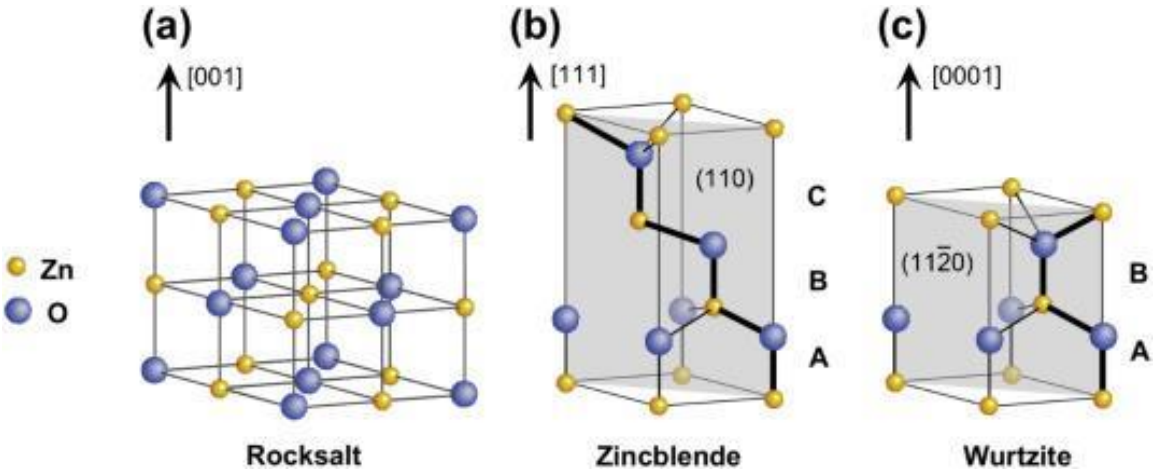

Fig.2.6: ZnO crystal structure (a) rock salt, (b) Zinc blende and (c) Wurtzite (**Source:** (Özgür, Avrutin and Morkoç, 2018))

2.7.3 Lattice parameters

By applying bond technique to symmetrical and asymmetrical reflections, high resolution x-ray diffraction (HRXRD) is often and widely used to estimate the lattice parameters of any crystalline material (Rodrigues *et al.*, 2022). The lattice parameters of a semiconductor are influenced by several factors (Morkoç and Özgür, 2008). These include the concentration of free electrons, which affects the deformation potential of the conduction-band minimum that these electrons occupy ((Özgür, Avrutin and Morkoç, 2018)). Additionally, the concentration of foreign atoms and defects, as well as their difference in ionic radii compared to the substituted matrix ion, can also impact lattice parameters (Morkoç and Özgür, 2008; Özgür, Avrutin and Morkoç, 2018). External strains induced by the substrate and temperature are also contributing factors.

Experimental measurements and theoretical calculations of the lattice constants for wurtzite ZnO at room temperature exhibit good agreement. The a parameter typically ranges from 3.2475 to 3.2501 Å, while the c parameter ranges from 5.2042 to 5.2075 Å (Morkoç and Özgür, 2008; Özgür, Avrutin and Morkoç, 2018). Slight variations are observed in the c/a ratio, ranging from 1.593 to 1.6035, and the u parameter, ranging from 0.383 to 0.3856 (Morkoç and Özgür, 2008; Rao *et al.*, 2022). These deviations from the ideal wurtzite crystal structure are likely attributed to factors such as lattice stability and ionicity (Gurbandurdyyev *et al.*, 2023). Studies indicate that the expansion of the lattice is primarily influenced by free charge, which is proportional to the deformation potential of the conduction-band minimum and inversely proportional to the carrier density and bulk modulus (Sa *et al.*, 2022).

2.7.4 Mechanical properties

The mechanical characteristics of materials include a range of fundamental principles, including but not limited to, hardness, stiffness, piezoelectric constants, young's and bulk moduli, and yield strength. The wurtzite ZnO crystal exhibits acoustic anisotropy, albeit to a minimal extent. Specifically, the difference between the shear sound velocities vTA1 and vTA2, which propagate along the (001) and (100) directions, respectively, is negligible, with a ratio of vTA2/vTA1 equal to 0.98 (Decremps *et al.*, 2001).

ZnO has been identified as the tetrahedrally bonded semiconductor with the most significant piezoelectric tensor (Hijazi and Xie, 2022). The significant attribute of this material renders it a crucial technological component in numerous applications that necessitate a substantial electromechanical coupling (Mula *et al.*, 2022). In crystals exhibiting hexagonal wurtzite phase, the piezoelectric tensor comprises three distinct and independent components, while in crystals exhibiting cubic zinc-blende phase, it comprises a single component. These components serve to fully characterize the piezoelectric tensors of said crystals. Two components in the wurtzite phase are capable of quantifying the polarization that is induced along the c axis, when there is no electric field present. This polarization is generated by a uniform strain that is either applied along the c axis or in the basal plane (Hijazi and Xie, 2022; Mula *et al.*, 2022).

2.7.5 Electronic properties

Due to its large direct band gap of 3.3 eV at room temperature, ZnO is transparent and colorless. It has many useful properties, including high breakdown voltages, resistance to electric fields,

and ability to function in high-heat and high-power environments (Singh, 2010). Understanding the electrical properties of ZnO nanostructures is of utmost importance for the future development of nanoelectronics applications. In its pure form, ZnO exhibits n-type characteristics primarily due to non-stoichiometry, including oxygen vacancies and zinc interstitials (Ellmer and Bikowski, 2016). This behavior is particularly evident in ZnO nanowires, which display n-type semiconductor behavior (Ellmer and Bikowski, 2016).

However, a significant challenge in utilizing ZnO for electronics and photonics applications lies in achieving effective p-type doping. Overcoming this obstacle and successfully achieving p-type doping in ZnO nanostructures would greatly enhance their potential for advanced applications in nanoscale electronics and optoelectronics. By achieving p-type doping, both p-type and n-type ZnO nanowires can be utilized to create p-n junction diodes and light-emitting diodes (LEDs), further expanding their functionality (Singh, 2010; Ellmer and Bikowski, 2016).

2.7.6 Optical properties

ZnO is a wide band gap semiconductor that displays luminescent properties in the near ultra violet and the visible regions (Morkoç and Özgür, 2008; Özgür, Avrutin and Morkoç, 2018). The emission properties of ZnO nanoparticles in the visible region widely depend on their synthetic method as they are attributable to surface defects. In ZnO, a photon with energy 3655 A corresponds to the gap in energy between the valence and conduction bands. It's visible-light transparent, however it has a high absorption of UV light with a wavelength below 3655A (Behera, 2011). Compared to other white pigments, it generally demonstrates higher absorption in this range. In the visible wavelength region, standard zinc oxide appears white. When exposed to UV light, zinc oxide exhibits photoconductive behaviour, as observed through analytical analysis. Doped zinc oxide further enhances its optical and semiconductor properties, making it a prime candidate for the development of next-generation devices (Özgür, Avrutin and Morkoç, 2018).

2.8 Application of ZnO NPs

ZnO NPs, a type of wide bandgap semiconductor that has garnered significant attention due to their versatility in various fields (Ahmed *et al.*, 2017). Apart from the various industrial applications of ZnO NPs discussed in Table 2.3. One notable advantage of these nanoparticles is their enhanced antibacterial activity against both gram positive and gram negative bacteria

(Jena *et al.*, 2015; Ahmed *et al.*, 2017), antifungal activity (Gunalan, Sivaraj and Rajendran, 2012). This heightened effectiveness is primarily attributed to the larger surface-to-volume ratio exhibited by the nanoparticles (Basnet *et al.*, 2018). Owing to the high band gap energy, it has exhibited widespread applications as photocatalyst for degradation of toxic compounds (Kaur *et al.*, 2023). Plants treated with different concentration of ZnO NPs enhanced carotenoids, biomass, chlorophyll a, total soluble proteins, SOD, and POX but reduced CAT and malondialdehyde. Antioxidant defense enzymes regulate isoenzyme expression and ROS. Thus, ZnO NPs in phycomolecules have agricultural potential (Venkatachalam *et al.*, 2017).

2.9 Concluding remarks

Existing conventional methods for nanomaterial syntheses and their physicochemical characterizations are not user-friendly, as they involve toxic reducing and stabilizing agents, non-biodegradable organic and inorganic compounds, high energy consumption, and a relatively low yield. In addition, the resultant nanomaterials retain the encapsulation of hazardous chemical reagents used in conventional synthesis, limiting their therapeutic application. To overcome these limitations, the development of green strategies has become crucial. In this study, ZnO NPs were synthesized from aqueous extracts of plants (Lemon grass) and algae (*A. variabilis* ARM 441), which were then characterized using different spectroscopic and microstructural techniques. Further, they were utilized for the photocatalytic degradation of organic pollutants (bisphenol-A) and textile dyes (bright green and indigo caramine) for future industrial applications.

CHAPTER-III Material and Methods

3.1 Material required

3.1.1 Chemicals and glassware

General (analytical) chemicals

Zinc acetate dihydrate ($Zn(CH_3COO)_2.2H_2O$)) (99.9%) was purchased from Merck EMSURE®, Germany. Both the dyes, brilliant green ($C_{27}H_{33}N_2.HO_4S$) and indigo carmine ($C_{16}H_8N_2Na_2O_8S_2$), Bisphenol-A ($(CH_3)_2C(C_6H_4OH)_2$) were purchased from Sigma Aldrich, USA. All the experiments were performed using analytical grade water with a resistivity of 18.2 MΩ cm from a Millipore Milli-Q Gradient filtration system (Millipore, USA). Unless otherwise stated, all other reagents and chemicals were of analytical grade and obtained from HiMedia Pvt. Ltd., India.

Plants

Cymbopogon citratus commonly known as Citronella grass or Lemon grass was procured from the Science and Technology Entrepreneur's Park, Thapar Institute of Engineering and Technology, Patiala, located at 30.3530° N, 76.3710° E, 310 m above sea level.

Algal strains

Anabaena variabilis ARM 441 was procured from the Centre for Conservation and Utilisation of Blue-Green Algae (CCUBGA), Indian Agricultural Research Institute (IARI), New Delhi (India).

Glassware and plastic ware

Glassware used in the entire study were procured from borosil, JSGW, or Schott Duran and the plastic ware used was from Tarsons or HiMedia.

3.1.2 Sterilization techniques

All the glassware used in the study were washed thoroughly with HiClean followed by treatment with aqua regia (HNO_3:HCl::1:3) and final rinsing with distilled water to remove all the accumulated salts and metals. Cleaned glassware were dried in oven at 60°C.

3.2 Preparation of extracts

Preparation of plant extracts

Lemon grass leaves were washed thoroughly with tap water and dried in shade at ambient temperature and cut into smaller pieces and stored in an airtight container. 10 g of Lemon grass pieces were was taken in 100 ml of milli-Q water in the Soxhlet apparatus for continuous solvent extraction, using water solvent at 90-95℃ for 6 h to prepare Lemon grass extract (Khan *et al.*, 2018) with deep yellow colour (Fig 3.1).

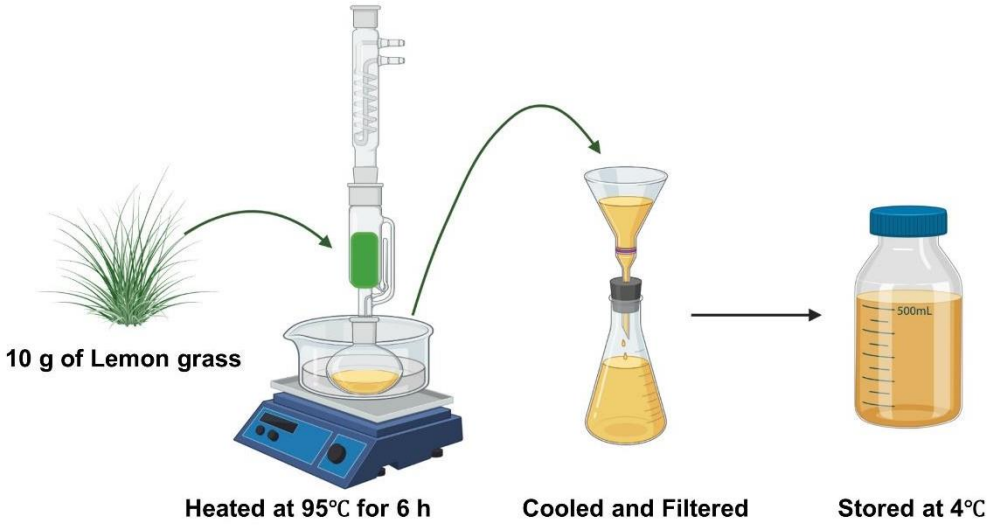

Fig. 3.1: Schematic flow illustrating the preparation of Lemon grass extract

Preparation of cyanobacterial cell extracts

Anabaena variabilis ARM 441 was cultivated for 21 days in Erlenmeyer flasks (5 L), stirred daily with continuous white light illumination (3000 Lux) at 28°C. The biomass was filtered with Whatman's filter no. 1, thoroughly washed with milli-Q water to remove adhering medium debris and shade dried at ambient temperature. Dried algal biomass was powdered using a sterile mortar and pestle and stored in airtight vials at room temperature. 3 g of dried biomass was taken in 100 ml of milli-Q water in the Soxhlet apparatus for continuous solvent extraction, using water solvent at 90-95℃ for 3 h to prepare algal extract (Khan *et al.*, 2018) until development of green colour.

Plant and algal extracts were allowed to cool at room temperature and filtered with Whatman's filter no. 1 to remove any biomass residues, leaving deep yellow and dark green solution respectively and stored in glass vials at 4℃ for further analysis.

3.3 GC-MS analysis, ^{1}H NMR, and ^{13}C NMR spectroscopy of extract

The aqueous extract of Lemon grass and *A. variabilis* ARM 441 was concentrated using a rotary evaporator for GC-MS analysis, ^{1}H NMR, and ^{13}C NMR spectroscopy to detect the bioactive compounds of interest (Vinotha *et al.,* 2019). The compounds obtained from Lemon grass and *A. variabilis* ARM 441 were analyzed as per standard protocol using a Thermo Scientific TSQ 800 GC-MS. The extract components were identified by comparing the retention time and fragmentation pattern with mass spectra of the NIST database. The relative percentage of compounds was expressed along with peak area normalization, ^{1}H NMR and ^{13}C NMR were carried out using FT NMR Spectrometer model advance II (Bruker) at 400 MHz with a 5 mm inverse probe.

3.4 Green synthesis of ZnO NPs

Plant-mediated synthesis of ZnO NPs

Bioactive components from aqueous extracts of Lemon grass were utilized as reducing and a capping agent for the fabrication of ZnO NPs. Initially, the dark yellow extract prepared from Lemon grass was diluted by 1:10 (v/v) to obtain a stock solution by addition of milli-Q water. Thereafter, 10 ml of $Zn(CH_3COO)_2$ (0.2M) solution was added drop by drop to 90 ml of plant extract stock solution in a round bottom flask. The mixture was maintained at 80 ℃ using a silicone oil bath and continuously stirred at 500 rpm on a magnetic stirrer for 6 h until the colour changed from dark yellow to cloudy light yellow.

Phycosynthesis of ZnO NPs

Water soluble bioactive components from cell extracts of *A. variabilis* ARM 441 were utilized as reducing and a capping agent for the fabrication of ZnO NPs. Initially, the dark green extract prepared from *A. variabilis* ARM 441 was diluted by 1:5 (v/v) to obtain a stock solution by addition of milli-Q water. Thereafter, 10 ml of $Zn(CH_3COO)_2$ (0.2M) solution was added drop by drop to 90 ml of cyanobacterial stock solution in a round bottom flask. The mixture was maintained at 80 ℃ using a silicone oil bath, continuously stirred at 500 rpm on a magnetic stirrer for 6 h until the colour changed from dark green to cloudy light green.

After cooling at room temperature, both the samples were centrifuged at 8000 rpm for 10 min to obtain the pellets and the supernatant was discarded. Pellets were washed twice with milli-

Q water followed by ethanol (99.9%) to remove the impurities and dried in vacuum oven at 100℃ for 12 h. The dried powder was uniformly ground using motar and pestle, sieved, and stored at room temperature for subsequent analyses.

3.5 Analytical characterization of ZnO NPs

3.5.1 UV-Visible spectroscopy

After visual identification, to affirm the complete reduction of zinc acetate to ZnO NPs was confirmed by UV Spectrophotometer using UV Win Software. The absorption maxima were determined by scanning the sample in a quartz cuvette from 200 to 800 nm where the cuvette path length was set 1 cm (Dutta, Maji and Adhikary, 2014).

3.5.2 Particle size, polydispersity index (PDI), and zeta potential

The stability of nanoparticles was evaluated by zeta potential whereas, PDI reveals homogeneity of the sample. 1 mg of ZnO NPs powder was added to 1 ml of milli-Q water and sonicated for 20 min (Thakur, Singh and Pal, 2021). The average hydrodynamic size, PDI and zeta potential of synthesized ZnO NPs was determined using the principle of dynamic light scattering by Malvern Zen 3600 particle sizer.

3.5.3 Fourier transform spectroscopy (FT-IR) analysis

Functional groups on the surface were identified using a PerkinElmer's FTIR. Lemon grass extract, *A. variabilis* ARM 441 extract, and ZnO NPs were triturated with pure KBr (Sigma Aldrich) and pressed in a mechanical press to generate pellets (Ezealisiji *et al.*, 2019). These pellets were analyzed along with pure KBr pellets at the background, and FT-IR spectrum was recorded in 4000-400 cm^{-1} to ascertain the possible secondary metabolites responsible for capping and stabilizing nanoparticles (Akhtar, Goyal and Goyal, 2017).

3.5.4 Brunauer–Emmett–Teller (BET)

Estimation of pore diameter, surface area, and porosity of ZnO NPs were characterized under liquid nitrogen temperature using Quanta Chrome Nova-1000 surface analyzer instrument. It involves multilayer adsorption-desorption of N_2 as a function of relative pressure. After degassing the samples at 150°C for 2h in N_2, final measurements were carried out. BET and de

Boer t-plot methods were used to determine surface area and pore volume (Kaur, Goyal and Agnihotri, 2021).

3.5.5 X-ray powder diffraction (XRD) analysis

XRD analysis of as-synthesized ZnO NPs was carried out in reflection geometry with PANalytical X'Pert PRO diffractometer using Cu Kα radiation (1.5406 Å) for an angle (2θ) range of 20°- 80° with step size 0.02 and counting time 5 s per step operating at 10 kV and 30 mA for identification of structure and crystalline phase. The crystallite size was calculated from XRD peaks by Debye Schererr equation $D = k\lambda/ \beta\cos\theta$ where D is the crystallite size, λ is the wavelength for Cu Kα, β is full width half maxima (FWHM), θ is Bragg's diffraction angle, and k is constant (0.9). XRD data was analyzed by reitveild refinement by using crystallographic computing software Jana 2006 (Agarwal *et al.*, 2020). The phase composition was confirmed using the JCPDS PDF database (Agarwal *et al.*, 2021).

3.5.6 X-ray photoelectron spectroscopy (XPS)

The atomic concentration and binding energy of synthesized ZnO NPs was analyzed using the X-ray Photoelectron Spectroscopy PHI 5000 VersaProbe III (Physical Electronics). The binding energy was corrected for the charge shift using the C1s peak of graphitic carbon (BE ¼ 284.6 eV) as a reference. XPS measurement was performed with a step size of 0.2 eV. Spectra were processed and fitted by Origin 9.0 software using Gaussian–Lorentzian curve profile and Shirley baseline (Diallo *et al.*, 2015).

3.5.7 Field emission scanning electron microscopy (FE-SEM) and energy-dispersive X-ray spectroscopy (EDX), High-resolution transmission electron microscopy (HR-TEM), and Selected area diffraction (SAED) analysis

Size, morphology, and size distribution were analyzed using FE-SEM and elemental analysis was done using EDX. Powdered sample was used for FE-SEM at an accelerating voltage of 15 kV on MIRA3 TESCAN-XMU (Czech Republic). One drop of sonicated ZnO NPs in ethanol (99.9%) was dropped over the copper grid (200 mesh) and dried for surface analysis (Brazuna *et al.*, 2019). The micrographs and SAED pattern of as-synthesized ZnO NPs was recorded on high-resolution transmission electron microscope Jeol, JEM2100 at 200kV. The microstructural analysis for obtained results from SEM and TEM was determined with ImageJ software.

3.5.8 Thermogravimetric analysis (TGA)

Thermal stability of the synthesized ZnO NPs was studied using thermogravimetric analysis on Mettler Toledo Instrument under N_2 atmosphere, over a temperature range of 25- 1000°C and heating rate of 10 °C min^{-1}.

3.6 Optimization of nanoparticle synthesis using Response surface methodology (RSM)

Response surface methodology (RSM), a widely employed method for the optimization of a multivariable system was used for nanoparticle synthesis optimization of gram scale synthesis from Lemon grass and *A. variabilis* ARM 441 extracts. A three level Box-Behnken Design (BBD) was assessed for regression analysis taking three independent factors. The polynomial coefficients for every term of the equation were determined by the analysis of multiple regressions. The three independent factors employed for the optimization were zinc initial concentration (mM), reaction time (h), and extract (%). The yield (mg) was recorded as a response. The ranges and the levels of the independent variables based on experimental design are given in Table 3.1 and Table 3.2 for Lemon grass and *A. variabilis* ARM 441 respectively.

Table 3.1: The ranges and levels of variables in Box–Behnken statistical experimental design for Lemon grass

Variables	**Symbol**	**Coded level**		
		Low	**Centre**	**High**
		-1	**0**	**+1**
Zinc (mM)	A	100	550	1000
Reaction time (h)	B	6	8	10
Extract (%)	C	10	45	80

Table 3.2: The ranges and levels of variables in Box–Behnken statistical experimental design for *A. variabilis* ARM 441

Variables	**Symbol**	**Coded level**		
		Low	**Centre**	**High**
		-1	**0**	**+1**
Zinc (mM)	A	100	250	400
Reaction time (h)	B	4	6	8
Extract (%)	C	10	30	50

The nanoparticle yield (mg), obtained as the response (dependent variable) was represented as a second order polynomial equation to express the effect of different variables (Eq.1).

$$Y = \beta_0 + \sum \beta_i + X_I + \sum \beta_{ii} X_i^2 + \sum \beta_{ij} X_i X_j \ldots\ldots\ldots\ldots\ldots\ldots\ldots\ldots (1)$$

Where Y= represents response, X_i and X_j= independent variables which affect the response. The β_0 defines regression coefficient for the intercept, β_i for linear, β_{ij} for cross product terms and β_{ii} for quadratic.

Model adequacy for the investigated parameters was assessed *via* Analysis of Variance (ANOVA). ANOVA is an analytical tool to evaluate the enactment of tested experiments, by perceiving the value of "p", multiple correlation coefficients (R^2), lack of fit, as well as adjusting coefficient of determination (R^2-adj). The Box-Behnken Design was employed to evaluate the influence of three independent variables in 17 sets of experiments. The generated model by RSM was then validated by performing experiments at the generated optimum variable conditions.

3.7 Photocatalytic degradation

3.7.1 Photocatalytic degradation of Brilliant green (BG) and Indigo carmine (IC) by ZnO NPs synthesized by *A. variabilis* ARM 441

The photocatalytic efficiency of as-synthesized ZnO NPs was estimated by the photodegradation of BG and IC dyes. The impact of major parameters (pH, dye concentration, catalyst dosage and time) affecting the dye degradation was evaluated individually. The ZnO NPs and dye mixture was stirred in the dark for 20 minutes to achieve the adsorption-desorption equilibrium and eliminate the adsorption errors.

3.7.2 Photocatalytic degradation of Bisphenol-A by ZnO NPs synthesized by Lemon grass

The photocatalytic efficiency of as-synthesized ZnO NPs was estimated by the photodegradation of Bisphenol-A (BPA). The impact of major parameters (pH, dye concentration, catalyst dosage and time) affecting the dye degradation was evaluated individually. The ZnO NPs and dye mixture was stirred in the dark for 10 minutes to achieve the adsorption-desorption equilibrium and eliminate the adsorption errors.

Each mixture was placed inside two 15W low-pressure mercury lamps (LP Hg lamps, Cole-Parmer) with monochromatic emission at 253.7 nm. The fluency rate of the lamp was

calculated to be 1.3 W/cm^2 photoreactor and exposed to UV light with continuous stirring. All the photochemical experiments were done in triplicates and at 40-45 ℃. Milli-Q water was used in the preparation of sample solutions. Over desired time intervals (0-130 min for BG, IC and 0-45 min for BPA) about 5 ml solution was collected and centrifuges to separate the catalyst. The absorption spectra for the supernatant were analysed using UV-Visible spectrophotometer in the 200-800 nm range.

3.7.3 Degradation kinetics

The degradation efficiency (%) of the respective ZnO NPs was calculated by the following reference (Eq.2).

$$Degradation\ efficiency\ (\%) = \frac{C_0 - C}{C_0} \times 100 \ldots\ldots\ldots\ldots\ldots\ldots\ldots\ldots (2)$$

The kinetics of degradation of different dyes and organic pollutants was studied by testing four kinetic models: first order, pseudo-first order, second order, and pseudo-second order (Kaur, Goyal and Agnihotri, 2021). These models were expressed by the following equations:

First order: $$lnC = lnC_0 - kt$$

Pseudo-first order: $$ln\ ln\ [C - C_0] = ln\ ln\ C - kt$$

Second order: $$\frac{1}{C} = \frac{1}{C_0} + kt$$

Pseudo-second order: $$\frac{t}{C} = \frac{t}{C_0} - \frac{1}{kC_0^2}$$

Where C_0 and C are the initial concentration (t=0) and concentration at a given time interval of each dye at $\lambda_{max,}$ respectively and k is the kinetic rate constant.

3.8 Liquid chromatography mass spectroscopy (LC-MS) analysis of by-products

The photodegradation by-products of degraded dye solution were analysed at different time intervals using an Alliance 2795, Q-TOF Micromass Mass spectrometer (Waters Corporation, UK) instrument. The mobile phase was a blend of water (A) and acetonitrile (B) at 0.6 ml min^{-1} of the flow rate. The gradient was set as follows: t = 0 min, A:B = 5:95 (v/v); t = 30 min, A:B = 95:5 (v/v) (Aminuzzaman *et al.*, 2018). Using an auto sampler, the injection volume was 20.00 µl and the column temperature was 30°C. The mass fragments were studied in the range of 40 to 400 m/z.

CHAPTER-IV Results and Discussion

4.1 Green Synthesis of ZnO nanoparticles

4.1.1 Synthesis of ZnO NPs using Lemon grass extract

Lemon grass was chosen, as it is a herb known worldwide for its high essential oil content. It is easily available and cultivable. In the present investigation, bioactive components from the prepared aqueous extract of Lemon grass were utilized as a reducing and a capping agent for the fabrication of ZnO NPs.

4.1.1.1 Determination of the content of Lemon grass bio-active compounds

GC-MS analysis of extract from Lemon grass

A large variety of bioactive compounds (23) are present in crude extract of Lemon grass since chromatogram shows a number of peaks with various retention times (Fig. 4.1). The major components present in the aqueous extract of Lemon grass, along with the molecular formula, molecular weight, retention time, and peak area, are presented in Table 4.1. The principle bioactive compounds present in the extract are Citral (13.9%), 2,6-Octadienal, 3,7-dimethyl-, (Z)- (10.3%), 2-Isopropenyl-5-methylhex-4-enal (9.8%), Photocitral B (4.68%), 2-Pentanone, 4-hydroxy-4-methyl- (4.69%), (S)(-) Citronellic acid, methyl ester (2.83%), Geraniol (2.63%), Geranic acid (2.19%), Limonene oxide (1.71%), phytol (1.71%), cis-Vaccenic acid (1.44%), hexadecanoic acid, methyl ester (1.14%) (Gandhi *et al.*, 2017; Gurusamy *et al.*, 2019). Potential compounds as capping agents could be various forms of terpenoids, monoterpenes, keto-enol compounds, fatty acids, palmitic acid and phytol with some other ancillary phytochemicals.

^{1}H and ^{13}C NMR spectroscopic analysis Lemon grass extract

NMR spectroscopy is suitable for metabolite profiling and analysis as it provides an overview of all the metabolites and detects diverse groups of secondary metabolites. ^{1}H and ^{13}C NMR spectroscopic investigations were done to determine the components present in the Lemon grassf. The Indian Lemon grass is composed of 75% oil which largely contains (75-85%) citral (Do *et al.*, 2021). Amongst the numerous constituents of the oil, some common constituents include linalool, geraniol, citronellol, nerol, 1,8- cineole, citronellal, linalyl acetate, geranyl

acetate, α-pinene, limonene, caryophyllene, β- pinene, β- thujene, myrcene, β- ocimene, terpenolene, methyl heptanone and α-terpineol (Do *et al.*, 2021).

The ^{1}H NMR spectral data show chemical shift values ranging between δ = 0 to 10.0, as displayed in Fig. 4.2 and Table 4.2. The chemical shift values δ 1.09, 1.15, 1.16, 1.17 signify 1° alkanes; δ 1.22 represent 2° alkanes and δ 1.53, 1.58 correspond to 3° alkanes whereas δ 1.62, 1.65 indicate the presence of allylic protons and δ 1.93, 1.99, 2.17, 2.60 imply for germinal alkenes. The chemical shifts δ 3.39, 3.49, 3.52, 3.54, 3.59, 3.60, 3.62, 3.64, 3.66, 3.69, 3.70, 3.76, 4.00 represent the alcoholic groups, δ 5.04, 5.26 correspond to vinylic groups and δ 5.83, 5.87, 6.23, 6.31, 6.54, 6.64. 6.69, 6.89 indicate conjugated vinylic chain. Finally, the peaks arising from δ 9.97, 9.99 indicate the aldehyde groups, according to the standard chart.

The chemical shifts for ^{13}C NMR ranged between δ = 0 to 200.0, as shown in Fig. 4.3 and Table 4.2. The ^{13}C spectrum showed resonance at δ 18.38, 18.21 representing 1° alkanes; δ 25.62, 26.13, 26.29, 27.22 corresponding to 2° alkanes and δ 32.81, 34.41 signifying 3° alkanes whereas δ 102.59, 104.63, 116.65, 123.79, 127.53, 133.43, 135.42, 142.37 indicate the presence of allylic carbons and δ 102.59, 104.63, 116.65, 123.79, 127.53, 133.43, 135.42, 142.37 represent germinal alkenes. The chemical shifts δ 52.69, 52.92, 61.28, 61.94, 62.65, 63.11, 70.47, 70.92, 72.28, 72.52, 72.91, 73.66, 75.53, 77.18, 82.80, 92.78, 93.03 represent alcohol bearing carbons, δ 161.27 signify vinylic groups and δ 168.13, 168.82, 169.46, 171.72, 172.97, 173.56 indicate conjugated vinylic components. Finally, the peaks arising from δ 193.55, 194.32 represent the aldehyde group affirming the ^{1}H NMR spectral data.

4.1.1.2 Biosynthesis of ZnO NPs using extracts from Lemon grass

Lemon grass mediated synthesis of ZnO NPs was achieved using a co-precipitation method. 10 ml of $Zn(CH_3COO)_2$ (0.2M) solution was added drop by drop to 90 ml of plant extract stock solution in a round bottom flask. The mixture was maintained at 80°C using a silicone oil bath, continuously stirred at 500 rpm on a magnetic stirrer for 6 h until the colour changed from dark yellow to cloudy light yellow. In the present study, the development of light yellow colour in the reaction mixture confirmed the fabrication of ZnO NPs.

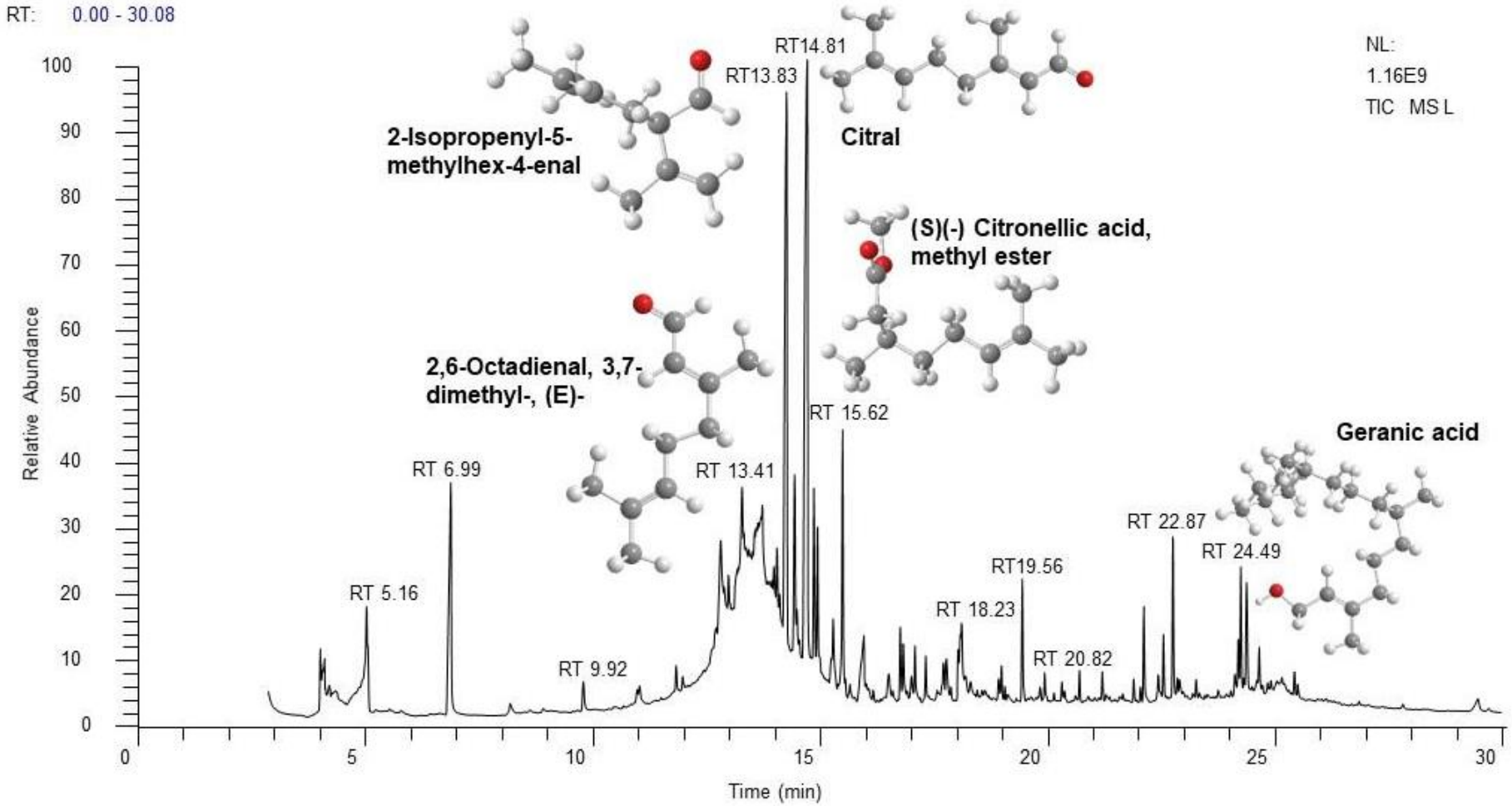

Fig. 4.1: GCMS of Lemon grass extract

Table 4.1: Bioactive compounds of Lemon grass extract identified through GC–MS analysis

Peak No.	Retention time (RT)	Area%	Compound Name	Molecular Formula	Compound nature
1	4.19	3.07	Thiocyanic acid, propyl ester	C_4H_7NS	Ester
2	5.16	3.63	Propane, 1,1-dipropoxy-	$C_9H_{20}O_2$	Aldehyde
3	6.99	4.6	2-Pentanone, 4-hydroxy-4-methyl-	$C_6H_{12}O_2$	Diacetone alcohol
4	13.41	6.91	2,6-Octadienal, 3,7-dimethyl-, (E)-	$C_{10}H_{16}O$	Citral
5	13.83	9.8	2-Isopropenyl-5-methylhex-4-enal	$C_{10}H_{16}O$	-
6	14.17	4.68	Photocitral B	$C_{10}H_{16}O$	Citral
7	14.37	10.3	2,6-Octadienal, 3,7-dimethyl-, (Z)-	$C_{10}H_{16}O$	Citral
8	14.56	2.63	Geraniol	$C_{10}H_{18}O$	Monoterpenoid
9	14.81	13.9	Citral	$C_{10}H_{16}O$	Monoterpene aldehyde
10	15.41	1.16	2,6-Octadiene-1,8-diol, 2,6-dimethyl-	$C_{10}H_{18}O_2$	-
11	15.62	2.83	(S)(-) Citronellic acid, methyl ester	$C_{11}H_{20}O_2$	Monoterpenoid
12	16.06	2.19	Geranic acid	$C_{10}H_{16}O_2$	Fatty Acid
13	16.89	1.5	Glutaric acid, 4chlorobenzyl tetradecyl ester	$C_{26}H_{41}ClO_4$	Carboxylic Acid
14	17.21	1.07	2-Heptanone, 7,7 dimethoxy-5-(1-methylethyl)-	$C_{12}H_{24}O_3$	Ketone
15	17.89	1.71	Limonene oxide	$C_{10}H_{16}O$	Terpene oxide
16	18.22	3.06	3-Nonanol, 1,2:6,7-diepoxy-3,7-dimethyl-, acetate	$C_{13}H_{22}O_4$	-
17	19.10	0.81	Caryophyllene oxide	$C_{15}H_{24}O$	Sesquiterpenoid oxide
18	19.56	1.19	Selina-6-en-4-ol	$C_{15}H_{26}O$	Terpenoids
19	22.23	1.05	1-Hexadecanol	$C_{16}H_{34}O$	Cetyl alcohol
20	22.67	1.14	Hexadecanoic acid, methyl ester	$C_{17}H_{34}O_2$	Palmitic acid
21	22.88	2.35	2,6-Octadien-1-ol, 3,7-dimethyl-, propanoate, (E)-	$C_{13}H_{22}O_2$	-
22	24.49	1.71	Phytol	$C_{20}H_{40}O$	Diterpene
23	25.26	1.44	cis-Vaccenic acid	$C_{18}H_{34}O_2$	Trans- fatty acid

Table 4.2: Characteristic peaks of Lemon grass extract identified through of ^{1}H and ^{13}C NMR

Compound	^{1}H NMR chemical shift values	^{13}C NMR chemical shift values
Alkane		
1°	1.09, 1.15, 1.16, 1.17	18.38, 18.21
2°	1.22	25.62, 26.13, 26.29, 27.22
3°	1.53, 1.58	32.81, 34.41
Allylic	1.62, 1.65	38.91, 39.58, 40.88, 42.21
Alkene (geminal)	1.93, 1.99, 2.17, 2.60	102.59, 104.63, 116.65, 123.79, 127.53, 133.43, 135.42, 142.37
Alcohol	3.39, 3.49, 3.52, 3.54, 3.59, 3.60, 3.62, 3.64, 3.66, 3.69, 3.70, 3.76, 4.00	52.69, 52.92, 61.28, 61.94, 62.65, 63.11, 70.47, 70.92, 72.28, 72.52, 72.91, 73.66, 75.53, 77.18, 82.80, 92.78, 93.03
Vinylic	5.04, 5.26	161.27
Vinylic (conjugated)	5.83, 5.87, 6.23, 6.31, 6.54, 6.64. 6.69, 6.89	168.13, 168.82, 169.46, 171.72, 172.97, 173.56
Aldehyde/Ketone	9.97, 9.99	193.55, 194.32

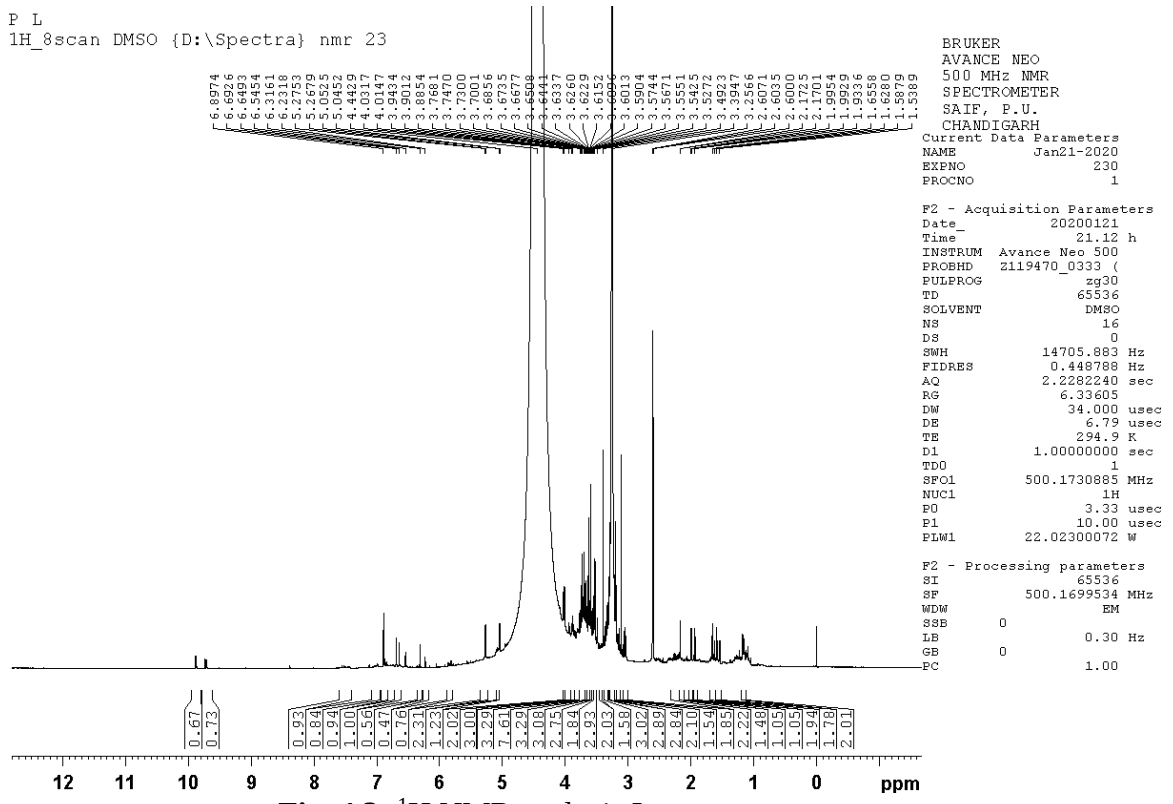

Fig. 4.2: ^{1}H NMR analysis Lemon grass extract

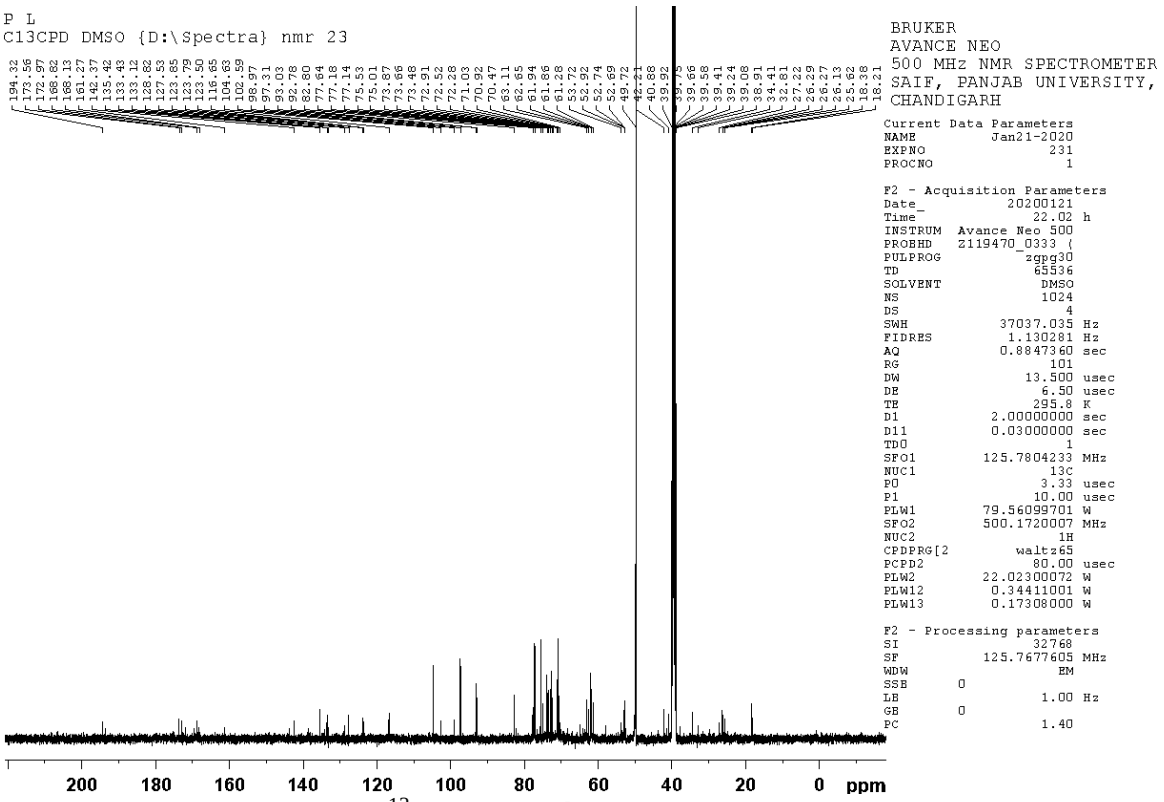

Fig. 4.3: ^{13}C NMR analysis Lemon grass extract

4.1.1.3 Mechanism of synthesis of ZnO NPs from Lemon grass extract

Lemon grass aqueous extract as a novel, cost-effective yet safe source was selected for the production of ZnO nanoparticles. Plant extracts had been exploited as natural stabilizing and capping agent due to the presence of distinctive consortia of secondary metabolites. Recent research has indicated that bioactive components present in the extract of lemongrass may have significant role in the synthesis of diverse nanoparticles (Anvekar, Rajendra and Kadam, 2017; Ajayi and Afolayan, 2017; Motelica *et al*., 2021; Riyanto *et al.*, 2022; Mohammed *et al*., 2023). The extract of Lemon grass is rich in phytochemical compounds that serve as critically important reducing and stabilising agents in the production of ZnO NPs, resulting in a high-quality yield. Citral and photocitral-B constitute approximately 37% of the aqueous crude extract of Lemon grass. Thus, it could be inferred that the reduction of Zn^{2+} ions to stable Zn atoms is predominantly facilitated by citral and photocitral-B. The probable chemical equations for synthesis of Lemon grass /ZnO NPs as shown in Eqs. (3) and (4). Fig. 4.4 illustrates a plausible mechanism of interaction of Zn^{2+} ions and the main components of Lemon grass extract (Mohamad Sukri *et al*., 2019).

$$Lemon\ grass + H_2O_{(L)} + Zn^{2+} \rightarrow [Lemon\ grass/Zn^{2+}] \ldots\ldots\ldots\ldots\ldots\ldots\ldots\ldots (3)$$

$$[Lemon\ grass/Zn^{2+}] + O_2 \rightarrow [Lemon\ grass/ZnO\ NPs] + CO_{2(g)} \ldots\ldots\ldots\ldots\ (4)$$

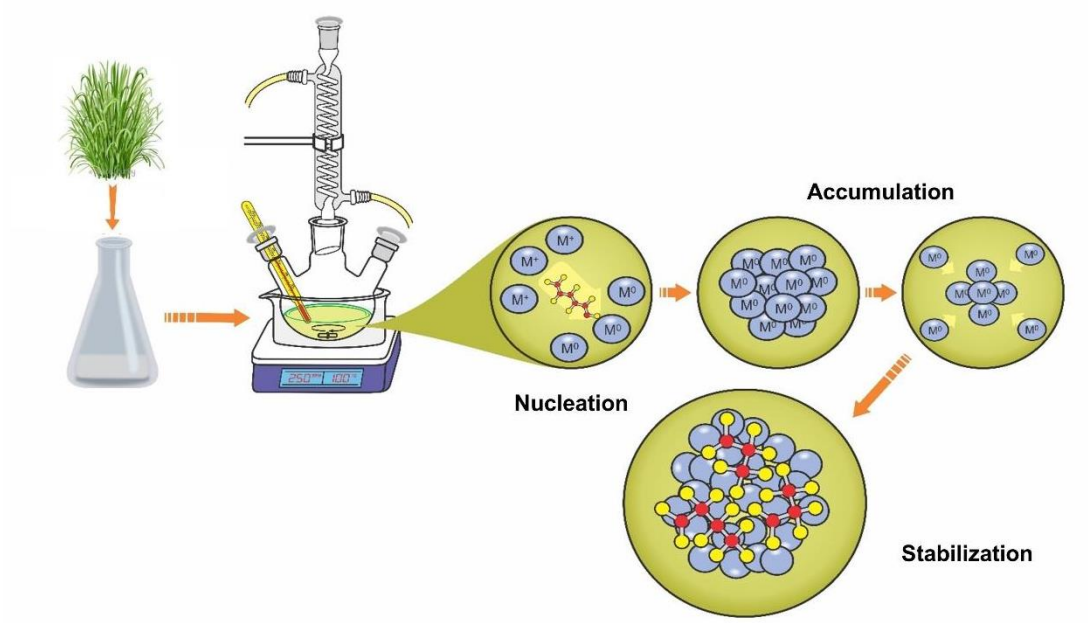

Fig. 4.4: Schematic presentation of synthesis of ZnO NPs from Lemon grass extract

The aforementioned phenomenon demonstrates that an abundance of negatively charged atoms within the extract contribute their electrons, thereby stabilizing complex ions of Zn^{2+} that carry a positive charge. Consequently, the Zn^{2+} complex ions undergo a conversion process leading to the formation of ZnO NPs.

4.1.2 Synthesis of ZnO NPs using *A.variabilis* ARM 441 extract

Anabaena variabilis ARM 441 was chosen because it grows luxuriantly in paddy fields and it can be easily cultivated in inorganic media (Chittora *et al.*, 2020). The present investigation was focused to explore the role of aqueous cellular extract of diazotrophic cyanobacterium *A. variabilis* ARM 441 in the fabrication of ZnO NPs (Malek Shahkouhi and Motamedian, 2020).

4.1.2.1 Determination of the content of *A. variabilis* ARM 441 bio-active compounds

GC-MS analysis of extract from A.variabilis ARM 441

Chromatogram of *A.variabilis* ARM 441 extract shows a number of peaks of bioactive compounds with variable retention times (Fig. 4.5). The major components present in the cyanobacterial extract of *A.variabilis* ARM 441, along with the molecular formula, molecular weight, retention time, and peak area, are presented in Table 4.3. The principle bioactive compounds (21) present in the extract include 13-tetradecenal (33.19 %), chloromethyl 5-

chloroundecanoate (19.91%), n-hexadecanoic acid (12.83%), 4-hydroxy-4-methyl-2-pentanone (9.39%), octadecanoic acid (5.69%), 2-chloroethyl linoleate (3.09%), tetradecanoic acid, 10,13-dimethyl-, methyl ester (2.15%) hexadecanoic acid, 2-hydroxy-1-(hydroxymethyl) ethyl ester (1.86%), ricinoleic acid (0.81%), phytol (0.44%)(Gandhi *et al.*, 2017; Gurusamy *et al.*, 2019) Thus, potential candidates for capping agents could be fatty acids, palmitic acid, and phytol along with protein moieties and some other ancillary phytochemicals. The abundance of n-hexadecanoic acid and 13-tetradecenal in cyanobacterial cell extract act as a coating and provide stability to ZnO NPs (Gandhi *et al.*, 2017; Gnanakani *et al.*, 2019; Gurusamy *et al.*, 2019).

^{1}H and ^{13}C NMR spectroscopic analysis A. variabilis ARM 441 extract

^{1}H and ^{13}C NMR spectroscopic investigations were performed to determine the components present in the *A.variabilis* ARM 441 cyanobacterial extract. The ^{1}H NMR spectral data show chemical shift values ranging between δ = 0 to 9.0, as displayed in Fig. 4.6 and Table 4.4. The chemical shift values δ 0.83, 0.85, 0.91, 0.93, 0.94 signify 1° alkanes; δ 1.21, 1.22, 1.31 represent 2° alkanes and δ 1.48 correspond to 3° alkanes whereas δ 1.78, 1.80, 1.91, 1.96, 2.02, 2.04, 2.05, 2.16, 2.18, 2.19 indicate the presence of alkenes and δ 2.31 imply for alkynes. The chemical shifts δ 3.89, 3.90, 3.91, 3.93 represent alkyl chloride and δ 2.53, 3.60, 3.62, 3.64 correspond to acids and esters (Vinotha *et al.*, 2019). Finally, the peaks arising from δ 3.06, 3.13, 3.20 indicate alcohols, δ 5.32, 5.33 signify the presence of 2-furanoyl group and δ 8.36 as aldehyde/ketone components, according to the standard chart (Silverstein *et al.*, 2014).

The chemical shifts for ^{13}C NMR ranged between δ = 0 to 200.0, as shown in Fig. 4.7 and Table 4.4. The ^{13}C spectrum showed resonance at δ 14.0, 14.1, 16.9, 20.2, 20.9 representing 1° alkanes; δ 21.3, 22.3, 24.7, 25.2 corresponding to 2° alkanes and δ 31.5, 34.0 signifying 3° alkanes whereas δ 125.7, 127.1, 127.7, 128.1, 128.2, 128.4, 129.7, 130.0, 131.6 indicate the presence of alkenes and δ 72.6 represent alkynes. The chemical shifts δ 48.7, 49.9, 63.0, 63.2 represent alkyl chloride and δ 172.5, 174.8 signify acids and esters. Finally, the peaks arising from δ 66.8, 70.6, 172.6, and 174.9 indicate the presence of the 2-furanoyl group and δ 177.8 as aldehyde/ketone components affirming the ^{1}H NMR spectral data (Silverstein and Bassler, 1962). Vinotha et al., 2019(Vinotha *et al.*, 2019) point out that the potential of NMR-based metabolomics is indiscriminating classes of compounds that may contribute to nanoparticles' surface stabilization. The obtained ^{1}H and ^{13}C NMR spectral analysis further corroborates with the GC-MS spectroscopic data.

Table 4.3: Bioactive compounds of *A. variabilis* ARM 441 extract identified through GC–MS analysis

Peak No.	Retention time (RT)	Area %	Compound Name	Molecular Formula	Compound nature
1	5.03	0.61	4-Methyl-3-penten-2-one	$C_6H_{10}O$	Mesityl oxide
2	6.39	9.39	4-Hydroxy-4-methyl-2-pentanone	$C_6H_{12}O_2$	Diacetone alcohol
3	15.41	0.15	Dodecamethyl-cyclohexasiloxane	$C_{12}H_{36}O_6Si_6$	
4	20.47	0.26	Dodecane, 2,7,10-trimethyl-	$C_{15}H_{32}$	Sesquiterpene
5	21.18	0.33	Tetradecanoic acid	$C_{14}H_{28}O_2$	Myristic acid, Fatty acid
6	21.86	0.44	Phytol, acetate	$C_{22}H_{42}O_2$	Diterpene
7	22.83	2.15	Tetradecanoic acid, 10,13-dimethyl-, methyl ester	$C_{17}H_{34}O_2$	
8	23.08	1.32	cis,cis,cis-7,10,13-Hexadecatrienal	$C_{16}H_{26}O$	
9	23.32	12.83	n-Hexadecanoic acid	$C_{16}H_{32}O_2$	Palmitic acid
10	24.29	0.86	13-Hexyloxacyclotridec-10-en-2-one	$C_{18}H_{32}O_2$	
11	24.50	3.09	2-Chloroethyl linoleate	$C_{20}H_{35}ClO_2$	Fatty acid
12	25.08	33.19	13-Tetradecenal	$C_{14}H_{26}O$	Volatile steroid
13	25.25	5.69	Octadecanoic acid	$C_{18}H_{36}O_2$	Oleic acid
14	25.42	3.79	cis-7,cis-11-Hexadecadien-1-yl acetate	$C_{18}H_{32}O_2$	Alkyl Chalcogenides
15	25.66	0.29	17-Octadecynoic acid	$C_{18}H_{32}O_2$	Long-chain fatty alcohols
16	25.84	1.36	(R)-(-)-14-Methyl-8-hexadecyn-1-ol	$C_{17}H_{32}O$	Long-chain fatty alcohols
17	26.50	0.99	Methyl 12-hydroxy-9-octadecenoate	$C_{19}H_{36}O_3$	Fatty acid methyl ester
18	27.14	19.91	Chloromethyl 5-chloroundecanoate	$C_{12}H_{22}Cl_2O_2$	
19	27.47	0.81	Ricinoleic acid	$C_{18}H_{34}O_3$	Fatty acid
20	29.39	0.68	cis, 6-Octadecenoic acid, trimethylsilyl ester	$C_{21}H_{42}O_2Si$	Oleic acid
21	29.72	1.86	Hexadecanoic acid, 2-hydroxy-1-(hydroxymethyl)ethyl ester	$C_{19}H_{38}O_4$	Palmitic acid

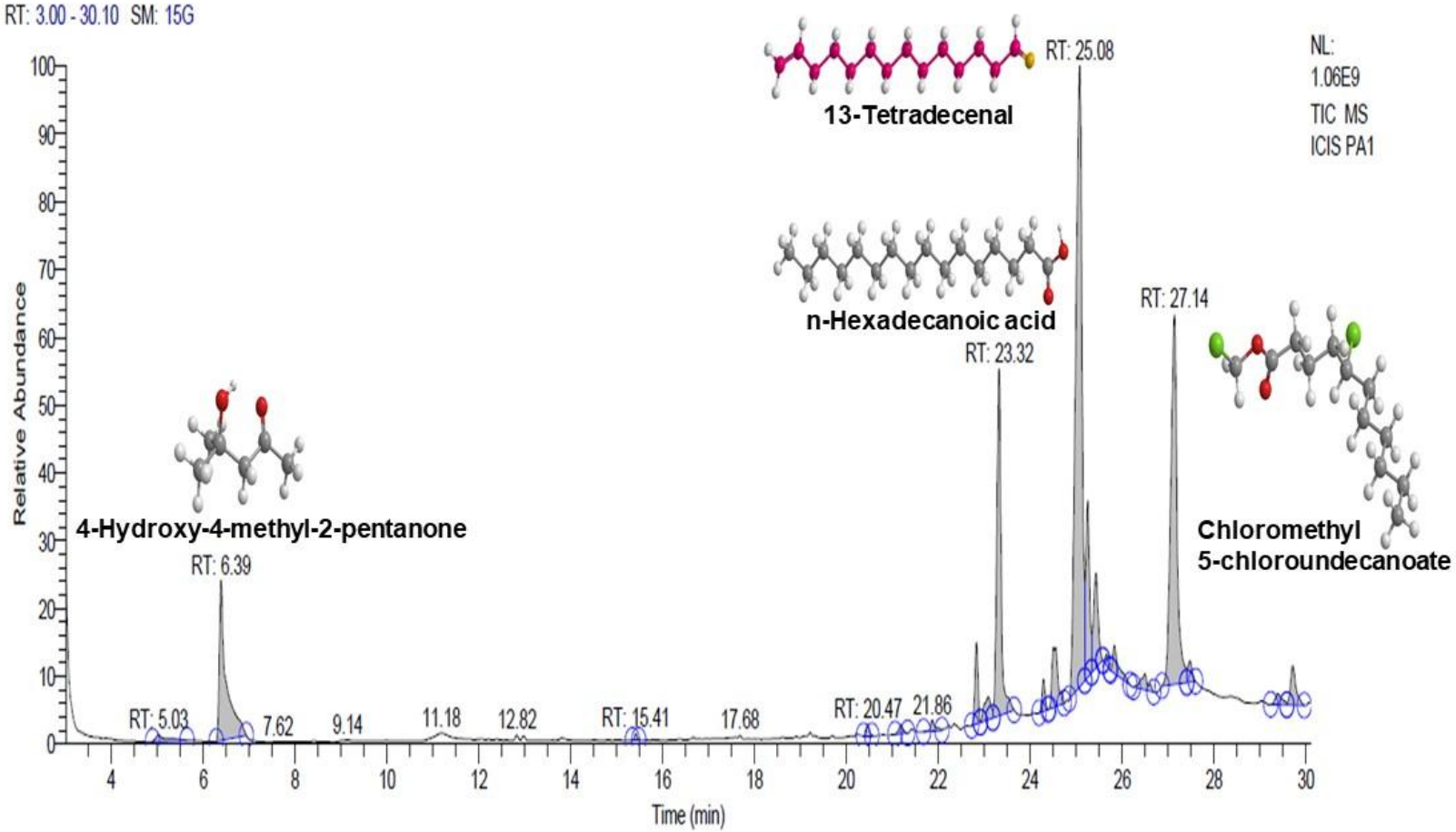

Fig. 4.5: GCMS of *A.varaibilis* ARM 441 extract

Table 4.4: Characteristic peaks of *A. variabilis* ARM 441 extract identified through of ^{1}H and ^{13}C NMR

Compound	^{1}H NMR chemical shift values	^{13}C NMR chemical shift values
Alkane		
1°	0.83, 0.85, 0.91, 0.93, 0.94	14.1, 14.0, 16.9, 20.2, 20.9
2°	1.21, 1.22, 1.31, 1.31	21.3, 22.3, 24.7, 25.2
3°	1.48	31.5, 34.0
Alkene	1.78, 1.80, 1.91, 1.96, 2.02, 2.04, 2.05, 2.16, 2.18, 2.19	125.7, 127.1, 127.7, 128.1, 128.2, 128.4, 129.7, 130.0, 131.6
Alkyne	2.31	72.6
Alkyl chloride	3.89, 3.90, 3.91, 3.93	48.7, 49.9, 63.0, 63.2
Acid/Ester	2.53, 3.60, 3.62, 3.64	172.5, 174.8
Alcohol	3.06, 3.13, 3.20	
Aldehyde/Ketone	8.36	177.8
2-Furanoyl group	5.32, 5.33	66.8, 70.6, 172.6, 174.9

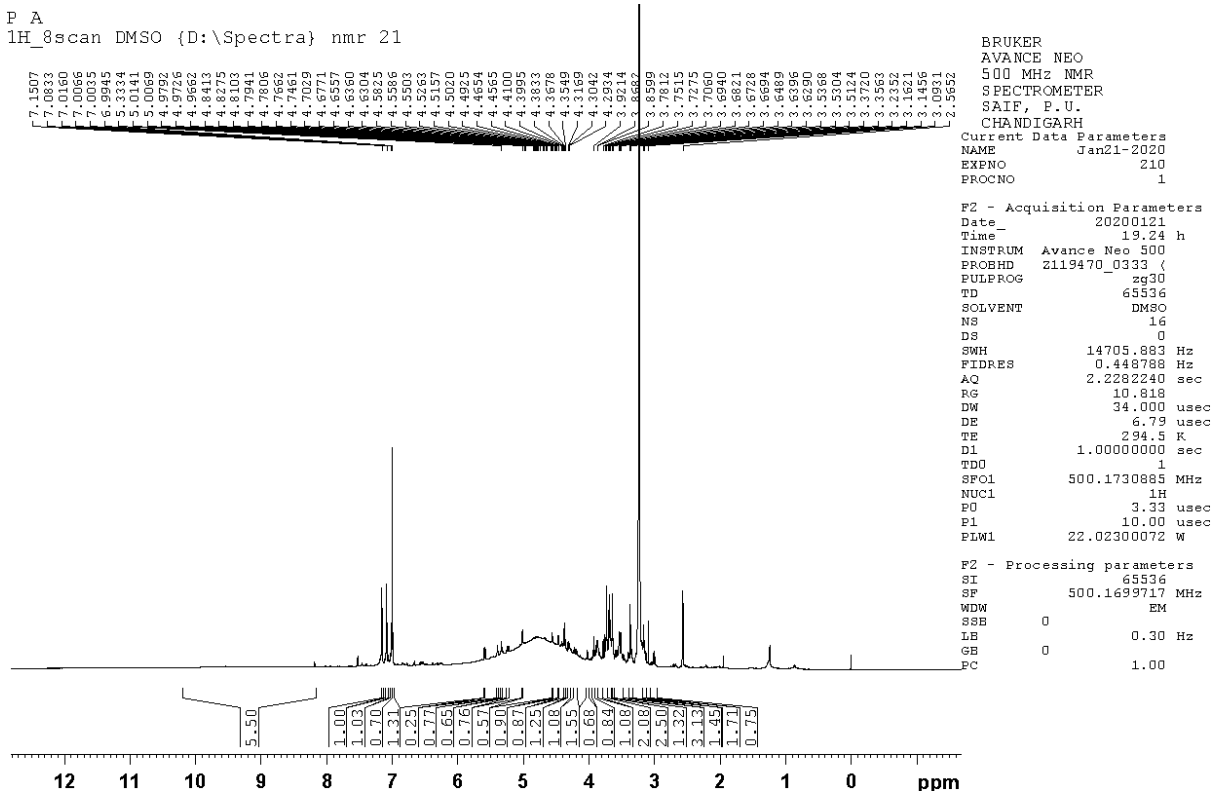

Fig. 4.6: ^{1}H NMR analysis *A. variabilis* extract

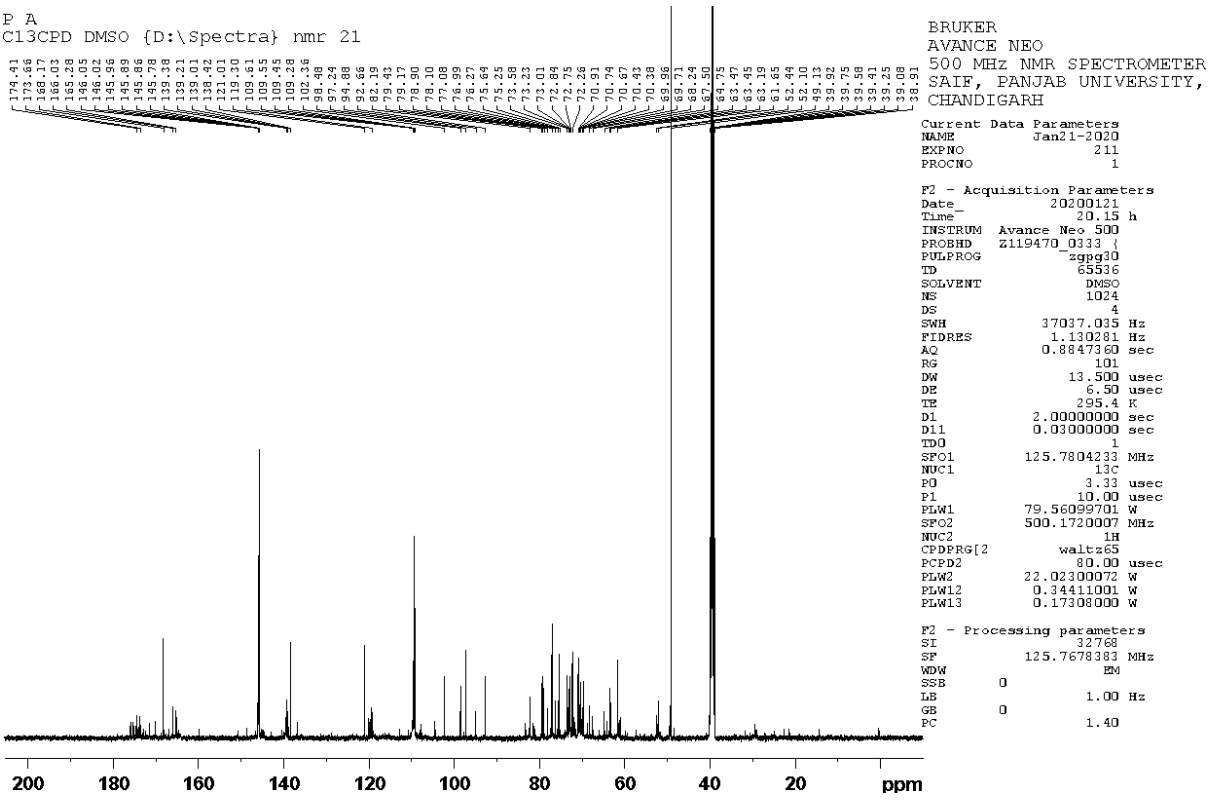

Fig. 4.7: ^{13}C NMR analysis *A. variabilis* extract

4.1.2.2 Biosynthesis of ZnO NPs using extracts from *A.variabilis* ARM 441

A.variabilis ARM 441 mediated synthesis of ZnO NPs was achieved using a co-precipitation method. The development of cloudy green colour in the reaction mixture confirmed the fabrication of ZnO NPs, which might be attributed to the interaction of functional groups of bioactive moieties of the cyanobacterial extract with zinc acetate to reduce it into Zn^0 ions, thus stabilizing ZnO NPs (Fig 4.8). The gradual change in colour during the reaction between zinc acetate and aqueous extract of *A.variabilis* ARM 441 indicated the phycoreduction of zinc acetate to ZnO NPs as reported by (Naseer *et al.*, 2020).

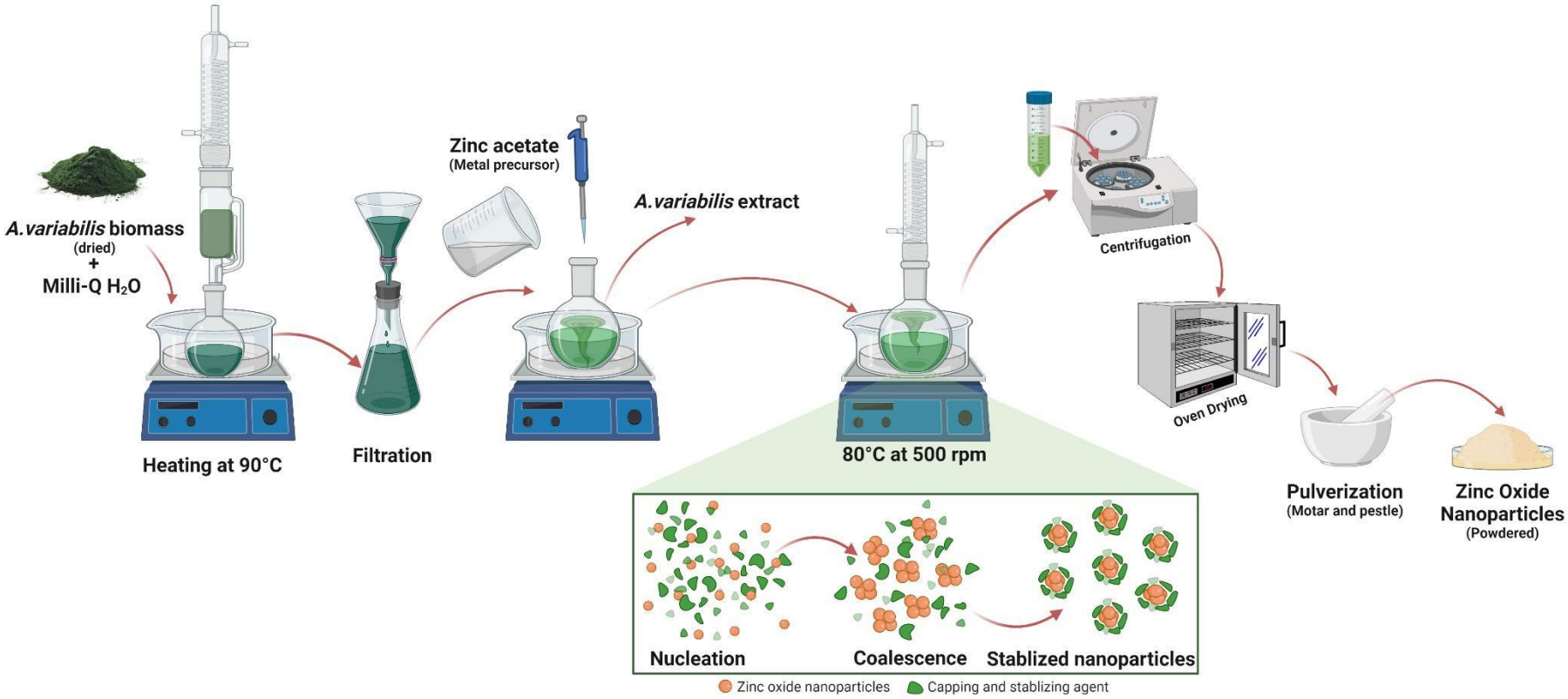

Fig. 4.8: Schematic flow illustrating the preparation of *A. variabilis* ARM441 extract and formation-mechanism of the ZnO NPs

4.1.2.3 Mechanism of synthesis of ZnO NPs from *A.variabilis* ARM 441 extract

Aqueous extract from *A.variabilis* ARM 441 as a new, safe and inexpensive source for the synthesis of ZnO NPs. The unique consortia of secondary metabolites present in algal extracts are commonly utilized as a native stabilizing and capping agent (Król *et al.*, 2019). Recent studies have revealed that n-hexadecanoic acid has a potential role in synthesizing various nanoparticles (Ebadi *et al.*, 2019; Borah *et al.*, 2020) *A.variabilis* ARM 441 extract contains phytochemical compounds that plays a vital role as reducing and stabilizing agents for obtaining a good yield of ZnO NPs. Amongst all, 13-tetradecenal and n-hexadecanoic acid make up about 46% of *A.variabilis* ARM 441 aqueous crude extract with a percentage of 33.19% and 12.83% respectively. Therefore, it is assumed that 13-tetradecenal and n-hexadecanoic acid primarily lead to the process of reducing Zn^{2+} ions to stable Zn atoms. The probable chemical equations for synthesis of *A.variabilis* /ZnO NPs as shown in Eqs. (5) and (6). Fig. 4.9 illustrates a plausible mechanism of interaction of Zn^{2+} ions and the main components of *A.variabilis* ARM 441 extract.

$$A.variabilis + H_2O_{(L)} + Zn^{2+} \rightarrow [A.variabilis/Zn^{2+}] \quad \text{(5)}$$

$$[A.variabilis/Zn^{2+}] + O_2 \rightarrow [A.variabilis/ZnO\ NPs] + CO_{2(g)} \quad \text{(6)}$$

This illustrates, excess of negatively charged atoms present in the extract donate their electrons and stabilize positively charged Zn^{2+} complex ions. As a result, the Zn^{2+} complex ions get converted to ZnO NPs (Indramahalakshmi, 2017; Mohamad Sukri *et al.*, 2019).

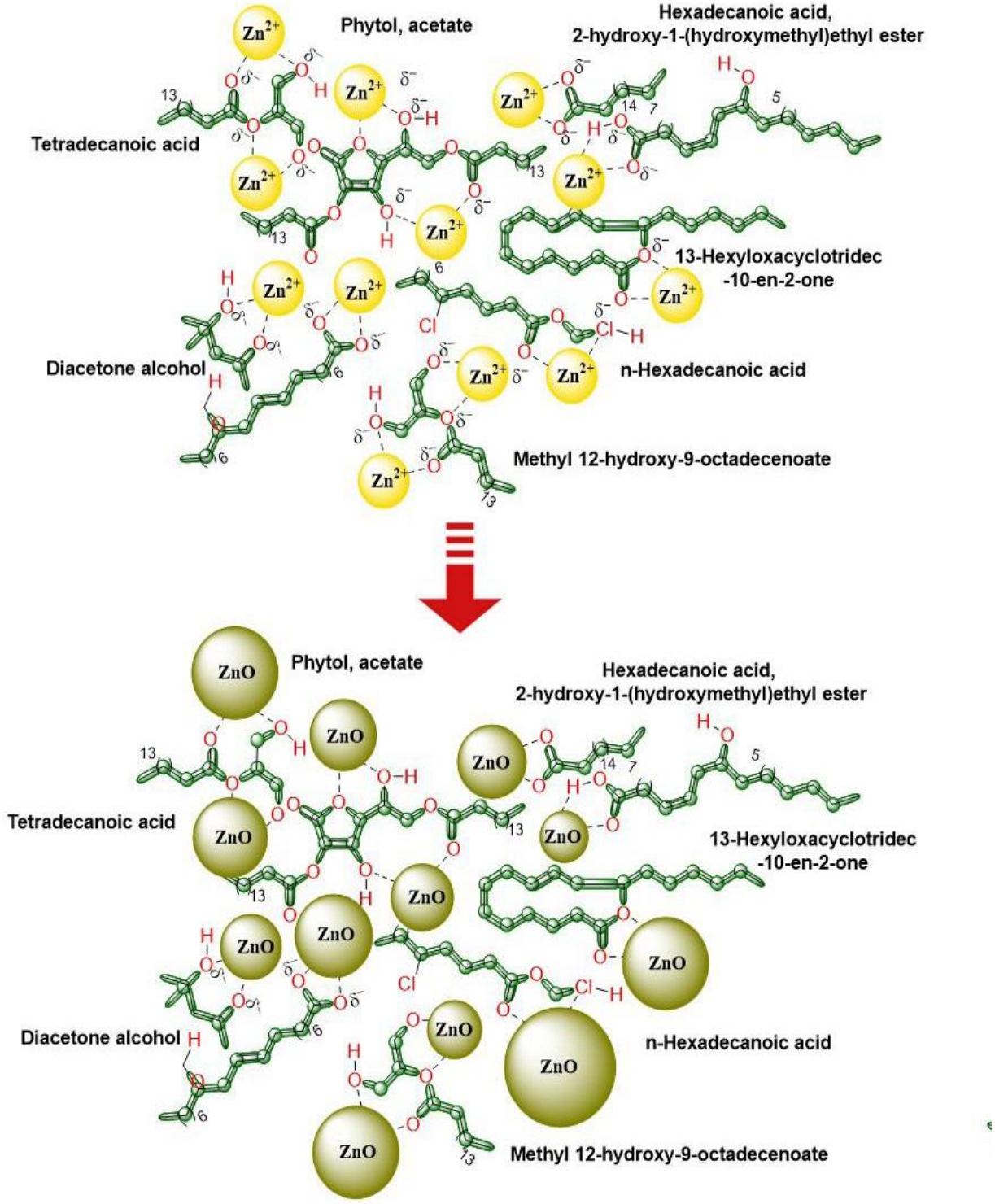

Fig. 4.9: Schematic diagram of interaction of Zn^{2+} ions with main compounds found in *A.variabilis* ARM 441 to produce ZnO NPs

4.2 Characterization of ZnO nanoparticles

4.2.1 Characterization of ZnO NPs synthesized using Lemon grass

4.2.1.1 UV-Vis of ZnO NPs synthesized using Lemon grass

The gradual change in colour during the reaction between zinc acetate and aqueous extract of Lemon grass indicated the reduction of zinc acetate to ZnO NPs as reported by (Naseer *et al.*, 2020). The absorbance band edge of synthesized ZnO NPs was approximately 351 nm as shown in Fig. 4.10, which coincides with the findings of Agarwal and Shanmugam (2019) (Agarwal and Shanmugam, 2019). The optical absorption seems to be enhanced in the 325–375 nm region. This indicates the blue shift in the absorption energies of ZnO NPs which are the manifestations of quantum size confinement in ZnO NPs. The broad band observed for ZnO NPs indicated the formation of varied sizes and shapes of the nanoparticles (Fig. 4.10). However, the dynamic absorption peak within 200-250 nm suggests the presence of secondary metabolites such as citral, terpenoids, keto-enol components, fatty acids, polyphenols which might have been responsible for reduction of $Zn(CH_3COO)_2$ to ZnO NPs. The band gap energy of green synthesized ZnO NPs was calculated by Wood's Tauc relation. It is 3.19 eV which is similar to the previous reports (Brazuna *et al.*, 2019). The enhanced radiative absorptions in 325–375 nm region and broadening of the corresponding adsorption region (3.19 eV) could be due to the discrete inter-band absorptions between the energy state of conduction band and valence band.

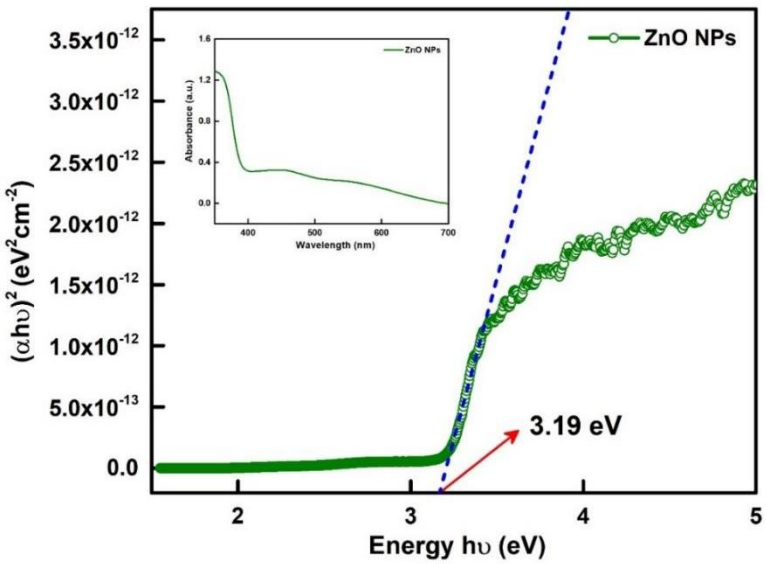

Fig. 4.10: Plot of $(\alpha h\upsilon)^2$ vs hυ inset UV–vis spectra of the ZnO NPs synthesized using Lemon grass extract

4.2.1.2 Particle size, polydispersity index (PDI), and zeta potential of ZnO NPs synthesized using Lemon grass

Malvern Zeta sizer was utilized to analyse the particle size, polydispersity index (PDI), and Zeta potential of the ZnO nanoparticles. Prior to analysis, 5 mg sample was subjected to dilution at a ratio of 1:1 (w/v) using 5 ml of milli-Q water. The resulting mixture was sonicated for 15 minutes. The graph displays a hydrodynamic size of 129.36 nm at its highest point (Fig. 4.11). The observed PDI value of 0.597 suggests the presence of polydispersed ZnO nanoparticles. In comparison to their solid-state counterparts, as-synthesized ZnO NPs had a larger hydrodynamic size. The hydrodynamic size of ZnO NPs increased in aqueous environment due to the addition of hydrate layers by the phytochemicals and ions or molecules involved during the fabrication of ZnO NPs (Telgmann *et al.*, 2016; Rolim *et al.*, 2019). Furthermore, an additional factor that contributed to a certain extent was agglomeration, as reported in literature (Santos *et al.*, 2016; Ahluwalia *et al.*, 2018). The bio-moieties present in Lemon grass extract could influence the zeta potential of green synthesized ZnO NPs (Ezealisiji *et al.*, 2019). In addition, the stability and biological activity of nanoparticles can be associated with the surface charge. The green synthesized ZnO exhibited a negative charge of -10.17 mV, as observed in the present study. The surface negative charge of ZnO nanoparticles was ascribed to the existence of negative charge on monoterpene aldehydes. The findings suggest that citral and photocitral-B are present on the surface of ZnO nanoparticles. Several other studies have shown negative zeta potential values for biogenic metallic nanoparticles (Sudha, Jeyakanthan and Srinivasan, 2017). Furthermore, the magnitude of the zeta potential in the present study suggests that the suspension of ZnO NPs exhibits a limited stability (Ezealisiji *et al.*, 2019; Jain *et al*., 2020).

4.2.1.3 Fourier transform spectroscopy (FT-IR) analysis of ZnO NPs synthesized using Lemon grass

FT-IR study was performed to recognize the active biomolecules present in the Lemon grass extract involved in ZnO synthesis (Fig. 4.12). The O-H hydrogen bonds of alkaloids and steroids identified by a broad peak at 3432.8 cm^{-1}, which closely correlated with the ZnO peak at 3391.6 cm^{-1}. Absorption peaks at 2961.5 cm^{-1} indicated vibrational motion of the alkyl (methyl) group's C-H bonds in ZnO NPs. Weak stretching in the range of 1700-1600 correspond to C = O and C = C of ketone and aldehyde. The spectra observed in the range of 1400-1000 suggest N-H stretching of amines and the C-O stretching of polyphenolic groups

such as flavonoids, terpenoids, and polysaccharides (Basera *et al.*, 2019). A distinct high intensity band was observed at 471.1 cm^{-1}, resulting from the presence of the oxygen and zinc bands while this peak was not observed in Lemon grass extract. Moreover, the less intense peaks that appeared at 698.9 cm^{-1} were attributed to mono-substituted aromatic compounds found in Lemon grass extract, confirmed the incorporation of synthesis ZnO NPs. The existence of functional groups such as -N-H, -OH, C = C, and C-H suggests that the plant extract contains hydroxyl and amine groups, which indicates the presence of flavonoids and terpenoids. The principal molecules accountable for stabilization are fatty acids, which have been corroborated by the results of GC-MS and NMR analyses.

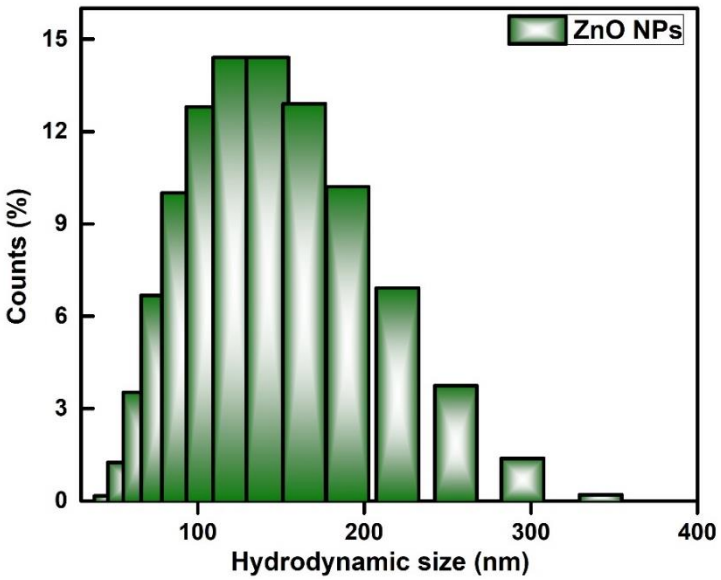

Fig. 4.11: Particle size distribution of the ZnO NPs synthesized using Lemon grass extract

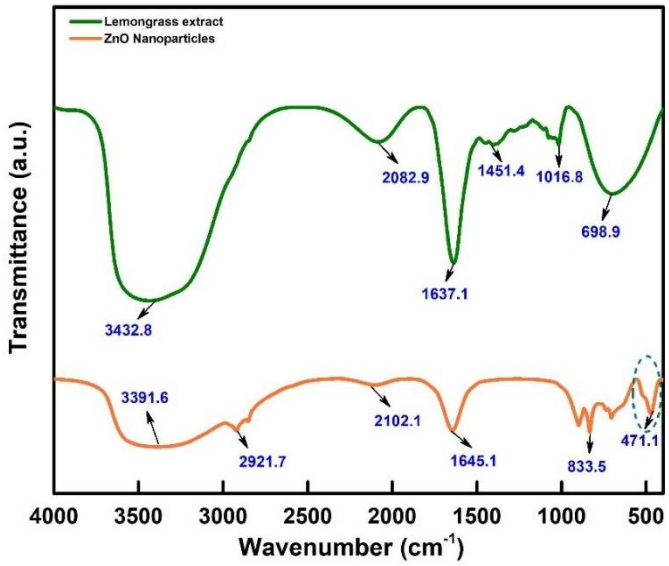

Fig. 4.12: FT-IR spectra of the ZnO NPs synthesized using Lemon grass extract

4.2.1.4 Thermal behaviour of ZnO NPs synthesized using Lemon grass

The investigation of the green synthesized ZnO NPs stability under varying temperatures is a crucial aspect of the analysis. The present study utilized thermogravimetric analysis (TGA) to investigate the as-synthesized ZnO nanoparticles within a temperature range of 25 to 800 °C (Fig. 4.13). The weight of ZnO nanoparticles exhibited a slight reduction of 1% at 100°C, which attributed to the presence of residual moisture and the resulting dehydration phenomenon. A significant and uninterrupted reduction in weight of approximately 8% was noted above 200°C, due to the organic components present in the extract of Lemon grass. Upon reaching a temperature of 431°C, the extract undergoes complete decomposition and acts as capping agent on ZnO NPs (Rambabu *et al.*, 2019). Nevertheless, it is noteworthy that ZnO exhibits stability at significantly elevated temperatures beyond the scope of the investigated range (Khatami *et al.*, 2018).

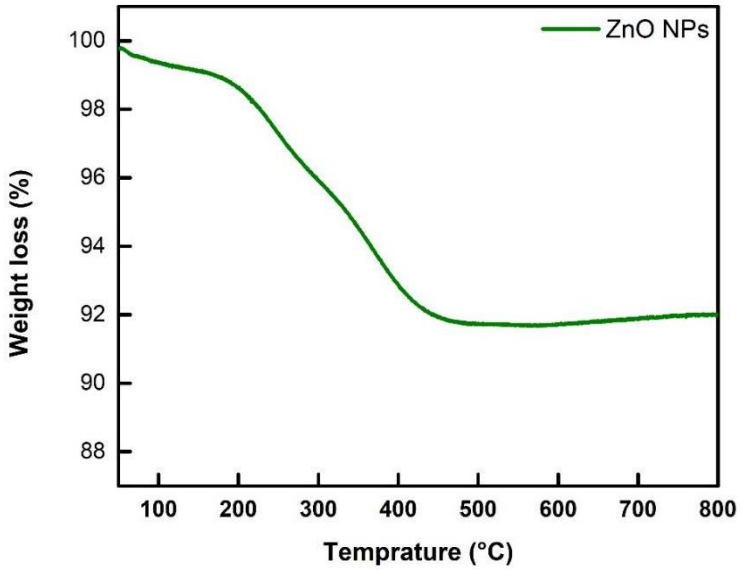

Fig. 4.13: TG thermogram of the ZnO NPs synthesized using Lemon grass extract

4.2.1.5 Nitrogen adsorption-desorption isotherms analysis (BET analysis) of ZnO NPs synthesized using Lemon grass

Nitrogen adsorption and desorption experiments were performed to investigate the surface characteristics such as surface area and porous nature of synthesized ZnO NPs mediated via Lemon grass. The results revealed a typical type IV isotherm attended by a type H3 hysteresis loop which authenticates mesoporous dominance (Fig. 4.14 (a)) (Anupama, Keune and Sahoo, 2017). The pore size distribution is shown in Fig. 4.14 (b), with an average pore diameter 12.036 nm, surface area was 57.865 m^2/g with pore volume 0.233 cc/g. The average diameter

was found to be smaller, with a greater surface area expectation. As the diameter decreases, surface area increases; hence the as-synthesized nanoparticles can be utilized as a catalyst involving adsorption and desorption of reactants (Anupama, Keune and Sahoo, 2017). A decrease in pore diameter of ZnO NPs can be another reason for its enlarged active sites (Bayrami, Alioghli, *et al.*, 2019; Bayrami, Ghorbani, *et al.*, 2019).

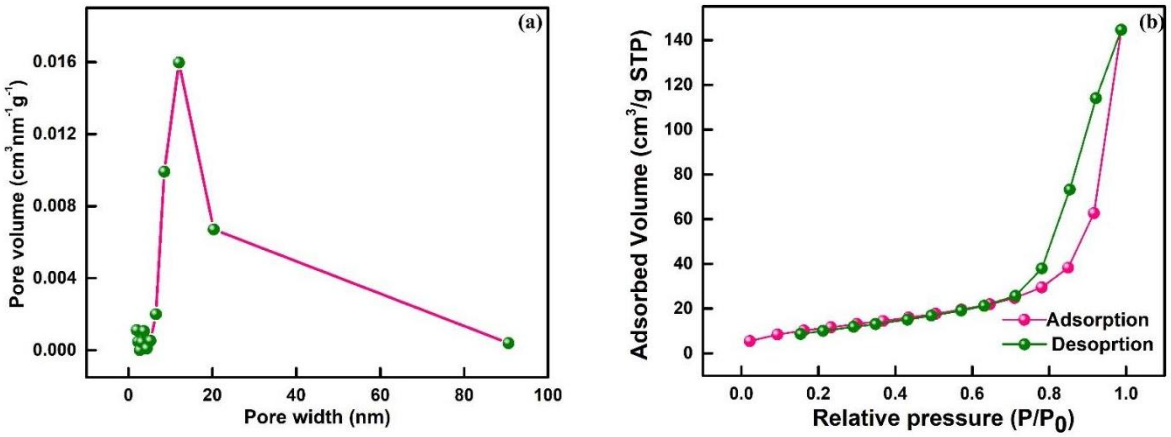

Fig. 4.14: (a) Nitrogen adsorption-desorption isotherm (b) Pore size distribution curve

4.2.1.6 Crystallinity Study of ZnO NPs synthesized using Lemon grass

The diffraction patterns obtained *via* green synthesis were indexed as hexagonal wurtzite structure according to ICDS data (JCPDS 01-079-0208) as shown in Fig 4.15 (a). The fabricated nanoparticles were pure and crystalline in nature as no evidence of peak related to any foreign moiety or bulk remnant was observed. Subsequently, narrow and sharp diffraction peaks at 2θ and indexed with planes at 31.54° (100), 34.20° (002), 36.95° (101), 47.17° (102), 56.28° (110), 62.48° (103), 67.23° (112), 68.78° (201) provide the evidence for the synthesis of single-phase wurtzite crystal structure (Saloga and Thünemann, 2019). Further, the XRD pattern was refined and analyzed employing Rietveld whole profile fitting method based on refinement technique with the help of the Jana (2006) in Fig. 4.15 (b,c and d) and Table 4.5.

Table 4.5: Refined Parameters and phase data of ZnO NPs synthesized using Lemon grass

Cell parameters	a=b= 3.2648 Å; c=5.2194 Å
	α=β= 90; γ=120
Space group	$P6_3mc$ 186
R-factor	R_{wp} = 4.63 %, R_{exp} = 5.94%
	GOF=1.59
Damping factor	0.1000
Volume	48.18 $Å^3$

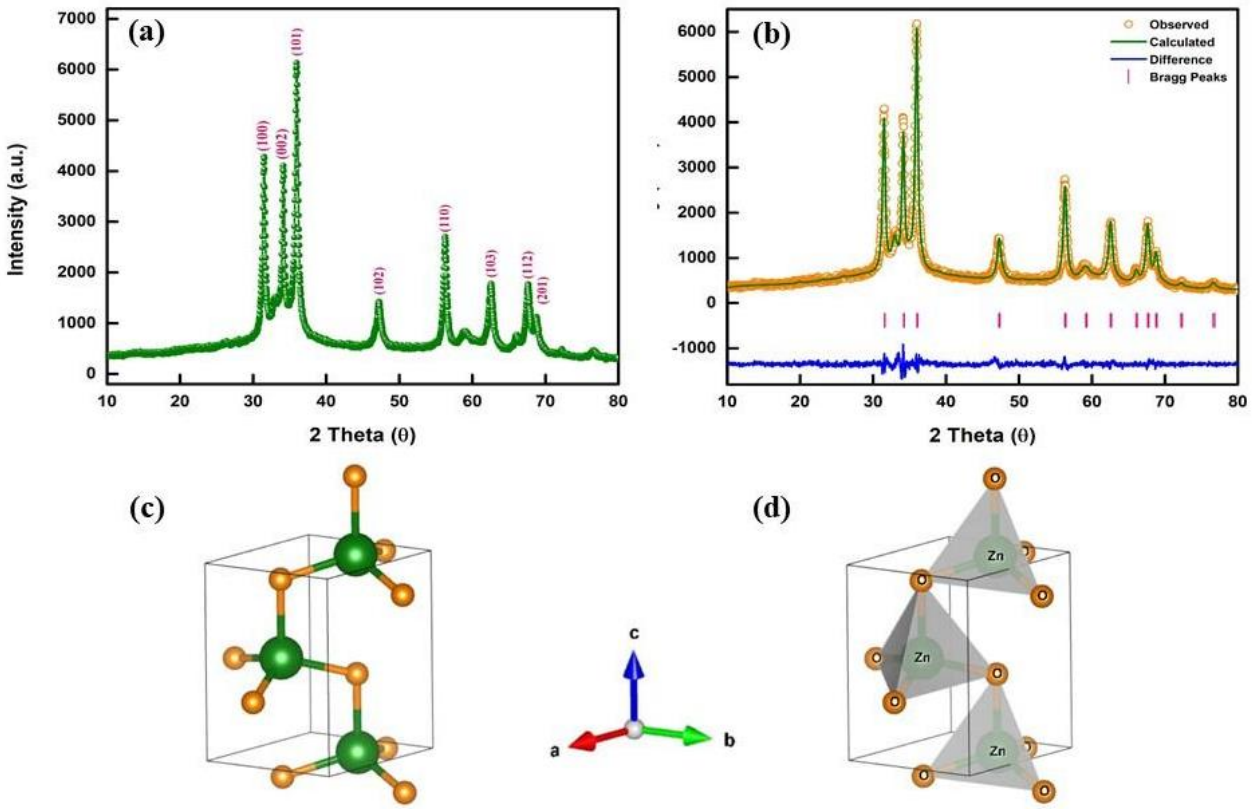

Fig. 4.15: (a) Crystallographic (XRD) pattern (b) Reitveild refinement (c,d) Wurzite hexagonal structure of the ZnO NPs synthesized using Lemon grass extract

4.2.1.7 Structural and chemical nature of ZnO NPs synthesized using Lemon grass

The XPS survey spectra of green synthesised ZnO nanoparticles are shown in (Fig. 4.16 (a)). The presence of C, O, and Zn elements predominantly confirms the composition as ZnO. The deconvolutions of high resolutions scan of Zn 2p peak revealed two prominent peaks centered around at 1021.28 eV and 1044.78 eV corresponding to Zn 2p3 and Zn 2p1, respectively (Fig. 4.16 (b)). Here, the binding energy difference between Zn 2p3 and Zn 2p1 peaks was recorded to be 23.5 eV, which is the characteristic value for ZnO nanoparticles. Furthermore, the sharp peak of Zn 2p3 is indicative of Zn^{2+} state form of Zn element. In addition, high resolution spectra of O 1s and corresponding deconvolution also resulted in emergence of two distinctive peaks (Fig. 4.16 (c)). The two peaks at 530.2 and 532.8 corresponds to two symmetrical signals namely O 1s1 and O 1s2, respectively. These signals are attributed to the presence of O element in O^{2-} state with Zn^{2+}, validating the successful synthesis of ZnO nanoparticles.

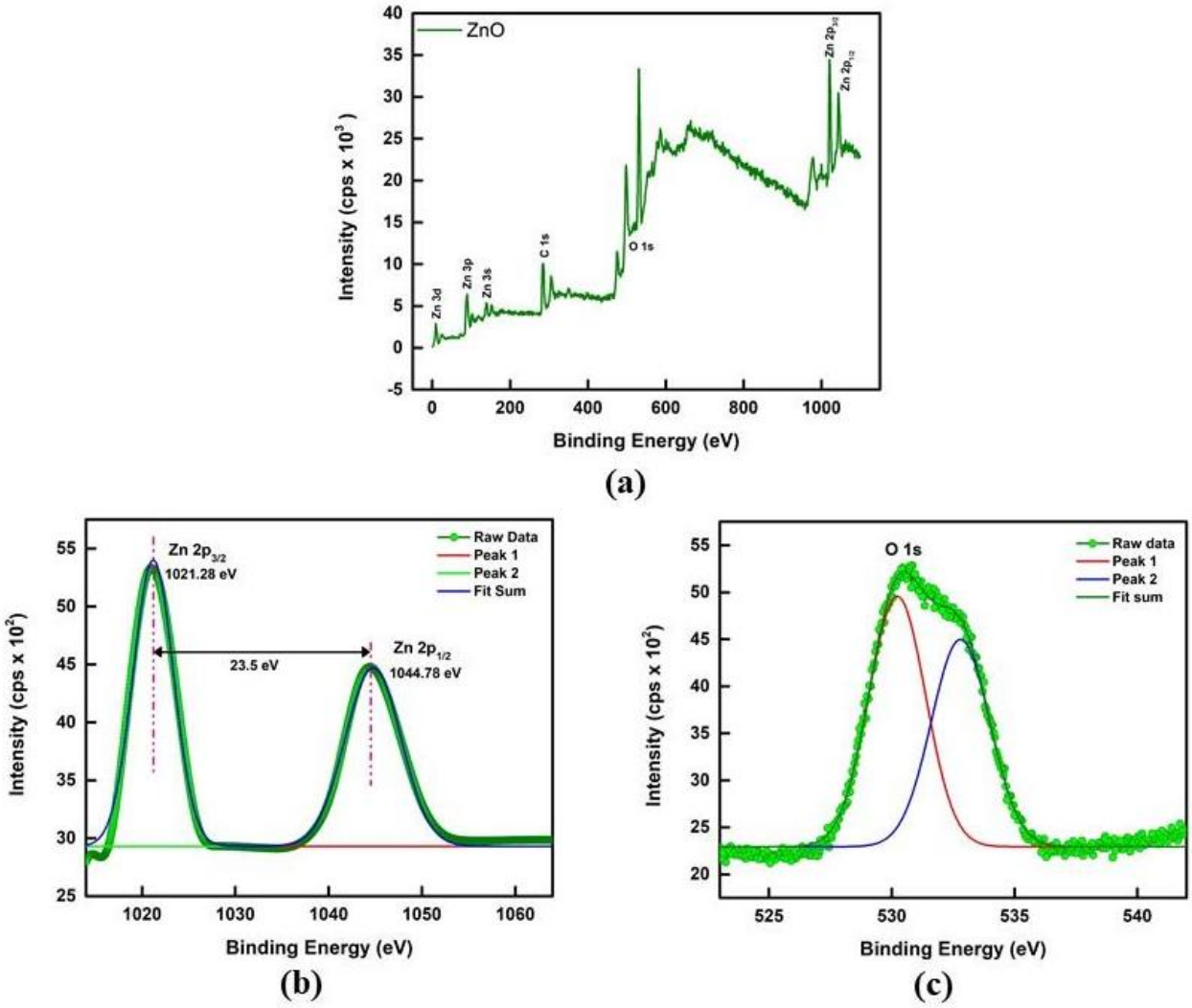

Fig. 4.16: (a) XPS survey scan; Deconvolution spectra of (b) Zn 2p (c) O1s of the ZnO NPs synthesized using Lemon grass extract

4.2.1.8 Microstructural features of ZnO NPs synthesized using Lemon grass

Fig. 4.17 represents the microscopic analysis of synthesized ZnO NPs. FE-SEM micrographs illustrate that nanoparticles are of various shapes and sizes, primarily polygonal and spherical (Fig. 4.17 (a)). Aggregation was also visible. The drop-off in size was noticeable, which can be due to the entrapment of extract over ZnO NPs. The entrapment of extract played a vital role in remodeling hexagonal shape to spherical nanoparticles in SEM images and EDX analysis was also done as shown in Fig. 4.17 (b). Three peaks were observed between 1.1, 8.5 and 9.5 keV, characteristic of elemental zinc which certifies the formation of high purity ZnO NPs (Fakhar-e-Alam *et al.*, 2014; Król *et al.*, 2019). Apart from zinc (64.27%), a finite percentage of oxygen (35.73%) was also detected (Demissie *et al.*, 2020). Elemental mapping

of the synthesized ZnO NPs is shown in Fig. 4.17 (c, d). It was observed that zinc and oxygen are homogenously distributed throughout the sample.

To elucidate the crystalline nature and morphology of ZnO nanoparticles, HRTEM analysis was performed on the dried powder. HRTEM micrograph revealed the hexagonal shape of biogenically synthesised ZnO nanoparticles (Fig 4.18). The definite edges of these hexagonal nanoparticles along with faded boundaries of extracts over the particles were clearly observed with average particle size 91.25± 2.9 nm. Small agglomeration of nanoparticles was also observed which is attributed to the high surface energy employed in synthesized ZnO nanoparticles by Lemon grass extract. Furthermore, the lattice spacing observed from magnified HRTEM micrograph aligned well with interplaner distance of (100) and (101) planes. The lattice spacing parameters of synthesised ZnO nanoparticles 2.81 Å (100) and 2.46 Å (101) were ascribed to the wurtzite type structure of the ZnO nanoparticles. The obtained crystallite size and lattice spacing corroborated well with parameters obtained using XRD analysis.

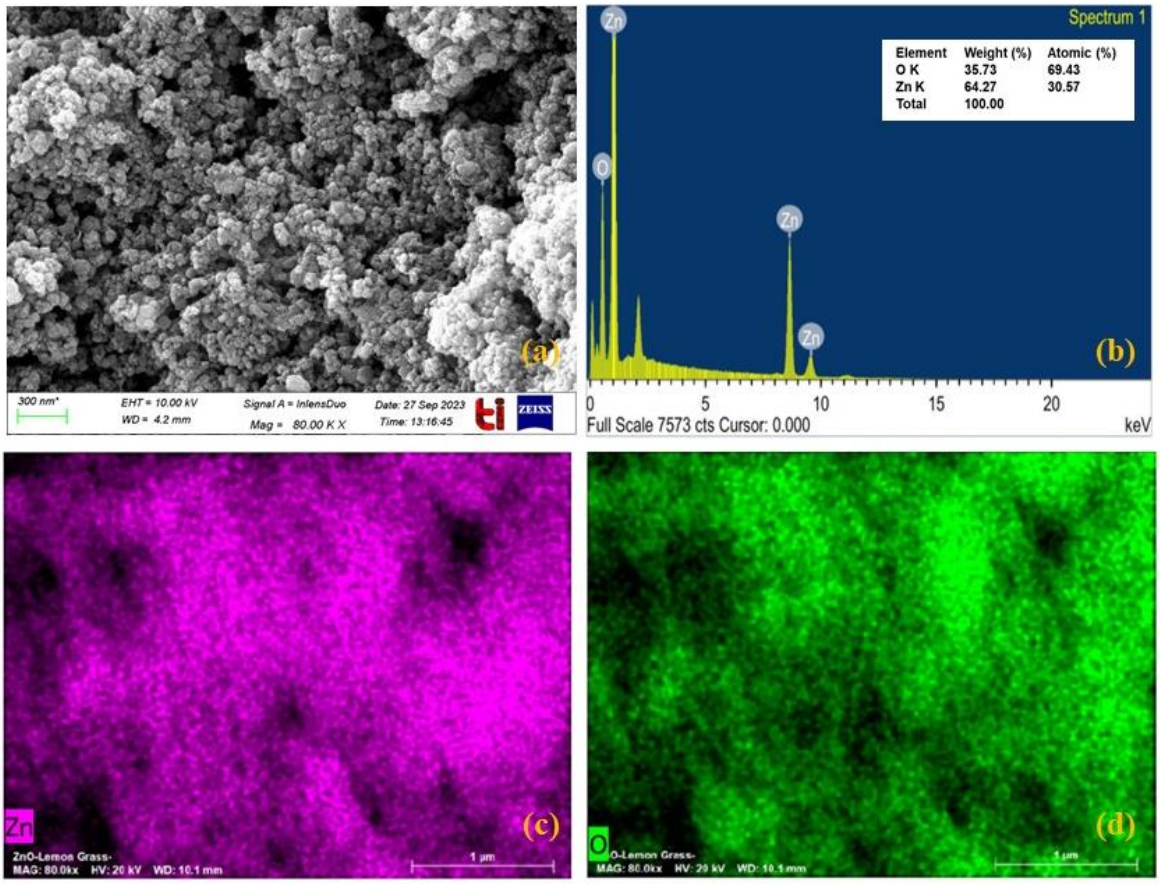

Fig. 4.17: Micrographs of ZnO NPs synthesized using Lemon grass extract (a) FE-SEM image (b) EDX Spectra (c) Elemental Mapping of Zinc (d) Elemental Mapping of Oxygen

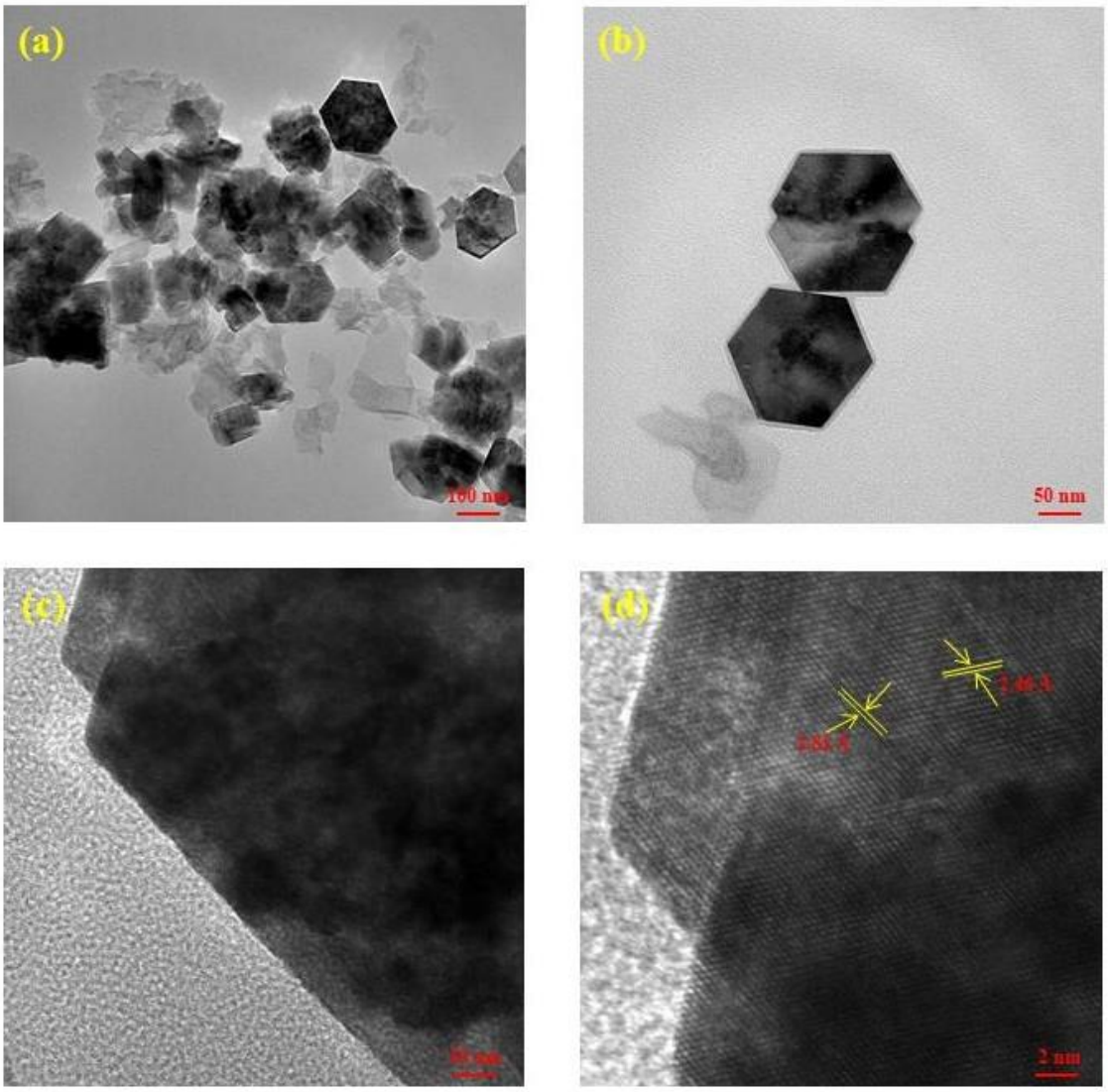

Fig 4.18: (a,b,c,d) HRTEM image of ZnO NPs synthesized using Lemon grass extract

4.2.2 Characterization of ZnO NPs synthesized using *A.variabilis* ARM 441

4.2.2.1 UV-Vis Spectroscopy of ZnO NPs synthesized using *A.variabilis* ARM 441

The absorbance band edge of synthesized ZnO NPs was approximately 356 nm as shown in Fig. 4.19, which coincides with the findings of Agarwal and Shanmugam (2019) (Agarwal and Shanmugam, 2019). The optical absorption seems to be enhanced in the 325–375 nm region. This indicates the blue shift in the absorption energies of ZnO NPs which are the manifestations of quantum size confinement in ZnO NPs. The broad band observed for ZnO NPs indicated the formation of varied sizes and shapes of the nanoparticles (Fig. 4.19). However, the dynamic absorption peak within 200-250 nm suggests the presence of secondary metabolites such as

fatty acids, polyphenols which might have been responsible for reduction of $Zn(CH_3COO)_2$ to ZnO NPs. The band gap energy of phycosynthesized ZnO NPs was calculated by Wood's Tauc relation (Eq. 7),

$$[h\upsilon\alpha = c(h\upsilon - E_g)^n] \ldots\ldots\ldots\ldots\ldots\ldots (7)$$

where, α is absorption coefficient, c is constant, hυ is the photon energy, and E_g is band gap. The parameter 'n' varies with the type of electronic transitions i.e. n=2, 1/2, 2/3 or 3 for the direct-allowed, indirect-allowed, direct-forbidden, and indirect-forbidden transitions, respectively. As ZnO is a direct bandgap material, value of n=2. Fig. 4.19 shows the replotted data between hυ v/s $(\alpha h\upsilon)^2$ using Origin 9.0 and the band gap was obtained by the extrapolation of a linear regression on the X-axis. It is 3.21 eV which is similar to the previous reports (Brazuna *et al.*, 2019). The enhanced radiative absorptions in 325–375 nm region and the broadening of the corresponding adsorption region (3.21 eV) could be due to the discrete inter-band absorptions between the energy state of conduction band and valence band.

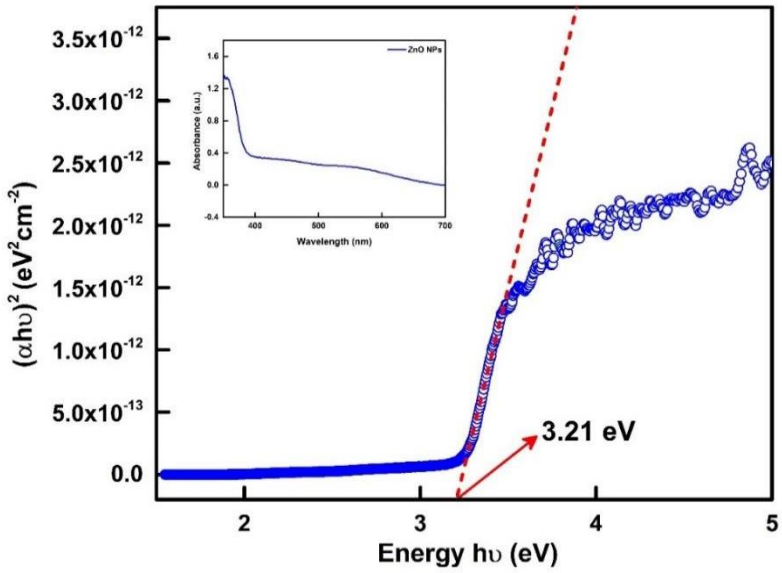

Fig. 4.19: Plot of $(\alpha h\upsilon)^2$ vs hυ inset UV–vis spectra of the ZnO NPs synthesized using *A.variabilis* ARM 441 extract

4.2.2.2 Particle size, polydispersity index (PDI), and Zeta potential of ZnO NPs synthesized using *A.variabilis* ARM 441

Particle size, polydispersity index (PDI), and Zeta potential of the ZnO NPs were done using a Malvern Zeta sizer. Before analysis, the sample (5mg) was diluted (1:1, w/v) using 5 ml of milli-Q water and sonicated for 15 min. The peak of the graph (Fig. 4.20) depicted 138.23 nm hydrodynamic size. Further, the PDI value was observed to be 0.753, which anticipated the

presence of polydispersed ZnO NPs. The hydrodynamic size of as-synthesized ZnO NPs was relatively higher in contrast to the solid-state. The phytochemicals and ions or molecules involved in the synthesis of ZnO NPs add extra hydrate layers, thus, higher hydrodynamic size in aqueous environment (Telgmann *et al.*, 2016; Rolim *et al.*, 2019). Also, as an additional aid to a certain degree was agglomeration, as reported (Santos *et al.*, 2016; Ahluwalia *et al.*, 2018). The Zeta potential of phycosynthesized ZnO NPs can be affected by the bio-moieties present in *A.variabilis* ARM 441 extract (Ezealisiji *et al.*, 2019). On the contrary, nanoparticles' stability and biological activity can be derived from the surface charge. In this study, phycosynthesized ZnO NPs had a negative charge of -9.32 mV. The negative charge on ZnO NPs' surface was attributed to the presence of negative charge on long-chain fatty acids and aldehydes. This result indicated the presence of n-hexadecanoic acid and 13-tetradecenal on the surface of ZnO NPs. Several other reports are demonstrating comparable negative zeta potential for biogenic metallic nanoparticles (Sudha, Jeyakanthan and Srinivasan, 2017). Additionally, the magnitude of the zeta potential in the present study suggests that the suspension of ZnO NPs have limited stability (Jain et al., 2020).

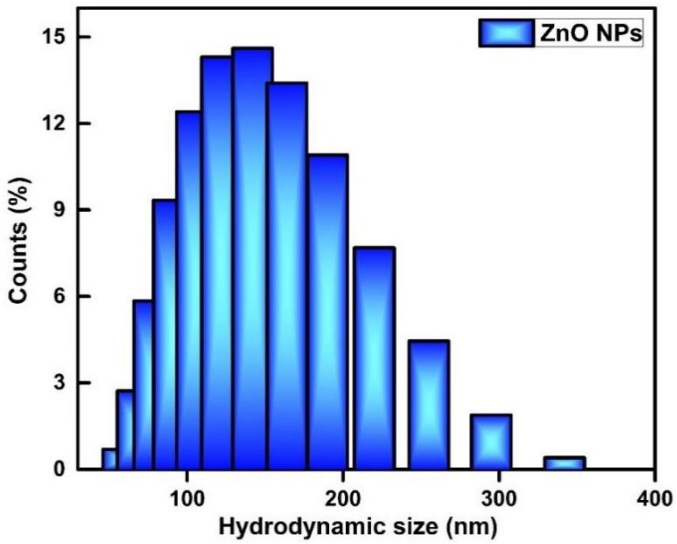

Fig. 4.20: Particle size distribution (DLS histogram) of the ZnO NPs synthesized using *A.variabilis* ARM 441 extract

4.2.2.3 Fourier transform spectroscopy (FT-IR) analysis of ZnO NPs synthesized using *A.variabilis* ARM 441

FT-IR study was performed to recognize the active biomolecules present in the *A. variabilis* extract involved in ZnO synthesis (Fig. 4.21). A broad peak at 3395 cm^{-1} is an indication of O-H hydrogen bonds of alkaloids and steroids, which is in good correlation with the ZnO peak at

3397.42 cm^{-1}. Absorption peaks at 2961.5 cm^{-1} and 2954.7 cm^{-1} correspond to the alkyl (methyl) group's C-H vibration in ZnO NPs *A. variabilis* extract, respectively. Prominent peaks of proteins were observed in *A. variabilis* extract for C=O stretching (amide I) and C–N stretching and N–H deformation (amide II) at 1561.2 cm^{-1}. The weak stretching of peaks at 1413.7 cm^{-1}, 1047.8 cm^{-1}, and 1413.7 cm^{-1}, 1052.6 cm^{-1} revealed the presence of C=O and C-O-C stretching in ZnO NPs and *A. variabilis* ARM 441 extract, respectively (Ebadi *et al.*, 2019). The spectrum of ZnO NPs showed a significant peak at 1649.9 cm^{-1}, which was characteristic stretching of fatty acid and carboxylic O-H bending vibration of fatty acid (Carballo *et al.*, 2008; Sankar *et al.*, 2014; Sharma *et al.*, 2019). A distinct high intensity band was observed at 451.2 cm^{-1}, resulting from the presence of the oxygen and zinc bands while this peak was not observed in cyanobacterial extract. It is reported that secondary metabolites present in *A. variabilis* ARM 441 could be responsible for the reduction of zinc acetate dihydrate into ZnO NPs. Thus, it can be inferred that the nanoparticle is synthesized and stabilized by replacing acidic protons with methyl and hydroxyl groups (Rolim *et al.*, 2019). Moreover, the less intense peaks that appeared at 861.7 cm^{-1} and 657.2 cm^{-1} were attributed to C-Cl and C≡C group of alkyl halides, and alkynes found in cyanobacterial extract, confirmed the incorporation of synthesis ZnO NPs. The primary molecules responsible for the stabilization are fatty acids, which have been validated with the findings of GC-MS and NMR.

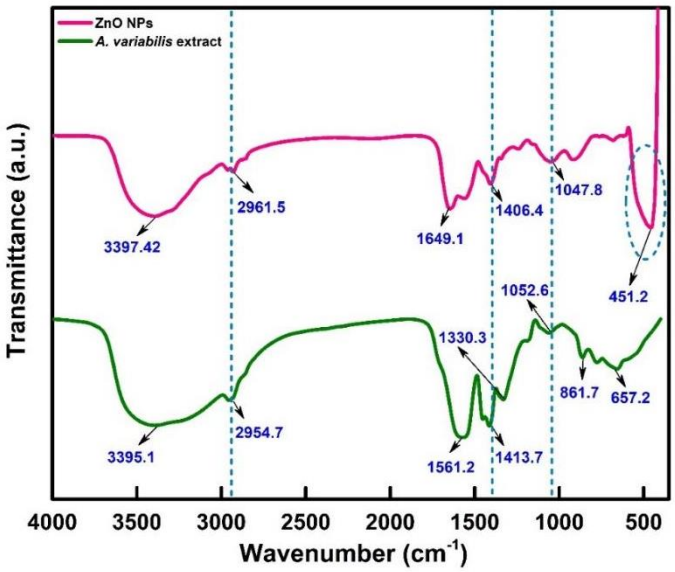

Fig. 4.21: FT-IR spectra of *A.variabilis* ARM 441 extract and ZnO NPs

4.2.2.4 Thermal behaviour of ZnO NPs synthesized using *A.variabilis* ARM 441

The synthesis of ZnO NPs was manipulated *via* moderate thermal treatment and stability of the product with temperature variations is an important aspect of the analysis. Thermogravimetric analysis (TGA) was employed to as-synthesized ZnO NPs at the temperature range of 25 to 800 °C (Fig. 4.22). The ZnO NPs showed a minimal (1%) decrease in weight at 100°C due to residual moisture ascribed to the dehydration phenomenon. A substantial continuous weight loss of about (~12%) was observed at above 200°C due to the organic moieties of the cyanobacterial extract. After 442°C, the extract is completely decomposed as a capping agent on ZnO NPs (Rambabu *et al.*, 2019). However, ZnO itself is stable at much higher temperatures than the studied range (Khatami *et al.*, 2018). The weight loss was mainly attributed to the decomposition of bioactive compounds. Predominant reduction of Zn $(CH_3COO)_2$ to Zn^{2+} by biomoieties occurred in the initial phase of the synthesis with low formation levels of *A.variabilis*/Zn^{2+} complex which is further reduced to ZnO NPs (Rambabu *et al.*, 2021). Thus, secondary metabolites and other bioactive components in the extract of *A. variabilis* ARM 441 were present in significant amount over synthesized ZnO NPs which was confirmed through this analysis as well (Vimala *et al.*, 2014).

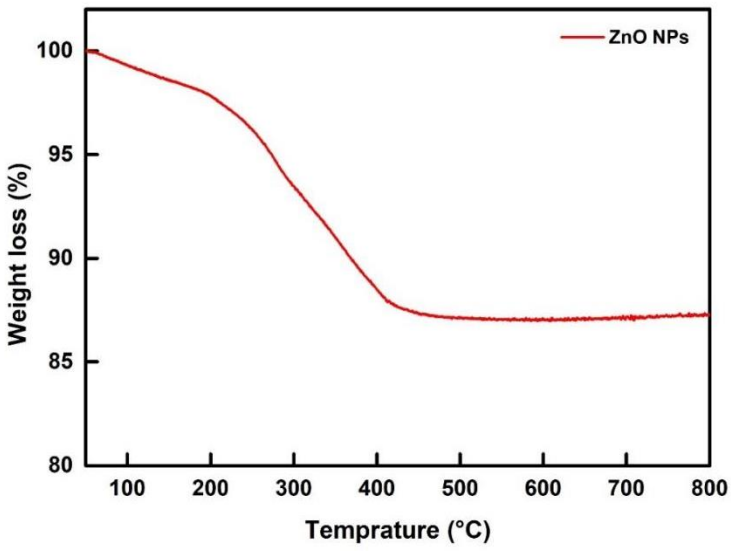

Fig. 4.22: TG thermogram ZnO NPs synthesized using *A.variabilis* ARM 441 extract

4.2.2.5 Nitrogen adsorption-desorption isotherms analysis (BET analysis) of ZnO NPs synthesized using *A.variabilis* ARM 441

Nitrogen adsorption and desorption experiments were performed to investigate the surface characteristics such as surface area and porous nature of synthesized ZnO NPs mediated *via A.*

variabilis ARM 441. The results revealed a typical type IV isotherm attended by a type H3 hysteresis loop which authenticates mesoporous dominance (Fig. 4.23(a)) (Anupama, Keune and Sahoo, 2017). The pore size distribution is shown in Fig. 4.23 (b), with an average pore diameter 11.551 nm, surface area was 38.718 m^2/g with pore volume 0.1633 cc/g. The average diameter was found to be smaller, with a greater surface area expectation. As the diameter decreases, surface area increases; hence the as-synthesized nanoparticles can be utilized as a catalyst involving adsorption and desorption of reactants (Anupama, Keune and Sahoo, 2017). A decrease in pore diameter of ZnO NPs can be another reason for its enlarged active sites (Bayrami, Alioghli, *et al.*, 2019; Bayrami, Ghorbani, *et al.*, 2019).

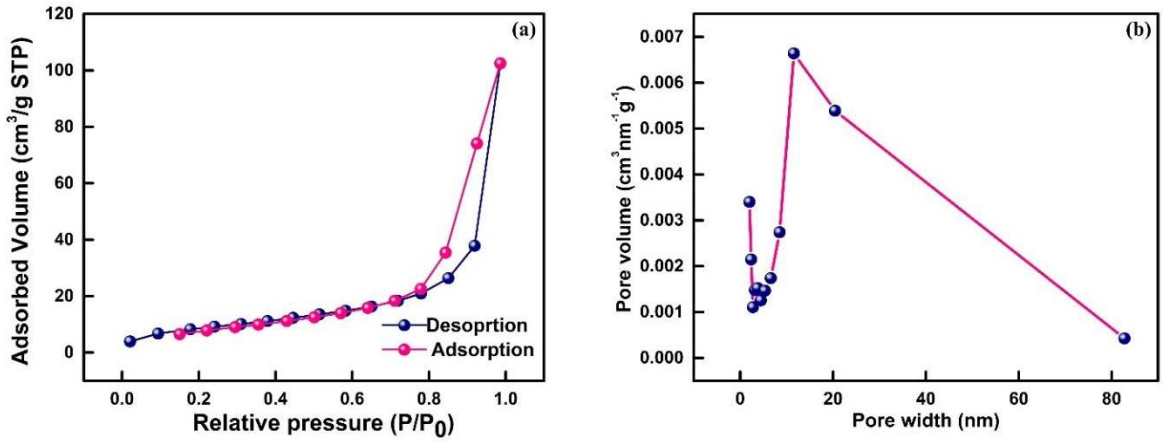

Fig. 4.23: (a) Nitrogen adsorption-desorption isotherm (b) Pore size distribution curve

4.2.2.6 Crystallinity Study of ZnO NPs synthesized using *A.variabilis* ARM 441

XRD is the primary tool for characterizing synthesized ZnO NPs. It was performed to analyse the structural properties of pulverized ZnO NPs. The diffraction patterns obtained *via* phycosynthesis were indexed as hexagonal wurtzite structure according to ICDS data (JCPDS 01-079-2205) as shown in Fig. 4.24 (a). The fabricated nanoparticles were pure and crystalline in nature as no evidence of peak related to any foreign moiety or bulk remnant was observed. Subsequently, narrow and sharp diffraction peaks at 2θ and indexed with planes at 31.79° (100), 34.45° (002), 36.28° (101), 47.56° (102), 56.62° (110), 62.89° (103), 67.97° (112), 69.09° (201) provide the evidence for the synthesis of single-phase wurtzite crystal structure (Saloga and Thünemann, 2019). Further, the XRD pattern was refined and analyzed employing Rietveld whole profile fitting method based on refinement technique with the help of the Jana (2006) in Fig. 4.24 (b,c and d) and Table 4.6.

Table 4.6: Refined parameters and phase data of ZnO NPs synthesized using *A.variabilis* ARM 441

Cell parameters	a=b= 3.2488 Å; c=5.2054 Å
	α=β= 90; γ=120
Space group	$P6_3mc$ 186
R-factor	R_{wp} = 5.60 %, R_{exp} = 6.83% GOF=1.61
Damping factor	0.1000
Volume	47.58 $Å^3$

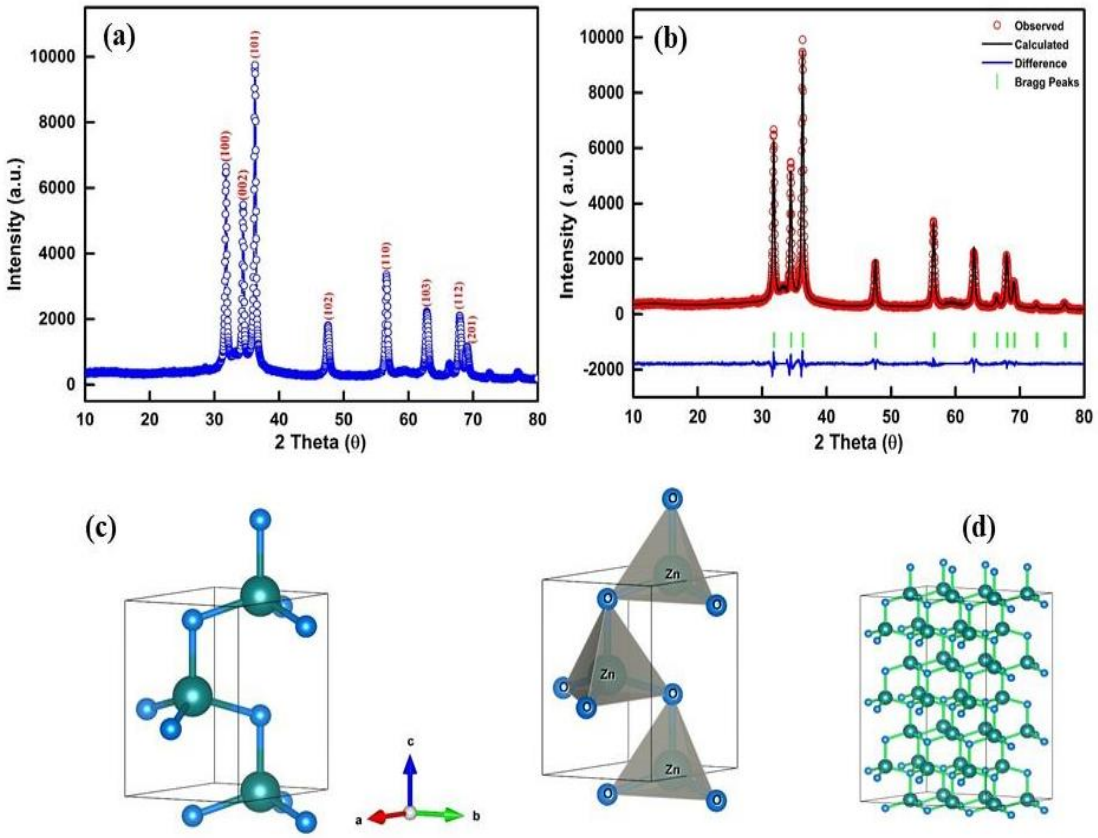

Fig. 4.24: (a) Crystallographic (XRD) pattern (b) Reitveild refinement (c,d) Wurzite hexagonal structure of ZnO NPs synthesized using *A.variabilis* ARM 441 extract

4.2.2.7 Structural and chemical nature of ZnO NPs synthesized using *A.variabilis* ARM 441

To validate the wurtzite structure and chemical purity of *A.variabilis* ARM 441 mediated ZnO NPs, XPS analysis was performed. Fig. 4.25 (a) shows the survey spectrum indicating the presence of Zn, O along with adventitious carbon (Morozov *et al.*, 2015). The sample was chemically pure and devoid of any contaminants. High-resolution XPS spectra of the elements Zn and O are shown in Fig. 4.25 (b) and (c) respectively. The Zn 2p spectrum was deconvoluted

(Fig. 4.25 (b)) and displayed a strong spin-orbit coupling doublet at 1022.39 eV and 1045.57 eV corresponding to core levels Zn $2p_{3/2}$ and Zn $2p_{1/2}$ respectively with binding energy 23.18 eV. Sharp peaks of Zn $2p_{3/2}$ were observed; thus it confirmed that the Zn element exists in the form of Zn^{2+} (Liqiang *et al.*, 2006). In the case of O1s, an asymmetric peak was observed in Fig. 4.25 (c). XPS line was fitted by Gauss profile functions including linear background (Säuberlich *et al.*, 2003). O1s emission was composed of two contributions, with significant peaks centered at 531.77 and 533.17 eV. As per the literature, these peaks can be ascribed to Zn-OH bonding and to the presence of C=O bonding originating from surface defects and chemisorbed oxygen, respectively (Diallo *et al.*, 2015; Steffy *et al.*, 2018). Also, Zn 2p and O1s regions are consistent with stoichiometric ZnO. To pre-conclude, it can be deduced that Zn atoms in ZnO NPs crystal are in oxidation state 2p. The results show that the ratio O/Zn is slightly lower than unity, confirming that the synthesized powders are pure ZnO as confirmed by XRD results. In view of the XPS and EDX results, no impurities were found in their detection limits.

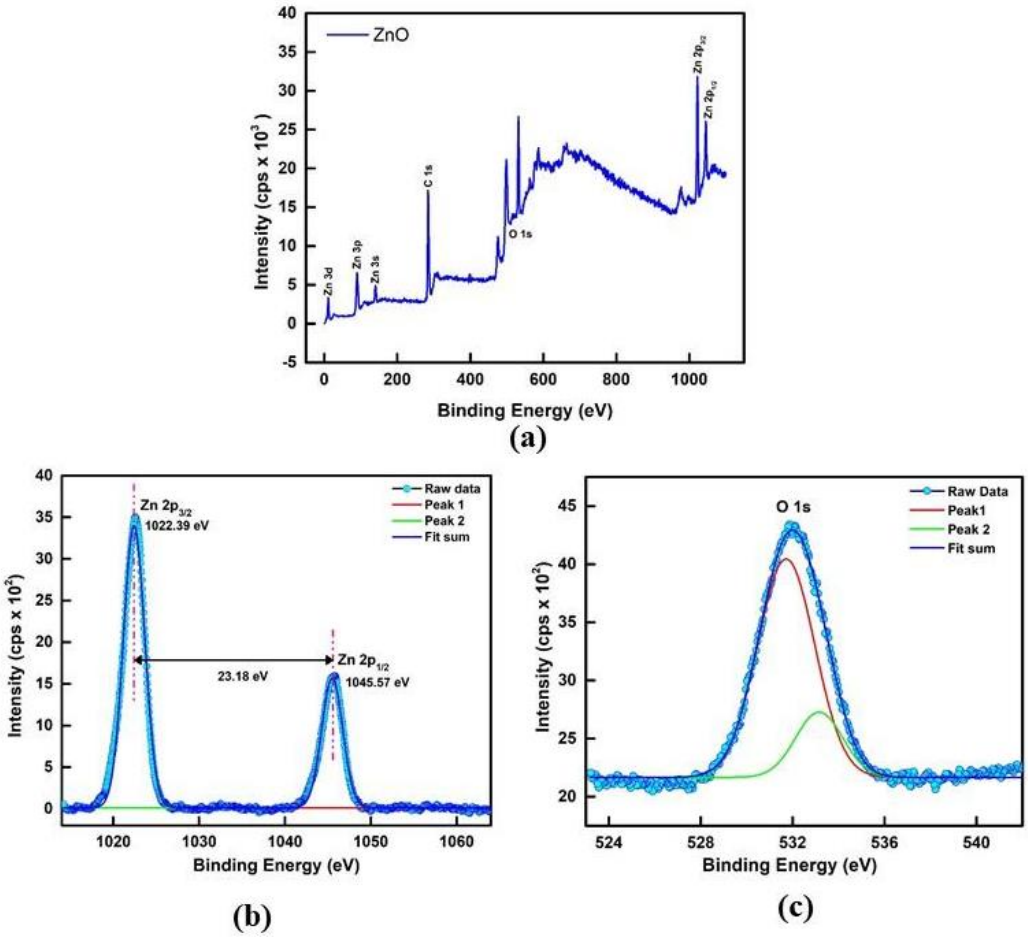

Fig. 4.25: (a) XPS survey scan; Deconvolution spectra of (b) Zn 2p (c) O1s

4.2.2.8 Microstructural features of ZnO NPs synthesized using *A.variabilis* ARM 441

Fig. 4.26 represents the microscopic analysis of synthesized ZnO NPs. FE-SEM micrographs illustrate that nanoparticles are of various shapes and sizes, primarily polygonal and spherical (Fig. 4.26 (a,b)). Aggregation was also visible. The drop-off in size was noticeable, which can be due to the entrapment of extract over ZnO NPs. The entrapment of extract played a vital role in remodeling hexagonal shape to spherical nanoparticles in SEM images and EDX analysis was also done as shown in Fig. 4.26 (c). Three peaks were observed between 1.1, 8.5 and 9.5 keV, characteristic of elemental zinc which certifies the formation of high purity ZnO NPs (Fakhar-e-Alam *et al.*, 2014; Król *et al.*, 2019). Apart from zinc (42.89%), a finite percentage of oxygen (57.11%) was also detected (Demissie *et al.*, 2020). These results undoubtedly imply that even after several washings some residual portion of the extract was carried over the surface of ZnO NPs which establishes the strong bonding of bioactive molecules with ZnO NPs (Król *et al.*, 2019). Reports have suggested that the use of different zinc salt precursors influence the morphological, textural and optical properties of ZnO NPs. As reported by Mayekar et al 2014, (Mayekar, Dhar and Radha, 2014) the ZnO NPs fabricated from zinc acetate possessed highest purity whereas ZnO NPs fabricated from other zinc salts show similar crystallite size with different shapes. Additionally, it was predicted that acetate ions provide shielding effect during the synthesis preventing nanoparticle fusion during growth (Pourrahimi *et al.*, 2014).

Further, HR-TEM images clearly illustrated the presence of faded but clear boundaries of extracts over the particles (Fig. 4.27 (a)) (Bayrami, Alioghli, *et al.*, 2019). Hence, capping action of phytochemicals of cyanobacterial extract can be associated with reducing the size by preventing them from growing further and changing the shape during the crystallization process. The average particle size calculated from HR-TEM was 33.31nm (Fig. 4.27 (a)). The interplanar adjacent planes were 0.256 nm, which corresponds to the inter-planar separation of 002 face-centered cubic ZnO NPs (Fig. 4.27 (a)). SAED pattern of ZnO NPs was also studied. In Fig. 4.27 (b), the presence of bright rings suggested the crystalline nature of fabricated ZnO NPs. The hexagonal wurtzite phase of ZnO NPs was evident from the concentric rings assigned to (100), (002), (101), (102), (110), (103), (112), (201)(Gao *et al.*, 2019). These findings agree well with the estimated calculations of XRD.

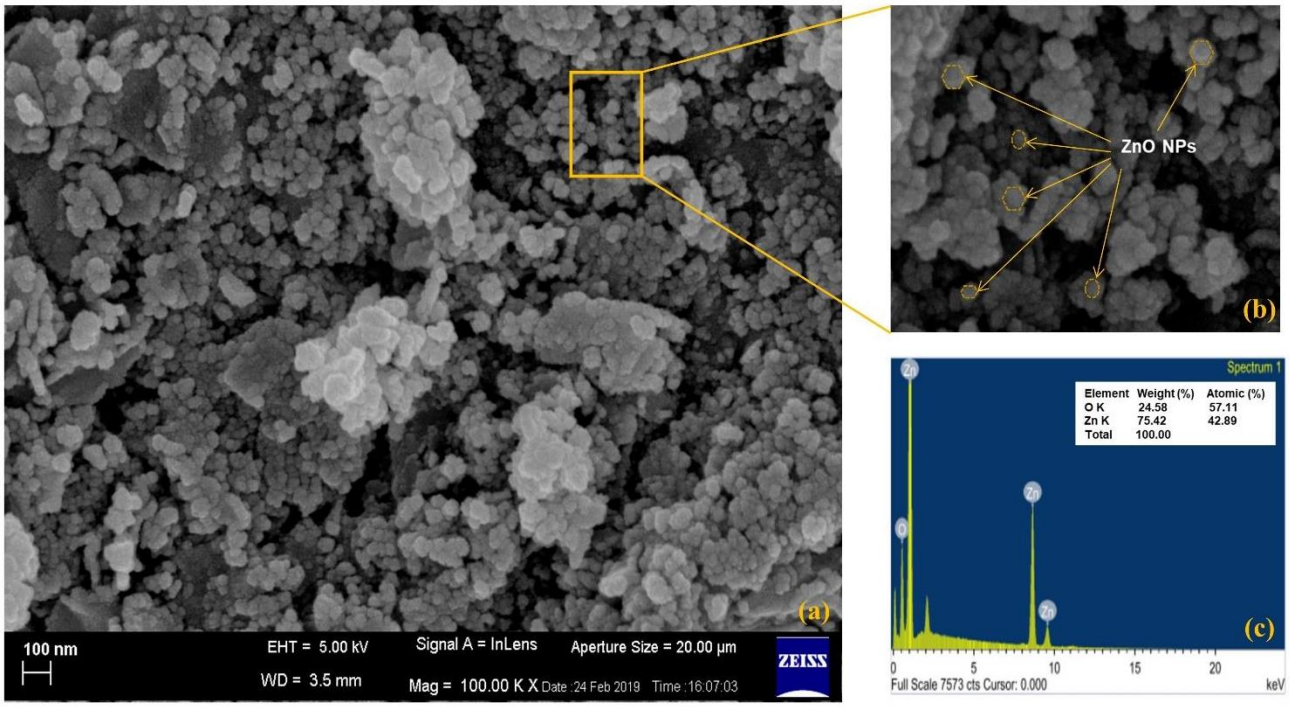

Fig. 4.26: Micrographs of ZnO NPs synthesized using *A.variabilis* ARM 441 extract (a, b) FE-SEM image (c) EDX Spectra (Unlabelled peak is of gold)

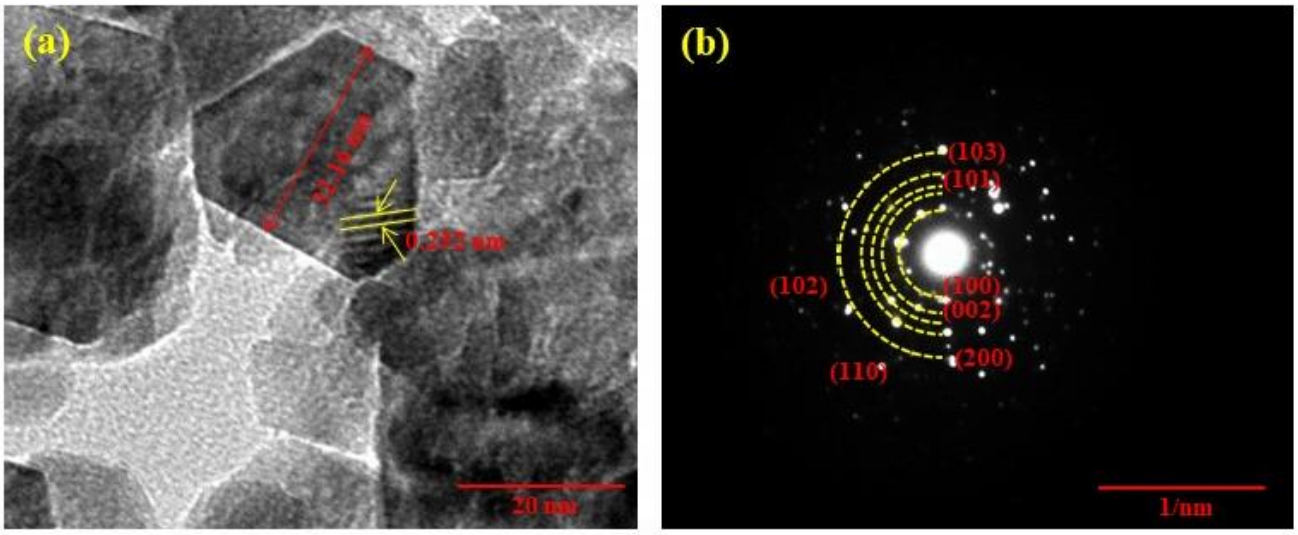

Fig. 4.27: (a) HRTEM image; (b) SAED pattern of ZnO NPs synthesized using *A.variabilis* ARM 441 extract

4.3 Process optimization for gram scale synthesis of ZnO nanoparticles

4.3.1 Gram scale synthesis of Lemon grass mediated ZnO NPs using Response surface methodology (RSM)

The impact of three crucial parameters, *i.e.* zinc concentration (mM), reaction time (h) and extract concentration (%) was investigated using RSM. The response recorded at the experimental conditions were placed and the model generated the predicted values as shown in Table 4.7. The model generated an equation in terms of the actual factors with significant terms, having impact on the nanoparticles synthesis process (yield (mg)) as follows (Eq.8):

$$Yield\ (\%) = -5177.549 + 5.828A + 1113.477B + 40.676C - 0.0027A^2 - 70.512B^2 - 0.498C^2 - 0.235AB - 0.0054AC + 1.792BC \ldots\ldots\ldots\ldots\ldots\ldots (8)$$

where, A is the zinc concentration (mM); B is reaction time (h); and C is extract concentration (%).

The competence of the experimental data was interpreted by the analysis of variance (ANOVA) as shown in Table 4.8. The ANOVA of second order quadratic polynomial model for nanoparticles yield (mg) revealed F-value (34.79) with p-value less than 0.0001 at 95% confidence level indicating a high significance of the generated model. Furthermore, the lack of fit F-value of 4.21 corroborates well with the obtained R^2 value (0.9781). The obtained results indicated a great correlation between predicted and experimental values of operational parameters. It was envisaged that the response change possibly occurred due to a change in independent parameters not due to error or noise**.** Precision parameter was also recorded as 18.281 revealing the usefulness of the employed model.

Table 4.7: RSM based BBD design for the independent variables and their corresponding response for nanoparticle synthesis using Lemon grass extract

Run	Zinc (mM)	Reaction time (h)	Extract (%)	Yield (mg)	
				Actual	Predicted
1	100	10	45	725.32	828.30
2	1000	10	45	965.23	971.53
3	1000	6	45	1754.56	1651.58
4	1000	8	80	1025.23	1148.24
5	100	8	10	201.56	78.55
6	550	8	45	1857.2	1873.84
7	550	10	80	1359.23	1229.93
8	550	8	45	2015.3	1873.84
9	1000	8	10	844.23	817.91
10	550	8	45	1845.23	1873.84
11	100	6	45	665.23	658.94
12	100	8	80	725.4	751.72
13	550	10	10	457.21	477.24
14	550	6	80	1254.36	1234.33
15	550	8	45	1795.23	1873.84
16	550	8	45	1856.24	1873.84
17	550	6	10	854.23	983.53

Table 4.8: ANOVA results of response surface quadratic model for nanoparticle yield (mg) using Lemon grass extract

Source	Sum of square	DF	Mean square	F-value	Prob>F
Model	5.134E+006	9	5.704E+005	34.79	< 0.0001
Residual	1.148E+005	7	16395.66		
Lack of Fit	87173.95	3	29057.98	4.21	0.0993
Pure Error	27595.65	4	6898.91		
Total	5.248e+006	16			
	R^2=0.9781				

The coefficients of regression were also analyzed using ANOVA as shown in Table 4.9. It can be clearly observed that zinc concentration (A) has the greatest impact on the nanoparticles yield with highest F-value (39.35). The extract concentration (C) was second most influential

parameter (F-value=30.71), while reaction time (B) had least impact on the nanoparticles yield (mg) with F-value of 7.95. The overall availability of the zinc ions present in the solution and the reducing capability of the concentration dependent extract (%) determined the nanoparticles yield. The reaction time had lesser impact due to the fast pace reaction between zinc ions and bioactive molecules in the extract (Surendra *et al.*, 2016). All the quadratic terms (A^2, B^2, and C^2) also had significant impact on the nanoparticles yield (mg). The interaction between zinc concentration and reaction time (AB) was observed to impact the nanoparticles yield (mg), whereas other interactions (AC, and BC) had no significant impact. Subsequently the model adequacy was confirmed by the conducting experiments at the optimum conditions generated by the model (Shabaani *et al.*, 2020).

Table 4.9: ANOVA results for the coefficients of response surface quadratic model for nanoparticles yield (mg) using Lemon grass extract

Factor	Coefficient	DF	Standard error	F-value	95% CI low	95% CI high	p-value
Intercept	1873.84	1	57.26	-	1738.43	2009.25	-
A	283.97	1	45.27	39.35	176.92	391.02	0.0004
B	-127.67	1	45.27	7.95	-234.72	-20.62	0.0258
C	250.87	1	45.27	30.71	143.82	357.92	0.0009
A^2	-564.20	1	62.40	81.75	-711.76	-416.65	<0.0001
B^2	-282.05	1	62.40	20.43	-429.61	-134.49	0.0027
C^2	-610.53	1	62.40	95.72	-758.09	-462.98	<0.0001
AB	-212.35	1	64.02	11.00	-363.74	-60.96	0.0128
AC	-85.71	1	64.02	1.79	-237.10	65.68	0.2225
BC	125.47	1	64.02	3.84	-25.92	276.86	0.0908

The combinational impacts are graphically represented as two dimensional contour plots and three-dimensional response surface plots (Fig. 4.28). One variable was kept constant and the impact of two variables on the nanoparticles yield (mg) was plotted.

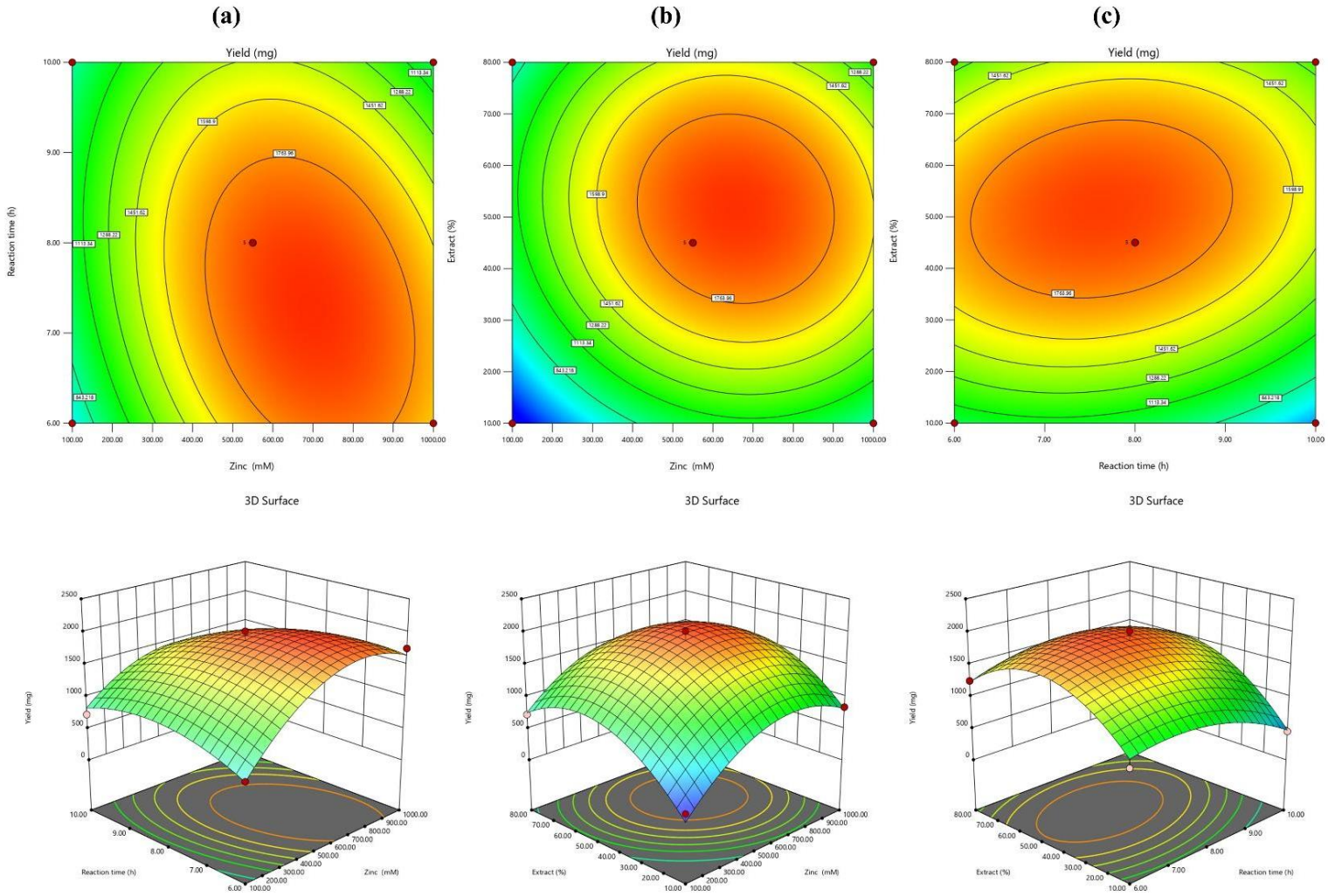

Fig. 4.28: 2D contour and 3D response surface plots for analyzing the interaction effects between (a) Zinc concentration and reaction time, (b) Zinc concentration and Lemon grass extract concentration and (c) Reaction time and Lemon grass extract concentration

4.3.2 Gram scale synthesis of *A.variabilis* ARM 441 mediated ZnO NPs using Response Surface Methodology (RSM)

The impact of three crucial parameters, *i.e.* zinc concentration (mM), reaction time (h) and extract concentration (%) was investigated using RSM. The response recorded at the experimental conditions were placed and the model generated the corresponding values as shown in Table 4.10. The model generated an equation in terms of the actual factors with significant terms, having impact on the nanoparticles synthesis process (yield (mg)) as follows (Eq. 9):

$$Yield\ (\%) = -3769.922 + 14.522A + 738.513B + 57.754C - 0.02233A^2 - 59.909\ B^2 - 0.6149C^2 - 0.8334\ AB - 0.0525\ AC + 0.6775\ BC \ldots\ldots\ldots\ldots\ldots \quad (9)$$

where, A is the zinc concentration (mM); B is reaction time (h); and C is extract concentration (%).

Table 4.10: RSM based BBD design for the independent variables and their corresponding response for nanoparticle synthesis using *A.variabilis* ARM 441 extract

Run	Zinc (mM)	Reaction time (h)	Extract (%)	Yield (mg)	
				Actual	Predicted
1	250	8	10	785.21	810.97
2	250	6	30	1498.26	1521.44
3	400	6	50	1021.23	1043.26
4	250	6	30	1565.26	1521.44
5	250	6	30	1509.24	1521.44
6	100	6	10	209.56	187.53
7	100	4	30	487.25	524.13
8	400	4	30	954.26	957.98
9	100	6	50	985.56	974.43
10	250	6	30	1512.23	1521.44
11	400	6	10	875.26	886.39
12	400	8	30	1021.23	984.35
13	250	8	50	1322.21	1337.06
14	250	6	30	1522.23	1521.44
15	100	8	30	654.23	650.51
16	250	4	50	1232.25	1206.49
17	250	4	10	803.65	788.80

The competence of experimental data was interpreted by the analysis of variance (ANOVA) as shown in Table 4.11. The ANOVA of second order quadratic polynomial model for nanoparticles yield (mg) revealed F-value (237.03) with p-value less than 0.0001 at 95% confidence level indicating a high significance of the generated model. Furthermore, the lack of fit F-value of 2.84 corroborates well with the obtained R^2 value (0.9967). The obtained results indicated a great correlation between predicted and experimental values of operational parameters. It was envisaged that the response changes possibly occurred due to a change in independent parameters not due to error or noise. Precision parameter was also recorded as 50.127 revealing the usefulness of the employed model.

Table 4.11: ANOVA results of response surface quadratic model for nanoparticle yield (mg) using *A.variabilis* ARM 441 extract

Source	Sum of square	DF	Mean square	F-value	Prob>F
Model	2.568E+06	9	2.853E+05	237.03	< 0.0001
Residual	8426.85	7	1203.84		
Lack of Fit	5735.06	3	1911.69	2.84	0.1695
Pure Error	2691.79	4	672.95		
Total	2.577E+06	16			
	R^2= 0.9967				

The coefficients of regression were also analyzed using ANOVA as shown in Table 4.12. It can be clearly observed that extract concentration (C) has the greatest impact on the nanoparticles yield with highest F-value (369.96). The zinc ion concentration (A) was second most influential parameter (F-value= 244.78), while reaction time (B) had least impact on the nanoparticles yield (mg) with F-value of 9.69. The reducing capability of the extract (%) impacts the overall availability of the zinc ions present in the solution and hence, determines the nanoparticles yield (Surendra *et al.*, 2016). The reaction time had lesser impact due to the fast pace reaction between zinc ions and bioactive molecules in the extract. All the quadratic terms (A^2, B^2, and C^2) also had significant impact on the nanoparticles yield (mg). The interaction between zinc concentration and reaction time (AB) was observed to impact the nanoparticles yield (mg), whereas other interactions (AC, and BC) had no significant impact. Subsequently the model adequacy was confirmed by the conducting experiments at the optimum conditions generated by the model (Shabaani *et al.*, 2020).

Table 4.12: ANOVA results for the coefficients of response surface quadratic model for nanoparticles yield (mg) using *A.variabilis* ARM 441 extract

Factor	Coefficient	DF	Standard error	F-value	95% CI low	95% CI high	p-value
Intercept	1521.44	1	15.52	-	1484.75	1558.14	-
A	191.92	1	12.27	244.78	162.92	220.93	< 0.0001
B	38.18	1	12.27	9.69	9.18	67.19	0.0170
C	235.95	1	12.27	369.96	206.94	264.95	< 0.0001
A^2	-25.00	1	17.35	2.08	-66.02	16.02	0.1927
B^2	-157.51	1	17.35	82.43	-198.53	-116.49	< 0.0001
C^2	27.10	1	17.35	2.44	-13.92	68.12	0.1622
AB	-502.56	1	16.91	883.39	-542.55	-462.58	< 0.0001
AC	-239.64	1	16.91	200.85	-279.62	-199.65	< 0.0001
BC	-245.98	1	16.91	211.62	-285.96	-205.99	< 0.0001

The combinational impacts are graphically represented as two dimensional contour plots and three-dimensional response surface plots (Fig. 4.29). One variable was kept constant and the impact of two variables on the nanoparticles yield (mg) was plotted.

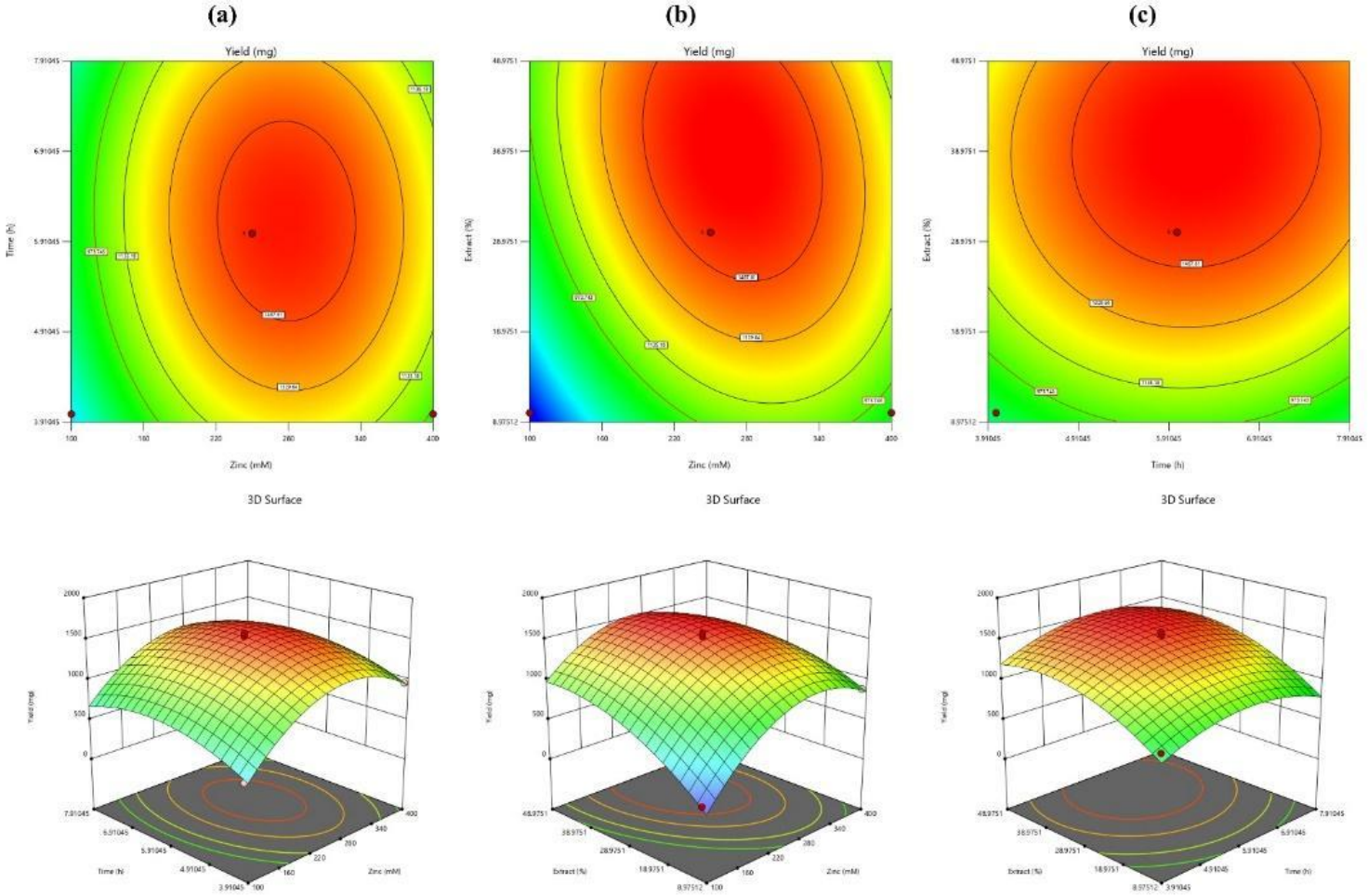

Fig. 4.29: 2D contour and 3D response surface plots for analyzing the interaction effects between (a) Zinc concentration and reaction time, (b) Zinc concentration and *A.variabilis* ARM 441 extract concentration (c) Reaction time and *A.variabilis* ARM 441 extract concentration

4.4 Photocatalytic activity of ZnO NPs

4.4.1 Photocatalytic activity of Bisphenol-A using ZnO NPs synthesized from Lemon grass

The photocatalytic behaviour of Lemon grass synthesized ZnO NPs was estimated by the photodegradation of Bisphenol-A (BPA) under UV illumination. A study was performed to test the photocatalytic efficiency of ZnO NPs to analyse impact of various operational parameters such as dye concentration, pH, catalyst dosage, and time were studied for BPA (Fig. 4.31). Fig. 4.30 (a) illustrate the absorption spectra of BPA (λ_{max}= 276 nm) during UV illumination for 45 minutes. The absorption peak of BPA decreased noticeably with progression of reaction time, hence the decreased relative concentration (C/C_0) of BPA (Fig. 4.32 (a)). After 45 min of exposure of BPA to UV light, about 97.41 % of BPA was degraded with a rate constant 5.15×10^{-2} min^{-1} (Table 4.13) (Yan *et al.*, 2020). Photodegradation was also observed and its degradation products were analysed the by-products by LC-MS analysis. The photodegradation of BPA followed pseudo first order kinetics with catalytic dosage (50mg/100mL), BPA concentration (0.5 mM); pH (6). Concerning the interference of absorbance with photodegradation the control set of experiments were being conducted in the absence of UV light with ZnO NPs. No significant changes in the concentration of BPA was observed after attaining the adsorption-desorption equilibrium. Additionally, another control test for the photocatalytic degradation of the organic pollutant in the absence of ZnO NPs was performed and the results were not significantly different (Fig. 4.32), which confirms the high photostability of BPA under the presence of UV light. Further, the reusability experiments for BPA were performed and the results are shown in Fig. 4.30 (b). The figure clearly illustrates the decline in degradation efficiency. It was observed that after 5 cycles, the degradation efficiency of ZnO NPs for BPA was 86.9%. The stable crystal structure of ZnO NPs is mainly what makes catalytic reusability work well (Udayabhanu *et al.*, 2017).

Table 4.13: Kinetic parameters for degradation of BPA via ZnO NPs under UV- illumination

Model	**Equation**	**Rate constant, *k***	**R^2 values**
First order	$lnC = lnC_0 - kt$	8.31×10^{-2}min^{-1}	0.71604
Pseudo-first order	$ln\, ln\, [C - C_0] = ln\, ln\, C - kt$	5.15×10^{-2} min^{-1}	0.96439
Second order	$\frac{1}{C} = \frac{1}{C_0} + kt$	5.3×10^{-3}mg^{-1}L^{-1}min^{-1}	0.35134
Pseudo-second order	$\frac{t}{C} = \frac{t}{C_0} - \frac{1}{kC_0^2}$	9.2×10^{-4}mg^{-1}L^{-1}min^{-1}	0.3551

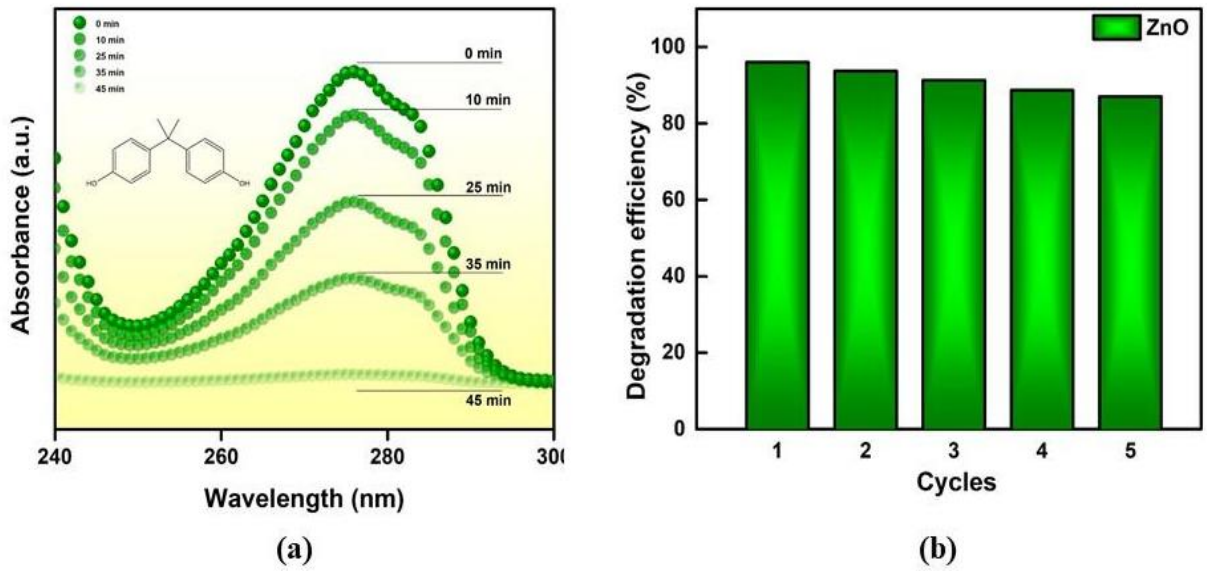

Fig. 4.30: (a) Time dependent photocatalytic degradation studies by ZnO NPs, absorption spectra of BPA samples and (b) Reusability efficiency of ZnO NPs for BPA

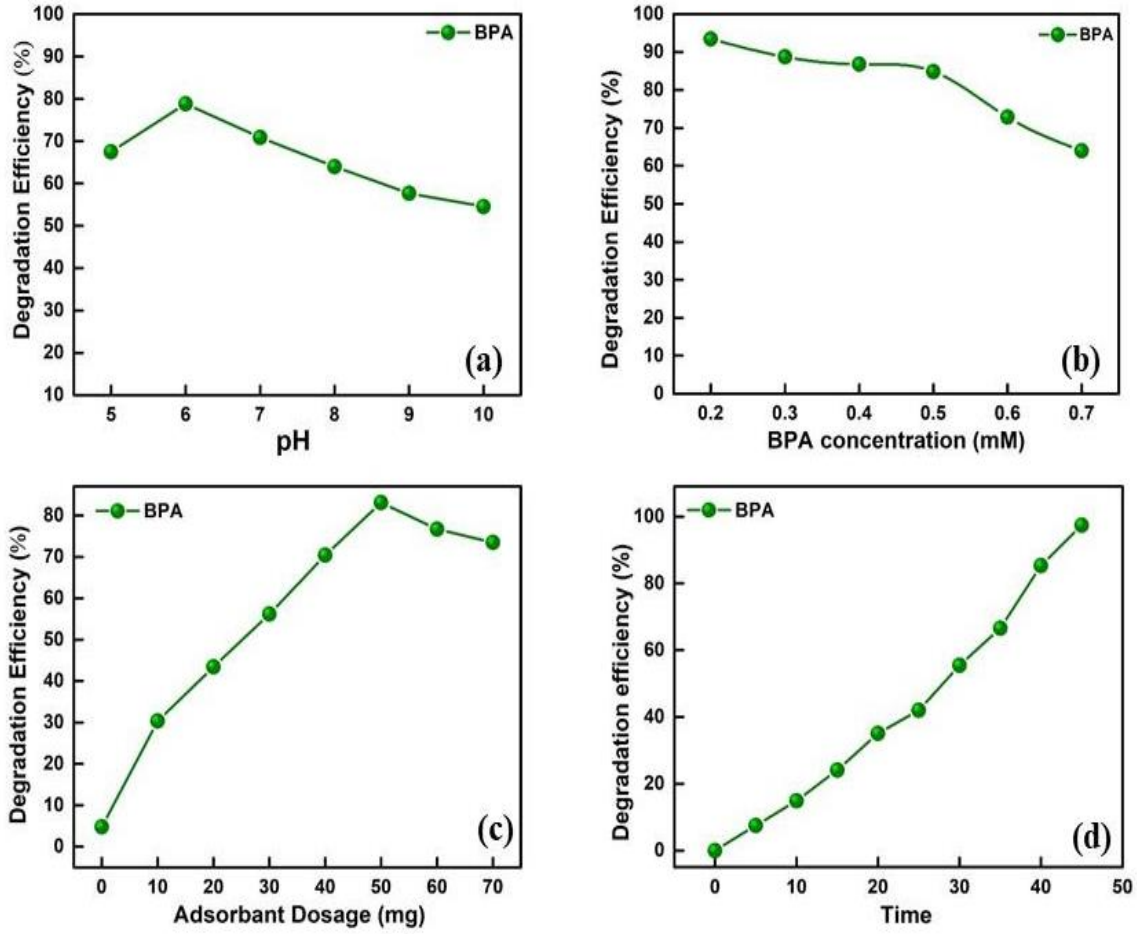

Fig. 4.31: Effect of operational parameters on degradation efficiency of ZnO NPs on BPA (a) pH, (b) dye concentration, (c) catalyst dosage and (d) time

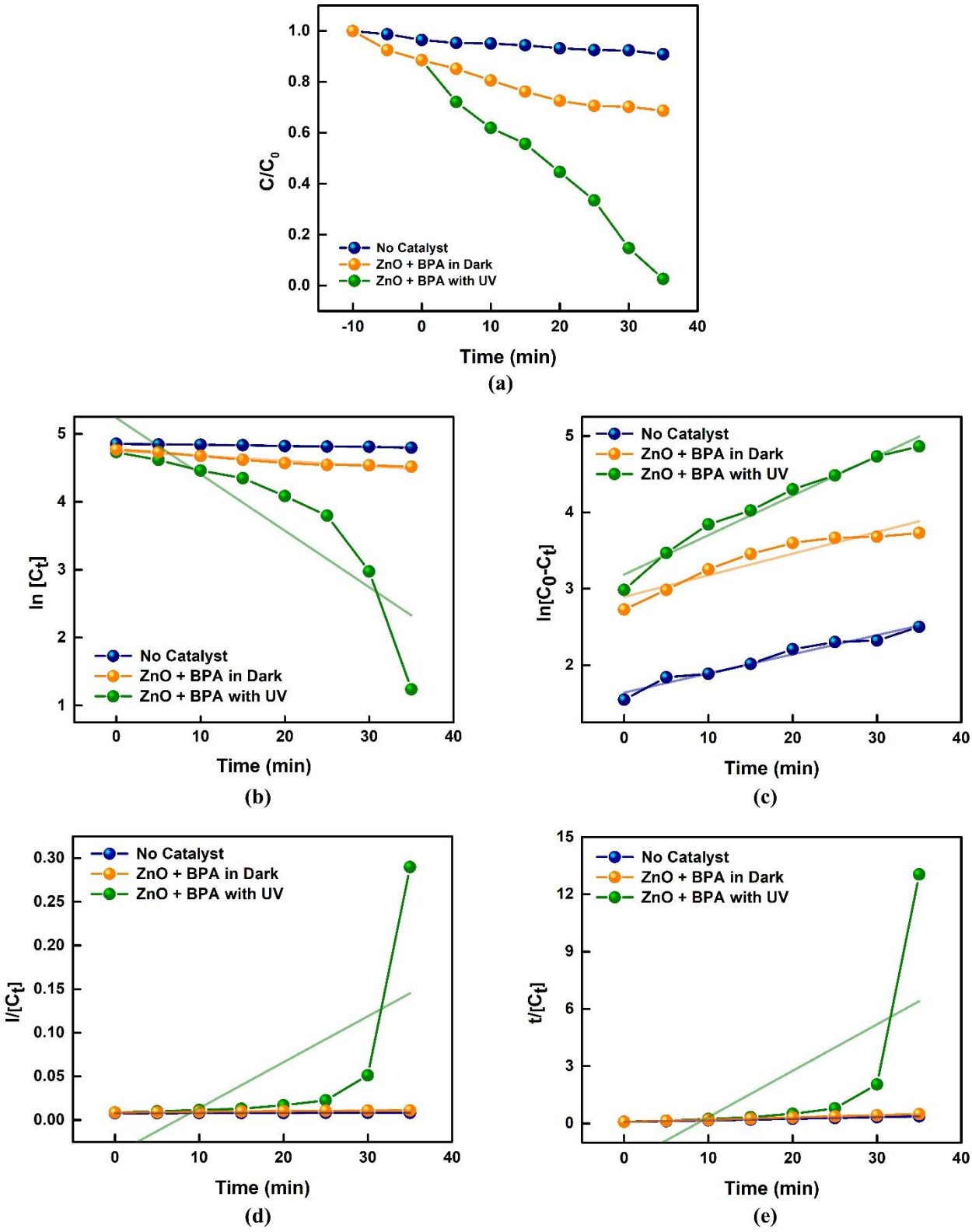

Fig. 4.32: Plots of BPA (a) Time dependent degradation, (b) First order kinetics, (c) Pseudo first order kinetics, (d) Second order kinetics and (e) Pseudo second order

4.4.1.1 Mechanism of photodegradation of Bisphenol-A

The abundant production of oxidizing radicals during the process was highly beneficial for decolourization of BPA. Further, the degradation products were studied *via* LC-MS analysis. Fig. 4.33 (a) represents the mass spectrum of standard BPA and its characteristic peak was identified at 228.90 *m/z* and Fig. 4.33 (b, c) depict their mass spectrum in presence of ZnO NPs under UV irradiation after 20 min and 45 min respectively. Various by-products (BP) of lower masses (*m/z*) at different degradation stages were observed (Fig. 4.33 (b, c)) and their plausible fragmentation pattern is illustrated in Fig. 4.34.

Intermediate DBP1 was formed when radicals in the aqueous solution attacked the C-C bond of BPA (Wang *et al.*, 2020). DBP2 and DBP4 were generated by the attack of electrophilic •OH radical on DBP1 and BPA respectively. DBP3 was produced through oxidation reaction of DBP2 by cleavage of the C-C bridge and the aromatic ring. DBP5 was formed by hydroxylation and dehydration of DBP4 (Garg, Gupta and Bansal, 2021). DBP11 was generated *via* different routes, i.e directly from DBP4 or after the formation of intermediate DBP5 and DBP6 (Garg, Gupta and Bansal, 2021). Reactive species generated during the process had the ability to attack the C-C bonds between the two aromatic rings, leading to the formation of an intermediate DBP6. Additionally, BPA gets oxidized by •OH radicals and produces another intermediate compound DBP7 which undergoes ring cleavage and further induces the production of intermediate DBP8. The intermediate compound DBP8 oxidizes to DBP9 by cleavage of C-C bond adjacent to ring and gave compound DBP10. DBP10 was also produced by the dehydrogenation of DBP6 (Wang *et al.*, 2020). Further DBP10 either produces smaller fragments like DBP13 or undergoes enolization to produce DBP12, which gets oxidized by cleavage of ring to produce smaller by-products which ultimately mineralized to CO_2 and H_2O (Yan *et al.*, 2020).

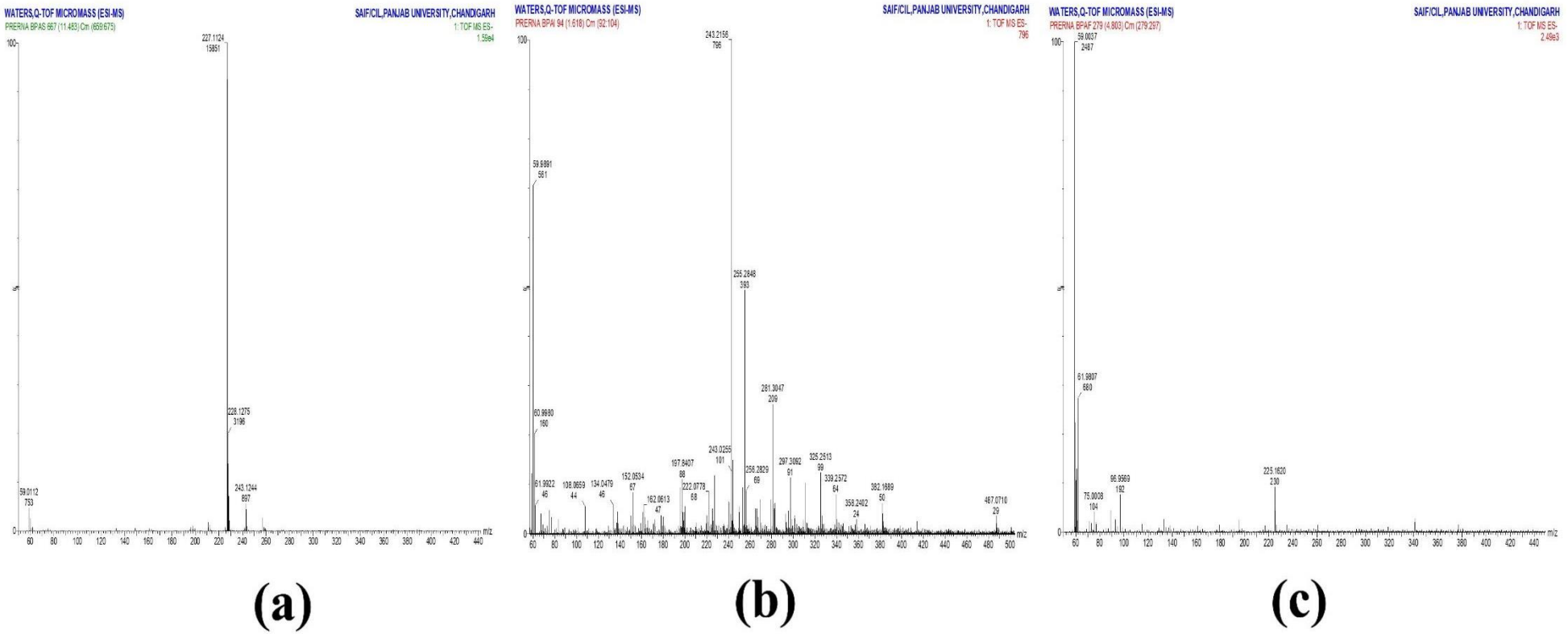

Fig. 4.33: Mass spectra of BPA (a) Before irradiation and (b) after UV irradiation in the presence of ZnO NPs for 20 and 45 min, respectively

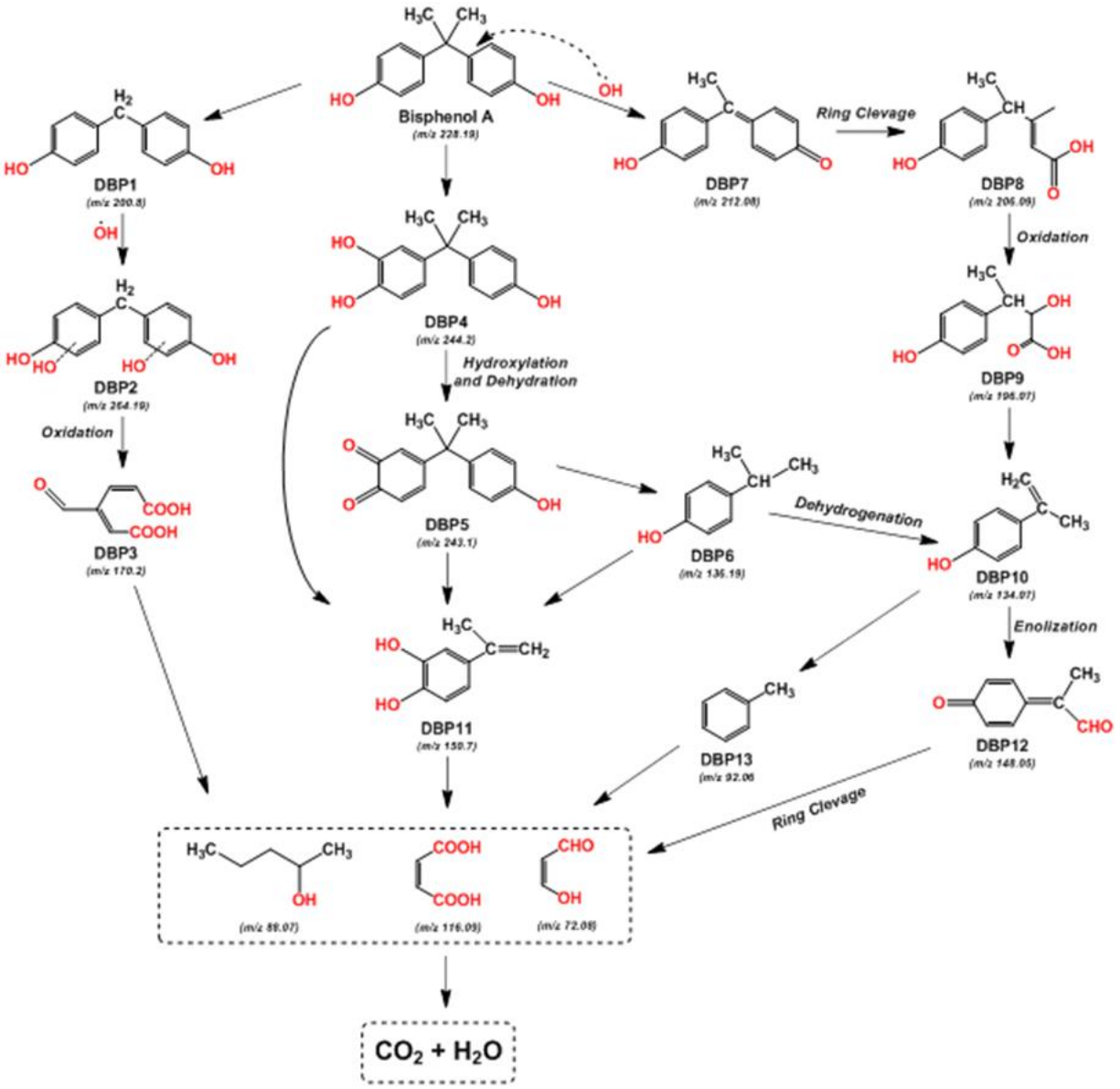

Fig. 4.34: Detailed photocatalytic degradation mechanism of BPA by ZnO NPs under UV irradiation

4.4.2 Photocatalytic activity of BG and IC using ZnO NPs synthesized from *A.variabilis* ARM441

Semiconductors like ZnO under the illumination of UV light absorb photons of energy equal or higher than the band gap energy, electrons and holes are created on the surface of a photocatalyst and generate highly reactive species which lead to the degradation of dyes (Suresh *et al.*, 2015; Udayabhanu *et al.*, 2017). Photocatalytic efficiency of a catalyst is dependent on several factors, such as crystallinity, phase composition, particle size, morphology, band gap, surface area and surface hydroxyl density, etc. (Rambabu *et al.*, 2021). The photocatalytic behaviour of *A.variabilis* ARM 441 synthesized ZnO NPs was estimated

by the photodegradation of Brilliant green (BG) and Indigo caramine (IC) under UV illumination. A comparative study was performed to test the photocatalytic efficiency of ZnO NPs over cationic and anionic dyes. Various operational parameters such as dye concentration, pH, catalyst dosage, and time were studied for both BG and IC (Fig 4.35). Fig. 4.36 (a) and (b) illustrate the absorption spectra of BG (λ_{max}= 625 nm) and IC (λ_{max}= 610 nm) during UV illumination for 130 minutes. The absorption peak of BG and IC decreased noticeably with progression of reaction time, hence the decreased relative concentration (C/C_0) of BG and IC (Fig. 4.37 (a)). After 130 min of exposure of BG to UV light, about 98.07 % of BG dye was degraded with a rate constant 26.4×10^{-3} min^{-1} (Table 4.14). Photodegradation was also visible by the gradual disappearance of BG's bluish green colour to a colourless solution, indicating the complete removal of chromophore in BG molecules, which was further analysed the by-products by LC-MS analysis. The photodegradation of BG dye followed first order kinetics with catalytic dosage (50mg/100mL), dye concentration (30mM); pH (7) (Fig. 4.37 (b)). However, in the case of IC, after the exposure of 130 minutes, about 80.8% of the dye was degraded and it also followed first order kinetics with catalytic dosage (50mg/100ml), dye concentration (30mM), and pH (5) (Fig. 4.37 (b)).

Table 4.14: Kinetic parameters for degradation of BG and IC via ZnO NPs under UV-illumination

		Brilliant Green		**Indigo Carmine**	
Model	**Equation**	**Rate constant, k**	**R^2 values**	**Rate constant, k**	**R^2 values**
First order	$lnC = lnC_0 - kt$	$26.4 \times 10^{-3}$$min^{-1}$	0.98743	12.1×10^{-3} min^{-1}	0.99499
Pseudo-first order	$ln\ ln\ [C - C_0] = ln\ ln\ C - kt$	10.9×10^{-3} min^{-1}	0.75623	12.4×10^{-3} min^{-1}	0.85349
Second order	$\frac{1}{C} = \frac{1}{C_0} + kt$	$1.2 \times 10^{-3}$$mg^{-1}L^{-1}min^{-1}$	0.73602	$2.2 \times 10^{-4}$$mg^{-1}L^{-1}min^{-1}$	0.92604
Pseudo-second order	$\frac{t}{C} = \frac{t}{C_0} - \frac{1}{kC_0^2}$	$5.2 \times 10^{-3}$$mg^{-1}L^{-1}min^{-1}$	0.66775	1.7×10^{-3} $mg^{-1}L^{-1}min^{-1}$	0.88115

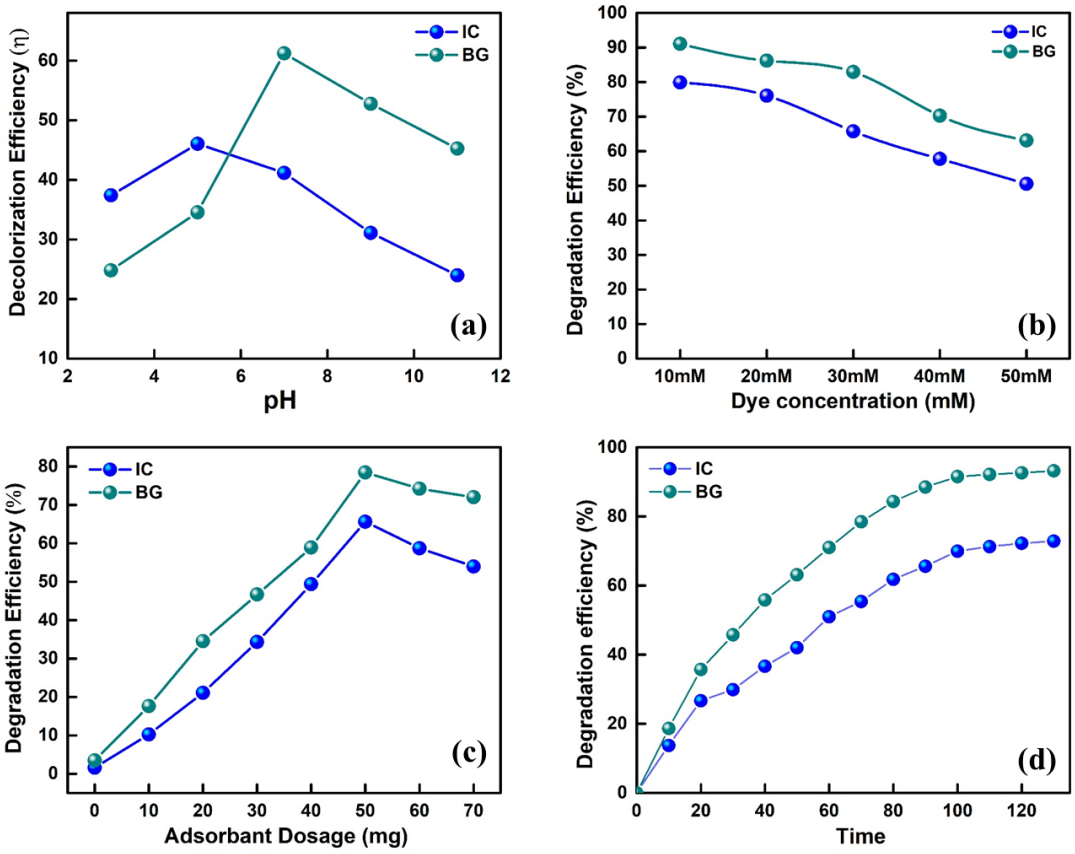

Fig. 4.35: Effect of operational parameters on degradation efficiency of ZnO NPs on BG and IC dyes (a) pH, (b) dye concentration, (c) catalyst dosage and (d) time

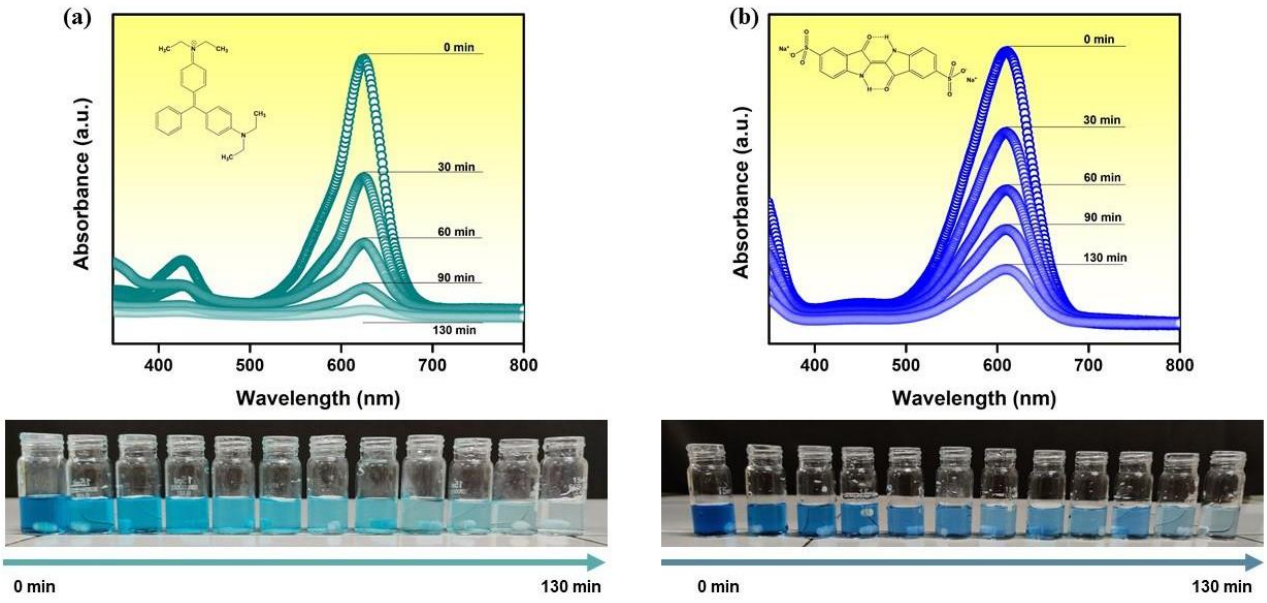

Fig. 4.36: Time dependent photocatalytic degradation studies by ZnO NPs (a) Absorption spectra of BG dye samples and (b) Absorption spectra of IC dye samples

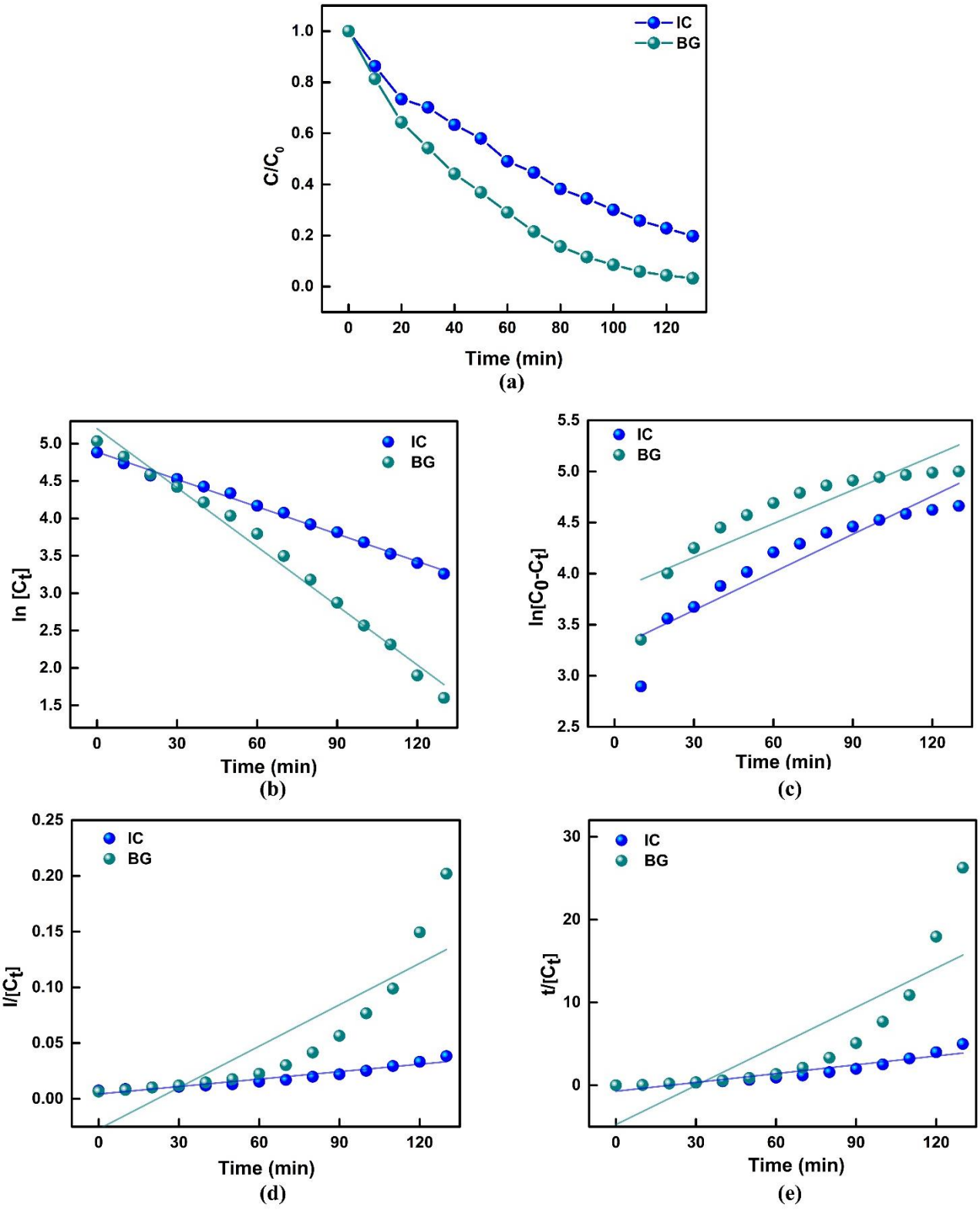

Fig. 4.37: Plots of BG and IC dyes (a) Time dependent degradation, (b) First order kinetics, (c) Pseudo first order kinetics, (d) Second order kinetics and (e) Pseudo second order

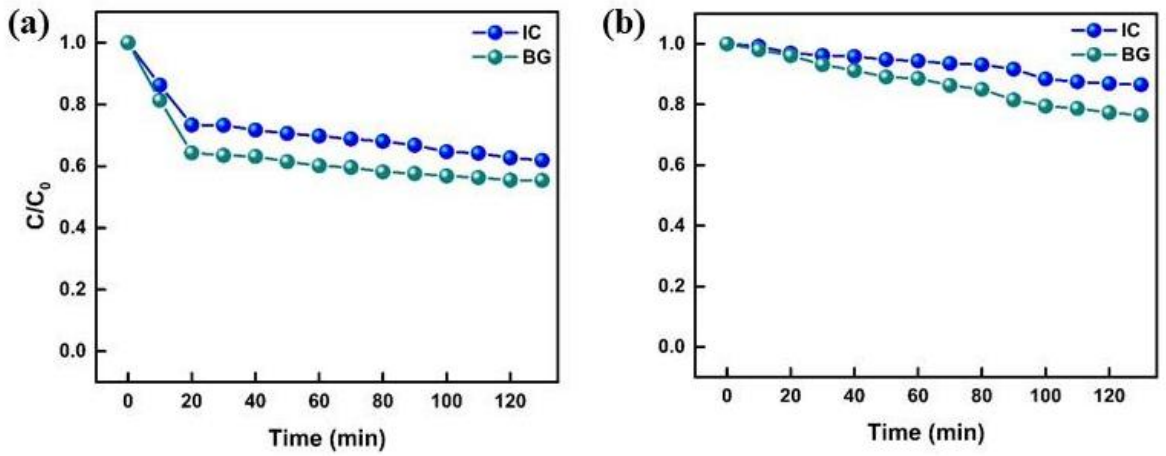

Fig. 4.38: Degradation of IC and BG (a) in presence ZnO NPs and absence of UV light and (b) in absence of ZnO NPs and presence of UV light

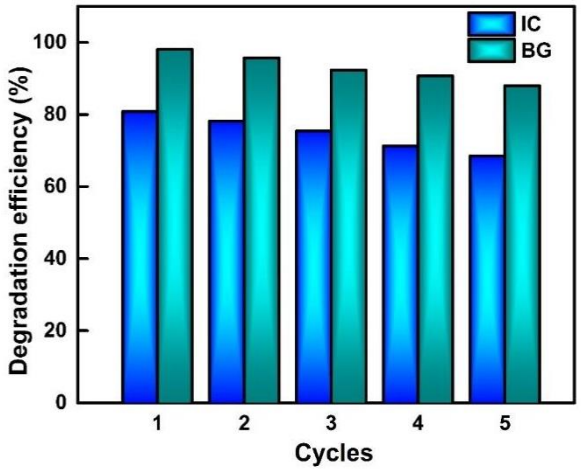

Fig. 4.39: Reusability efficiency of ZnO NPs for BG and IC

Concerning the interference of absorbance with photodegradation the control set of experiments (Fig. 4.38 (a)) were being conducted in the absence of UV light with ZnO NPs. No significant changes in the concentration of dyes was observed after attaining the adsorption-desorption equilibrium. Additionally, another control test for the photocatalytic degradation of the respective dyes in the absence of ZnO NPs was performed and the results were not significantly different (Fig. 4.38 (b)), which confirms the high photostability of dyes under the presence of UV light. Further, the decolouration reusability experiments for BG and IC were performed and the results are shown in Fig. 4.39. The figure clearly illustrates the decline in degradation efficiency. It was observed that after 5 cycles, the degradation efficiency of ZnO NPs for BG and IC was 88% and 69% respectively. The stable crystal structure of ZnO NPs is mainly what makes catalytic reusability work well (Udayabhanu *et al.*, 2017).

4.4.2.1 Mechanism of photodegradation of brilliant green dye

Photodegradation of dyes under UV illumination is governed by simultaneous photooxidation followed by photosensitization. In photooxidation, photoelectron-hole pairs are generated in the conduction and valence band, which pair with free oxygen and water molecules of the solution to generate hydroxyl radicals and superoxide anions. OH· generated is the potential oxidizing agent that assists the degradation of dyes (Eq. 10-17) (Zhang *et al.*, 1998; Udayabhanu *et al.*, 2017; Bhattacharya *et al.*, 2019).

$$ZnO + h\upsilon \rightarrow ZnO\ (e^-_{C.B.} + h^+_{V.B}) \text{.....(10)}$$

$$e^-_{C.B.} + O_2 \rightarrow \cdot O_2^- \text{.....(11)}$$

$$h^+_{V.B} + OH^- \rightarrow \cdot OH^- \text{.....(12)}$$

$$h^+_{V.B} + H_2O \rightarrow H^+ + OH^- \text{.....(13)}$$

$$\cdot O_2^- + H^+ \rightarrow \cdot HO_2 \text{.....(14)}$$

$$BG + \cdot OH^- \rightarrow Degradation\ Product \text{.....(15)}$$

$$BG + h^+_{V.B} \rightarrow Oxidation\ Product \text{.....(16)}$$

$$BG + e^-_{C.B.} \rightarrow Reduction\ Product \text{.....(17)}$$

Simultaneously, the photosensitization mechanism, adsorbed dye molecules (BG), are excited by energy from UV irradiation. This leads to the formation of dye radicals (BG*) by jumping electrons to the conduction band of ZnO NPs and further producing extra oxygen radicals (O_2^-) (Eq. 18-21) (Zhang *et al.*, 1998, 2019; Bhattacharya *et al.*, 2019).

$$BG + h\upsilon \rightarrow BG^* \text{.....(18)}$$

$$BG + ZnO \rightarrow \cdot BG^+ + ZnO(e^-_{C.B.}) \text{.....(19)}$$

$$ZnO(e^-_{C.B.}) + O_2 \rightarrow \cdot O_2^- + ZnO \text{.....(20)}$$

$$\cdot BG^+ \rightarrow Degradation\ Products \text{.....(21)}$$

As brilliant green is a cationic dye, its excited dye radicals interact with the hydroxyl radicals and oxide radicals to generate degraded products (Eq. 22-29) (Shanmugam *et al.*, 2016).

$$\cdot BG^+ + OH^- \rightarrow BG + HO \cdot \text{.....(22)}$$

$$BG + 2HO \cdot \rightarrow H_2O + Oxidation\ products \text{.....(23)}$$

$$\cdot O_2^- + H^+ \rightarrow \cdot HO_2 \text{.....(24)}$$

$$\cdot HO_2 + H^+ + e^-_{C.B.} \rightarrow H_2O_2 \text{.....(25)}$$

$$H_2O_2 + e^-_{C.B.} \rightarrow HO \cdot + HO^- \text{.....(26)}$$

$$\cdot BG^{+} + \cdot O_2^{-} \rightarrow Degradation\ Products \text{.....(27)}$$

$$\cdot BG^{+} + \cdot HO_2 \rightarrow Degradation\ Products \text{.....(28)}$$

$$\cdot BG^{+} + HO \cdot \rightarrow Degradation\ Products \text{.....(29)}$$

The abundant production of oxidizing radicals during the process was highly beneficial for decolourization of BG (Shanmugam *et al.*, 2016; Aminuzzaman *et al.*, 2018). Further, the degradation products were studied *via* LC-MS analysis and identified by interpretation of their *m/z* value (where *m* is molecular weight of the intermediates in the mass spectra and *z* is charge number) (Qi *et al.*, 2020). Fig. 4.40 (a) represents the mass spectrum of standard BG dye and its characteristic peak was identified at 386.50 *m/z* and Fig. 4.40 (b, c) depict their mass spectrum in presence of ZnO NPs under UV irradiation after 60 min and 130 min respectively. Various by-products (BP) of lower masses (*m/z*) at different degradation stages were observed (Fig. 4.40 (b, c)) and their plausible fragmentation pattern is illustrated in Fig. 4.42.

Initial de-ethylation of BG either by direct photolysis or •OH have contributed to the independent formation of BP1 with *m/z* 357.23. The removal of the HO_2• group from peroxy radical and then upon subsequent reaction with H_2O can lead to the generation of degradation product BP1, an enol (ethenol) (Rehman *et al.*, 2018). This ethenol can undergo keto-enol tautomerism forming acetaldehyde. These de-ethylated byproducts were also reported by Rehman et al (Rehman *et al.*, 2018). Another degradation product BP9 (m/z 399.36) was formed, and its hydroxylation can lead to the formation of BP10 with *m/z* 415.34 (Rehman *et al.*, 2018). Direct photolysis of BP9 can form BP4 *m/z* 254.18; following the same mechanistic pathway BP10 can lead to production of BP5 (*m/z* 270.13). Such types of hydroxylation byproducts have been reported in literature (Shah *et al.*, 2016, 2019; He *et al.*, 2018). The addition of •OH net resulted in the formation of intermediate by product BP4 with *m/z* 254.13(Rehman *et al.*, 2018). Hydroxylation of BP4, possibly at the aromatic ring, could lead to the formation of BP5, *m/z* 270.13 whereas its de-ethylation can lead to the formation of degradation product BP6, *m/z* 226.12 (Rehman *et al.*, 2018; Shah *et al.*, 2019). There is the elimination of the $–NCH_2CH_3$ group, followed by the insertion of H^+, forming BP2 with *m/z* 347.21. The OH group added to BP2 and easily oxidized to –CO and forming benzophenone (BP3) as the oxidizing agent (Migliorini *et al.*, 2016). Due to presence of excess •OH, and subsequent addition to BP3 intermediate degradation products were obtained followed by an internal cycle process resulting in formation of BP7 (*m/z* 149.12) identified as phthalic anhydride. Subsequently, decarboxylation process followed by addition of •OH led to

formation of BP8. Further, the opening of the aromatic rings occurred and aliphatic compounds were converted into oxalic acid, which ultimately oxidized into CO_2 and H_2O. After that, further degradation and abstraction of H-atom from the resulting intermediates causes *m/z* to dip further into the lowest value of 60.

The final solution consisted of smaller hydrocarbons and other organic residues. It was evident that photodegradation was more efficient and selective for cationic dye brilliant green compared to anionic indigo caramine because of the electrostatic interaction between the dye molecules and photocatalyst (Fig 4.41). ZnO NPs were negatively charged (Zeta potential -9.32 mV) in a neutral solution which elucidated the selectivity for cationic dyes.

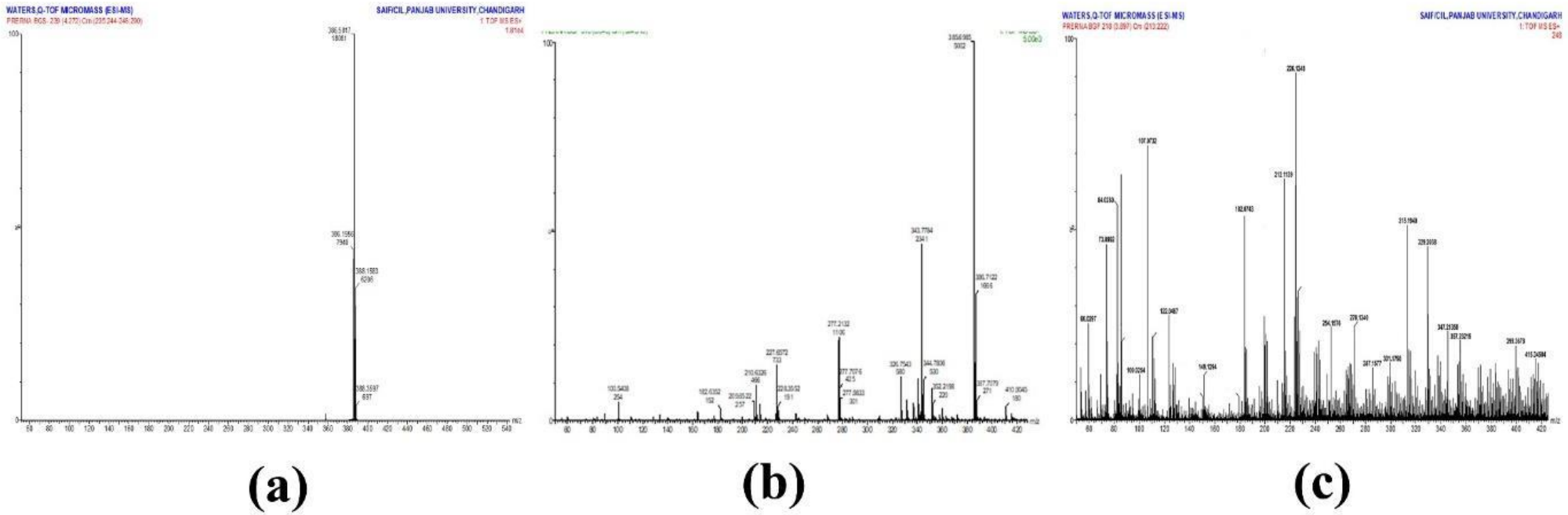

Fig. 4.40: Mass spectra of BG Dye (a) before irradiation and (b, c) after UV irradiation in the presence of ZnO NPs for 60 and 130 min, respectively

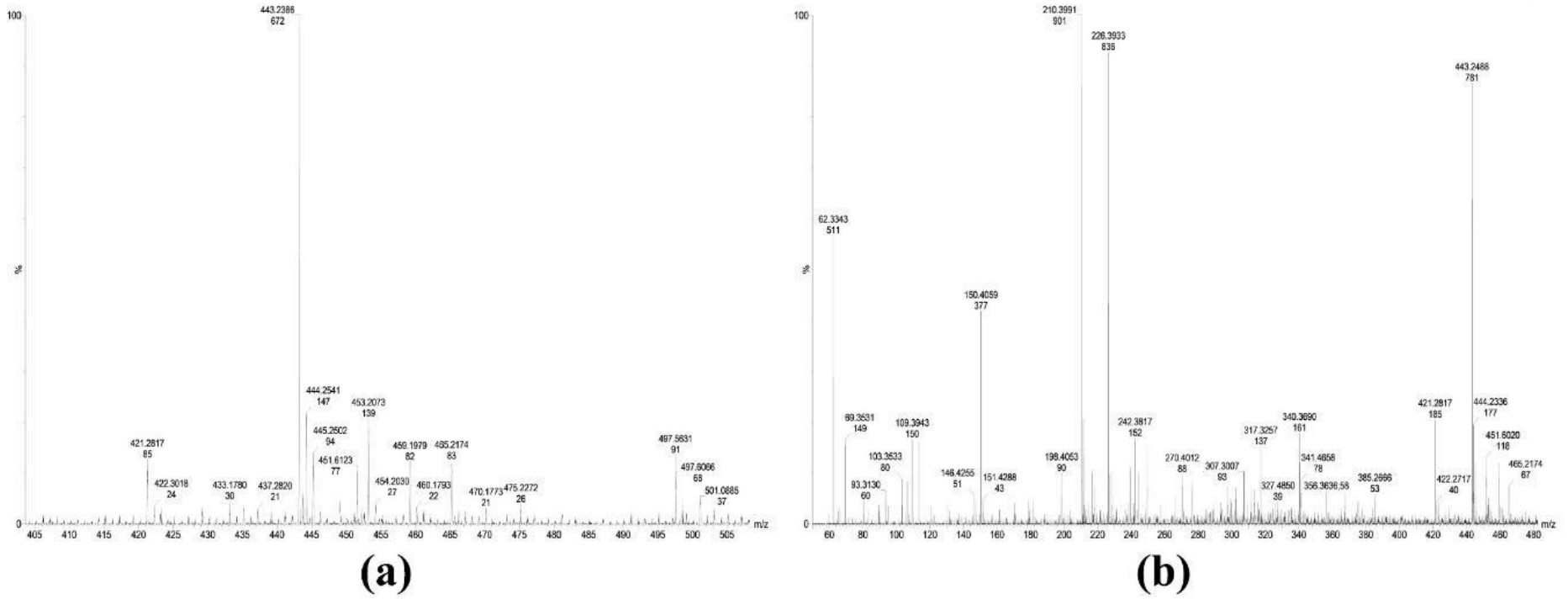

Fig. 4.41: Mass spectra of IC Dye (a) efore ibrradiation and (b) after UV irradiation in the presence of ZnO NPs for 130 min

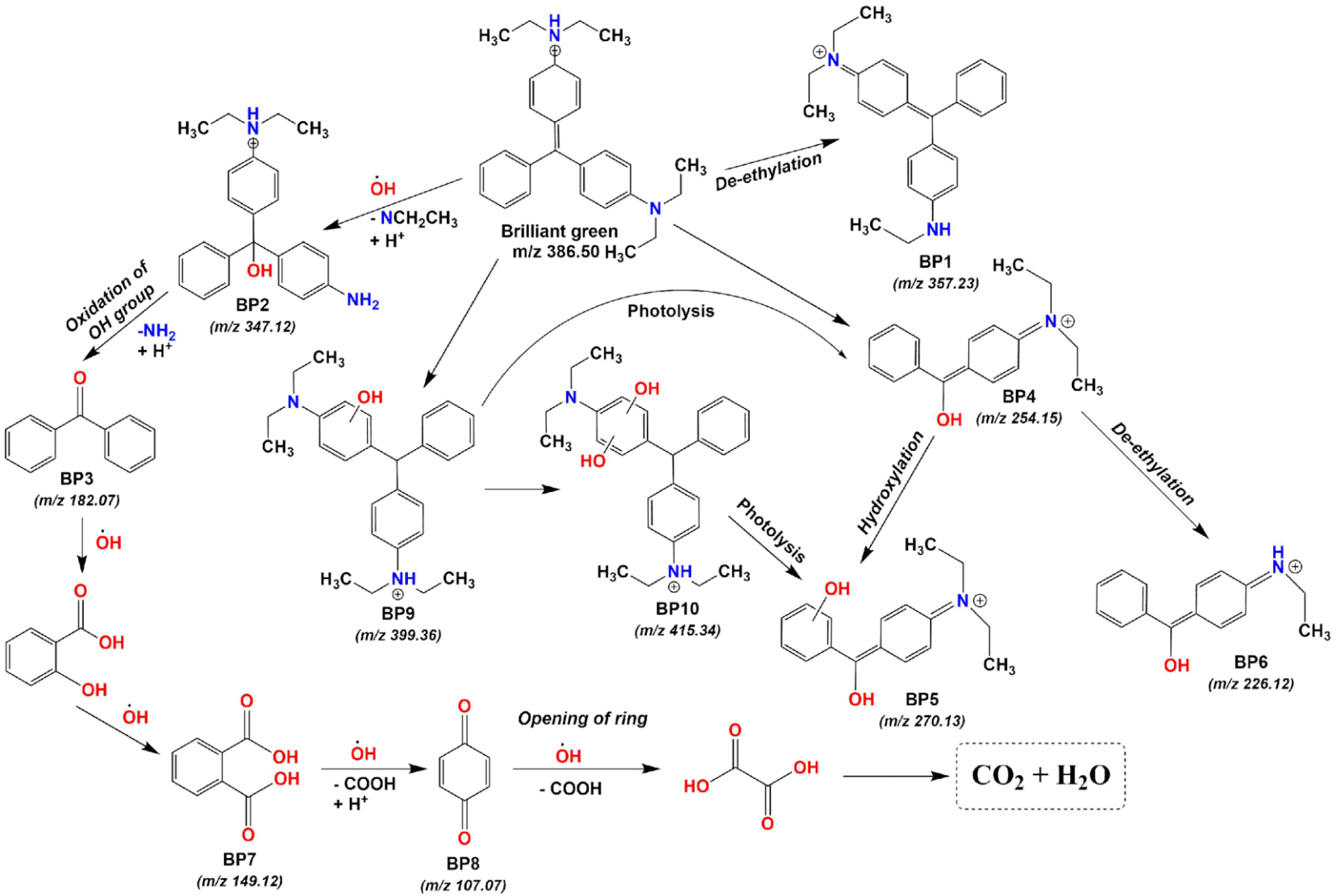

Fig. 4.42: Detailed photocatalytic degradation mechanism of BG dye by ZnO NPs under UV irradiation

A comparative literature search with current experimental data is represented in Table 4.15, revealed better photocatalytic efficiency of synthesized ZnO NPs than other catalysts.

Table 4.15: Comparison of photocatalytic performance of green synthesized ZnO NPs with other green synthesized ZnO nanomaterials on degradation of different organic pollutants

Nanomaterial	Green source	Dye	Irradiation source	Degradation time (min)	Degradation efficiency (%)	Reference
ZnO	*Hylocereus polyrhizus*	Methylene blue	Sunlight	120	95.0	Aminuzzaman et al., 2018
ZnO	*Carissa edulis*	Congo Red	Photo-reactor	130	97.0	Fowsiya et al. 2016
ZnO	*Calotropis procera*	Methyl Orange	UV light	100	81.0	Gawade et al. 2017
ZnO	*Ulva lactuca*	Methylene Blue	Sunlight	120	90.4	Ishwarya et al. 2018
ZnO	*Coriandrum sativum*	Reactive Yellow 186	Sunlight	130	93.4	Singh et al. 2019
ZnO	*Ruellia tuberosa*	Methylene blue	Sunlight	150	94	Vasantharaj et al. 2021
ZnO	*Ruellia tuberosa*	Malachite green	Sunlight	150	92	Vasantharaj et al. 2021
ZnO	*Phoenix dactylifera*	Methylene blue	UV light	180	90.6	Rambabu et al. 2021
ZnO	*Phoenix dactylifera*	Eosin yellow	UV light	180	90.5	Rambabu et al. 2021
ZnO	*Salvia officinalis*	Methyl Orange	UV light	120	92.47	Abomuti et al. 2021
Al-ZnO	*Amomum longiligulare*	Malachite green	UV light	60	38.1	Liu et al., 2020
Al-ZnO	*Amomum longiligulare*	Methylene blue	UV light	60	66	Liu et al., 2020
ZnO	*Lemon grass*	Bisphenol- A	UV Light	45	97.41	Current study
ZnO	*Anabaena variabilis* ARM 441	Brilliant Green	UV light	130	98.1	Current study

Salient Findings

1. The abundant presence of citral and photocitral-B in lemon grass extract identified by GC-MS and NMR (^{13}C and ^{1}H NMR) spectroscopy acted as a coating and provided stability to ZnO NPs.
2. One-pot synthesis of lemongrass-capped ZnO nanoparticles had a size of 43.58±3.2 nm and exhibited a hexagonal shape based on HR-TEM analysis.
3. GC-MS and NMR (^{13}C and ^{1}H NMR) spectroscopic characterization of the aqueous algal extract revealed 21 different bioactive compounds, of which n-hexadecanoic acid and 13-tetradecane from algal extract had reducing and capping properties that were needed for the synthesis of ZnO NPs the synthesis of ZnO NPs.
4. XRD and HR-TEM revealed the properties of *A. variabilis* ARM 441 mediated ZnO NPs, which include crystals of nanoscale dimension (33.31 nm) possessing hexagonal wurtzite phases and exhibiting promising optical properties.
5. Gram-scale synthesis of ZnO NPs from aqueous extracts of lemon grass and *A. variabilis* ARM 441 *via* a single-step co-precipitation method was accomplished.
6. Numerical optimization of lemon grass mediated ZnO NPs, revealed that the concentration of zinc ions had the greatest impact to achieve an overall yield of 1857.2 mg with optimized conditions.
7. *A. variabilis* ARM 441-mediated ZnO NPs yield was improved by the RSM optimization procedure with an overall yield of 1565.26 mg of ZnO NPs, which is six-fold higher as compared to the yield at a lower scale.
8. 97.41 % of BPA photodegradation was achieved by ZnO NPs synthesized from lemon grass extract with a reusability efficiency of 86.9% after 5 cycles.
9. The photocatalytic degradation of brilliant green and indigo carmine dyes in aqueous solution by *A. variabilis* ARM 441 mediated ZnO NPs was 98.07% and 80.8% for BG and IC, respectively, which followed first-order kinetics.
10. The photocatalytic degradation studies revealed amphoteric and rapid photocatalytic activity of *A.variabilis* ARM 441 mediated ZnO NPs exhibiting excellent degradation of cationic dye BG as compared to anionic IC dye.
11. Biosynthesized ZnO NPs showed evidence of their ability to act as an effective photocatalyst, which can be appropriate for industrial wastewater treatment, especially to degrade harmful and toxic pollutants that persist in aquatic environment.

Future Scope of Work

The photocatalytic efficiency of biosynthesized ZnO NPs makes them suitable for industrial effluent treatment, particularly for the degradation of persistently harmful and toxic pollutants. We have developed a low-cost, eco-friendly protocol that can be implemented on a pilot scale to increase overall yield. The plausible mechanisms for the synthesis of nanoparticles using lemon grass and *A. variabilis* ARM 441 have been proposed. However, further studies such as carbon dioxide estimation and electrochemical potential of the compounds in the extracts need to be performed to explore the exact mechanism. Moreover, we synthesized nanomaterials that can improve the industrial applications of these NPs, thereby making them sustainable. Our newly developed green synthesis method has the potential to enhance industrial effluent management. Further evaluation could be conducted in the textile, food processing, and water purification industries. In addition, the use of synthesized ZnO NPs may be an excellent strategy to explore in agriculture, biologics, and therapeutics.

References

1. Abboud, Y. *et al.* (2014) 'Biosynthesis, characterization and antimicrobial activity of copper oxide nanoparticles (CONPs) produced using brown alga extract (Bifurcaria bifurcata)', *Applied Nanoscience*, 4(5), pp. 571–576.
2. Abdel-Raouf, N., Al-Enazi, N.M. and Ibraheem, I.B.M. (2017) 'Green biosynthesis of gold nanoparticles using Galaxaura elongata and characterization of their antibacterial activity', *Arab J Chem*, 10, pp. S3029–S3039.
3. Abdelsattar, A.S. et al. (2022) 'Utilization of Ocimum basilicum extracts for zinc oxide nanoparticles synthesis and their antibacterial activity after a novel combination with phage', Materials letters, 309, p. 131344.
4. Abdul Salam, H., Sivaraj, R. and Venckatesh, R. (2014) 'Green synthesis and characterization of zinc oxide nanoparticles from Ocimum basilicum L. var. purpurascens Benth.-Lamiaceae leaf extract', Materials letters, 131, pp. 16–18.
5. Aboelfetoh, E.F., El-Shenody, R.A. and Ghobara, M.M. (2017) 'Eco-friendly synthesis of silver nanoparticles using green algae (Caulerpa serrulata): reaction optimization, catalytic and antibacterial activities', *Environmental monitoring and assessment*, 189(7), p. 349.
6. Abomuti, M.A. *et al.* (2021) 'Green Synthesis of Zinc Oxide Nanoparticles Using Salvia officinalis Leaf Extract and Their Photocatalytic and Antifungal Activities', *Biology*, 10(11). Available at: https://doi.org/10.3390/biology10111075.
7. Agarwal, H. and Shanmugam, V.K. (2019) 'Synthesis and optimization of zinc oxide nanoparticles using Kalanchoe pinnata towards the evaluation of its anti-inflammatory activity', *Journal of drug delivery science and technology*, 54, p. 101291.
8. Agarwal, H. *et al.* (2020) 'Magnetization spin reversal and neutron diffraction study of polycrystalline $Tb_{0.55}Sr_{0.45}MnO_3$', *Journal of alloys and compounds*, 845, p. 156355.
9. Agarwal, H. *et al.* (2021) 'Evolution from sinusoidal to collinear A-type antiferromagnetic spin-ordered magnetic phase transition in Tb1-xPrxMnO3solid solution', *Journal of physics. Condensed matter: an Institute of Physics journal*, 33(26), p. 265802.
10. Agarwal, H., Venkat Kumar, S. and Rajeshkumar, S. (2017) 'A review on green synthesis of zinc oxide nanoparticles – An eco-friendly approach', Resource-efficient technologies, 3(4), pp. 406–413

11. Agnihotri, S., Mukherji, S. and Mukherji, S. (2014) 'Size-controlled silver nanoparticles synthesized over the range 5–100 nm using the same protocol and their antibacterial efficacy', *RSC advances*, 4(8), pp. 3974–3983.
12. Ahluwalia, V. *et al.* (2018) 'Nano silver particle synthesis using Swertia paniculata herbal extract and its antimicrobial activity', *Microbial pathogenesis*, 114, pp. 402–408.
13. Ahmed, S. *et al.* (2017) 'A review on biogenic synthesis of ZnO nanoparticles using plant extracts and microbes: A prospect towards green chemistry', *Journal of photochemistry and photobiology. B, Biology*, 166, pp. 272–284.
14. Ajayi, E. and Afolayan, A. (2017) 'Green synthesis, characterization and biological activities of silver nanoparticles from alkalinized Cymbopogon citratus Stapf', *Advances in Natural Sciences: Nanoscience and Nanotechnology*, 8(1), p. 015017.
15. Akhtar, N., Goyal, D. and Goyal, A. (2017) 'Characterization of microwave-alkali-acid pre-treated rice straw for optimization of ethanol production via simultaneous saccharification and fermentation (SSF)', *Energy Conversion & Management*, 141, pp. 133–144.
16. Alderman, D.J. (1985) 'Malachite green: a review', *Journal of Fish Diseases*, pp. 289–298.
17. Ali, K. *et al.* (2016) 'Aloe vera extract functionyzed zinc oxide nanoparticles as nanoantibiotics against multi-drug resistant clinical bacterial isolates', *Journal of colloid and interface science*, 472, pp. 145–156.
18. Ali, S.A. *et al.* (2019) 'Fast removal of methylene blue and Hg(II) from aqueous solution using a novel super-adsorbent containing residues of glycine and maleic acid', *Journal of hazardous materials*, 369, pp. 642–654.
19. Almoisheer, N. *et al.* (2018) 'Adsorption and anion exchange insight of indigo carmine onto CuAl-LDH/SWCNTs nanocomposite: kinetic, thermodynamic and isotherm analysis', *RSC advances*, 9(1), pp. 560–568.
20. Ambika, S. and Sundrarajan, M. (2015) 'Antibacterial behaviour of Vitex negundo extract assisted ZnO nanoparticles against pathogenic bacteria', Journal of photochemistry and photobiology. B, Biology, 146, pp. 52–57.
21. Amendola, V. and Meneghetti, M. (2009) 'Laser ablation synthesis in solution and size manipulation of noble metal nanoparticles', *Physical chemistry chemical physics: PCCP*, 11(20), pp. 3805–3821.

22. Aminuzzaman, M. *et al.* (2018) 'Green synthesis of zinc oxide nanoparticles using aqueous extract of Garcinia mangostana fruit pericarp and their photocatalytic activity', *Bulletin of Materials Science.* Available at: https://doi.org/10.1007/s12034-018-1568-4.
23. Aminuzzaman, M. *et al.* (2021) 'Biosynthesis of NiO nanoparticles using soursop (Annona muricata L.) fruit peel green waste and their photocatalytic performance on crystal Violet dye', *Journal of Cluster Science*, 32(4), pp. 949–958.
24. Anbuvannan, M. *et al.* (2015) 'Synthesis, characterization and photocatalytic activity of ZnO nanoparticles prepared by biological method', *Spectrochimica acta. Part A, Molecular and biomolecular spectroscopy*, 143, pp. 304–308.
25. Anbuvannan, M. *et al.* (2015a) 'Anisochilus carnosus leaf extract mediated synthesis of zinc oxide nanoparticles for antibacterial and photocatalytic activities', *Materials Science in Semiconductor Processing*, 39, pp. 621–628.
26. Anbuvannan, M. *et al.* (2015b) 'Synthesis, characterization and photocatalytic activity of ZnO nanoparticles prepared by biological method', *Spectrochimica acta. Part A, Molecular and biomolecular spectroscopy*, 143, pp. 304–308.
27. Ankamwar, B., Chaudhary, M. and Sastry, M. (2005) 'Gold Nanotriangles Biologically Synthesized using Tamarind Leaf Extract and Potential Application in Vapor Sensing', *Synthesis and Reactivity in Inorganic, Metal-Organic, and Nano-Metal Chemistry*, 35(1), pp. 19–26.
28. Annamalai, J. and Nallamuthu, T. (2016) 'Green synthesis of silver nanoparticles: characterization and determination of antibacterial potency', *Applied nanoscience*, 6, pp. 259–265.
29. Anshup, A. and Venkataraman, J.S., 2005. Subramaniam c., Kumar rr, Priya S., Kumar tr, Omkumar rV, John A., Pradeep t. *Langmuir*, *21*(25), pp.11562-11567.
30. Anupama, A.V., Keune, W. and Sahoo, B. (2017) 'Thermally induced phase transformation in multi-phase iron oxide nanoparticles on vacuum annealing', *Journal of magnetism and magnetic materials*, 439, pp. 156–166.
31. Anvekar, T., Rajendra, V. and Kadam, H. (2017) 'Green synthesis of ZnO nano particles, its characterization and application', *Material science research India*, 14(2), pp. 153–157.
32. Apolinário, A. *et al.* (2014) 'Bottom-up nanofabrication using self-organized porous templates', *Journal of physics. Conference series*, 534(1), p. 012001.
33. Arbain, R., Othman, M. and Palaniandy, S. (2011) 'Preparation of iron oxide nanoparticles by mechanical milling', *Minerals engineering*, 24(1), pp. 1–9.
34. Armendariz, V. *et al.* (2004) 'Size controlled gold nanoparticle formation by Avena sativa

biomass: use of plants in nanobiotechnology', *Journal of nanoparticle research: an interdisciplinary forum for nanoscale science and technology*, 6(4), pp. 377–382.

35. Arsiya, F., Sayadi, M.H. and Sobhani, S. (2017) 'Green synthesis of palladium nanoparticles using Chlorella vulgaris', *Materials letters*, 186, pp. 113–115.
36. Asha, K.S. *et al.* (2015) 'Extracellular synthesis of silver nanoparticles from a marine alga, Sargassum polycystum C. Agardh and their biopotentials', *World J Pharm Pharm Sci.*, 4(9), pp. 1388–1400.
37. Ashour, A.F., El-Awady, A.T. and Tawfik, M.A. (2022) 'Numerical investigation on the thermal performance of a flat plate solar collector using ZnO & CuO water nanofluids under Egyptian weathering conditions', *Energy*, 240, p. 122743.
38. Asiya, S.I. and Pal, K. (2022) 'Introduction of ZnO nanomaterial integration nanospikes to nanocombs dispersed into HBLCs phase transition and novel switching', in *Functional Materials Processing for Switchable Device Modulation*. Elsevier, pp. 3–22.
39. Asmathunisha, N. and Kathiresan, K. (2013) 'A review on biosynthesis of nanoparticles by marine organisms', *Colloids and surfaces. B, Biointerfaces*, 103, pp. 283–287.
40. Aspoukeh, P.K., Barzinjy, A.A. and Hamad, S.M. (2022) 'Synthesis, properties and uses of ZnO nanorods: a mini review', *International Nano Letters*, 12(2), pp. 153–168.
41. Aziz, N. *et al.* (2015) 'Facile Algae-Derived Route to Biogenic Silver Nanoparticles: Synthesis, Antibacterial, and Photocatalytic Properties', *Langmuir: the ACS journal of surfaces and colloids*, 31(42), pp. 11605–11612.
42. Azizi, S. *et al.* (2014) 'Green biosynthesis and characterization of zinc oxide nanoparticles using brown marine macroalga Sargassum muticum aqueous extract', *Materials letters*, 116, pp. 275–277.
43. Azizi, S. *et al.* (2015) 'Facile biosynthesis and characterization of palm pollen stabilized ZnO nanoparticles', *Materials letters*, 148, pp. 106–109.
44. Azizi, S. *et al.* (2016) 'Effect of annealing temperature on antimicrobial and structural properties of bio-synthesized zinc oxide nanoparticles using flower extract of Anchusa italica', *Journal of photochemistry and photobiology. B, Biology*, 161, pp. 441–449.
45. Baker, S. *et al.* (2013) 'Marine microbes: Invisible nanofactories', *Journal of pharmacy research*, 6(3), pp. 383–388.
46. Bala, N. *et al.* (2015) 'Green synthesis of zinc oxide nanoparticles using Hibiscus subdariffa leaf extract: effect of temperature on synthesis, anti-bacterial activity and anti-diabetic activity', *RSC advances*, 5(7), pp. 4993–5003.

47. Bandeira, M. *et al.* (2020) 'Green synthesis of zinc oxide nanoparticles: A review of the synthesis methodology and mechanism of formation', *Sustainable Chemistry and Pharmacy*, 15, p. 100223.
48. Bar, H. *et al.* (2009) 'Green synthesis of silver nanoparticles using latex of Jatropha curcas', *Colloids and surfaces. A, Physicochemical and engineering aspects*, 339(1), pp. 134–139.
49. Barsanti, L. and Gualtieri, P. (2014) *Algae: Anatomy, Biochemistry, and Biotechnology, Second Edition*. CRC Press.
50. Barwal, I. *et al.* (2011) 'Cellular oxido-reductive proteins of Chlamydomonas reinhardtii control the biosynthesis of silver nanoparticles', *Journal of nanobiotechnology*, 9, p. 56.
51. Basera, P. *et al.* (2019) 'Analytical Investigation of Cymbopogon citratus and Exploiting the Potential of Developed Silver Nanoparticle Against the Dominating Species of Pathogenic Bacteria', *Frontiers in microbiology*, 10, p. 282.
52. Basnet, P. *et al.* (2018) 'A review on bio-synthesized zinc oxide nanoparticles using plant extracts as reductants and stabilizing agents', *Journal of photochemistry and photobiology. B, Biology*, 183, pp. 201–221.
53. Bayrami, A. *et al.* (2018) 'Bio-extract-mediated ZnO nanoparticles: microwave-assisted synthesis, characterization and antidiabetic activity evaluation', *Artificial cells, nanomedicine, and biotechnology* , 46(4), pp. 730–739.
54. Bayrami, A., Alioghli, S., *et al.* (2019) 'A facile ultrasonic-aided biosynthesis of ZnO nanoparticles using Vaccinium arctostaphylos L. leaf extract and its antidiabetic, antibacterial, and oxidative activity evaluation', *Ultrasonics sonochemistry*, 55, pp. 57–66.
55. Bayrami, A., Ghorbani, E., *et al.* (2019) 'Enriched zinc oxide nanoparticles by Nasturtium officinale leaf extract: Joint ultrasound-microwave-facilitated synthesis, characterization, and implementation for diabetes control and bacterial inhibition', *Ultrasonics sonochemistry*, 58, p. 104613.
56. Begum, S., Ahmaruzzaman and Adhikari, P.P. (2018) 'Ecofriendly bio-synthetic route to synthesize ZnO nanoparticles using Eryngium foetidum L. and their activity against pathogenic bacteria', *Materials letters*, 228, pp. 37–41.
57. Behera, O. (2011) *Synthesis and Characterization of ZnO nanoparticles of various sizes and Applications in Biological systems*. ethesis.nitrkl.ac.in.
58. Bhattacharya, D. *et al.* (2019) 'Visible light driven degradation of brilliant green dye using titanium based ternary metal oxide photocatalyst', *Results in Physics*, 12, pp. 1850–1858.

59. Bhaviripudi, S. *et al.* (2010) 'Role of kinetic factors in chemical vapor deposition synthesis of uniform large area graphene using copper catalyst', *Nano letters*, 10(10), pp. 4128–4133.
60. Bhunia, A.K. *et al.* (2016) *Morphological Properties and Raman Spectroscopy of ZnO Nanorods*, 21. pp.111-118.
61. Borah, D. *et al.* (2020) 'Alga mediated facile green synthesis of silver nanoparticles: Photophysical, catalytic and antibacterial activity', *Applied organometallic chemistry*, 34(5), p. 852.
62. Brayner, R. *et al.* (2009) 'Photosynthetic microorganism-mediated synthesis of akaganeite (beta-FeOOH) nanorods', *Langmuir: the ACS journal of surfaces and colloids*, 25(17), pp. 10062–10067.
63. Brazuna, L.P. *et al.* (2019) 'Effect of lithium and sodium ions on the size and morphology of ZnO nanoparticles synthesized by a glycerol–urea route', *New journal of chemistry = Nouveau journal de chimie*, 43(48), pp. 18988–18995.
64. Buazar, F. *et al.* (2016) 'Potato extract as reducing agent and stabiliser in a facile green one-step synthesis of ZnO nanoparticles', *Journal of Experimental Nanoscience*, 11(3), pp. 175–184.
65. Carballo, J.A. *et al.* (2008) 'Phosphorylation of the axial element protein Hop1 by Mec1/Tel1 ensures meiotic interhomolog recombination', *Cell*, 132(5), pp. 758–770.
66. Chandran, S.P. *et al.* (2006) 'Synthesis of gold nanotriangles and silver nanoparticles using Aloe vera plant extract', *Biotechnology progress*, 22(2), pp. 577–583.
67. Chaudhuri, S.K. and Malodia, L. (2017) 'Biosynthesis of zinc oxide nanoparticles using leaf extract of Calotropis gigantea: characterization and its evaluation on tree seedling growth in nursery stage', *Applied Nanoscience*, 7(8), pp. 501–512.
68. Chauhan, A.K., Kataria, N. and Garg, V.K. (2020) 'Green fabrication of ZnO nanoparticles using Eucalyptus spp. leaves extract and their application in wastewater remediation', *Chemosphere*, 247, p. 125803.
69. Chemingui, H. *et al.* (2019) 'Facile green synthesis of zinc oxide nanoparticles (ZnO NPs): antibacterial and photocatalytic activities', *Materials Research Express*, 6(10), p. 1050b4.
70. Chen, F. and Jiang, Y. (2013) *Algae and their Biotechnological Potential*. Springer Science & Business Media.
71. Chen, G. *et al.* (2023) 'Preparation and performance of epoxy resin-based thermal conductive composites with different morphologies of ZnO', *Journal of Sol-Gel Science and Technology* [Preprint].

72. Cheng, W. *et al.* (2016) 'Etching synthesis of iron oxide nanoparticles for adsorption of arsenic from water', *RSC advances*, 6(19), pp. 15900–15910.
73. Chisti, Y. (2007) 'Biodiesel from microalgae', *Biotechnology advances*, 25(3), pp. 294–306.
74. Chisti, Y. (2008) 'Biodiesel from microalgae beats bioethanol', *Trends in biotechnology*, 26(3), pp. 126–131.
75. Chisti, Y. and Moo-Young, M. (1986) 'Disruption of microbial cells for intracellular products', *Enzyme and microbial technology*, 8(4), pp. 194–204.
76. Chittora, D. *et al.* (2020) 'Cyanobacteria as a source of biofertilizers for sustainable agriculture', *Biochemistry and biophysics reports*, 22, p. 100737.
77. D'Amato, R. *et al.* (2013) 'Synthesis of ceramic nanoparticles by laser pyrolysis: From research to applications', *Journal of analytical and applied pyrolysis*, 104, pp. 461–469.
78. Dahoumane, S.A. *et al.* (2012) 'Recycling and adaptation of Klebsormidium flaccidum microalgae for the sustained production of gold nanoparticles', *Biotechnology and bioengineering*, 109(1), pp. 284–288.
79. Dahoumane, S.A. *et al.* (2012) 'Species selection for the design of gold nanobioreactor by photosynthetic organisms', *Journal of nanoparticle research: an interdisciplinary forum for nanoscale science and technology*, 14(6), p. 883.
80. Dahoumane, S.A. *et al.* (2016) 'Microalgae: An outstanding tool in nanotechnology', *Bionatura*, 1(4).
81. Dahoumane, S.A., Wujcik, E.K. and Jeffryes, C. (2016) 'Noble metal, oxide and chalcogenide-based nanomaterials from scalable phototrophic culture systems', *Enzyme and microbial technology*, 95, pp. 13–27.
82. Darvishi, E., Kahrizi, D. and Arkan, E. (2019) 'Comparison of different properties of zinc oxide nanoparticles synthesized by the green (using Juglans regia L. leaf extract) and chemical methods', *Journal of molecular liquids*, 286, p. 110831.
83. Davar, F., Majedi, A. and Mirzaei, A. (2015) 'Green synthesis of ZnO nanoparticles and its application in the degradation of some dyes', *Journal of the American Ceramic Society*, 98(6), pp. 1739–1746.
84. de Aragão, A.P. *et al.* (2019) 'Green synthesis of silver nanoparticles using the seaweed Gracilaria birdiae and their antibacterial activity', *Arabian Journal of Chemistry*, 12(8), pp. 4182–4188.
85. Decremps, F. *et al.* (2001) 'Pressure-induced softening of shear modes in ZnO', *Physical review. B, Condensed matter*, 63(22), p. 224105.

86. Demirbas, A. (2009) ‘Agricultural based activated carbons for the removal of dyes from aqueous solutions: a review’, *Journal of hazardous materials*, 167(1-3), pp. 1–9.
87. Demissie, M.G. *et al.* (2020) ‘Synthesis of Zinc Oxide Nanoparticles Using Leaf Extract of Lippia adoensis (Koseret) and Evaluation of Its Antibacterial Activity’, *Journal of chemistry and chemical engineering*, 2020.
88. Devi, J.S. and Bhimba, B.V. (2012) ‘Anticancer Activity of Silver Nanoparticles Synthesized by the Seaweed Ulva lactuca Invitro’, *Sci. Rep.*, 1(4), p. 242.
89. Devi, J.S., Bhimba, B.V. and Ratnam, K. (2012) ‘In vitro anticancer activity of silver nanoparticles synthesized using the extract of Gelidiella sp’, *International journal of pharmacy and pharmaceutical sciences*, 4(4), pp. 710–715.
90. Dhanemozhi, A.C., Rajeswari, V. and Sathyajothi, S. (2017) ‘Green Synthesis of Zinc Oxide Nanoparticle Using Green Tea Leaf Extract for Supercapacitor Application’, *Materials Today: Proceedings*, 4(2, Part A), pp. 660–667.
91. Dhas, T.S. *et al.* (2014) ‘Facile synthesis of silver chloride nanoparticles using marine alga and its antibacterial efficacy’, *Spectrochimica acta. Part A, Molecular and biomolecular spectroscopy*, 120(C), pp. 416–420.
92. Diallo, A. *et al.* (2015) ‘Green synthesis of ZnO nanoparticles by Aspalathus linearis: Structural & optical properties’, *Journal of alloys and compounds*, 646, pp. 425–430.
93. Do, D.N. *et al.* (2021) ‘Fractionating of Lemongrass (Cymbopogon citratus) Essential Oil by Vacuum Fractional Distillation’, *Processes*, 9(4), p. 593.
94. Dobrucka, R., Dlugaszewska, J. and Kaczmarek, M. (2017) ‘Cytotoxic and antimicrobial effects of biosynthesized ZnO nanoparticles using of Chelidonium majus extract’, *Biomedical microdevices*, 20(1), p. 5.
95. Dubey, M., Bhadauria, S. and Kushwah, B.S. (2009) *Green synthesis of nanosilver particles from extract of eucalyptus hybrida (safeda) leaf.*
96. Dubey, S.P., Lahtinen, M. and Sillanpää, M. (2010) ‘Tansy fruit mediated greener synthesis of silver and gold nanoparticles’, *Process Biochemistry*, 45(7), pp. 1065–1071.
97. Dutta, A.K., Maji, S.K. and Adhikary, B. (2014) ‘γ-Fe2O3 nanoparticles: An easily recoverable effective photo-catalyst for the degradation of rose bengal and methylene blue dyes in the waste-water treatment plant’, *Materials research bulletin*, 49, pp. 28–34.
98. Duvauchelle, V., Meffre, P. and Benfodda, Z. (2023) ‘Green methodologies for the synthesis of 2-aminothiophene’, *Environmental chemistry letters*, 21(1), pp. 597–621.
99. Ebadi, M. *et al.* (2019) ‘A bio-inspired strategy for the synthesis of zinc oxide nanoparticles (ZnO NPs) using the cell extract of cyanobacterium Nostoc sp. EA03: from

biological function to toxicity evaluation', *RSC advances*, 9(41), pp. 23508–23525.

100. Elavarasan, N. *et al.* (2017) 'Evaluation of photocatalytic activity, antibacterial and cytotoxic effects of green synthesized ZnO nanoparticles by Sechium edule leaf extract', *Research on Chemical Intermediates*, 43(5), pp. 3361–3376.

101. Ellmer, K. and Bikowski, A., 2016. Intrinsic and extrinsic doping of ZnO and ZnO alloys. *Journal of Physics D: Applied Physics*, *49*(41), p.413002.

102. El-Rafie, H.M., El-Rafie, M.H. and Zahran, M.K. (2013) 'Green synthesis of silver nanoparticles using polysaccharides extracted from marine macro algae', *Carbohydrate polymers*, 96(2), pp. 403–410.

103. El-Said, W.A. *et al.* (2014) 'Synthesis of metal nanoparticles inside living human cells based on the intracellular formation process', *Advanced materials* , 26(6), pp. 910–918. *Applied surface science*, 345, pp. 329–336.

104. Elumalai, S., Santhose, B.I. and Devika, R. (2013) 'Collection, isolation, identification, and biosynthesis of silver nanoparticles using microalga Chlorella pyrenoidosa', *Nanomechanics Sci Technol Int J*, 4(1), pp. 59–66.

105. Eroglu, E. *et al.* (2012) 'Biogenic production of palladium nanocrystals using microalgae and their immobilization on chitosan nanofibers for catalytic applications', *RSC advances*, 3(4), pp. 1009–1012.

106. Espitia, P.J.P. *et al.* (2012) 'Zinc oxide nanoparticles: Synthesis, antimicrobial activity and food packaging applications', *Food and Bioprocess Technology*, 5(5), pp. 1447–1464.

107. Ezealisiji, K.M. *et al.* (2019) 'Green synthesis of zinc oxide nanoparticles using Solanum torvum (L) leaf extract and evaluation of the toxicological profile of the ZnO nanoparticles–hydrogel composite in Wistar albino rats', *International nano letters*, 9(2), pp. 99–107.

108. Fakhar-e-Alam, M. *et al.* (2014) 'Corrigendum: ZnO nanoparticles as drug delivery agent for photodynamic therapy (2014 Laser Phys. Lett. 11 025601)', *Laser Physics Letters*, p. 039501.

109. Fatimah, I., Pradita, R.Y. and Nurfalinda, A. (2016) 'Plant Extract Mediated of ZnO Nanoparticles by Using Ethanol Extract of Mimosa Pudica Leaves and Coffee Powder', *Procedia Engineering*, 148, pp. 43–48.

110. Fawcett, D., Verduin, J.J., Shah, M., Sharma, S.B. and Poinern, G.E.J., 2017. A review of current research into the biogenic synthesis of metal and metal oxide nanoparticles via marine algae and seagrasses. *Journal of Nanoscience*, *2017*.

111. Fowsiya, J. *et al.* (2016) 'Photocatalytic degradation of Congo red using Carissa edulis

extract capped zinc oxide nanoparticles', *Journal of photochemistry and photobiology. B, Biology*, 162, pp. 395–401.

112. Gandhi, P.R. *et al.* (2017) 'Acaricidal, pediculicidal and larvicidal activity of synthesized ZnO nanoparticles using Momordica charantia leaf extract against blood feeding parasites', *Experimental parasitology*, 181, pp. 47–56.
113. Ganesan, V. *et al.* (2020) 'Periconium sp. (endophytic fungi) extract mediated sol-gel synthesis of ZnO nanoparticles for antimicrobial and antioxidant applications', *Materials Science in Semiconductor Processing*, 105, p. 104739.
114. Gao, S. *et al.* (2019) 'Creation of passivated Nb/N p-n co-doped ZnO nanoparticles and their enhanced photocatalytic performance under visible light illumination', *Journal of Materials Science & Technology*, 35(4), pp. 610–614.
115. Garg, R., Gupta, R. and Bansal, A. (2021) 'Degradation mechanism, reaction pathways and kinetics for the mineralization of Bisphenol A using hybrid ZnO/graphene oxide nano-catalysts', *The Korean journal of chemical engineering*, 38(3), pp. 485–497.
116. Gawade, V.V. *et al.* (2017) 'Green synthesis of ZnO nanoparticles by using Calotropis procera leaves for the photodegradation of methyl orange', *Journal of Materials Science: Materials in Electronics*, 28(18), pp. 14033–14039.
117. Gharpure, S., Yadwade, R. and Ankamwar, B. (2022) 'Non-antimicrobial and Non-anticancer Properties of ZnO Nanoparticles Biosynthesized Using Different Plant Parts of Bixa orellana', *ACS omega*, 7(2), pp. 1914–1933.
118. Ghodake, G.S. *et al.* (2010) 'Pear fruit extract-assisted room-temperature biosynthesis of gold nanoplates', *Colloids and surfaces. B, Biointerfaces*, 75(2), pp. 584–589.
119. Ghorbani, H.R., 2014. A review of methods for synthesis of Al nanoparticles. *Orient. J. chem*, *30*(4), pp.1941-1949.
120. Gnanakani, P.E. *et al.* (2019) 'Nannochloropsis Extract–Mediated Synthesis of Biogenic Silver Nanoparticles, Characterization and In Vitro Assessment of Antimicrobial, Antioxidant and Cytotoxic Activities', *Asian Pacific Journal of Cancer Prevention*, pp. 2353–2364.
121. González-Ballesteros, N. *et al.* (2017) 'Green synthesis of gold nanoparticles using brown algae Cystoseira baccata: Its activity in colon cancer cells', *Colloids and surfaces. B, Biointerfaces*, 153, pp. 190–198.
122. Govindaraju, K. *et al.* (2008) 'Silver, gold and bimetallic nanoparticles production using single-cell protein (Spirulina platensis) Geitler', *Journal of Materials Science*, 43(15), pp. 5115–5122.

123. Govindaraju, K. *et al.* (2009) 'Extracellular synthesis of silver nanoparticles by a marine alga, Sargassum wightii Grevilli and their antibacterial effects', *Journal of nanoscience and nanotechnology*, 9(9), pp. 5497–5501.
124. Govindaraju, K. *et al.* (2015) 'Green synthesis of silver nanoparticles for selective toxicity towards cancer cells', *IET nanobiotechnology / IET*, 9(6), pp. 325–330.
125. Gunalan, S., Sivaraj, R. and Rajendran, V. (2012) 'Green synthesized ZnO nanoparticles against bacterial and fungal pathogens', *Progress in Natural Science: Materials International*, 22(6), pp. 693–700.
126. Gupta, M. *et al.* (2018) 'Effective Antimicrobial Activity of Green ZnO Nano Particles of Catharanthus roseus', *Frontiers in microbiology*, 9, p. 2030.
127. Gurbandurdyyev, G. *et al.* (2023) 'Robust, conformal ZnO coatings on fabrics via atmospheric-pressure spatial atomic layer deposition with in-situ thickness control', *ChemNanoMat: chemistry of nanomaterials for energy, biology and more* [Preprint]
128. Gurentsov, E.V., Eremin, A.V. and Schulz, C. (2007) 'Formation of carbon nanoparticles by the condensation of supersaturated atomic vapor obtained by the laser photolysis of C3O2', *Kinetics and Catalysis*, 48, pp. 194–203.
129. Gurusamy, S. *et al.* (2019) 'Environmental friendly synthesis of TiO2-ZnO nanocomposite catalyst and silver nanomaterials for the enhanced production of biodiesel from Ulva lactuca seaweed and potential antimicrobial properties against the microbial pathogens', *Journal of photochemistry and photobiology. B, Biology*, 193, pp. 118–130.
130. Guzmán, M.G., Dille, J. and Godet, S. (2009) 'Synthesis of silver nanoparticles by chemical reduction method and their antibacterial activity', *International Journal of Chemical and Biomolecular Engineering*, 2(3), pp. 104–111.
131. Hameed, S., Khalil, A.T., Ali, M., Numan, M., Khamlich, S., Shinwari, Z.K. and Maaza, M., 2019. Greener synthesis of ZnO and Ag–ZnO nanoparticles using Silybum marianum for diverse biomedical applications. *Nanomedicine*, *14*(6), pp.655-673.
132. Hashemi, S. *et al.* (2016) 'Green synthesis of ZnO nanoparticles by Olive (Olea europaea)', *IET nanobiotechnology / IET*, 10(6), pp. 400–404.
133. Hassan, S.S.M. *et al.* (2015) 'Green synthesis and characterization of ZnO nanoparticles for photocatalytic degradation of anthracene', *Advances in Natural Sciences: Nanoscience and Nanotechnology*, 6(4), p. 045012.
134. Haverkamp, R.G. and Marshall, A.T. (2009) 'The mechanism of metal nanoparticle formation in plants: limits on accumulation', *Journal of nanoparticle research: an interdisciplinary forum for nanoscale science and technology*, 11(6), pp. 1453–1463.

135. He, W. *et al.* (2018) 'Thermal conversion of primary alcohols to disulfides via xanthate intermediates: an extension to the Chugaev elimination', *Organic & biomolecular chemistry*, 16(10), pp. 1659–1666.
136. He, Y. *et al.* (2017) 'Green synthesis of silver nanoparticles using seed extract of Alpinia katsumadai, and their antioxidant, cytotoxicity, and antibacterial activities', *RSC advances*, 7(63), pp. 39842–39851.
137. Herrera-Becerra, R. *et al.* (2008) 'Electron microscopy characterization of biosynthesized iron oxide nanoparticles', *Applied Physics A: Materials Science & Processing*, 91(2), pp. 241–246.
138. Heyman, H.M. and Meyer, J.J.M. (2012) 'NMR-based metabolomics as a quality control tool for herbal products', *South African journal of botany: official journal of the South African Association of Botanists = Suid-Afrikaanse tydskrif vir plantkunde: amptelike tydskrif van die Suid-Afrikaanse Genootskap van Plantkundiges*, 82, pp. 21–32.
139. Hijazi, I. and Xie, R. (2022) 'Study of the Piezoelectric Properties of UV-Selective Optically Transparent Zn(O,S) Based Solar Cells', *ASME 2022 16th International Conference on Energy Sustainability collocated with the ASME 2022 Heat Transfer Summer Conference*, p. V001T10A005.
140. Huang, J. *et al.* (2007) 'Biosynthesis of silver and gold nanoparticles by novel sundried Cinnamomum camphora leaf', *Nanotechnology*, 18(10), p. 105104.
141. Hulkoti, N.I. and Taranath, T.C. (2014) 'Biosynthesis of nanoparticles using microbes—A review', *Colloids and surfaces. B, Biointerfaces*, 121, pp. 474–483.
142. Husain, S. *et al.* (2020) 'Corrigendum to "Cyanobacteria as a bioreactor for synthesis of silver nanoparticles-an effect of different reaction conditions on the size of nanoparticles and their dye decolorization ability", *Journal of microbiological methods*, 168, p. 105764.
143. Husain, S., Sardar, M. and Fatma, T. (2015) 'Screening of cyanobacterial extracts for synthesis of silver nanoparticles', *World journal of microbiology & biotechnology*, 31(8), pp. 1279–1283.
144. Hussain, A. *et al.* (2019) 'Biogenesis of ZnO nanoparticles using Pandanus odorifer leaf extract: anticancer and antimicrobial activities', *RSC advances*, 9(27), pp. 15357–15369.
145. Ibraheem, I., AbdElaziz, B. and Saad, W.F. (2016) 'Green biosynthesis of silver nanoparticles using marine Red Algae Acanthophora specifera and its antimicrobial activity', *J Nanomed Nanotech*, 7(6), pp. 1–4.
146. Indramahalakshmi, G. (2017) 'Characterization and Antibacterial Activity of Zinc Oxide Nanoparticles Synthesized Using Opuntia ficus indica Fruit Aqueous Extract', *Asian*

Journal of Physical and Chemical Sciences, pp. 1–7.

147. Ingham, B. (2015) 'X-ray scattering characterisation of nanoparticles', *Crystallography Reviews*, 21(4), pp. 229–303.

148. Iravani, S. (2011) 'Green synthesis of metal nanoparticles using plants', *Green chemistry: an international journal and green chemistry resource: GC*, 13(10), pp. 2638–2650.

149. Ishwarya, R. *et al.* (2018) 'Facile green synthesis of zinc oxide nanoparticles using Ulva lactuca seaweed extract and evaluation of their photocatalytic, antibiofilm and insecticidal activity', *Journal of photochemistry and photobiology. B, Biology*, 178, pp. 249–258.

150. Jafarirad, S. *et al.* (2016) 'Biofabrication of zinc oxide nanoparticles using fruit extract of Rosa canina and their toxic potential against bacteria: A mechanistic approach', *Materials science & engineering. C, Materials for biological applications*, 59, pp. 296–302.

151. Jaffri, S.B. and Ahmad, K.S. (2019) 'Neoteric environmental detoxification of organic pollutants and pathogenic microbes via green synthesized ZnO nanoparticles', *Environmental technology*, 40(28), pp. 3745–3761.

152. Jain, D. et al. (2020) 'Microbial Fabrication of Zinc Oxide Nanoparticles and Evaluation of Their Antimicrobial and Photocatalytic Properties', Frontiers in chemistry, 8, p. 778.

153. Janaki, A.C., Sailatha, E. and Gunasekaran, S. (2015) 'Synthesis, characteristics and antimicrobial activity of ZnO nanoparticles', *Spectrochimica acta. Part A, Molecular and biomolecular spectroscopy*, 144, pp. 17–22.

154. Jayarambabu, N., Rao, K.V. and Rajendar, V. (2018) 'Biogenic synthesis, characterization, acute oral toxicity studies of synthesized Ag and ZnO nanoparticles using aqueous extract of Lawsonia inermis', *Materials letters*, 211, pp. 43–47.

155. Jeffryes, C., Agathos, S.N. and Rorrer, G. (2015) 'Biogenic nanomaterials from photosynthetic microorganisms', *Current opinion in biotechnology*, 33, pp. 23–31.

156. Jena, J. *et al.* (2012) 'Biosynthesis and characterization of silver nanoparticles using microalga Chlorococcum humicola and its antibacterial activity', *International Journal of Nanomaterials and Biostructures*, 3(1), pp. 1–8.

157. Jena, J. *et al.* (2014) 'Microalga Scenedesmus sp.: A potential low-cost green machine for silver nanoparticle syntheses, *Journal of microbiology and biotechnology*, 24(4), pp. 522–533.

158. Jena, J. *et al.* (2015) 'Biological sequestration and retention of cadmium as CdS nanoparticles by the microalga Scenedesmus-24', *Journal of applied phycology*, 27(6), pp. 2251–2260.

159. Jha, A.K. and Prasad, K. (2010) 'Green Synthesis of Silver Nanoparticles Using Cycas

Leaf', *International Journal of Green Nanotechnology: Physics and Chemistry*, 1(2), pp. P110–P117.

160. Jia, L. *et al.* (2009) 'The biosynthesis of palladium nanoparticles by antioxidants in Gardenia jasminoides Ellis: long lifetime nanocatalysts for p-nitrotoluene hydrogenation', *Nanotechnology*, 20(38), p. 385601.

161. Kalabegishvili, T.L. and Kirkesali, E.I. (2012) 'Synthesis of gold nanoparticles by some strains of Arthrobacter genera', *Proceedings of the Institution of Mechanical Engineers, Part L: Journal of Materials: Design and Applications*, 7, pp. 1–7.

162. Kannan, R.R.R. *et al.* (2013) 'Green synthesis of silver nanoparticles using marine macroalga Chaetomorpha linum', *Applied Nanoscience*, 3(3), pp. 229–233.

163. Kannan, R.R.R., Stirk, W.A. and Van Staden, J., 2013. Synthesis of silver nanoparticles using the seaweed Codium capitatum PC Silva (Chlorophyceae). *South African Journal of Botany*, *86*, pp.1-4.

164. Karimi, N. *et al.* (2018) 'Enhancing the secondary metabolite and anticancer activity of Echinacea purpurea callus extracts by treatment with biosynthesized ZnO nanoparticles', *Advances in Natural Sciences Nanoscience and Nanotechnology*, 9(4), p. 045009.

165. Karthik, S. *et al.* (2017) 'Acalypha indica–mediated green synthesis of ZnO nanostructures under differential thermal treatment: Effect on textile coating, hydrophobicity, UV resistance, and antibacterial activity', *Advanced Powder Technology*, 28(12), pp. 3184–3194.

166. Kasthuri, J., Veerapandian, S. and Rajendiran, N. (2009) 'Biological synthesis of silver and gold nanoparticles using apiin as reducing agent', *Colloids and surfaces. B, Biointerfaces*, 68(1), pp. 55–60.

167. Kathiraven, T. *et al.* (2015) 'Green synthesis of silver nanoparticles using marine algae Caulerpa racemosa and their antibacterial activity against some human pathogens', *Applied Nanoscience*, 5(4), pp. 499–504.

168. Kaur, R. *et al.* (2023) 'A high-performance Calix@ ZnO based bifunctional nanomaterial for selective detection and degradation of toxic azinphos methyl in environmental samples', *Chemosphere* [Preprint].

169. Kaur, R., Goyal, D. and Agnihotri, S. (2021) 'Chitosan/PVA silver nanocomposite for butachlor removal: Fabrication, characterization, adsorption mechanism and isotherms', *Carbohydrate polymers*, 262, p. 117906.

170. Kavitha, S. *et al.* (2017) 'Synthesis and characterisation of zinc oxide nanoparticles using terpenoid fractions of Andrographis paniculata leaves', *International Nano Letters*, 7(2),

pp. 141–147.

171. Keat, C.L. *et al.* (2015) 'Biosynthesis of nanoparticles and silver nanoparticles', *Bioresources and Bioprocessing*, 2(1), p. 47.

172. Khalil, A.T. *et al.* (2017) 'Sageretia thea (Osbeck.) mediated synthesis of zinc oxide nanoparticles and its biological applications', *Nanomedicine* , 12(15), pp. 1767–1789.

173. Khan, I., Saeed, K. and Khan, I., 2017. Nanoparticles: Properties, applications and toxicities. *Arabian journal of chemistry*, *12*(7), pp.908-931.

174. Khan, M.M. *et al.* (2019) 'Phytogenic Synthesis of Band Gap-Narrowed ZnO Nanoparticles Using the Bulb Extract of Costus woodsonii', *BioNanoScience*, 9(2), pp. 334–344.

175. Khan, S.A. *et al.* (2018) 'Green synthesis of ZnO and Cu-doped ZnO nanoparticles from leaf extracts of Abutilon indicum, Clerodendrum infortunatum, Clerodendrum inerme and investigation of their biological and photocatalytic activities', *Materials science & engineering. C, Materials for biological applications*, 82, pp. 46–59.

176. Khan, Z.U.H. *et al.* (2019) 'Greener synthesis of zinc oxide nanoparticles using Trianthema portulacastrum extract and evaluation of its photocatalytic and biological applications', *Journal of photochemistry and photobiology. B, Biology*, 192, pp. 147–157.

177. Kharissova, O.V. *et al.* (2013) 'The greener synthesis of nanoparticles', *Trends in biotechnology*, 31(4), pp. 240–248.

178. Khatami, M. *et al.* (2018) 'Rectangular shaped zinc oxide nanoparticles: Green synthesis by Stevia and its biomedical efficiency', *Ceramics International*, 44(13), pp. 15596–15602.

179. Korbekandi, H., Iravani, S. and Abbasi, S. (2009) 'Production of nanoparticles using organisms', *Critical reviews in biotechnology*, 29(4), pp. 279–306.

180. Koupaei, M.H. *et al.* (2016) 'Green synthesis of zinc oxide nanoparticles and their effect on the stability and activity of proteinase K', *RSC advances*, 6(48), pp. 42313–42323.

181. Krishnaraj, C. *et al.* (2010) 'Synthesis of silver nanoparticles using Acalypha indica leaf extracts and its antibacterial activity against water borne pathogens', *Colloids and surfaces. B, Biointerfaces*, 76(1), pp. 50–56.

182. Król, A. *et al.* (2019) 'Phytochemical investigation of Medicago sativa L. extract and its potential as a safe source for the synthesis of ZnO nanoparticles: The proposed mechanism of formation and antimicrobial activity', *Phytochemistry letters*, 31, pp. 170–180.

183. Kumar, P. *et al.* (2013) 'Photocatalytic degradation of methyl orange dye using silver (Ag) nanoparticles synthesized from Ulva lactuca', *Colloids and surfaces. B, Biointerfaces*,

103, pp. 658–661.

184. Kumar, P., Selvi, S.S., *et al.* (2012) 'Antibacterial activity and in-vitro cytotoxicity assay against brine shrimp using silver nanoparticles synthesized from Sargassum ilicifolium', *Dig J Nanomater Biostruct*, 7(4), pp. 1447–1455.

185. Kumar, P., Senthamil Selvi, S. and Govindaraju, M. (2013) 'Seaweed-mediated biosynthesis of silver nanoparticles using Gracilaria corticata for its antifungal activity against Candida spp', *Applied Nanoscience*, 3(6), pp. 495–500.

186. Kumar, P., Senthamilselvi, S., *et al.* (2012) 'Efficacy of bio-synthesized silver nanoparticles using Acanthophora spicifera to encumber biofilm formation', *Dig J Nanomater Biostruct*, 7(2), pp. 511–522.

187. Kumar, P.P. *et al.* (2021) 'Synthesis of magnesium oxide nanoparticle by eco friendly method (green synthesis) – A review', *Materials Today: Proceedings*, pp. 3028–3030.

188. Lakshmi, U.R. *et al.* (2009) 'Rice husk ash as an effective adsorbent: evaluation of adsorptive characteristics for Indigo Carmine dye', *Journal of environmental management*, 90(2), pp. 710–720.

189. Lengke, M.F. *et al.* (2006) 'Mechanisms of gold bioaccumulation by filamentous cyanobacteria from gold (III)− chloride complex', *Science & technology in China*, 40(20), pp. 6304–6309.

190. Lengke, M.F., Fleet, M.E. and Southam, G. (2006) 'Synthesis of platinum nanoparticles by reaction of filamentous cyanobacteria with platinum(IV)-chloride complex', *Langmuir: the ACS journal of surfaces and colloids*, 22(17), pp. 7318–7323.

191. Lengke, M.F., Fleet, M.E. and Southam, G. (2007a) 'Biosynthesis of silver nanoparticles by filamentous cyanobacteria from a silver(I) nitrate complex', *Langmuir: the ACS journal of surfaces and colloids*, 23(5), pp. 2694–2699.

192. Lengke, M.F., Fleet, M.E. and Southam, G. (2007b) 'Synthesis of palladium nanoparticles by reaction of filamentous cyanobacterial biomass with a palladium(II) chloride complex', *Langmuir: the ACS journal of surfaces and colloids*, 23(17), pp. 8982–8987.

193. Li, X. *et al.* (2011) 'Biosynthesis of Nanoparticles by Microorganisms and Their Applications', *Journal of nanomaterials*, 2011, pp. 1–16.

194. Liqiang, J. *et al.* (2006) 'Effects of noble metal modification on surface oxygen composition, charge separation and photocatalytic activity of ZnO nanoparticles', *Journal of molecular catalysis. A, Chemical*, 244(1), pp. 193–200.

195. Liu, Y.C. *et al.* (2020) 'Biosynthesis of zinc oxide nanoparticles by one-pot green synthesis using fruit extract of Amomum longiligulare and its activity as a photocatalyst', *Optik*,

218, p. 165245.

196. Lu, J. *et al.* (2019) ‘Photocatalytic degradation of methylene blue using biosynthesized zinc oxide nanoparticles from bark extract of Kalopanax septemlobus’, *Optik*, 182, pp. 980–985.

197. Luangpipat, T. *et al.* (2011) ‘Gold nanoparticles produced in a microalga’, *Journal of nanoparticle research: an interdisciplinary forum for nanoscale science and technology*, 13, pp. 6439–6445.

198. Madhumitha, G. *et al.* (2019) ‘Green synthesis, characterization and antifungal and photocatalytic activity of Pithecellobium dulce peel–mediated ZnO nanoparticles’, *The Journal of physics and chemistry of solids*, 127, pp. 43–51.

199. Maensiri, S. *et al.* (2008) ‘Indium oxide (In2O3) nanoparticles using Aloe vera plant extract: Synthesis and optical properties’, *Journal of Optoelectronics and Advanced Materials*, 10(3), pp. 161–165.

200. Mahdavi, M. *et al.* (2013) ‘Green Biosynthesis and Characterization of Magnetic Iron Oxide (Fe3O4) Nanoparticles Using Seaweed (Sargassum muticum) Aqueous Extract’, *Molecules* , 18(5), pp. 5954–5964.

201. Mahdieh, M. *et al.* (2012) ‘Green biosynthesis of silver nanoparticles by Spirulina platensis’, *Scientia Iranica*, 19(3), pp. 926–929.

202. Mahlaule-Glory, L.M. *et al.* (2019) ‘ZnO nanoparticles via Sutherlandia frutescens plant extract: physical and biological properties’, *Materials research express*, 6(8), p. 085006.

203. Makarov, V.V., Love, A.J. and Sinitsyna, O.V. (2014) ‘“Green” nanotechnologies: synthesis of metal nanoparticles using plants’, *Acta naturae*, 6(1), pp. 35–44.

204. Malek Shahkouhi, A. and Motamedian, E. (2020) ‘Reconstruction of a regulated two-cell metabolic model to study biohydrogen production in a diazotrophic cyanobacterium Anabaena variabilis ATCC 29413’, *PloS one*, 15(1), p. e0227977.

205. Manzano, C.V., Philippe, L. and Serrà, A. (2022) ‘Recent progress in the electrochemical deposition of ZnO nanowires: synthesis approaches and applications’, *Critical Reviews in Solid State and Materials Sciences*, 47(5), pp. 772–805.

206. Mata, Y.N. *et al.* (2009) ‘Gold(III) biosorption and bioreduction with the brown alga Fucus vesiculosus’, *Journal of hazardous materials*, 166(2), pp. 612–618.

207. Matsumura, Y. and Tarin, D. (2020) *Cancer Drug Delivery Systems Based on the Tumor Microenvironment*. Springer Nature.

208. Mayekar, Dhar and Radha (2013) ‘Role of salt precursor in the synthesis of zinc oxide nanoparticles’, *International journal of research in advance engineering*, 3(3), pp. 43–45.

209. Menon, S., S., R. and S., V.K. (2017) ‘A review on biogenic synthesis of gold nanoparticles, characterization, and its applications’, *Resource-Efficient Technologies*, 3(4), pp. 516–527.
210. Michalak, I. and Chojnacka, K. (2015) ‘Algae as production systems of bioactive compounds’, *Engineering in life sciences*, 15, pp. 160–176.
211. Migliorini, F.L. *et al.* (2016) ‘Efficiency study and mechanistic aspects in the Brilliant Green dye degradation using BDD/Ti electrodes’, *Diamond and related materials*, 65, pp. 5–12.
212. Mittal, A.K., Chisti, Y. and Banerjee, U.C. (2013) ‘Synthesis of metallic nanoparticles using plant extracts’, *Biotechnology advances*, 31(2), pp. 346–356.
213. Mochochoko, T. *et al.* (2013) ‘Green synthesis of silver nanoparticles using cellulose extracted from an aquatic weed; water hyacinth’, *Carbohydrate polymers*, 98(1), pp. 290–294.
214. Mohamad Sukri, S.N.A. *et al.* (2019) ‘Cytotoxicity and antibacterial activities of plant-mediated synthesized zinc oxide (ZnO) nanoparticles using Punica granatum (pomegranate) fruit peels extract’, *Journal of molecular structure*, 1189, pp. 57–65.
215. Mohammadi Arvanag, F. *et al.* (2019) ‘A comprehensive study on antidiabetic and antibacterial activities of ZnO nanoparticles biosynthesized using Silybum marianum L seed extract’, *Materials Science and Engineering: C*, 97, pp. 397–405.
216. Mohammadi-Aloucheh, R. *et al.* (2018) ‘Enhanced anti-bacterial activities of ZnO nanoparticles and ZnO/CuO nanocomposites synthesized using Vaccinium arctostaphylos L. fruit extract’, *Artificial cells, nanomedicine, and biotechnology* , 46(sup1), pp. 1200–1209.
217. Mohammed, Y.H.I. *et al.* (2023) ‘Green Synthesis of Zinc Oxide Nanoparticles Using Cymbopogon citratus Extract and Its Antibacterial Activity’, *ACS omega*, 8(35), pp. 32027–32042.
218. Mohseniazar, M. *et al.* (2011) ‘Potential of microalgae and lactobacilli in biosynthesis of silver nanoparticles’, *BioImpacts : BI*, 1(3), pp. 149–152.
219. Molina Grima, E. *et al.* (2003) ‘Recovery of microalgal biomass and metabolites: process options and economics’, *Biotechnology advances*, 20(7), pp. 491–515.
220. Mondal, S. *et al.* (2011) ‘Biogenic synthesis of Ag, Au and bimetallic Au/Ag alloy nanoparticles using aqueous extract of mahogany (Swietenia mahogani JACQ.) leaves’, *Colloids and surfaces. B, Biointerfaces*, 82(2), pp. 497–504.
221. Morkoç, H. and Özgür, Ü. (2008) *Zinc Oxide: Fundamentals, Materials and Device*

Technology. John Wiley & Sons.

222. Morozov, I.G. *et al.* (2015) 'Structural, optical, XPS and magnetic properties of Zn particles capped by ZnO nanoparticles', *Journal of alloys and compounds*, 633, pp. 237–245.

223. Motelica, L. *et al.* (2021) 'Antibacterial Biodegradable Films Based on Alginate with Silver Nanoparticles and Lemongrass Essential Oil-Innovative Packaging for Cheese', *Nanomaterials (Basel, Switzerland)*, 11(9). Available at: https://doi.org/10.3390/nano11092377.

224. MubarakAli, D. *et al.* (2012) 'Synthesis and characterization of CdS nanoparticles using C-phycoerythrin from the marine cyanobacteria', *Materials letters*, 74(Supplement C), pp. 8–11.

225. Mude, N. *et al.* (2009) 'Synthesis of Silver Nanoparticles Using Callus Extract of Carica papaya — A First Report', *Journal of plant biochemistry and biotechnology*, 18(1), pp. 83–86.

226. Mukherjee, P. *et al.* (2002) 'Extracellular synthesis of gold nanoparticles by the fungus Fusarium oxysporum', *Chembiochem: a European journal of chemical biology*, 3(5), pp. 461–463.

227. Mukherji, S., Ruparelia, J. and Agnihotri, S. (2012) 'Antimicrobial activity of silver and copper nanoparticles: variation in sensitivity across various strains of bacteria and fungi', *Nano-antimicrobials*, pp. 225–251.

228. Mula, S. *et al.* (2022) 'Structure–Property Relationship of Piezoelectric Properties in Zeolitic Imidazolate Frameworks: A Computational Study', *ACS applied materials & interfaces*, 14(45), pp. 50803–50814.

229. Murugesan, S., Elumalai, M. and Dhamotharan, R. (2011) 'Green synthesis of silver nano particles from marine alga Gracilaria edulis', *Biosci. Biotech. Res. Comm*, 4(1).

230. Nagarajan, S. and Arumugam Kuppusamy, K. (2013) 'Extracellular synthesis of zinc oxide nanoparticle using seaweeds of gulf of Mannar, India', *Journal of nanobiotechnology*, 11, p. 39.

231. Namvar, F. *et al.* (2015) 'Green synthesis and characterization of gold nanoparticles using the marine macroalgae Sargassum muticum', *Research on Chemical Intermediates*, 41(8), pp. 5723–5730.

232. Narayanan, K.B. and Sakthivel, N. (2008) 'Coriander leaf mediated biosynthesis of gold nanoparticles', *Materials letters*, 62(30), pp. 4588–4590.

233. Naseer, M. *et al.* (2020) 'Green route to synthesize Zinc Oxide Nanoparticles using leaf

extracts of Cassia fistula and Melia azadarach and their antibacterial potential', *Scientific reports*, 10(1), p. 9055.

234. Nath, D. and Banerjee, P. (2013) 'Green nanotechnology–A new hope for medical biology', *Environmental toxicology and pharmacology*, 36(3), pp. 997–1104.

235. Nath, D.C.D. and Sahajwalla, V. (2012) 'Analysis of Carbon Nanotubes Produced by Pyrolysis of Composite Film of Poly (Vinyl Alcohol) and Modified Fly Ash', *Materials Sciences and Applications*, pp. 103–109.

236. Nayak, S. *et al.* (2020) 'Two fold increase in synthesis of gold nanoparticles assisted by proteins and phenolic compounds in Pongamia seed cake extract: response surface methodology approach', *SN Applied Sciences*, 2(4), p. 634.

237. Oza, G. *et al.* (2012) 'Facile biosynthesis of gold nanoparticles exploiting optimum pH and temperature of fresh water algae Chlorella pyrenoidusa', *Adv Appl Sci Res*, 3(3), p. 1405.

238. Özgür, Ü., Avrutin, V. and Morkoç, H. (2018) 'Chapter 16 - Zinc Oxide Materials and Devices Grown by Molecular Beam Epitaxy', in M. Henini (ed.) *Molecular Beam Epitaxy (Second Edition)*. Elsevier, pp. 343–375.

239. Parashar, U.K., Saxena, P.S. and Srivastava, A., 2009. Bioinspired synthesis of silver nanoparticles. *Digest Journal of Nanomaterials & Biostructures (DJNB)*, *4*(1).

240. Parial, D. and Pal, R. (2015) 'Biosynthesis of monodisperse gold nanoparticles by green alga Rhizoclonium and associated biochemical changes', *Journal of applied phycology*, 27(2), pp. 975–984.

241. Parial, D. *et al.* (2012) 'Gold nanorod production by cyanobacteria—a green chemistry approach', *Journal of applied phycology*, 24(1), pp. 55–60.

242. Parial, D. *et al.* (2012) 'Screening of different algae for green synthesis of gold nanoparticles', *European journal of phycology*, 47(1), pp. 22–29.

243. Parveen, A. *et al.* (2022) 'Asparagus racemosus leaf extract mediated bioconversion of nickel sulfate into nickel/nickel hydroxide nanoparticles: in vitro catalytic, antibacterial, and antioxidant activities', *Biomass conversion and biorefinery* [Preprint].

244. Pathak, J. *et al.* (2019) 'Chapter 12 - Recent Developments in Green Synthesis of Metal Nanoparticles Utilizing Cyanobacterial Cell Factories', in D.K. Tripathi et al. (eds) *Nanomaterials in Plants, Algae and Microorganisms*. Academic Press, pp. 237–265.

245. Perez, J.V.D. *et al.* (2017) 'Response surface methodology as a powerful tool to optimize the synthesis of polymer-based graphene oxide nanocomposites for simultaneous removal of cationic and anionic heavy metal contaminants', *RSC advances*, 7(30), pp. 18480–

18490.

246. Philip, D. and Unni, C. (2011) 'Extracellular biosynthesis of gold and silver nanoparticles using Krishna tulsi (Ocimum sanctum) leaf', *Physica E: Low-dimensional Systems and Nanostructures*, 43(7), pp. 1318–1322.

247. Pinjarkar, H. *et al.* (2016) 'Phycofabrication of silver nanoparticles and their antibacterial activity against human pathogens', *Adv Mater Lett.*, 7(12), pp. 1010–1014.

248. Poinern, G.E.J. (2014) *A Laboratory Course in Nanoscience and Nanotechnology*. CRC Press.

249. Pourrahimi *et al.* (2014) 'Water-based synthesis and cleaning methods for high purity ZnO nanoparticles–comparing acetate, chloride, sulphate and nitrate zinc salt precursors', *RSC advances*, (4), pp. 35568–35577.

250. Prasad, B. and Padmesh, T. (2014) 'Seaweed (Sargassum ilicifolium) assisted green synthesis of palladium nanoparticles', *Int J Sci Eng Res*, 5(3), pp. 229–231.

251. Prasad, R., Pandey, R. and Barman, I. (2016) 'Engineering tailored nanoparticles with microbes: quo vadis?', *Wiley interdisciplinary reviews. Nanomedicine and nanobiotechnology*, 8(2), pp. 316–330.

252. Prasad, T.N.V.K., Kambala, V.S.R. and Naidu, R. (2013) 'Phyconanotechnology: synthesis of silver nanoparticles using brown marine algae Cystophora moniliformis and their characterisation', *Journal of applied phycology*, 25(1), pp. 177–182.

253. Prathna, T.C. *et al.* (2011) 'Biomimetic synthesis of silver nanoparticles by Citrus limon (lemon) aqueous extract and theoretical prediction of particle size', *Colloids and surfaces. B, Biointerfaces*, 82(1), pp. 152–159.

254. Priyadharshini, R.I., Prasannaraj, G. and Geetha, N. (2014) 'Microwave-mediated extracellular synthesis of metallic silver and zinc oxide nanoparticles using macro-algae (Gracilaria edulis) extracts and its anticancer activity against human PC3 cell lines', *Appl Biochem Biotechnol*, 174(8), pp. 2777–2790.

255. Qi, C. *et al.* (2020) 'Synthesis and application of magnetic materials-barium ferrite nanomaterial as an effective microwave catalyst for degradation of brilliant green', *Chemosphere*, 260, p. 127681.

256. Qu, J., Luo, C. and Hou, J. (2011) 'Synthesis of ZnO nanoparticles from Zn-hyperaccumulator (*Sedum alfredii* Hance) plants', *Micro & nano letters*, 6(3), pp. 174–176.

257. Quester, K., Avalos-Borja, M. and Castro-Longoria, E. (2013) 'Biosynthesis and microscopic study of metallic nanoparticles', *Micron* , 54-55, pp. 1–27.

258. Rachna, Rani, M. and Shanker, U. (2019) 'Sunlight active ZnO@FeHCF nanocomposite for the degradation of bisphenol A and nonylphenol', *Journal of environmental chemical engineering*, 7(3), p. 103153.
259. Rafique, M. et al. (2022) 'Plant-mediated green synthesis of zinc oxide nanoparticles from Syzygium Cumini for seed germination and wastewater purification', International journal of environmental analytical chemistry, 102(1), pp. 23–38.
260. Raghunandan, D. *et al.* (2009) 'Biosynthesis of Stable Polyshaped Gold Nanoparticles from Microwave-Exposed Aqueous Extracellular Anti-malignant Guava (Psidium guajava) Leaf Extract', *NanoBiotechnology*, 5(1), pp. 34–41.
261. Raghunandan, D. *et al.* (2010) 'Rapid biosynthesis of irregular shaped gold nanoparticles from macerated aqueous extracellular dried clove buds (Syzygium aromaticum) solution', *Colloids and surfaces. B, Biointerfaces*, 79(1), pp. 235–240.
262. Rahmah, M.I., Sabry, R.S. and Aziz, W.J. (2022) 'Preparation and Antibacterial Activity of Superhydrophobic Modified ZnO/PVC Nanocomposite', *Journal of bionic engineering*, 19(1), pp. 139–154.
263. Rahman, A. *et al.* (2010) 'Synthesis of copper oxide nano particles by usinG Phormidium cyanobacterium', *Indonesian Journal of Chemistry*, 9(3), pp. 355–360.
264. Raj, V.J. *et al.* (2022) 'Application of zinc oxide nanoflowers in environmental and biomedical science', *BBA advances*, 2, p. 100051.
265. Rajasulochana, P., Krishnamoorthy, P. and Dhamotharan, R. (2012) 'Potential application of Kappaphycus alvarezii in agricultural and pharmaceutical industry', *Journal of chemical and pharmaceutical research*, 4(1), pp. 33–37.
266. Rajathi, A.A.F. *et al.* (2012) 'Biosynthesis of antibacterial gold nanoparticles using brown alga, Stoechospermum marginatum (kützing)', *Spectrochimica acta. Part A, Molecular and biomolecular spectroscopy*, 99(Supplement C), pp. 166–173.
267. Rajesh, S. *et al.* (2012) 'Biosynthesis of silver nanoparticles using Ulva fasciata(Delile) ethyl acetate extract and its activity against Xanthomonas campestris pv. malvacearum', *J Biopest*, 5, pp. 119–128.
268. Rajeshkumar, S. *et al.* (2013) 'Antibacterial activity of algae mediated synthesis of gold nanoparticles from Turbinaria conoides', *Der Pharma Chemica*, 5(2), pp. 224–229.
269. Rajeshkumar, S. *et al.* (2013) 'Seaweed-mediated synthesis of gold nanoparticles using Turbinaria conoides and its characterization', 3(1), pp. 1–1.
270. Rajeshkumar, S. *et al.* (2014) 'Algae Mediated Green Fabrication of Silver Nanoparticles and Examination of Its Antifungal Activity against Clinical Pathogens', *International*

Journal of Metals, 2014, pp. 1–8.

271. Rajeshkumar, S., Kannan, C. and Annadurai, G. (2012) 'Green synthesis of silver nanoparticles using marine brown algae Turbinaria conoides and its antibacterial activity', *Int J Pharm Bio Sci*, 3(4), pp. 502–510.
272. Rajeshkumar, S., Kannan, C. and Annadurai, G. (2012) 'Synthesis and characterization of antimicrobial silver nanoparticles using marine brown seaweed Padina tetrastromatica', *Drug Invention Today*, 4(10), pp. 511–513.
273. Rakesh, S. *et al.* (2015) 'Cell disruption methods for improving lipid extraction efficiency in unicellular microalgae', *Engineering in life sciences*, 15(4), pp. 443–447.
274. Ramakrishna, M. *et al.* (2016) 'Green synthesis of gold nanoparticles using marine algae and evaluation of their catalytic activity', *J Nanostruct Chem*, 6(1), pp. 1–13.
275. Ramakrishnan, B. *et al.* (2010) 'The Impacts of Environmental Pollutants on Microalgae and Cyanobacteria', *Critical reviews in environmental science and technology*, 40(8), pp. 699–821.
276. Ramakrishnan, B. *et al.* (2023) 'Potential of microalgae and cyanobacteria in improving soil health and agricultural productivity--a critical view', *Environmental Science: Advances* [Preprint].
277. Rambabu, K. *et al.* (2019) 'Activated carbon from date seeds for chromium removal in aqueous solution', *Desalination and water treatment*, 156, pp. 267–277.
278. Rambabu, K. *et al.* (2021) 'Green synthesis of zinc oxide nanoparticles using Phoenix dactylifera waste as bioreductant for effective dye degradation and antibacterial performance in wastewater treatment', *Journal of hazardous materials*, 402, p. 123560.
279. Rao, K.J. *et al.* (2022) 'Biosynthesis and photocatalytic evaluation of ZnO nanoparticles using banana flower perianth', *Journal of cleaner production*, 380, p. 135180.
280. Ravindra, S. *et al.* (2010) 'Fabrication of antibacterial cotton fibres loaded with silver nanoparticles via "Green Approach"', *Colloids and surfaces. A, Physicochemical and engineering aspects*, 367(1), pp. 31–40.
281. Rehman, F. *et al.* (2018) 'Oxidative removal of brilliant green by UV/S2O82–, UV/HSO_5– and UV/H_2O_2 processes in aqueous media: a comparative study', *Journal of hazardous materials*.
282. Riyanto *et al.* (2022) 'Direct synthesis of lemongrass (Cymbopogon citratus L.) essential oil-silver nanoparticles (EO-AgNPs) as biopesticides and application for lichen inhibition on stones', *Heliyon*, 8(6), p. e09701.
283. Rodrigues, J.E.F.S. *et al.* (2022) 'Atomic Structure and Lattice Dynamics of CoSb3

Skutterudite-Based Thermoelectrics', *Chemistry of materials: a publication of the American Chemical Society*, 34(3), pp. 1213–1224.

284. Rolim, W.R. *et al.* (2019) 'Green tea extract mediated biogenic synthesis of silver nanoparticles: Characterization, cytotoxicity evaluation and antibacterial activity', *Applied surface science*, 463, pp. 66–74.

285. Roychoudhury, P. and Pal, R. (2014) 'Spirogyra submaxima–a green alga for nanogold production', *J Algal Biomass Utln*, 5(1), pp. 15–19.

286. Ryali, S. and Sanasi, P.D. (2018) 'Graphene oxide–nano-titania composites for efficient photocatalytic degradation of indigo carmine', *Journal of the Chinese Chemical Society*, 65(12), pp. 1423–1430.

287. Sa, N. *et al.* (2022) 'Anisotropy Engineering of ZnO Nanoporous Frameworks: A Lattice Dynamics Simulation', *Nanomaterials (Basel, Switzerland)*, 12(18).

288. Sahayaraj, K., Rajesh, S. and Rathi, J.M. (2012) 'Silver nanoparticles biosynthesis using marine alga Padina pavonica (linn.) and its microbicidal activity', *Dig J Nanomater Biostruct*, 7(4), pp. 1557–1567.

289. Sahoo, P.C. *et al.* (2014) 'Facile fabrication of silver nanoparticle embedded CaCO3 microspheres via microalgae-templated CO 2 biomineralization: application in antimicrobial paint application', *RSC advances*, 4, pp. 32562–32569.

290. Sailaja, A.K., Amareshwar, P. and P.Chakravarty. (2011) 'Formulation of solid lipid nanoparticles and their applications', *Journal of Current Pharma Research*, 1(2), pp. 197–203.

291. Salari, Z. *et al.* (2016) 'Sustainable synthesis of silver nanoparticles using macroalgae Spirogyra varians and analysis of their antibacterial activity', *J Saudi Chem Soc*, 20(4), pp. 459–464.

292. Saloga, P.E.J. and Thünemann, A.F. (2019) 'Microwave-Assisted Synthesis of Ultrasmall Zinc Oxide Nanoparticles', *Langmuir: the ACS journal of surfaces and colloids*, 35(38), pp. 12469–12482.

293. Sangeetha, G., Rajeshwari, S. and Venckatesh, R. (2011) 'Green synthesis of zinc oxide nanoparticles by aloe barbadensis miller leaf extract: Structure and optical properties', *Materials research bulletin*, 46(12), pp. 2560–2566.

294. Sangeetha., N. and Saravanan., K. (2014) 'Biogenic Silver Nanoparticles using Marine Seaweed (Ulva lactuca) and Evaluation of its Antibacterial activity', *J Nanosci Nanotechnol*, 2(1), pp. 99–102.

295. Sankar, R. *et al.* (2014) 'Green synthesis of colloidal copper oxide nanoparticles using

Carica papaya and its application in photocatalytic dye degradation', *Spectrochimica acta. Part A, Molecular and biomolecular spectroscopy*, 121, pp. 746–750.

296. Santos, L.F.T.F. *et al.* (2016) 'Effect of home-bleaching gels modified by calcium and/or fluoride and the application of nano-hydroxyapatite paste on in vitro enamel erosion susceptibility', *Acta odontologica Scandinavica*, 74(2), pp. 121–126.
297. ay, M. *et al.* (2003) 'Biosynthesis of metal nanoparticles using fungi and actinomycete', *Current science*, 85(2), pp. 162–170.
298. Satapathy, S. *et al.* (2015) 'Evaluation of the performance of an algal bioreactor for silver nanoparticle production', *Journal of applied phycology*, 27(1), pp. 285–291.
299. Säuberlich, F. *et al.* (2003) 'Properties of sputtered ZnO films and its interfaces with CdS', *Thin solid films*, 431-432, pp. 378–381.
300. Schröfel, A. *et al.* (2011) 'Biosynthesis of gold nanoparticles using diatoms—silica-gold and EPS-gold bionanocomposite formation', *Journal of nanoparticle research: an interdisciplinary forum for nanoscale science and technology*, 13(8), pp. 3207–3216.
301. Sekine, N. *et al.* (2009) 'ZnO nano-ridge structure and its application in inverted polymer solar cell', *Organic electronics*, 10(8), pp. 1473–1477.
302. Senapati, S. *et al.* (2012) 'Intracellular synthesis of gold nanoparticles using alga Tetraselmis kochinensis', *Materials letters*, 79, pp. 116–118.
303. Shabaani, M. *et al.* (2020) 'Green synthesis of ZnO nanoparticles using loquat seed extract; Biological functions and photocatalytic degradation properties', *LWT*, 134, p. 110133.
304. Shah, L.A. *et al.* (2019) 'TiO2 nanotubes doped poly(vinylidene fluoride) polymer membranes (PVDF/TNT) for efficient photocatalytic degradation of brilliant green dye', *Journal of Environmental Chemical Engineering*, 7(5), p. 103291.
305. Shah, M. *et al.* (2015) 'Green Synthesis of Metallic Nanoparticles via Biological Entities', *Materials*, 8(11), pp. 7278–7308.
306. Shakibaie, M. *et al.* (2010) 'Green synthesis of gold nanoparticles by the marine microalga Tetraselmis suecica', *Biotechnology and applied biochemistry*, 57(2), pp. 71–75.
307. Shankar, P.D. *et al.* (2016) 'A review on the biosynthesis of metallic nanoparticles (gold and silver) using bio-components of microalgae: Formation mechanism and applications', *Enzyme and microbial technology*, 95, pp. 28–44.
308. Shankar, S.S. *et al.* (2004) 'Rapid synthesis of Au, Ag, and bimetallic Au core-Ag shell nanoparticles using Neem (Azadirachta indica) leaf broth', *Journal of colloid and interface science*, 275(2), pp. 496–502.
309. Shankar, S.S. *et al.* (2005) 'Controlling the Optical Properties of Lemongrass Extract

Synthesized Gold Nanotriangles and Potential Application in Infrared-Absorbing Optical Coatings', *Chemistry of materials: a publication of the American Chemical Society*, 17(3), pp. 566–572.

310. Shanmugam, N. *et al.* (2016) 'Photocatalytic degradation of brilliant green using undoped and Zn doped SnO2 nanoparticles under sunlight irradiation', *Applied surface science*, 360, pp. 283–290.

311. Shanmugapriya, P., Thanuja, M.Y. and Anusuya, T. (2013) 'Biologically Prepared ZnO Nanoparticles for Effective Transparent Sunscreen Applications', *Asian Journal of Chemistry* 25.

312. Sharma, A. *et al.* (2016) 'Algae as crucial organisms in advancing nanotechnology: a systematic review', *Journal of applied phycology*, 28(3), pp. 1759–1774.

313. Sharma, B. *et al.* (2014) 'Biosynthesis of gold nanoparticles using a freshwater green alga, Prasiola crispa', *Materials letters*, 116, pp. 94–97.

314. Sharma, D. *et al.* (2016) 'Biosynthesis of ZnO nanoparticles using Jacaranda mimosifolia flowers extract: Synergistic antibacterial activity and molecular simulated facet specific adsorption studies', *Journal of photochemistry and photobiology. B, Biology*, 162, pp. 199–207.

315. Sharma, D., Kanchi, S. and Bisetty, K., 2019. Biogenic synthesis of nanoparticles: a review. *Arab J Chem* 12: 3576–3600.

316. Sharma, P. *et al.* (2019) 'Green synthesis and characterization of copper nanoparticles by Tinospora cardifolia to produce nature-friendly copper nano-coated fabric and their antimicrobial evaluation', *Journal of microbiological methods*, 160, pp. 107–116.

317. Shinwari, Z.K. and Maaza, M. (2017) 'The study of structural, physical and electrochemical activity of Zno nanoparticles synthesized by green natural extracts of sageretia thea', *Arch. Med*, 3(9).

318. Shiny, P.J., Mukherjee, A. and Chandrasekaran, N. (2013) 'Marine algae mediated synthesis of the silver nanoparticles and its antibacterial efficiency', *Int J Pharm Pharm Sci*, 5(2), pp. 239–241.

319. Shiv Shankar, S. *et al.* (2003) 'Bioreduction of chloroaurate ions by geranium leaves and its endophytic fungus yields gold nanoparticles of different shapes', *Journal of materials chemistry*, 13(7), pp. 1822–1826.

320. Shukla, A.K. and Iravani, S. (2017) 'Metallic nanoparticles: green synthesis and spectroscopic characterization', *Environmental chemistry letters*, 15(2), pp. 223–231.

321. Shukla, M.K. *et al.* (2012) 'Synthesis and characterization of agar-based silver

nanoparticles and nanocomposite film with antibacterial applications', *Bioresource technology*, 107, pp. 295–300.

322. Sicard, C. *et al.* (2010) 'Nano- gold biosynthesis by silica -encapsulated micro-algae: a "living" bio-hybrid material', *Journal of materials chemistry*, 20(42), pp. 9342–9347.
323. Silverstein, R.M. and Bassler, G.C., 1962. Spectrometric identification of organic compounds. *Journal of Chemical Education*, *39*(11), p.546.
324. Silverstein, R.M. *et al.* (2014) 'A good general reference for more detailed information on interpretation of infrared spectra (as well as other spectroscopic techniques) is Silverstein, spectrometric identification of organic compounds'. New York: Wiley.
325. Singh, D.P. (2010) 'Synthesis and Growth of ZnO Nanowires', *Science and Technology of Advanced Materials*, 2(3), pp. 245–272.
326. Singh, G. *et al.* (2014) 'Synthesis of ZnO nanoparticles using the cell extract of the cyanobacterium, Anabaena strain L31 and its conjugation with UV-B absorbing compound shinorine', *Journal of photochemistry and photobiology. B, Biology*, 138, pp. 55–62.
327. Singh, J. *et al.* (2017) 'Facile Approach to Synthesize and Characterization of Silver Nanoparticles by Using Mulberry Leaves Extract in Aqueous Medium and its Application in Antimicrobial Activity', *Journal of Nanostructures*, 7(2), pp. 134–140.
328. Singh, J. *et al.* (2019) 'Biogenic ZnO nanoparticles: a study of blueshift of optical band gap and photocatalytic degradation of reactive yellow 186 dye under direct sunlight', *Green Processing and Synthesis*, 8(1), pp. 272–280.
329. Singh, J., Dutta, T., *et al.* (2018) '"Green" synthesis of metals and their oxide nanoparticles: applications for environmental remediation', *Journal of nanobiotechnology*, 16(1), p. 84.
330. Singh, J., Mehta, A., *et al.* (2018) 'Green synthesis of silver nanoparticles using sun dried tulsi leaves and its catalytic application for 4-Nitrophenol reduction', *Journal of Environmental Chemical Engineering*, 6(1), pp. 1468–1474.
331. Singh, M. *et al.* (2014) 'Drug Delivery System for Controlled Cancer Therapy Using PhysicoChemically Stabilized Bioconjugated Gold Nanoparticles Synthesized from Marine Macroalgae, Padina Gymnospora', *J Nanomed Nanotecho*, S5(009), pp. 1–7.
332. Sinha, S.N. *et al.* (2015) 'Green synthesis of silver nanoparticles using fresh water green alga Pithophora oedogonia (Mont.) Wittrock and evaluation of their antibacterial activity', *Applied Nanoscience*, 5(6), pp. 703–709.
333. Song, J.Y. and Kim, B.S. (2008) 'Biological synthesis of bimetallic Au/Ag nanoparticles

using Persimmon (Diopyros kaki) leaf extract', *The Korean journal of chemical engineering*, 25(4), pp. 808–811.

334. Steffy, K. *et al.* (2018) 'Enhanced antibacterial effects of green synthesized ZnO NPs using Aristolochia indica against Multi-drug resistant bacterial pathogens from Diabetic Foot Ulcer', *Journal of infection and public health*, 11(4), pp. 463–471.
335. Subramani, A.K. *et al.* (2007) 'Photocatalytic degradation of indigo carmine dye using TiO2 impregnated activated carbon', *Bulletin of Materials Science*, pp. 37–41.
336. Subramaniyam, V. *et al.* (2015) 'Chlorococcum sp. MM11—a novel phyco-nanofactory for the synthesis of iron nanoparticles', *Journal of applied phycology*, 27(5), pp. 1861–1869.
337. Sudha, A., Jeyakanthan, J. and Srinivasan, P. (2017) 'Green synthesis of silver nanoparticles using Lippia nodiflora aerial extract and evaluation of their antioxidant, antibacterial and cytotoxic effects', *Resource-Efficient Technologies*, 3(4), pp. 506–515.
338. Suganya, K.S.U. *et al.* (2015) 'Blue green alga mediated synthesis of gold nanoparticles and its antibacterial efficacy against Gram positive organisms', *Materials science & engineering. C, Materials for biological applications*, 47, pp. 351–356.
339. Supraja, P. *et al.* (2022) 'A simple and low-cost triboelectric nanogenerator based on two dimensional ZnO nanosheets and its application in portable electronics', *Sensors and actuators. A, Physical*, 335, p. 113368.
340. Surendra, T.V. *et al.* (2016) 'RSM optimized Moringa oleifera peel extract for green synthesis of M. oleifera capped palladium nanoparticles with antibacterial and hemolytic property', *Journal of photochemistry and photobiology. B, Biology*, 162, pp. 550–557.
341. Suresh, D. *et al.* (2015) 'Green synthesis of multifunctional zinc oxide (ZnO) nanoparticles using Cassia fistula plant extract and their photodegradative, antioxidant and antibacterial activities', *Materials Science in Semiconductor Processing*, 31, pp. 446–454.
342. Suriya, J. *et al.* (2012) 'Biosynthesis of silver nanoparticles and its antibacterial activity using seaweed Urospora sp', *African journal of biotechnology*, 11(58), pp. 12192–12198.
343. Tanaka, Y. (2018) 'Synthesis of nanosize particles in thermal plasmas', *Handbook of Thermal Science and Engineering;*, pp. 2791–2828.
344. Telgmann, L. *et al.* (2016) 'Single particle ICP-MS as a tool for determining the stability of silver nanoparticles in aquatic matrixes under various environmental conditions, including treatment by ozonation', *Analytical and bioanalytical chemistry*, 408(19), pp. 5169–5177.
345. Thakkar, K.N., Mhatre, S.S. and Parikh, R.Y. (2010) 'Biological synthesis of metallic

nanoparticles', *Nanomedicine: nanotechnology, biology, and medicine*, 6(2), pp. 257–262.

346. Thakur, S., Singh, S. and Pal, B. (2021) 'Superior adsorptive removal of brilliant green and phenol red dyes mixture by CaO nanoparticles extracted from egg shells', *Journal of Nanostructure in Chemistry*.

347. Thangaraju, N. *et al.* (2012) 'Synthesis of silver nanoparticles and the antibacterial and anticancer activities of the crude extract of Sargassum polycystum C', *Agardh Nano Biomed Eng*, 4(2), pp. 89–94.

348. Thanighaiarassu, R.R., Nambikkairaj, B. and Ramya, D.R. (2018) 'Green synthesis of silver nanoparticles and characterization using plant leaf essential oil compound citral and their antifungal activity against human pathogenic fungi', *Journal of Pharmacognosy and Phytochemistry*, 7(6), pp. 902–907.

349. Türk, M. and Erkey, C. (2018) 'Synthesis of supported nanoparticles in supercritical fluids by supercritical fluid reactive deposition: Current state, further perspectives and needs', *The Journal of supercritical fluids*, 134, pp. 176–183.

350. Udayabhanu *et al.* (2017) 'Vitis labruska skin extract assisted green synthesis of ZnO super structures for multifunctional applications', *Ceramics International*, 43(15), pp. 11656–11667.

351. Varun, S., Sudha, S. and Kumar, P.S. (2014) 'Biosynthesis of Gold Nanoparticles from Aqueous Extract of Dictyota Bartayresiana and Their Antifungal Activity', *Indian J Adv Chem Sci*, 2(3), pp. 190–193.

352. Vasantharaj, S. *et al.* (2021) 'Enhanced photocatalytic degradation of water pollutants using bio-green synthesis of zinc oxide nanoparticles (ZnO NPs)', *Journal of Environmental Chemical Engineering*, 9(4), p. 105772.

353. Veerasamy, R. *et al.* (2011) 'Biosynthesis of silver nanoparticles using mangosteen leaf extract and evaluation of their antimicrobial activities', *Journal of Saudi Chemical Society*, 15(2), pp. 113–120.

354. Venkatachalam, P. *et al.* (2017) 'Enhanced plant growth promoting role of phycomolecules coated zinc oxide nanoparticles with P supplementation in cotton (Gossypium hirsutum L.)', *Plant physiology and biochemistry: PPB / Societe francaise de physiologie vegetale*, 110, pp. 118–127.

355. Vijayan, S.R. *et al.* (2016) 'Seaweeds: A resource for marine bionanotechnology', *Enzyme and microbial technology*, 95, pp. 45–57.

356. Vimala, K. *et al.* (2014) 'Green synthesized doxorubicin loaded zinc oxide nanoparticles regulates the Bax and Bcl-2 expression in breast and colon carcinoma', *Process*

Biochemistry, 49(1), pp. 160–172.

357. Vinotha, V. *et al.* (2019) 'Synthesis of ZnO nanoparticles using insulin-rich leaf extract: Anti-diabetic, antibiofilm and anti-oxidant properties', *Journal of photochemistry and photobiology. B, Biology*, 197, p. 111541.
358. Vivek, M. *et al.* (2011) 'Biogenic Silver Nanoparticles by Gelidiella acerosa Extract and their Antifungal Effects', *Avicenna journal of medical biotechnology*, 3(3), pp. 143–148.
359. Wang, Y. *et al.* (2020) 'Facile Synthesis of Porous ZnO Nanoparticles Efficient for Photocatalytic Degradation of Biomass-Derived Bisphenol A Under Simulated Sunlight Irradiation', *Frontiers in bioengineering and biotechnology*, 8, p. 616780.
360. Xi, Y. and Rocke, D.M. (2008) 'Baseline correction for NMR spectroscopic metabolomics data analysis', *BMC bioinformatics*, 9, p. 324.
361. Yan, X. *et al.* (2020) 'Multi-catalysis of nano-zinc oxide for bisphenol A degradation in a dielectric barrier discharge plasma system: Effect and mechanism', *Separation & Purification Technology*, 231, p. 115897.
362. Yazdi, M.G. *et al.* (2018) 'Surface modified composite nanofibers for the removal of indigo carmine dye from polluted water', *RSC advances*, 8(43), pp. 24588–24598.
363. Ye, C. *et al.* (2019) 'Controllable synthesis of rhombohedral α-Fe2O3 efficient for photocatalytic degradation of bisphenol A', *Journal of Water Process Engineering*, 27, pp. 205–210.
364. Yousefzadi, M., Rahimi, Z. and Ghafori, V. (2014) 'The green synthesis, characterization and antimicrobial activities of silver nanoparticles synthesized from green alga Enteromorpha flexuosa (wulfen) J. Agardh', *Materials letters*, 137(Supplement C), pp. 1–4.
365. Yuvakkumar, R. et al. (2014) 'Novel green synthetic strategy to prepare ZnO nanocrystals using rambutan (Nephelium lappaceum L.) peel extract and its antibacterial applications', Materials science & engineering. C, Materials for biological applications, 41, pp. 17–27.
366. Zeghoud, S. *et al.* (2022) 'A review on biogenic green synthesis of ZnO nanoparticles by plant biomass and their applications', *Materials Today Communications*, 33, p. 104747.
367. Zhang, F. *et al.* (1998) 'TiO2-assisted photodegradation of dye pollutants II. Adsorption and degradation kinetics of eosin in TiO2 dispersions under visible light irradiation', *Applied catalysis. B, Environmental*, 15(1), pp. 147–156.
368. Zhang, M. *et al.* (2019) 'Fabrication of Zinc Oxide/Polypyrrole Nanocomposites for Brilliant Green Removal from Aqueous Phase', *Arabian Journal for Science and Engineering*, 44(1), pp. 111–121.

369. Zinicovscaia, I. (2012) ‘Use of bacteria and microalgae in synthesis of nanoparticles’, *Chem J Mold*, 7 (2), pp. 32–38.

Publications

Published

- **Prerna, K.**, Kaur, A., & Goyal, D. (2019), Algae-based Metallic Nanoparticles: Synthesis, Characterization, and Applications; Journal of Microbiological Methods, 163, 105656 (1-24) (IF 2.622)
- **Prerna,** Agarawal, H., & Goyal D. (2022), Photocatalytic degradation of textile dyes using phycosynthesised ZnO nanoparticles; Inorganic Chemistry Communications, 142, 109676(1-15) (IF 3.695)

Manuscript under preparation

- **Prerna** & Goyal D, Response Surface Statistical Optimization for Production of Hexagonal ZnO Nanoparticles from Lemon grass Extract
- **Prerna** & Goyal D, Photocatalytic degradation of pharmaceutical effluents using *Amla* extract mediated ZnO nanoparticles

Conferences and Symposia

1. **Prerna*** & Goyal D (2015). 56th Annual Conference of Association of Microbiologist of India (AMI), December 7-10, 2015, School of Life Sciences, Jawaharlal Nehru University, New Delhi, India (**Poster Presentation**)
2. **Prerna***, Kaur A, Agnihotri S, Goyal D (2017) Impact of Green Synthesized ZnO Nanoparticles on the Growth of Microalgae; 4th International Conference on Nanostructured Materials and Nanocomposites (ICNM 2017), Mahatma Gandhi University, Kottayam, Kerala, India (**Invited Talk**)
3. **Prerna***, Goyal D (2018) Biosynthesis of ZnO Nanoparticle and its Effect on the Growth of Crop Plants IFSC, 2018, 6-8 December, 2018, Thapar Institute of Engineering & Technology, Patiala, Punjab, India (**Poster Presentation**)
4. **Prerna**, Goyal D (2018) Characterization of Zinc Oxide (ZnO) Nanoparticles Biosynthesized from Aspergillus niger (MTCC 9652) MSI-MEET, 2018, 19-21 Nov, 2018, MACS' Agharkar Research Institute, Pune, India (**Oral Presentation)**

Synthesis of ZnO nanoparticles

ORIGINALITY REPORT

13%	4%	12%	1%
SIMILARITY INDEX	INTERNET SOURCES	PUBLICATIONS	STUDENT PAPERS

PRIMARY SOURCES

1	Fahad Khan, Ayesha Shahid, Hui Zhu, Ning Wang et al. "Prospects of algae-based green synthesis of nanoparticles for environmental applications", Chemosphere, 2022 Publication	<1%
2	Garvita Singh, Piyoosh K. Babele, Ashok Kumar, Anup Srivastava, Rajeshwar P. Sinha, Madhu B. Tyagi. "Synthesis of ZnO nanoparticles using the cell extract of the cyanobacterium, Anabaena strain L31 and its conjugation with UV-B absorbing compound shinorine", Journal of Photochemistry and Photobiology B: Biology, 2014 Publication	<1%
3	Shaheen, Th.I., Mehrez E. El-Naggar, Abdelrahman M. Abdelgawad, and A. Hebeish. "Durable antibacterial and UV protections of in situ synthesized zinc oxide nanoparticles onto cotton fabrics", International Journal of Biological Macromolecules, 2016. Publication	<1%

Journal of Microbiological Methods 163 (2019) 105656

Contents lists available at ScienceDirect

Journal of Microbiological Methods

journal homepage: www.elsevier.com/locate/jmicmeth

Review

Algae-based metallic nanoparticles: Synthesis, characterization and applications

Prerna Khanna, Amrit Kaur, Dinesh Goyal*

Department of Biotechnology, Thapar Institute of Engineering and Technology, Deemed University, Patiala 147 004, Punjab, India

ARTICLE INFO

Keywords:
Nanoparticles
algae
green chemistry
microbial synthesis
physicochemical properties

ABSTRACT

Nanomaterials (NMs) tailored *via* conventional physicochemical routes play havoc with the environment that has led to the evolution of competent green routes for the actualization of a circular economy on an industrial-scale. Algae belonging to the class *Cyanophyceae, Chlorophyceae, Phaeophyceae* and *Rhodophyceae* have been harnessed as nano-machineries through intracellular and extracellular synthesis of gold (Au), silver (Ag) and several other metallic nanoparticles. Algae are an appealing platform for the production of diverse NMs, primarily due to the presence of bioactive compounds such as pigments and antioxidants in their cell extracts that act as biocompatible reductants. *Chlorella* spp. and *Sargassum* spp. have been extensively explored for the synthesis of nanoparticles having antimicrobial properties, which can potentially substitute conventional antibiotics. Characterization of nanoparticles (NPs) synthesised from algae has been done using advanced spectroscopic, diffractographic and microscopic techniques such as UV-Vis FT-IR, DLS, XPS, XRD, SEM, TEM, AFM, HR-TEM, and EDAX. The present paper reviews the information available on algae-mediated biosynthesis of various NPs, their characterization and applications in different domains.

1. Introduction

Synergy between engineering and medical sciences has opened novel frontiers in the ever-growing new domain of nanotechnology aimed at genesis, implementation and use of nanomaterials (NMs) to integrate with biological research. The fountainhead of nano-biotechnology is the fabrication of nanoscale particles by virtue of biological moieties that influence the characteristics of nanoparticles (NPs). Synthesis of NMs of diverse sizes and shapes has underpinned great interest due to their novel properties as compared to their bulk counterparts. Consistency in the chemical, biochemical and physicochemical properties of materials varies immensely at the nanoscale mainly due to the high aspect ratio of surface area to volume. This leads to considerable differences in biological and catalytic activity, mechanical properties, melting point, optical absorption, thermal and electrical conductivity (Shah et al., 2015). Nanoparticles bridge the gap between bulk materials and atomic or molecular structures. Physicochemical synthesis of NPs is often cumbersome and costly with the release of harmful by-products posing a high risk to living systems (Sinha et al., 2009; Azizi et al., 2014). Biological synthesis of NPs using microbes, enzymes, plants, and algae has been proposed as an alternative to chemical and physical modes of synthesis. The prime focus is on selecting the compounds which are competent, harmless, eco-friendly and commercially viable. In the past few years, phyconanotechnology, though in its stage of infancy, is becoming an exciting and upcoming area with greater scope in the synthesis of algae-based NPs. Algae being the largest photoautotrophic group of microorganisms are the potential source for an array of secondary metabolites, pigments and proteins, which can serve as nanobiofactories for metallic nanoparticles (Ali et al., 2011; Prasad and Elumalai, 2013; Namvar et al., 2015; Aziz et al., 2015; Kalabegishvili et al., 2012; Patel et al., 2015; González-Ballesteros et al., 2017).

Simple methods have been developed comprising of extracellular or intracellular reduction of metal ions by biological extracts (Li et al., 2011; Roychoudhury and Pal, 2014; Parial and Pal, 2014). Extracts from plants (Sangeetha et al., 2011), bacteria (Li et al., 2011), fungi (Mukherjee et al., 2002), human cells (Anshup et al., 2005; El-Said et al., 2014) and diatoms (Schröfel et al., 2011) have successfully transformed metal precursors to their corresponding NPs. The synthesis of these NPs has been facilitated by a soup of compounds such as terpenoids, phenolics, flavonones, amines, amides, proteins, pigments, alkaloids etc., present in the extracts, which assists in metal reduction and their stabilization (Asmathunisha and Kathiresan, 2013). The high metal uptake potential of algae and their predominance makes them a low-cost raw material (Kannan et al., 2013a). The interaction and biochemical activities of every microbe and the internal factors such as

* Corresponding author.
E-mail address: dgoyal@thapar.edu (D. Goyal).

https://doi.org/10.1016/j.mimet.2019.105656
Received 26 September 2018; Received in revised form 14 June 2019
Available online 17 June 2019

pH and temperature eventually play a crucial role in the size and morphology of the NPs (Makarov et al., 2014; Shah et al., 2015; Pathak et al., 2019). The high surface area to volume ratio justifies their versatile applicability together with their ability to withstand harsh conditions (Dahoumane et al., 2016). Their synthesis plays a vital role due to their broad spectrum applications, which diverge from medical, industrial, electronic devices, sensors, cosmetics, pharmaceutical, agriculture and bioremediation.

The present paper comprehensively reviews work done on algae-mediated biosynthesis of gold (Au), silver (Ag), palladium (Pd), platinum (Pt), iron (Fe), cadmium (Cd), titanium oxide (TiO_2), zinc oxide (ZnO) and Ag-Au bimetallic nanoparticles and their mechanism of synthesis followed by advances in characterization techniques with their application in different domains.

2. Classification of nanoparticles

A wide range of NPs exists naturally in the environment or can be fabricated artificially; the latter is sometimes called anthropogenic NPs. Despite the presence of natural NPs in living organisms, their existence is assumed in the biosphere since the genesis of the earth. Natural NPs can be obtained as a result of forest fires, volcanic eruptions, weathering of rocks, explosion of clay minerals, soil erosions, and sandstorms (Baker et al., 2013). NPs are classified in different categories based on shape and dimension, phase composition and nature of the material (Fig. 1).

3. Synthesis and characterization of nanoparticles

Fundamentally there are two approaches for the synthesis of NPs, the top-down approach and the bottom-up approach). The top-down approach involves slicing of bulk materials into reduced size self-assembled nanoscale objects. It often uses microfabrication techniques, where externally controlled tools are used to cut, mill, and shape materials into the desired size and shape (Nath and Banerjee, 2013; Khan et al., 2017). A variety of metallic NPs were fabricated by top-down approaches like mechanical milling (Arbain et al., 2011), etching (Cheng et al., 2016), laser ablation (Amendola and Meneghetti, 2009), sputtering (Hatakeyama et al., 2011) and electro-explosion (Ghorbani, 2014). Whereas the bottom-up approach is reversed altogether therefore referred to as molecular nanotechnology involving assembly of a defined structure by joining atom by atom, molecule by molecule, cluster by cluster or self-organization (Thakkar et al., 2010). In this mode, self-assembled properties of single molecules are exploited to build up complex conformations at the nanoscale (Nath and Banerjee, 2013). Nanoscale structures that have been reported to be synthesised by bottom up approaches are supercritical fluid synthesis (Türk and Erkey, 2018), use of templates (Apolinário et al., 2014), plasma or frame spraying synthesis (Tanaka, 2018.) sol-gel process (Sekine et al., 2009), laser pyrolysis (D'Amato et al., 2013), chemical vapour deposition (Bhaviripudi et al., 2010), molecular condensation (Gurentsov et al., 2007), chemical reduction (Guzmán et al., 2009) and most significantly green synthesis (Sangeetha et al., 2011; González-Ballesteros et al., 2017) (Fig. 2). The main focus is inclined towards synthesis of NPs of different chemical composition, sizes, morphologies and monodispersity (Sastry et al., 2003; Iravani, 2011).

In top-down approaches, physicochemical processes are involved which may lead to surface imperfections that affect the NPs properties. Similarly, in bottom-up approaches, NPs are clustered from smaller units. So in both cases, the growth of the NPs is controlled *via* kinetic processes which determine the shape and size of the NPs. The energy and growth rate of crystals are monitored by introducing compatible templates or surfactants which can curtail the interfacial energy (Sharma et al., 2011; Khan et al., 2017). There is an array of various

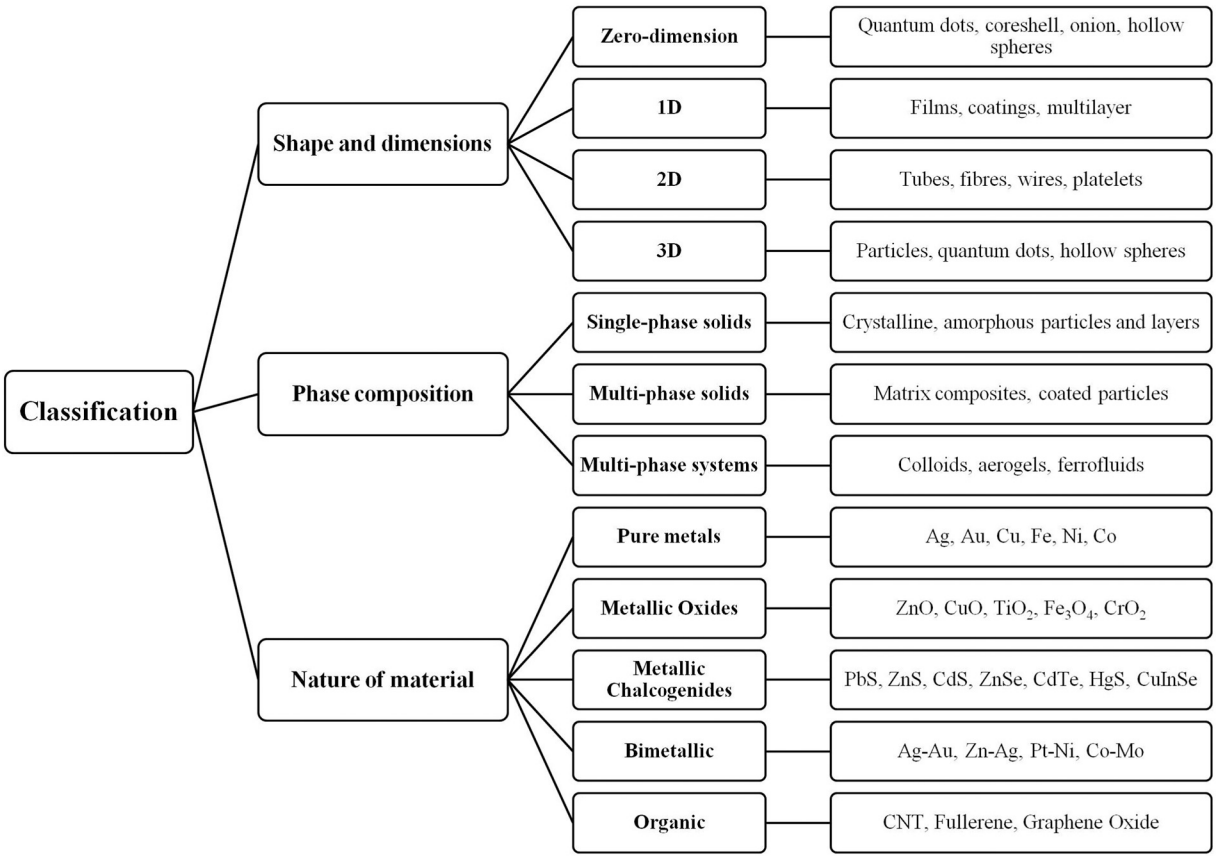

Fig. 1. Classification of nanomaterials (NMs).

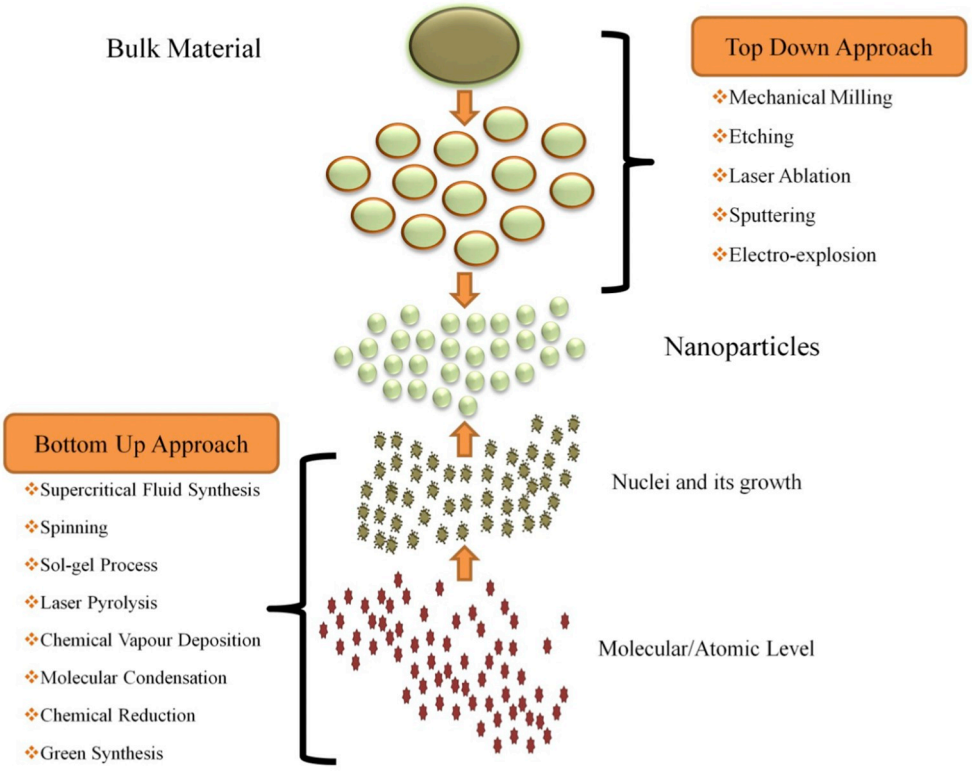

Fig. 2. Synthesis of nanomaterials (NPs) *via* top-down and bottom-up approaches.

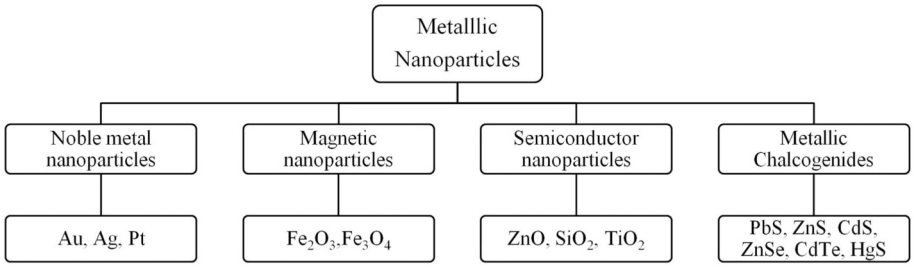

Fig. 3. Different types of metallic nanomaterials (NPs).

kinds of metallic NPs depending on their metallic behaviour, magnetic properties etc. (Fig. 3). Up until now, various commercial surfactants such as cetyl trimethyl ammonium bromide (CTAB), polyvinylpyrrolidone (PVP), sodium dodecyl sulfate (SDS), thioglycerol (TG), mercaptoethanol (ME), sodium hexametaphosphate (SHMP) (Rahdar, 2013) have been used as capping agents, which could directly modify the surface morphology of NPs during their synthesis. Usually, a colour change is the convenient visible signature and the qualitative indication for any reaction to take place in the biological/chemical synthetic process. Most of the NPs are fabricated in a colloidal solution which can be detected easily (Poinern, 2014; Khan et al., 2017). After completion of the reaction, the NPs are subjected to simple downstream processing such as high-speed centrifugation for their recovery (Poinern, 2014).

Thereafter, NPs are subjected to various characterization techniques to ascertain their size, shape, distribution, surface morphology, and surface area. Spectroscopic and diffractographic techniques involved in the characterization include UV-visible spectroscopy (UV-vis), dynamic lights scattering (DLS), energy dispersive spectroscopy (EDS), X-ray diffraction (XRD), Fourier transform infrared spectroscopy (FT-IR), X-ray photo-electron spectroscopy (XPS) and Raman spectroscopy (Menon et al., 2017; Shah et al., 2015). These are the indirect methods used to analyse composition, structure, and crystal phase. Whereas scanning electron microscopy (SEM), transmission electron microscopy (TEM), high-resolution transmission electron microscopy (HR-TEM), and atomic force microscopy (AFM) are employed to determine the size and morphological features of NPs (Quester et al., 2013; Hulkoti and Taranath, 2014).

3.1. Spectroscopic and diffractographic techniques

Generally, metallic NPs have striking optical properties due to surface plasmon resonance (SPR), which is monitored by UV-Vis spectroscopy within the range of 190–1100 nm (Sharma et al., 2016). These radiations interact with the metals and promote the electronic transition from ground to higher energy state and a specific SPR band is obtained which may help to obtain the size and shape of NPs up to a certain limit (2–100 nm) (Poinern, 2014). The absorption spectra for different materials is different e.g. for Ag-NPs it is 400–450 nm (Verma et al., 2010; Aboelfetoh et al., 2017), for Au-NPs it falls in between 500–550 nm and for ZnO-NPs it is between 350 and 390 nm (Poinern, 2014; Shukla and Iravani, 2017).

It has been suggested that the broadening of the SPR band width, which illustrates a shift toward the red or blue end is considered as an

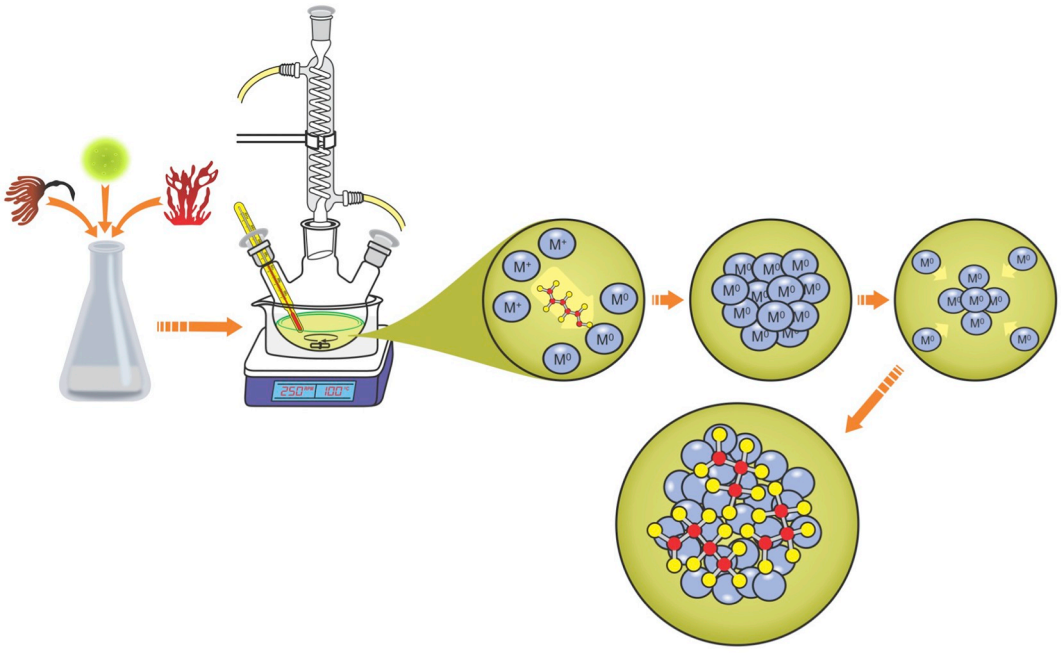

Fig. 4. Mechansim of synthesis of nanomaterials (NPs) from algae.

index of size, state of aggregation, shape, the type of capping or binding agents, polydispersity, and the surrounding dielectric medium (Govindaraju et al., 2008; Jena et al., 2013, Mahmudin et al., 2015). Furthermore, an increase in particle size in the aqueous solution is depicted by an increase in band intensity. UV/Vis- diffuse reflectance spectrometer (DRS) is a fully equipped device, which can be used to measure the optical absorption, transmittance and reflectance. DRS is an exceptional technique to calculate the bandgaps of NMs which is important for determining the photoactivity and conductance of the material (Khan et al., 2017; Shukla and Iravani, 2017).

To investigate the underlying mechanism of synthesis and surface chemistry, FT-IR spectroscopy is done to identify the functional groups attached to the NPs. Usually, it ranges between 4000 and 400 cm^{-1}, and a resolution of 4 cm^{-1} gives a clear idea about the reducing agents responsible for capping, reduction and stabilization. The comparison between the transmittance spectra of aqueous native extract and reaction medium gives an idea of the biomolecules involved in the process (Dahoumane et al., 2016). Most common functional groups, which adhere to the NPs are −C=O−, $-NH_2-$ and −SH− (Jena et al., 2013, 2014). However, FT-IR has limitations because of the high degree of overlapping of IR absorption bands in the complex biological matrix. Additionally, other characterization techniques, such as XPS, could shed light on the interaction between the produced NPs and their surrounding biomolecules (Dahoumane et al., 2016).

Surface charge, hydrodynamic diameter and distribution of NPs in liquid form is measured by DLS spectroscopy and particle stability is determined by zeta potential (Poinern, 2014). Whereas the purity, crystalline size, geometry, orientation and phases can be determined by XRD data, generally the diffraction patterns are compared with the standard crystallographic database like JCPDS to have the structural information (Shah et al., 2015). It gives a rough idea about the particle size determined by Debye Scherer formula (Ullah et al., 2017). XRD works well with both single and multiphase identification of NPs. Moreover, XRD diffractogram gets influenced with amorphous NMs having varied inter-atomic lengths (Ingham, 2015).

3.2. Advanced microscopic techniques

Properties of NPs are greatly influenced by their morphology which is studied by advanced microscopic techniques such as SEM, TEM, AFM and HR-TEM. SEM provides information about particles at the nanoscale and assists in determining the surface morphology and dispersion of NPs in bulk or matrix. TEM is most commonly used for size and shape, and it can also provide information about the number of material layers as it varies from low to high magnification. However when both are combined with EDAX or EDS, information is given about the metals present (Oza et al., 2012). In some cases of intracellular synthesis of NPs, localization of synthesized NPs is explored by SEM and TEM. However, in order to determine the exact shape, size and crystalline structure HR-TEM is absolutely required. AFM on the other hand provides information on surface topography. While TEM images mainly represent a two-dimensional image of three-dimensional nanoparticles, AFM can be used to obtain three-dimensional information of synthesized particles (Quester et al., 2013; Khan et al., 2017).

4. Mechanism of synthesis of nanoparticles from algae

Algae are known to hyperaccumulate heavy metal ions and possess an exceptional capability to remodel them into more malleable forms (Fawcett et al., 2017). Because of these alluring attributes, algae have been foreseen as model organisms for fabricating bio-nanomaterials. Algal extracts consist of carbohydrates, proteins, minerals, oil, fats, polyunsaturated fatty acids along with the soup of bioactive compounds such as antioxidants (polyphenols, tocopherols), and pigments such as carotenoids (carotene, xanthophyll), chlorophylls, and phycobilins (phycocyanin, phycoerythrin) (Michalak and Chojnacka, 2015). These potentially active compounds have been elucidated as reducing and stabilizing agents (Fig. 4). From the available reports, algae-mediated synthesis of NMs involves preparation of (i) algal extract, (ii) metal precursor solution, and (iii) incubation of algal extract with metal precursor solution (Sharma et al., 2016). The reaction is initiated by mixing the liquid algal extract with the molar solution of metal precursor. Typically, the colour change of the reaction mixture demarcates as a visible signature for the initiation of reaction illustrating nucleation, followed by growth of NPs in which the adjoining nucleonic particles club together, thus forming thermodynamically stable NPs of different size and shape (Sharma et al., 2016; Prasad et al., 2016; Fawcett et al., 2017). The bioactive component of extract supports the

cascade of nanoparticle synthesis and the controlling factors involved are pH, temperature, concentration and time. Keeping aside the controlling factors, there are two routes of synthesis i.e. extracellular and intracellular. Initially, the nanoparticle synthesis was reported to be intracellular (Lengke et al., 2007a) but later algae were exploited for an extracellular mode of synthesis (Dahoumane et al., 2012b; Aboelfetoh et al., 2017; Fawcett et al., 2017).

4.1. Intracellular mode of synthesis of nanoparticles

The term "intracellular" refers to the process which takes place inside the cell. There is no requirement for any pre-treatment of microalgae because the process relies on metabolic pathways likely to be responsible for synthesis such as photosynthesis, respiration and nitrogen fixation (Sharma et al., 2016). The reducing agents may be NADPH or NADPH dependent reductase in the energy generating steps during photosynthesis *via* electron transport system (ETS) or may be respiratory ETS at thylakoid membranes (Sicard et al., 2010) or at the cell wall (Senapati et al., 2012).

An example is of *Rhizoclonium fontinale* and *Ulva intestinalis* when treated with chloroauric acid for 72 h at 20 °C; there was a visual change in the colour of thallus from green to purple confirming the fabrication of Au-NPs. This was supported by the fact when the gold solution was incubated with dried biomass there was no change in colour, which affirms that the bioreduction process is not associated with any of the metabolic pathways involving enzymes or other metabolites and the cells were poisoned by Au^{3+} when converted to Au^0 (Parial et al., 2012a). Sicard et al. (2010) encapsulated *Klebsormidium flaccidum* in silica gel suspension. The evident colour change of chloroplasts from green to purple inside the cells demonstrated the capacity of the entrapped cells to reduce gold salts. TEM images showed dark spots of reduced gold salts in the thylakoid membranes suggesting involvement of enzymes (NADPH and NADPH dependent reductase) in the synthesis of nanoparticles (Sicard et al., 2010).

In line with this trend, Senapati and co-workers (2012) demonstrated the intracellular synthesis by the algal cell wall in *Tetraselmis kochinensis*. UV-visible spectroscopy clearly proved that there was no extracellular synthesis. The NPs were more densely present near the cell wall rather than the cytoplasmic area, which is most likely due to the presence of bioactive moieties responsible for bioreduction. Further XRD of gold nano-alga biofilm confirms the synthesis of NPs at the cell wall (Senapati et al., 2012). Another chlorophycean alga *Spirogyra submaxima*, was also found to be efficient in bioconversion of Au^{3+} to Au^0. After exposure to gold solution, colour of the biomass turned pinkish purple and Au-NPs were extracted using sodium citrate solution as a capping agent. The intracellular synthesis of crystalline gold was further supported by Bragg reflections of purple coloured biomass (Roychoudhury and Pal, 2014).

4.2. Extracellular mode of synthesis of nanoparticles

The term "extracellular" refers to the process which takes place outside the cell mainly supported by the exudates of cell metabolism comprising of metabolites, ions, pigments, various proteins (enzymes) and non-protein entities such as DNA, RNA, microbial by-products (hormones, antioxidants) and lipids (Mata et al., 2009; Vijayan et al., 2014). The algal biomass is subjected to rudimentary pre-treatments such as washing and blending (Dahoumane et al., 2016).

Kalabegishvili et al. (2012) hypothesized that the active moieties on the surface of cells are not solely responsible for the synthesis rather optimum concentration of metal precursor and a number of cells is essential. Gold NPs were customized by varying the cell number and dose of Au (III) ions. The presence of gold peak at 530 nm affirmed the extracellular synthesis assisted by biomolecules/ proteins and enzymes on the cell surface of *Spirulina platensis*. In addition, gold uptake is time dependent which takes place in two phases i.e. rapid phase in which metal ions are taken up quickly on the cell surface because of the presence of active biomolecules (amino, carboxylic, phosphate, thiol), and the slow phase in which metal ions cross the cell membrane using transport mechanisms of the cell (Kalabegishvili and Kirkesali 2012).

In another study, Parial and Pal (2014) reported extracellular synthesis of Au-NPs from *Lyngbya majuscula* and *Spirulina subsalsa,* where the gradual development of colour was a time-dependent convenient visible signature indicating massive bioconversion of Au^{3+} to Au^0 leading to a steady synthesis of Au-NPs (Parial and Pal, 2014). Shakibaie et al. (2010) were hesitant to confirm the exact mechanism involved in the synthesis of Au-NPs *via Tetraselmis suecica*. The gold NPs fabricated were not enzyme dependent as the organism is a non-thermophile since the clear band at 530 nm appeared after 90 °C. The formation and stabilization of Au-NPs at these conditions might be due to the presence of reducing agents such as polyols and water-soluble heterocyclic compounds respectively (Shakibaie et al., 2010). The dried biomass of epilithic green alga, *Prasiola crispa* was exercised to tailor spherical Au-NPs (Sharma et al., 2014a). The FT-IR spectrum clearly illustrated the extracellular production of protein and organic moieties which might be responsible for preventing agglomeration and facilitating synthesis. The colour of the algal biomass remained intact after the completion of the process, thus ruling out the intracellular mode. The authors believed an extracellular pathway was responsible indicated by the purple colour and an absorption peak at 535 nm (Sharma et al., 2014a).

Mata et al. (2009) coupled the recovery and reduction of gold nanospheres by brown alga *Fucus vesiculosus* extracellularly at varying pH. A two-stage approach was followed in which the initial introduction of metal precursor had no effect on the colour, however, a reduction of gold and a colour change was observed in the second stage by a large decrease in the concentration of Au ions and pH. They found that gold uptake and bioreduction was at its highest level at neutral pH 7, because both the processes took place simultaneously. Further, FT-IR analysis revealed that the hydroxyl groups present in the algal polysaccharides are the possible reducing and capping agents (Mata et al., 2009). Macrolaga *Sargassum wightii* was reported to synthesize stable and uniform gold nanospheres with an average diameter of 11 nm extracellularly in a shorter duration. Interestingly there was absence of capping material around NPs which were at a uniform distance and were not in physical contact as observed in TEM images (Singaravelu et al., 2007).

Fluorescent Au-NPs were successfully fabricated using the dried biomass of an edible freshwater epilithic red alga *Lemanea fluviatilis* (L.) C.Ag (Sharma et al., 2014b). The synthesis from an aqueous reaction mixture of chloroauric acid and *Lemanea fluviatilis* was found to be a function of reaction time as revealed by UV-visible spectra, which exhibited SPR at 530 nm. The NPs were stable up to 90 days as supported by the retention in red colour of the solution and negligible change in SPR band position. Proteins were believed to be the capping and reducing agents. The fabricated nanospheres were spherical and TEM images at low magnification corroborated that the NPs tend to assemble in chain-like structures (Sharma et al., 2014b; LewisOscar et al., 2016). Nitrate reductase helps in NADH dependent extracellular reduction of Au^{+3} to Au^0, and has been suggested to be involved in the synthesis of nanogold in freshwater alga *Chlorella pyrenoidosa* (Oza et al., 2012).

Apart from the intracellular and extracellular modes of synthesis of NPs, two research groups reported both the modes of synthesis simultaneously (Parial et al., 2012a, b; Jena et al., 2014). Though many theories and hypotheses have been postulated to date, not one could clearly explain the exact mechanism for the synthesis of NPs.

4.3. Factors controlling synthesis of nanoparticles

Physical factors such as pH, precursor concentration, reaction time, exposure time and temperature control the nucleation, formation and stabilization of NPs. These factors can be altered to change the size and

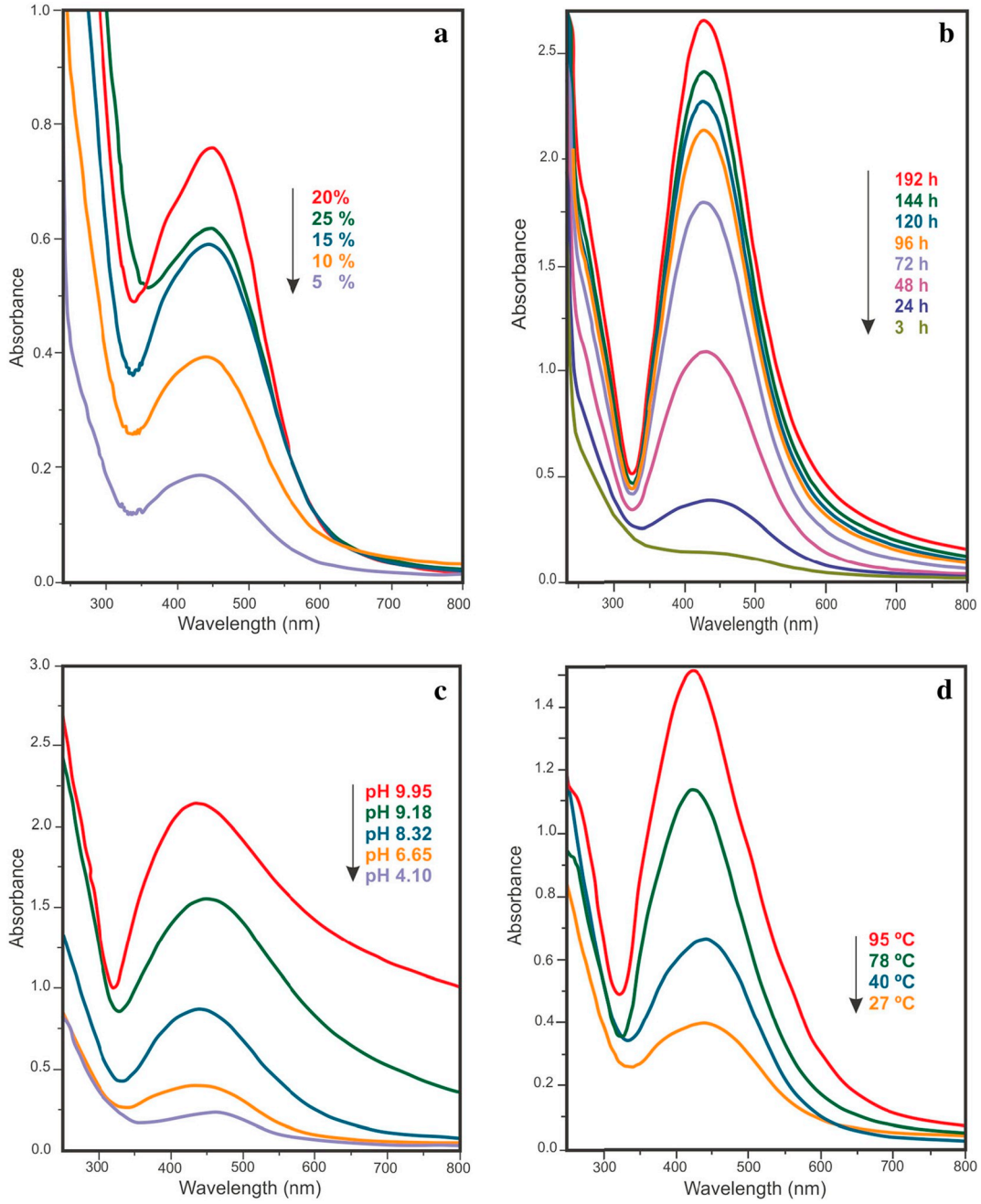

Fig. 5. UV–Vis spectra of Ag-NPs formed using 10^{-3}M $AgNO_3$ after 24 h at 27 °C with (a) various extract concentrations, (b) 10% extract as a function of contact time, (c) 10% extract at diverse pH values and (d) 10% extract at diverse temperatures (Abdel-Raouf et al., 2017).

morphology as well as to prevent agglomeration (Dahoumane et al., 2012b, 2014a, 2014b; Parial and Pal, 2015). The effect of extract concentration, pH, time and temperature were studied using UV-Vis spectroscopy (Fig. 5) for the optimization of synthesis of Ag-NPs using *Caulerpa serrulata* (Aboelfetoh et al., 2017).

4.3.1. Effect of extract concentration

Different concentrations of *C. serrulata* extract (5–25%) were added to 10^{-3} M $AgNO_3$ solution at room temperature after 24 h, and the effect was observed on Ag-NPs synthesis (Aboelfetoh et al., 2017). The increase in the concentration of extract from 5 to 20% lead to an increase in the SPR band intensity, causing a blue shift towards 435nm, indicating a decrease in average size of Ag-NPs (Fig. 5a). However, a further increase in the extract concentration up to 25% reduced the SPR band intensity which was perhaps due to particle agglomeration (Khalil et al., 2014; Velammal et al., 2016).

4.3.2. Effect of contact time

C. serrulata extract (10%) and Ag^+ ions were allowed to interact for 8 days at room temperature (Aboelfetoh et al., 2017). With gradual increase in contact time, SPR peak intensity increased without any shift leading to rapid synthesis of Ag-NPs. This clearly demonstrated the stability of Ag-NPs without agglomeration (Fig. 5b).

4.3.3. Effect of pH

Chromatic change in the reaction mixture and SPR band peak intensity were dependent on pH. The reducing and stabilizing power of *C. serrulata* extract was enhanced at basic pH. With an increase in pH from 6.65 to 9.95, a narrow SPR band at 427 nm was observed along with an increase in absorbance (Fig. 5c) (Aboelfetoh et al., 2017). However, in

acidic condition (pH-4.10), a broad SPR band was detected at 470 nm, reflecting the agglomeration of Ag-NPs or an increase in particle size, which indicates the formation of a large number of Ag-NPs with smaller diameter at higher pH values (Siddiqui et al., 2017).

4.3.4. Effect of temperature

Temperature plays a key role in the synthesis of Ag-NPs and at elevated temperature, the rate of reaction increases due to rapid utilization of reactants, leading to the formation of smaller NPs (Ibrahim, 2015). With increase in temperature from 27 to 95 °C, the less intense SPR band at 440 nm sharpens to 412 nm at 95 °C, decreasing the overall reaction time to 1 h (Fig. 5d) (Aboelfetoh et al., 2017).

5. Algae as a source for bionanomaterial

Algae are known to be one of the most primitive and influential biological entities existing autotrophically performing more than 50% of photosynthesis on this planet (Barsanti and Gualtieri, 2014). Being rich in biologically active compounds they are regarded as an appealing platform to serve as photosynthetic biorefineries capable of contriving a spectrum of high value-added products in addition to fuels (Jeffryes et al., 2015). Besides that, they are reported as hyperaccumulators of heavy metals and their chemical transformation and are believed to produce metal NPs (Zinicovscaia, 2012). Some of the pragmatic properties of the algae that make them as remarkable 'nanobiofactories' are (i) faster doubling time (Chisti, 2007) (ii) easily scalable and well developed systems (Chisti, 2007, 2008), (iii) cells can be readily disrupted (Chisti and Moo-Young, 1986), (iv) easily harvested (Grima et al., 2003) (v) low cost large-scale synthesis (Sharma et al., 2015b) and (vi) nucleation and crystal growth are accelerated due to the presence of negative charge on the surface of the cell (Sahoo et al., 2014). The chronicle, chemistry and the biological benefits of algae have been thoroughly discussed and documented elsewhere (Chen and Jiang, 2013; Namvar et al., 2015). More than a hundred different micro and macro algae have been reported that exhibit the ability to tailor NPs both intracellularly (Roychoudhury and Pal, 2014) and extracellularly (Mohseniazar et al., 2011), which can be recovered during downstream processing (Dahoumane et al., 2012a).

5.1. Gold nanoparticles

Conventionally, Au-NPs have been synthesized by physical and chemical processes (Table 1). These methods have been exploited extensively, however they have certain shortcomings such as release of unhealthy by-products, stringent chemicals, and are capital intensive (Shedbalkar et al., 2014). To refrain from the detrimental effects of toxic physicochemical techniques, research turned towards exploring living organisms. Enormous efforts have been made to understand the roles that organisms can play in the accumulation of gold and its conversion to non-toxic NPs (Parial et al., 2012a). The research in this niche has expanded rapidly with one or the other reports confirming the production of NPs by microbes (Baker et al., 2013). Rather than using all other biological entities, algae mediated synthesis is a straightforward approach for achieving the desired Au-NPs (Sharma et al., 2016).

Table 1
Physicochemical methods for synthesis of gold nanoparticle.

Synthesis of gold nanoparticles		
Physical method	**Chemical method**	**Physicochemical method**
● UV radiation ● Laser ablation ● Plasma synthesis	● Citrate synthesis ● Turkevich method ● Wet chemical synthesis ● Chemical reduction synthesis	● Sono-chemical ● Sono-electrochemical

However, the mechanism of synthesis, bioreduction, capping, and stabilization has been hypothesized by many researchers (Oza et al., 2012; Shabnam and Pardha-Saradhi, 2013; Parial and Pal, 2015; Namvar et al., 2015).

Algae have been proved as a boon with indefinite applications in numerous fields that have been employed as a substitute to chemical reductants for the tailoring of Au-NPs. Au-NPs have been synthesized from four different classes of algae such as *Cyanophyceae* (Blue-green algae) (Table 2), *Chlorophyceae* (Green algae) (Table 3), *Phaeophyceae* (Brown algae) (Table 4) and *Rhodophyceae* (Red algae) (Table 5). Material scientists have been consistently trying to fabricate Au-NPs by numerous methods with uniform size, shape, and monodispersity. It has been a challenging and vital mission to fabricate flexible and straightforward eco-friendly preparation methods to produce shape- and size-preferred Au-NPs (Namvar et al., 2015).

5.1.1. Synthesis of gold nanoparticles from cyanobacteria

Lengke et al. (2006a) used two different gold precursors [$AuCl_4^-$] and [Au $(S_2O_3)_2^{3-}$] and successfully demonstrated intracellular and extracellular synthesis of Au-NPs ranging in size from 10 to 25 nm. They used *Plectonema boryanum* UTEX 485 as a model organism because it is predominantly found in water bodies. In this study, cubical NPs and octahedral nanoplates were observed using TEM.

Parial et al. (2012a) performed a dual study of screening of potential algal strains and the effect of pH on the morphology of NPs. All three strains *Phormidium valderianum, Phormidium tenue* and *Microcoleus chthonoplastes* were able to synthesize NPs intracellularly. Among all *Phormidium valderianum,* could only synthesize gold nanospheres with a diameter of 15 nm at pH 5 along with triangular NPs (24 nm) at neutral pH and hexagonal NPs (25 nm) at basic pH 9. UV-Visible spectroscopy and TEM studies revealed the diversity in shapes and sizes of NPs. XRD peaks of the purple coloured biomass confirmed the reduction of Au (III) to Au (0) (Parial et al., 2012a).

Suganya et al. (2015) demonstrated the biosynthesis of Au-NPs using a protein extract of *Spirulina platensis* and 10 mM $HAuCl_4{\cdot}3H_2O$ in the ratio of 1:1. Addition of 1N NaOH under constant stirring for 3 h led to an instant colour change from green to greenish yellow. Further incubation of the reaction mixture at room temperature for 48 h produced a ruby red colour marking the formation of Au-NPs attributed to the collective oscillation of electron induction by the interacting electromagnetic field. Different UV-Vis peaks were observed at 685 nm, 524 nm and 385 nm for Au-NPs and *S. platensis* protein showed an excitation maximum at 620 nm. Stability of Au-NPs was evaluated at different temperatures (4, 15, 25, 60 and 80 °C) by monitoring λ_{max}. UV-Vis spectra revealed that Au-NPs were stable at 4-60 °C and at 80 °C stability was affected.

Many other researchers could collate the findings of the later by utilizing other species like *Plectonema boryanum* UTEX 485 (Lengke et al., 2006c), *Lyngbya majuscule* (Chakraborty et al., 2009), *Nostoc ellipsosporum* (Parial et al., 2012b) and *S. platensis* (Suganya et al., 2015) (Table 2). The factors affecting the morphology were mainly dependent on the cocktail of biological components present in the cell.

5.1.2. Synthesis of gold nanoparticles from green algae

The intracellular algae based synthesis of nano-gold was reported in unicellular green alga *Chlorella vulgaris* by Ting et al. (1995). Later on Xie et al. (2007a)) were successful in fabricating single-crystalline, triangular gold nanoplates from *Chlorella vulgaris.* They determined that there was a gold shaping protein (GSP of 28 kDa), involved in the bioreduction and shape regulation which was isolated and purified using SDS-PAGE and HPLC (Xie et al., 2007b).

Shakibaie et al. (2010) introduced the utilization of marine green microalgae *Tetraselmis suecica* for polydispersed and crystalline Au-NPs. The alternation of colour from yellow to red demonstrated the formation of spherical Au-NPs of size range 51-59 nm with an average size of 79 nm. They also tried to develop a rapid extracellular route, which was

Table 2
Cyanobacteria mediated synthesis of gold nanoparticles (Au-NPs).

Microalgae	Size & morphology	Application/Activity	Characterization	Bioreductant and capping agent	Reference
Plectonema boryanum UTEX 485	20–25 nm, cubic and octahedral gold plates	Synthesis of Au NPs from aqueous Au(I) thiosulfate and Au(III) chloride complexes in abiotic and cyanobacterial systems between 25-200 °C	TEM, SEM, XPS, TOF-SIMS	-	(Lengke et al., 2006a)
Lyngbya majuscula and *Spirulina subsalsa*	> 20 nm, spherical	Exposure to high concentration of Au salts can lead to synthesis initiation	TEM	Bioformation of Au NPs within the cells exposed in high gold level	(Chakraborty et al., 2009)
Synechocystis sp. PCC 6803	13 ± 2 nm, spherical	Intracellular biomineralization study	TEM, SERS, Zeta Potential	Carboxyl groups, polyphosphates, polysaccharides, cysteine or methionine compounds	(Focsan et al., 2011)
Nostoc ellipsosporum	20–40 nm, decahedral, icosahedra rods	Uniform distribution of aspect ratio of monodispersity	UV-Vis, TEM, DLS, Zeta Potential, XRD	Intracellular biotransformation, sodium citrate for extraction of nanorods	(Parial et al., 2012b)
Phormidium tenue	14.84 nm, spherical and irregular-shaped, fcc	Large-scale controlled synthesis of Au NPs	UV-Vis, TEM, XRD	Reduction of gold is associated with cellular metabolism and presumably involves reducing enzymes or synthesis of other metabolites	(Parial et al., 2012a)
Phormidium valderianum	pH 5: 15 nm, spherical, nanorods 411 × 32 nm pH 7: 7.92-17 nm, spherical; 24 nm triangular pH 9: 13.78 nm, spherical; 25 nm, hexagonal, fcc	Medicinally important gold nanorods	UV-Vis, TEM, XRD	Reduction of gold is associated with cellular metabolism and presumably involves reducing enzymes or synthesis of other metabolites	(Parial et al., 2012a)
Spirulina platensis	20–30 nm, spherical	Pharmaceutical technological purpose	UV-Vis, FT-IR, TEM, SEM-EDAX, XRD, NAA, AAS	Extracellular; biomolecules (amino, carboxylic, phosphate, thiol)	(Kalabegishvili et al., 2012)
Phormidium spp	25 nm, triangular	Antioxidant activity by DPPH, interaction with DNA, biolabelling	UV-Vis, HR-SEM, EDAX, FT-IR, TEM	Cytoplasmic protein moieties	(MubarakAli et al., 2013)
Lyngbya majuscule	2–25 nm, spherical, hexagonal	Low-cost production at ambient temperature and pressure	UV-Vis, TEM, DLS, XRD, FT-IR	Extracellular, Na citrate act as an capping agent, amino acid residue of protein shells act as stabilizer	(Parial and Pal, 2014)
Spirulina subsalsa	5–30 nm, spherical with few nanorods	Low-cost production at ambient temperature and pressure	UV-Vis, TEM, DLS, XRD, FT-IR	Extracellular, protein shells	(Parial and Pal, 2014)
Anabaena spp. (SAG 12.82)	10 nm, spherical	Self-reproducing bioreactor for *in vivo* biosynthesis	XRD, TEM	Protein or cellular enzymes	(Rösken et al., 2016)
Spirulina platensis	5 nm, spherical	Gram +ve strains: *B. subtilis* and *S. aureus;* stable for 2 months	UV-Vis, FT-IR, HR-TEM, EDAX	Carboxylate group in the reduction, Carboxyl, hydroxyl and primary amine are involved in stabilization	(Suganya et al., 2015)

Table 3
Green algae mediated synthesis of gold nanoparticles (Au-NPs).

Microalgae	Size & morphology	Application/Activity	Characterization	Bioreductant and capping agent	Reference
Green microalgae					
Chlorella vulgaris	0.8–2 μm along side, triangular, truncated triangular, hexagonal	Optical coatings and hyperthermia of cancer cells	TEM, FT-IR, AFM, XPS, HPLC, FESEM, SAED, UV-Vis	Gold shape-directing protein of 28kDa size	(Xie et al., 2007b)
Klebsormidium flaccidum	10–20 nm	Sol-gel methods for encapsulation of algal species within silica gels	UV-Vis, XRD, TEM, PAM, PEA, XPS, SERS	Insitu, gold reduction occurs in thylakoids where reducing enzymes	(Sicard et al., 2010)
Tetraselmis suecica	51–120 nm, spherical	First report on marine microalgae- based synthesis	UV-Vis, XRD, FT-IR	Extracellular, functional groups like -OH, -NH, -C=O of polyols and water-soluble heterocyclic compound	(Shakibaie et al., 2010)
Chlorella vulgaris	40–60 nm, spheroidal, polyhedral	Potentially attractive route to commercial production	XRD, TEM,XAS, AAS, XANES	Intracellular	(Luangpipat et al., 2011)
Klebsormidium flaccidum	9 ± 3.4 nm	Development of cell-based bioreactors for the production of metal NPs	PAM, TEM, UV-Vis	Intracellular	(Dahoumane et al., 2012)
Chlorella pyrenoidusa	25–30 nm, spherical, icosahedral, fcc	pH-dependent size controllable tuning of the synthesis of thermodynamically stable Au nanoparticle	UV-Vis, XRD, HR-TEM	NADH-dependent enzyme	(Oza et al., 2012)
Tetraselmis kochinensis	5–35 nm, spherical, triangular, fcc	Catalysis, electronics and coatings	UV-Vis, XRD, TEM	Intracellular, reduction by enzymes present in the cell wall and cytoplasmic membrane	(Senapati et al., 2012)
Coelastrella sp	30 nm sized spherical	Antioxidant activity by DPPH, interaction with DNA, biolabelling	UV-Vis, HR-SEM, EDAX, FT-IR, TEM	Cytoplasmic protein moieties	(MubarakAli et al., 2013)
Spirogyra submaxima	2–50 nm, spherical, triangular, hexagonal	Pure, easily extractable NPs are formed which can be used in biomedical applications	UV-Vis, DLS, XRD, TEM, Zeta Potential	Intracelluar synthesis at cell wall and the chloroplast	(Roychoudhury and Pal, 2014)
Cosmarium impressulum	5.7 ± 0.9 nm, spherical	Mechanism of synthesis studied thoroughly	UV-Vis, TEM	Enzymes and their cofactors	(Dahoumane et al., 2014b)
Green macroalgae					
Prasiola crispa	5–25 nm, fcc, spherical	Facile, one step and eco-friendly for the large scale synthesis	UV-Vis, XRD, FT-IR, DLS, HR-TEM	Protein and other molecules, extracellular	(Sharma et al., 2014a)
Rhizoclonium fontinale	pH 5: 5–20 nm spherical, 15–88 nm nanotriangles, 34 nm nanohexagons, rod-shaped (~100 × 51.5 nm); pH 7: spherical 13-22 nm, pH 9: 16 nm, nanospheres	Concentration of Au ions, pH and time play a vital role in synthesis. Alkaline pH induces formation of monodisperse nanoparticle	UV-Vis, HR-TEM, DLS, EDAX	Intracellular synthesis which is concentration dependent	(Parial and Pal, 2015)

Table 4
Brown algae mediated synthesis of gold nanoparticles (Au-NPs).

Macroalgae	Size & morphology	Application/Activity	Characterization	Bioreductant and capping agent	Reference
Sargassum sp.	300-400 nm along longest edge, 8-10 nm in thickness, fcc, hexagonal, truncated triangular,	Effect of pH, temperature, concentration, aging time, reaction time on the morphology of NPs	AFM, TEM, XRD, UV-Vis, FT-IR	Carbonyl, hydroxyl, amine functional groups and tannic materials	(Liu et al., 2005)
Sargassum wightii	8-12 nm, thin planer structure	Development of bioprocess for synthesis	UV-Vis, XRD, HR-TEM,	Biotransformation using algal species. Extracellular synthesis.	(Singaravelu et al., 2007)
Fucus vesiculosus	20–50 nm, spherical	Biogenic mechanisms of gold deposition involved in the formation of natural deposits	XRD, SEM, EDS, TEM, FT-IR, FAAS	Hydroxyl groups in polysaccharides of the algal cell wall, extracellular synthesis	(Mata et al., 2009)
Laminaria japonica	15–20 nm, spherical, crystalline, fcc	Extracellular biomineralization	UV-Vis, TEM, XRD, FT-IR,	Amide-I and amide-II groups of peptides and/or proteins	(Ghodake and Lee, 2011)
Turbinaria conoides	20–80 nm, crystalline	Mechanism of biosorption and bioreduction	UV-Vis, SEM, FE-SEM, EDX, XRD	Hydroxyl groups of polysaccharides	(Vijayaraghavan et al., 2011)
Sargassum myriocystum	15 nm; triangular and spherical, polydispersed	Cardiovascular treatment	UV-Vis, FT-IR, TEM, SEM-EDAX, XRD, GC-MS	1-cyclopentyl-4-(3 cyclopentylpropyl) dodecane	(Stalin Dhas et al., 2012)
Stoechospermum marginatum	18.7 to 93.7 nm, spherical, triangular and hexagonal	Antibacterial against Gram -ve *E. faecalis*	PL, SEM, TEM, XRD, FT-IR, WD-XRF	Hydroxyl groups present in the diterpenoids	(Rajathi et al., 2012)
Turbinaria conoides	6–10 nm, spherical	Antibacterial, biocompatible	UV-Vis, XRD, FT-IR, TEM	Fucoidan and polyphenolic groups	(Rajeshkumar et al., 2013a)
Turbinaria conoides	60 nm, triangle, rectangle and square	High antibacterial activity against *Streptococcus* sp, and medium for *B. subtilis* and *K. pneumoniae*	SEM, EDS	Biochemical material	(Rajeshkumar et al., 2013b)
Padina gymnospora	8–21 nm, spherical	Antitumor on liver cancer (HepG2) cell line	UV-Vis, XRD, AFM, HR-TEM, FT-IR	Fucoxanthin or flavonoids	(Singh et al., 2014a, 2014b)
Padina gymnospora	53–67 nm, fcc, nanoprisms and nano spheres	Cancer therapeutics	UV-Vis, FT-IR, AFM, SEM, XRD	Secondary metabolites, such as alkaloids having functional groups of hydroxyl, amines, alcohols, phenol and carboxylic acids	(Singh et al., 2013)
Dictyota bartayresiana	Spherical, poly-dispersed NPs	Antifungal against *Humiclo insulans* and *Fusarium dimerum*	UV-Vis, FT-IR, SEM	Carboxylic, amine and polyphenolic groups	(Varun et al., 2014)
Turbinaria conoides	2–19 nm, triangular, fcc	-	UV-Vis, FT-IR, XRD, FESEM, EDX, HR-TEM, CLSM	Free hydroxyl group and a carboxylic acid group	(Vijayan et al., 2014)
Ecklonia cava	20–50 nm, spherical, triangular, fcc	High antimicrobial activity against *E. coli* and *A. niger,* biocompatible as nontoxic for HaCaT cell lines	UV-Vis, XRD, FT-IR, FESEM-EDX, TEM	Biomolecules with primary amine group, hydroxyl group	(Venkatesan et al., 2014)
Sargassum muticum	5.42 ± 1.18 nm, spherical, fcc	Biomedical and pharmaceutical	UV-Vis, TEM, Zeta Potential, XRD	Capping of anionic bio-compounds, Bio-organic compounds/proteins	(Namvar et al., 2015)
Turbinaria conoides	12-57 nm, anistropic, poly-dispersed	Higher catalytic activity for reduction of aromatic nitro compounds and organic dye molecules	UV-Vis, HR-TEM, FT-IR, DLS, Zeta potential	Polyphenolic substances, hydroxyl group may act as capping agent	(Ramakrishna et al., 2016)
Sargassum tenerrimum	5–45 nm, anistropic, poly-dispersed	Dose dependent degradation of dyes like Rhodamine B, Sulforhodamine 101	UV-Vis, HR-TEM, FT-IR, DLS, Zeta potential	Secondary metabolites such as amino acids, alkaloids, carbohydrates, flavonoids, saponins, sterols, tannins, proteins and phenolic acids, hydroxyl group may act as capping agent	(Ramakrishna et al., 2016)
Cystoseira baccata	8.4 ± 2.2 nm, spherical, polycrystalline	Cytotoxic effect against human colon cancer cell lines HT-29 followed by Caco-2; biocompatibility with healthy cell line PCS-201-010	UV–Vis, TEM, HR-TEM, STEM, EELS, EDS, FT-IR, Zeta potential	Bioreduction by polyphenols and polysaccharides; Capping by proteins; Metal complexation by sulfonic groups from polysaccharides	(González-Ballesteros et al., 2017)

Table 5
Red algae mediated synthesis of gold nanoparticles (Au-NPs).

Macroalgae	Size & Morphology	Application/Activity	Characterization	Bioreductant and capping agent	Reference
Kappaphycus alvarezii	10–40 nm, polydisperse	Antibacterial against *Pseudomonas flouresences, S. aureus*	UV-Vis, XRD, TEM, FT-IR,FAAS	Extracellular, polyphenol compounds	(Rajasulochana et al., 2012)
Chondrus crispus	30–50 nm, spherical, polyhedral	Synthesis and possible route of metal recovery by sorption on the biomass surface	UV-Vis, TEM, SEM, EDS, FT-IR, FAAS	Stabilised in solution by amide I & II of proteins and xanthates	(Castro et al., 2013)
Galaxaura elongata	3.85–77.13 nm, rod, triangular, truncated, triangular, hexagonal	Antibacterial against *E. coli, K. pneumonia, S. aureus* and *Pseudomonas aeruginosa*	TEM, FT-IR, Zeta Potential, GC-MS, HPLC	Palmitic acid acts as stabilizing agent. Epigallocatechin catechin and epicatechin gallate are polyphenol compound as capping agents	(Abdel-Raouf et al., 2017)
Gracilaria corticata	45–57 nm	Gram +ve: *S. aureus, Enterococcus faecalis* Gram -ve: *E. coli, Enterobacter aerogenes* Antioxidant study by DPPH and ferric ion reducing ability	UV-Vis, SEM	Bioreduction	(Naveena and Prakash, 2013)
Lemanea fluviatilis (L.)	5–15 nm, nearly spherical polydispersed,	Antioxidant activity	UV-Vis, XRD, FT-IR, DLS, TEM, XRD	Protein and other organic molecules, extracellular	(Sharma et al., 2014b)

comparatively cheaper and convenient for downstream processing (Shakibaie et al., 2010).

Using dried biomass of a fresh water green alga, *Prasiola crispa* resulted in extracellular biosynthesis of highly stable nearly spherical Au-NPs. The progress of the reaction was routinely monitored by UV-Vis spectrum and colour change (yellow to purple). SPR band around 530 nm was observed after 1 h, which red shifted to 535 nm after 12 h, due to an increase in size with time. The differential intensity related to particle size distributions of Au-NPs was obtained from DLS study, which revealed average particle diameter and the cumulative mean diameter to be 10.0 ± 8.6 nm and 30.1 nm respectively. Greater particle size and high polydispersity observed in DLS in comparison to TEM are attributed to the fact that the measured size also included the biomaterials covering the surface of Au-NPs (Sharma et al., 2014a).

While searching for a suitable algal bioreagent for monodispersed Au-NPs, Parial and Pal (2015) reported a marine macroalgal strain *Rhizoclonium fontinale* which synthesized monodispersed gold nanospheres of 16 nm size with a maximum yield at pH 9. Variation in the physicochemical growth parameters like cell wall thickening, rapid akinete formation, pigment loss, giant cell formation, pyknosis, and purple coloration of the filaments during algae-gold interaction provided evidence for the synthesis of Au-NPs. In the context of obtaining better yield and monodispersed NPs, the effect of different concentrations of gold ions, biomass and pH of the reaction mixture were also studied. Maximum yield was obtained when alga was incubated for 72 h at pH 9 with 15 mg L^{-1} $AuCl_4^{-1}$. Polydispersed nanotriangles (15-88 nm), nanohexagons (34 nm) and nanorods (~100 × 51.5 nm) were formed at pH 5 and nanospheres at pH 7 (Parial and Pal, 2015).

Other strains in which *in-situ* synthesis of Au-NPs were reported are *Klebsormidium flaccidum* (Sicard et al., 2010; Dahoumane et al., 2012a), *Spirogyra submaxima* (Roychoudhury and Pal, 2014), and *Tetraselmis kochinensis* (Senapati et al., 2012). *Chlorella vulgaris* (Luangpipat et al., 2011), *Chlorella pyrenoidusa* (Oza et al., 2012), *Prasiola crispa* (Sharma et al., 2014a) produced gold nanospheres extracellularly with varied applications (Table 3).

5.1.3. Synthesis of gold nanoparticles from brown algae

After an exhaustive screening of a large number of marine brown algae, *Sargassum* spp. was reported as a promising candidate for the fabrication of gold nanoplates (Liu et al., 2005). Hexagonal, truncated triangular and triangular gold nanoplates were fabricated by the reduction of aqueous $AuCl_4^-$ ions from seaweed extract. Gold nanoplates of size 200-800 nm could be regulated by altering the initial concentration of the reactants. It was observed that the formation of gold nanoplates was dependent on various environmental factors such as the age of seaweed extract including reaction conditions such as pH, ionic concentration, temperature and time (Liu et al., 2005). Singaravelu et al. (2007) synthesized highly stable Au-NPs *via* the extracellular mode involving biotransformation of chloroauric acid. The bio-reduction process was highly efficient with nearly 95% of Au ions reduced to Au-NPs of size 8-12 nm within 12 h. A rapid bioprocess to scale up the yield of Au-NPs was developed (Singaravelu et al., 2007). Efficient recovery of Au-NPs was reported in *Fucus vesiculosus* and the process was nutrient independent, harmless and at a favourable neutral pH. This approach can replace the traditionally used hydrometallurgical method for gold recovery (Mata et al., 2009) (Table 4).

Novel brown alga *Ecklonia cava* was found to have potential reducing agents which help in the synthesis of Au-NPs. The appearance of ruby red colour after 1 min at 80 °C indicated the formation of Au-NPs with spherical and triangular morphologies with an average size of 30 ± 0.25 nm. UV-Vis spectra recorded at 532 nm attributed to the formation of Au-NPs. FT-IR spectra revealed that at 1628 cm^{-1} an N–H bend can be assigned to the 1° amine groups of the proteins. The intense medium absorbance at 1223 and 1031 cm^{-1} (C–N stretch) is the characteristic of the aliphatic amine groups. X-ray diffraction pattern showed high purity of biosynthesized Au-NPs which exhibited four

prominent Bragg reflections at around 38.39°, 44.54°, 64.89° and 77.72° which were indexed on the basis of face-centered cubic (fcc) of gold crystal planes corresponding to (111), (200), (220) and (311) respectively (Venkatesan et al., 2014).

González-Ballesteros et al. (2017) also demonstrated the biosynthesis of Au-NPs using aqueous extract of the brown alga *Cystoseira baccata* and $HAuCl_4$ solution (0.01 M) after 24 h with continuous stirring at room temperature. The reaction took place in few a minutes with progress of the reaction regularly monitored by UV-Vis spectroscopy. The end point was observed after 24 h as SPR peak intensity was stabilized at 532 nm. However, a slight dip in the pH (5.4 to 4.5) of the solution was noticed after the completion of the reaction. Au-NPs recovered were spherical in shape (mean diameter of 8.4 ± 2.2 nm), stable and polycrystalline in nature as demonstrated by TEM, HR-TEM, STEM and zeta potential measurements (González-Ballesteros et al., 2017).

5.1.4. Synthesis of gold nanoparticles from red algae

Presently there are very few reports which are industrially significant on red algae mediated synthesis of Au-NPs. Abdel-Raouf et al. (2017) found aqueous and ethanolic extracts of *Galaxaura elongata* separately could assist the synthesis of Au-NPs. The time reported for bioreduction of ethanolic and aqueous extracts was 2–5 min and 3 h, respectively. The change in colour of the solution was observed in both instances; however, there was a slight shift in λ_{max} from 535 nm (aqueous) to 536 nm (ethanol) which affirmed the synthesis of Au-NPs. While FT-IR determined that the carbonyl group of amino acids and peptides of proteins was responsible for capping, GC-MS and HPLC determined that the exact compound involved as stabilizing agent was palmitic acid and capping of Au-NPs was done by polyphenol compounds (epigallocatechin, catechin and epicatechin gallate) (Abdel-Raouf et al., 2017). An aqueous extract of *Lemanea fluviatilis*, an edible freshwater epilithic red alga, was used to biosynthesize Au-NPs. The initial yellow colour of chloroauric acid solution turned to red in 12 h. SPR band at 530 nm affirmed the synthesis and stability as colour was retained for 3 months. Polydispersed, crystalline, nearly spherical NPs of 5-15 nm were synthesized. HR-TEM revealed lattice fringes between the two adjacent planes to be 0.231 nm apart which corresponded to the interplanar separation of the (111) plane of face-centered cubic (fcc) Au-NPs. FT-IR revealed algal proteins were responsible for the reduction and stabilization of the Au-NPs (Sharma et al., 2014b). The majority of Au-NPs obtained from red algae are either rich in antioxidant activity (Sharma et al., 2014b) or have probable applications in therapeutics (Naveena and Prakash, 2013) (Table 5).

5.2. Silver nanoparticles

Silver is known to be a good conductor of heat and electricity, however, the high price limits its application in the electrical industry (Keat et al., 2015). For some time, the antimicrobial potential of silver has been explored in many medical fields, and has been successfully tested against 650 pathogenic microbes (Annamalai and Nallamuthu, 2016). Among the various noble metallic NPs known so far silver NPs (Ag-NPs) have gained the most attention, exhibiting the highest level of commercialization, accounting for 55.4% of the NMs based consumer products existing in the market (313 out of 565) (Agnihotri et al., 2014). Consequently, nanosilver is eventually becoming the nucleus of the nano-industry. Ag-NPs have been synthesised from different microalgae and macroalgae belonging to *Cyanophyceae* (Table 6), *Chlorophyceae* (Table 7), *Rhodophyceae* (Table 8) and *Phaeophyceae* (Table 9).

5.2.1. Synthesis of silver nanoparticles from cyanobacteria

Plectonema boryanum UTEX 485 was explored for the synthesis of Ag-NPs for the first time by Lengke et al. (2007a). Both intracellular and extracellular modes of synthesis were reported with considerable variation in the size of NPs from less than 10 nm and 1–200 nm

Table 6
Cyanobacteria mediated synthesis of silver nanoparticles (Ag-NPs).

Microalgae	Size & Morphology	Application/Activity	Characterization	Bioreductant and capping agent	Reference
Plectonema boryanum UTEX 485	Intracellularly (< 10 nm) and extracellularly (1–200 nm), octahedral	Temperature-dependent size control of NPs	TEM, XPS, TEM-EDS	Utilizing nitrate by reducing nitrate to nitrite and ammonium, which is fixed as glutamine before death	(Lengke et al., 2007a)
Oscillatoria willei NTDM01	10–25 nm, spherical		UV-Vis, SEM, EDS, FT-IR	Extracellular, reduced in the presence of nitrate reductase, and stabilized by the capping peptide tyrosine and tryptophan	(Ali et al., 2011)
Spirulina platensis	10–15 nm, fcc	Live algal mass can used for synthesis	UV-Vis, XRD, TEM	Cellular reductases	(Mahdieh et al., 2012)
Aphanothece spp., *Oscillitoria* spp., *Microcoleus* spp., *Aphanocapsa* spp., *Phormidium* spp., *Lynhbya* spp.	44-79 nm, spherical	Antimicrobial against Gram + ve: *S. aureus, E. faecalis* Gram -ve: *E. coli, E. aerogenes*	UV-Vis, SEM, EDX	Bioactive compounds	(Sudha et al., 2013)
Spirulina platensis	30–50 nm, spherical	Gram-ve: *E. coli, Proteus vulgaris, K. pneumoniae* Gram +ve: *S. aureus, S. epidermidis, B. cereus*	UV-Vis, SEM, TEM, and FT-IR	Monosubstituted amide of proteins	(Sharma et al., 2015b)
Cylindrospermum stagnale NCCU-104	38–88 nm, pentagonal	Extracellular cell free biosynthesis	UV-Vis, SEM	Proteins in the cell extract	(Husain et al., 2015)
Microchaete NCCU-342	60–80 nm, spherical, polydispersed	Degradation of azo dye methyl red.	UV-Vis, TEM, DLS, Zeta potential	Cellular metabolites	(Husain et al., 2019)

Table 7
Green Algae mediated synthesis of nanoparticles (Ag-NPs).

Microalgae	Size & Morphology	Application/Activity	Characterization	Bioreductant and capping agent	Reference
Microalgae					
Chlorella vulgaris	11.2 nm rods, 28.3 ± 3.1 nm triangular	Ag nanoplates was found to be a kinetically controlled process, depending on the ratio of carboxyl groups to Tyr per peptide molecule, as a result of the interactions between carboxyl groups with Ag ions, Ag reaction intermediates, and Ag surface	UV-Vis, FESEM, HR-TEM	Simple bifunctional tripeptide (DDY-OMe) with one Tyr residue as the reduction source and two carboxyl groups in the Asp residues as shape directors	(Xie et al., 2007a)
Nannochloropsis oculata, Chlorella vulgaris	15 nm, fcc	Cost effective, ecofriendly	AAS, XRD, TEM	Extracellular production, Protein	(Mohseniazar et al., 2011)
Chlamydomonas reinhardtii	Rounded/rectangular *in vitro* 5 ± 1 to 15 ± 2 nm *in vivo* 5 ± 1 to 35 ± 5 nm	Understanding the role of diverse cellular protein in the synthesis and capping	UV-Vis, ICP- MS, SEM, TEM, EDAX, MALDI-TOF, MS	Cellular proteins *viz* histone (H4), CA, FNR, SOD, SBPase, ATP synthase, RuBP carboxylase, and OEE.	(Barwal et al., 2011)
Chlorella sp.	34 nm, spherical, fcc	Scale up method	UV-Vis, XRD, FT-IR, SEM	Enzymes or Protein	(Elumalai et al., 2013)
Chlorococcum humicola	16 nm, spherical	Gram -ve: *E.coli*	UV-Vis, XRD, SEM, EDX, TEM, FT-IR	Intracellular and extracellular synthesis, protein molecules	(Jena et al., 2013)
Scenedesmus sp.	36 nm, spherical, fcc	Biological synthesis	UV-Vis, XRD, FT-IR, SEM	Enzymes or protein	(Elumalai et al., 2013)
Scenedesmus	15–20 nm, spherical,	Gram +ve: *S. mutans* Gram -ve: *E. coli*	AAS, UV-Vis, TEM, XRD, FT-IR, DLS, TGA	Intracellular, extracellular synthesis biomolecules, proteins and peptides	(Jena et al., 2014)
Euglena gracilis	15–60 nm, spherical, polydisperse	Comparison of *in vitro* and *in*B203 *vivo* both	UV-Vis, ICP-AES, HR-TEM, EDAX, FT-IR	Primary amines of proteins	(Li et al., 2015a)
Euglena intermedia	6–24 nm, spherical, polydisperse	Comparison of *in vitro* and *in vivo* both	UV-Vis, ICP-AES, HR-TEM, EDAX, FT-IR	Primary amines of proteins	(Li et al., 2015a)
Chlorella vulgaris	8–20 nm, fcc	Cost effective bioreactor for the conversion of ionic form of metals to NMs	UV-Vis, XRD, FT-IR, TEM, DLS, Zeta Potential, SEM-EDAX,	Extracellular, aromatic groups in the protein moiety	(Satapathy et al., 2015)
Chlorella vulgaris	50–70 nm	Synthesis of NPs using the algal biomass produced by waste water treatment	UV-Vis, SEM, FT-IR	Amines, phenols and alcohols, ethers and aromatic rings as reducing agents	(Karthikeyan et al., 2015)
Chlorella pyrenoidosa	5–20 nm with average 12 nm, fcc	Gram -ve: *K. pneumoniae, A. hydrophila, Acenetobacter* sp.; Gram +ve: *S. aureus;* Photocatalytic agent: Degradation of methylene blue	UV-Vis, XRD, SEM-EDS, TEM, XRD, FT-IR,	(NH)C=O group within the cage of cyclic peptides	(Aziz et al., 2015)
Euglena gracilis	47 nm	-	UV-Vis, DLS, Zeta Potential, ToF-SIMS, ICP-MS	-	(Li et al., 2015b)
Chlorella vulgaris	5–50 nm, fcc	Gram -ve: *E. coli, P. aeruginosa,* Fungus: *Candida albicans*	UV–vis, FT-IR, SEM, XRD, TEM, SAED	Protein moieties	(Annamalai and Nallamuthu, 2016)
Macroalgae					
Ulva reticulata	40–50 nm, spherical	-	UV-Vis, FT-IR,SEM, XRD	Carboxylic acids, benzene rings, fluoroalkanes	(Dhanalakshmi et al., 2012)
Enteromorpha compressa	40–50 nm, spherical	-	UV-Vis, FT-IR,SEM, XRD	Benzene rings and hydrogen bonded alcohols	(Dhanalakshmi et al., 2012)
Urospora sp	20–30 nm, fcc, spherical	Gram +ve: *S. aureus, B. subtilis;* Gram -ve: *E.coli, P. aeruginosa, K. pneumonia,*	UV-Vis, XRD, FT-IR, HR-TEM	Hydrogen bonded hydroxyl group, carbonyl and alcoholic group	(Suriya et al., 2012)
Ulva fasciata	28–41 nm, spherical	*Xanthomonas campestris* pv. *Malvacearum*	UV-Vis, FT-IR, XRD, SEM and EDX.	1-(Hydroxymethyl)–2, 5, 5, 8A-tetramethyl decahydro-2-napthalenol as reducing agent; Hexadecanoic acid as stabilizing agent	(Rajesh et al., 2012)
Ulva lactuca	20–56 nm, spherical	Anticancer: Hep2, MCF7 and HT29 cancer cell lines	UV-Vis, FT-IR, XRD, SEM, TEM, EDAX,	Release of protein molecules	(Devi and Bhimba, 2012)
Chaetomorpha linum	3–44 nm, 30 avg.	Non toxic method	UV-Vis, FT-IR, SEM	Peptides (secondary amines), flavonoids and terpenoids	(Kannan et al., 2013a)
Ulva lactuca	48.9 nm, spherical	Photocatalytic degradation of methyl orange dye	U-Vis, FT-IR, Zeta Potential, HRSEM, XRD,	phenolic compounds, amines and aromatic ring	(Kumar et al., 2013a)
Ulva faciata,	7–20 nm, spherical	Antimicrobial	UV-Vis, TEM, FT-IR, GLC	-C-O- groups of polyols of polysaccharides; -C-O-SO_4- of sulphated polysaccharides.	(El-Rafie et al., 2013)
Codium capitatum	3–44 nm, 30 avg.	First report on using seaweed from the widespread *Codium* genus, non toxic	UV-Vis, EDX, FT-IR,	Amine, peptide and sulphate groups	(Kannan et al., 2013b)

(*continued on next page*)

Table 7 (*continued*)

Microalgae	Size & Morphology	Application/Activity	Characterization	Bioreductant and capping agent	Reference
Enteromorpha flexuosa (wulfen) J.Agardh	15 + 1.5 nm, circular	Gram + ve: *B. subtilis, S. aureus, E. faecalis, S. epidermidis,* Gram -ve: *E.coli, K. pneumonia* Fungus: *C. albicans, S. cerevisiae*	UV-Vis, XRD, TEM, EDS	Amines, peptides and secondary metabolites	(Yousefzadi et al., 2014)
Ulva lactuca	20 nm, spherical	Gram + ve: *Bacillus* sp., Gram -ve: *Pseudomonas* sp., *E.coli*	UV-Vis, XRD, TEM, SEM, FT-IR	Aromatic compound or alkanes or amine	(Sangeetha and Saravanan, 2014)
Ulva lactuca	20–50 nm, spherical	Gram + ve: *Bacillus* sp., *S. aureus* Gram -ve: *E. coli, K. pneumonia, P. aeruginosa* Fungus: *C. albicans, A. niger, C. parapsilosis*	UV-Vis, TEM, XRD, SEM, EDAX, TGA	Release of extracellular protein molecules	(Bhimba and Kumari, 2014)
Caulerpa racemosa	5–25 nm, 10 nm, fcc	Gram + ve: *S. aureus* Gram -ve: *P. mirabilis*	UV-Vis, XRD, TEM, FT-IR	Cyclic peptides in stabilization and reduction	(Kathiraven et al., 2015)
Ulva flexousa	2–32 nm, circular, fcc	Method of synthesis at room temperature.	UV-Vis, XRD, FT-IR, TEM	Peptides are involved in reduction, cage of cyclic peptides in stabilization	(Rahimi et al., 2014)
Ulva lactuca	20–35 nm, cubical, fcc	Control of malarial plasmids. *P. falciparum.*	UV–vis, FT-IR, EDX, SEM, XRD	Organic components	(Murugan et al., 2015)
Pithophora oedogonia	25–44 nm, cubical and hexagonal-shaped	Gram -ve: *E. coli, P. aeruginosa, V. Cholera, Shigella flexneri* Gram + ve: *B. subtilis, S. aureus, Micrococcus luteus*	UV-Vis, EDS, SEM, DLS, FT-IR	Phytochemicals as reducing agents and protein as capping agents	(Sinha et al., 2015)
Spirogyra	40-80 nm, spherical	First report for using Ag_2SO_4 as a salt Gram + ve: *S. aureus* Gram -ve: *E. coli*	UV-Vis, FT-IR, TEM and NTA	Proteins	(Pinjarkar et al., 2016)
Spirogyra varians	17.6 nm, fcc structure, quasi-spheres	Gram + ve: *S. aureus, B. cereus, L. Monocytogenes* Gram -ve: *S. typhimurium, E. coli, P. aeruginosa, Klebsiella*	UV-Vis, XRD, FT-IR, SEM	Amino, carboxylic, hydroxyl and carbonyl groups, quinine	(Salari et al., 2016)
Caulerpa serrulata	10 ± 2 nm, spherical, fcc structure	Catalytic reduction of Congo red Antibacterial activity Gram + ve : *S. aureus* Gram –ve: *Salmonella typhi, E. coli, P. aeruginosa, Shigella*	UV-Vis, FT-IR, XRD, HR-TEM, ^1H and ^{13}C NMR	Caulerpenyne and/or its derivatives	(Aboelfetoh et al., 2017)

respectively. They observed a decline in nitrate concentration at 25 °C, which suggests the intracellular reduction of nitrate to ammonia. Ammonia is further converted to the amide group of glutamines, which shows that bioreduction of $AgNO_3$ to Ag-NPs is dependent on metabolic pathways of cyanobacteria. However, the release of organic moieties from dead cells attributed to extracellular bioreduction.

Tsibakhashvili et al. (2011) carried out extracellular synthesis *via Spirulina platensis* and studied the effect of short term and long term exposure of Ag ions along with its dependence on concentration. The shape and recovery of the NPs depend on both the factors *viz* on day 1, with the observation of scarcely dispersed 1 mM long $AgNO_3$ aggregates, and on day 5, NPs were distributed more uniformly on the surface of cells and were recovered completely (Tsibakhashvili et al., 2011). Cell free aqueous extract of *Microchaete* NCCU-342 was exposed to various cultural and physical conditions for optimizing synthesis of Ag-NPs. Optimal synthesis of Ag-NPs was obtained with biomass quantity of 80 μg/ml at pH 5.5 and 60 °C with UV light exposure (60 min) and 1 mM $AgNO_3$. Spherical, polydispersed NPs of size in the range of 60-80 nm were synthesized as revealed by TEM and DLS (Husain et al., 2019).

Screening of cyanobacterial species *Aphanothece, Oscillatoria, Microcoleus, Aphanocapsa, Phormidium, Lyngbya, Gloeocapsa,* and *Synechococcus,* isolated from mangroves was performed by Sudha et al. (2013) and *Microcoleus* spp could only fabricate spherical Ag-NPs with an average diameter of 55 nm. Cyanobacterial mediated synthesis of Ag-NPs at large scale was conducted by Sharma et al. (2015b) (Table 6).

5.2.2. Synthesis of silver nanoparticles from green algae

Over the past decade, researchers have proved the vitality of green microalgae in fabrication of Ag-NPs (Barwal et al., 2011; Jena et al., 2013; Annamalai and Nallamuthu, 2016). Xie et al. (2007b) used the extract of economically important unicellular green alga *Chlorella vulgaris,* for the synthesis of silver nanoplates. Synthesis of Ag nanoplates is a kinetically controlled process in which hydroxyl groups in tyrosine residues are the most active functional groups responsible for Ag^+ ion reduction and anisotropic growth and the shape control is regulated by carboxyl groups in Aspartic acid and/or Glutamic acid of the protein fraction in the extract (Xie et al., 2007a). Barwal et al. (2011) reported *in vitro* and *in vivo* biosynthesis of rounded and rectangular Ag-NPs from *Chlamydomonas reinhardtii*. *In vitro* synthesis was found to be slower, taking 13 days, and so-formed NPs possessed size in the range of 5 ± 1 to 15 ± 2 nm, while *in vivo* synthesis was a comparatively faster process which took 10 h, and the NPs produced were in the range of 5 ± 1 to 35 ± 5 nm. The formed NPs were in the peripheral cytoplasm and the basal body (end of the flagella). Such NPs were observed to be associated with oxidative reductive machinery and proteins involved in photosynthesis, stress response and ATP synthesis, i.e. ATP synthase, RUBP carboxylase, ferredoxin $NADP^+$ reductase, superoxide dismutase, sedoheptulose-1,7-bisphosphatase and oxygen evolving enhancer proteins. The involvement of these proteins was confirmed by the alteration in size and biosynthesis rate of NPs in protein-depleted fractions (Sharma et al., 2016).

Chlorophyte *Chlorococcum humicola* was exploited for intracellular and extracellular biosynthesis of Ag-NPs using fresh extracts (*in vitro*) and whole cells (*in vivo*) (Jena et al., 2013). After incubation of algal extract and whole cells with $AgNO_3$ (5 mM) solution for 48 h at 28 °C, spherical, crystalline Ag-NPs ranging from 2 to 16 nm with fcc geometry were obtained. The binding of proteins to the Ag-NPs through free amine groups, cysteine residue and electrostatic attraction of carboxylic groups in the cell wall was reported which probably stabilized the Ag-NPs as revealed by FT-IR (Jena et al., 2013; Sharma et al., 2016). *Chlorella* spp. was tailored for the synthesis of Ag-NPs both intracellularly and extracellularly for their application as antibacterial agents (Satapathy et al., 2015; Annamalai and Nallamuthu, 2016), in wastewater treatment (Karthikeyan et al., 2015; Aziz et al., 2015) and for large-scale synthesis (Elumalai et al., 2013) (Table 7). Li and co-

Table 8
Red Algae mediated synthesis of nanoparticles (Ag-NPs).

Macroalgae	Size & Morphology	Application/Activity	Characterization	Bioreductant and capping agent	Reference
Gelidiella acerosa	22 nm, spherical, fcc	Antifungal against *Humicola insolens, Fusarium dimerum, Mucor indicus, Trichoderma reesei*	UV-Vis, SEM, TEM, XRD, FT-IR,	Aromatic compound or alkanes or amines	(Vivek et al., 2011)
Gracilaria edulis	12.5–100 nm, spherical	Downstream processing	UV-Vis, SEM, TEM, XRD, FT-IR,	Proteins while terpenoids are implicated in stabilization extra cellular synthesis	(Murugesan et al., 2011)
Acanthophora spicifera	48 nm, spherical	Antimicrobial against biofilm forming bacteria *S. typhii* and *S. flexneri*	UV-Vis, FT-IR, TEM	Alcohols and phenols, carboxylic acids and its derivatives and chloroalkanes	(Kumar et al., 2012b)
Gelidiella sp.	40–50 nm, spherical	Anticancer against Hep 2 cell lines	UV-Vis, XRD, FT-IR, SEM, EDS,	Protein molecules	(Devi et al., 2012)
Gracilaria dura	6.0 ± 2 nm, sphere	Antibacterial against *B.pumilus,* food preservation and wound dressing	EDX, SAED, XRD, TGA, DSC, TEM	Polymer	(Shukla et al., 2012)
Kappa phycus sp	52–104 nm	-	UV-Vis, AFM, FT-IR,	-	(Baskar, 2013)
Kappaphycus alverazii	73 nm, fcc	-	UV-Vis, XRD, FT-IR, SEM, EDX,	Polysaccharides and -C-O groups of glycogen	(Ganesan et al., 2013)
Gracilaria corticata	18–46 nm	Antifungal activity against *C. albicans* and *C. glabrata*	UV-Vis, FT-IR, TEM, DLS, Zeta Potential	Phenolic compounds, amide I group and aromatic rings were responsible for stabilization	(Kumar et al., 2013b)
Pterocladia capillacae,	7 nm, spherical	Gram +ve: *S.aureus* Gram -ve: *E.coli*	UV-Vis, TEM, FT-IR, GLC	Reducing sugar, carbonyl groups and sulphated polysaccharides	(El-Rafie et al., 2013)
Jania rubins	12 nm, spherical	Gram +ve: *S.aureus* Gram -ve: *E.coli*	UV-Vis, TEM, FT-IR, GLC	Carbonyl group from amino acid residues and proteins	(El-Rafie et al., 2013)
Gracilaria edulis	55–99 nm, fcc, spherical,	Anticancerous against Human PC3 cell lines and non-toxic to normal Vero cell lines	UV-Vis, EDX, FT-IR, FESEM, XRD	Free and bound amide groups	(Priyadharshini et al., 2014)
Gracilaria birdiae	20.3 nm, spherical	Gram -ve: *E.coli*	UV-Vis, TEM, FT-IR, DLS, Zeta Potential,	Reduction of the silver ions is coupled to the oxidation of the hydroxyl and carbonyl group	(de Aragao et al., 2016)
Acanthophora specifera	33–81 nm, cubic	Gram +ve: *S. aureus, B. subtillis*; Gram -ve: *Salmonella sp., E. coli* Fngus: *C. albicans*	XRD, FT-IR	Monosaccharide, polysaccharide, uronic acids and secondary metabolites	(Ibraheem et al., 2016)
Amphiroa fragilissima	Crystalline	Gram +ve: *B. subtilis, S. aureus*; Gram -ve: *E. coli, K. pneumonia, P. aeruginosa*	UV-Vis, FT-IR, XRD and	Peptides	(Sajidha and Lakshmi, 2016

Table 9
Brown algae mediated synthesis of nanoparticles (Ag-NPs).

Macroalgae	Size & morphology	Application/Activity	Characterization	Bioreductant and capping agent	Reference
Sargassum wightii grevilli	8–27 nm, spherical,	Gram +ve :*S. aureus, B. rhizoids* Gram -ve: *E. coli, P. aeruginosa*	UV-Vis, FT-IR, XRD, HR-TEM	Extracellular, oxidation of alcoholic group to aldehyde, carboxylate ions	(Govindaraju et al., 2009)
Sargassum ilicifolium	33–40 nm, spherical	Gram +ve: *S. aureus* Gram -ve: *E. coli, K pneumoniae, S. typhii, Vibrio cholera;* Cytotoxic against *Artemia salina*	UV-Vis, SEM, TEM	Biologically active compounds	(Kumar et al., 2012a)
Sargassum plagiophyllum	20–50 nm, spherical	-	UV-Vis, FT-IR,SEM, XRD	Presence of primary amines, carboxylic acids, benzene rings, acetates in the phytochemicals	(Dhanalakshmi et al., 2012)
Sargassum polycystum	5–7 nm, spherical, fcc	Gram +ve: *S. aureus* Gram -ve: *E. coli, P. aeruginosa, K. pneumonia* Anticancer against MCF-7 breast cancer cell lines	UV-Vis, FT-IR, HR-TEM, XRD, GC-MS	Hexadecane, hexadecanoicacid, cis -9- octadecanol, 1-eicosanol, octadecanoic acid	(Thangaraju et al., 2012)
Padina pavonica	10-72 nm, spherical, polydisperse	Cotton pathogens: Fungus: *Fusarium oxysporum* Bacteria: *Xanthomonas campestris*	UV-Vis, FT-IR, XRD, SEM, TEM.	Extracellular, terpenoids	(Sahayaraj et al., 2012)
Padina tetrastromatica	14 nm, spherical	Gram +ve: *Bacillus* spp, *B. Subtilis* Gram -ve: *Klebsiella planticola, Pseudomonas* sp	UV-Vis, XRD, TEM, FT-IR	Broalkanes engage in recreation the foremost role in the NPs synthesis	(Rajeshkumar et al., 2012b)
Turbinaria conoides	96 nm, spherical	Gram +ve: *B. subtilis* Gram -ve: *K. planticola*	XRD, SEM, FT-IR, UV-Vis	Amines and polyphenols	(Rajeshkumar et al., 2012a)
Padina gymnospora	25-40 nm, spherical	Gram +ve: *B.cereus* Gram -ve: *E. coli*	UV-Vis, TEM	Aqueous extract of *Padina gymnospora*	(Shiny et al., 2013)
Colpmenia sinusa	20 nm, spherical	Gram +ve: *S.aureus* Gram -ve: *E.coli*	UV-Vis, TEM, FT-IR, GLC	-C-O- groups of polyols of polysaccharides; -C-O-SO_4- of sulphated polysaccharides.	(El-Rafie et al., 2013)
Cystophora moniliformis	75 nm, fcc	Temperature-dependent variation of the size of NPs	XRD, UV-Vis, SEM, DLS EDAX, Zeta Potential	Metabolites, phenolic compounds	(Prasad et al., 2013)
Sargassum cinereum	45 to 76 nm, triangular	Gram +ve: *S. aureus,* Gram -ve: *S. typhi, E. aerogenes, P. vulgaris*	UV-Vis, SEM		(Mohandass et al., 2013)
Sargassum longifolium	30 nm, cubical	Anticancer against Hep 2 cell line	UV-Vis, SEM, EDS, FT-IR,	Extracelluar, terpenoids with aldehyde, ketone, carboxylic acid groups, carbonyl group form amino acid residues that form the NP capping	(Devi et al., 2013)
Sargassum muticum	5–15 nm, spherical	Antifungal, antiviral, antiplatelet, antiangiogenesis	FT-IR, XRD, TEM, UV–Vis	Sulfate and hydroxyl moieties of polysaccharides	(Azizi et al., 2013)
Scaberia agardhii	40–50 nm, polydispersed	Soil microbial community	UV-Vis, SEM, EDAX	Proteins/ enzyme in cell wall	(Prasad and Elumalai, 2013)
Turbinaria conoides	2–17 nm, spherical, fcc	*E. coli*, followed by *Salmonella* sp., *S. liquefaciens*, *A. hydrophila* Cytotoxicity & anticrustacean: *Artemia salina*	UV-Vis, FT-IR, XRD, FESEM, EDX, and HR-TEM, CLSM	Free hydroxyl group and a carboxylic acid group	(Vijayan et al., 2014)
Sargassum longifolium	40–85 nm, spherical, fcc	Antifungal: *A. fumigatus, C. albicans, Fusarium* sp. *S.longifolium*	SEM, XRD. TEM. FT-IR, UV-Vis, EDX	Proteins for capping; carboxylic groups involved in stability	(Rajeshkumar et al., 2014)
Sargassum polycystum C. Agardh	-	Antibacterial: *E. coli, Streptococcus pyogenes, P. aeruginosa, S. flexneri, Morengilla morrgani;* Cytotoxic: Dalton's lymphoma ascites (DLA)	UV-Vis, FT-IR, XRD	Capped by proteins and metabolites such as phenolic acid, carboxylic acid and flavonoids	(Kanimozhi et al., 2015)
Sargassum vulgare	10 nm, spherical	Anticancer: Human myeloblastic leukemic cells HL60, cervical cancer cells HeLa	TEM, FACS, XRD, HR-TEM, FT-IR, EDX	Alginate moieties, secondary OH groups	(Govindaraju et al., 2015)
Turbinaria ornata	22 nm, spherical, polydisperse	Gram +ve: *B. litoralis, Bacillus* sp., *Micrococcus* sp., *Corynebacterium* sp., *S. aureus* Gram -ve: *Flavobacterium* sp., *Pseudomonas* sp., *Shigella* sp., *Aeromonas* sp., *V. cholerae, E. coli, Salmonella* sp., *E. aerogens, Klebsiella* sp., *Chromohalobacter* sp. *Artemia marina* and *Balanus Amphitrite*	UV-Vis, FE-SEM, EDS, XRD, FT-IR	Organic moieties as stabilizing agents	(Krishnan et al., 2015)
Sargassum muticum	43–79 nm, spherical, crystalline, fcc	Ovicidal and ovideterrent activity against *Aedes aegypti, Anopheles stephensi,* and *Culex quinquefasciatus* Gram +ve: *B. subtilis* Gram –ve: *S. typhi* and *K. pneumoniae*	UV–Vis, FT-IR, SEM, EDX, and XRD	Sulfate or hydroxyl groups	(Madhiyazhagan et al., 2015)

workers (2015b) for the first time reported *in vitro* and *in vivo* biosynthesis of Ag-NPs from *Euglena* spp. and found that the decreased concentrations of silver ions in the solutions, which were treated with *Euglena gracilis* and *Euglena intermedia* were almost equal. They also confirmed that concentration of chlorophyll plays a role in controlling the size and primary amines are the potential bioreductants (Li et al., 2015b).

In addition, other green algal species like *Nannochloropsis oculata* (Mohseniazar et al., 2011), *Chlorococcum humicola* (Jena et al., 2013), *Euglena gracilis* (Li et al., 2015a), *Scenedesmus* sp. (Jena et al., 2014) etc. have been reported to synthesize Ag-NPs with variable shapes and applications (Table 7). Other macroalgae have been investigated extensively for the synthesis of Ag-NPs are *Enteromorpha compressa* (Dhanalakshmi et al., 2012), *Urospora* sp. (Suriya et al., 2012), *Codium capitatum* (Kannan et al., 2013b), *Pithophora oedogonia* (Sinha et al., 2015) and *Spirogyra varians* (Salari et al., 2016) (Table 7).

During synthesis of Ag-NPs, chromatic changes in the reaction mixture act as a visual marker affirming the continuity of the process. Kannan et al., 2013b observed an obvious change of brown to yellow colour after 48 h during reduction of $AgNO_3$ by the extract of *Codium capitatum* and a time-dependent increase in brown colour intensity at 422 nm. Moreover during reduction of $AgNO_3$ by *Chaetomorpha linum* extract, the same colour change was observed within 30 minutes and with the increase in incubation time, the brown colour intensity decreased at 422 nm *viz* characteristic absorption peak of Ag-NPs (Kannan et al., 2013a). The role of amines and peptides in reduction and stabilization of NPs was the same in both the cases (Kannan et al., 2013a, 2013b).

Ulva lactuca, cheap seaweed readily available in the coastal areas of south India has been widely exploited as a facile method of synthesis by various scientific groups. The synthesized Ag-NPs have varied applications (Table 7). Kumar et al. (2013a) successfully fabricated spherical Ag-NPs with an average size of 48.59 nm at room temperature within 48 h of incubation, biometrically (Table 7).

5.2.3. Synthesis of silver nanoparticles from red algae

Coralline algae (red seaweeds) grow extensively in the marine environment, which are being used for commercial production of agar and its derivatives (Table 8). Unlike the conventional green synthesis approaches, a rapid and novel microwave-mediated protocol was devised by Priyadharshini et al. (2014) for the synthesis of Ag-NPs extracellularly from *Gracilaria edulis*. The presence of quinines in the aqueous extract was found to be responsible for the synthesis of nanospheres of 55-99 nm size which was confirmed by FT-IR and FE-SEM. Vivek et al. (2011) obtained spherical Ag-NPs of an average size of 22 nm using the aqueous extract of the red alga *Gelidiella acerosa*. Ag-NPs present in the filtrate were well distributed as non-aggregates and showed a broad λ_{max} peak at 408 nm. Aromatic compounds, alkanes or amines were attributed to be the capping ligand of the Ag-NPs (LewisOscar et al., 2016). The algal polysaccharides present in the decoction of *Gracilaria birdiae* played triple roles, i.e. complex formation with silver ions, control of reduction and stabilization of Ag-NPs. Effect of pH and polysaccharide concentration of (0.02, 0.03 and 0.05%, v/v) was done to optimize the process. The resulting NPs were effective against *Escherichia coli* (de Aragão et al., 2016) (Table 8).

5.2.4. Synthesis of silver nanoparticles from brown algae

Prasad et al. (2013) employed Australasian brown marine alga *Cystophora moniliformis* for the first time. Effect of temperature on the size and agglomeration showed that at temperatures lower than 65 °C, spherical Ag-NPs with size range 50-100 nm and higher temperatures up to 95 °C, NPs of size greater than 2 μm were formed. The NPs so formed were of crystalline nature with FCC geometry as suggested by XRD pattern (Prasad et al., 2013). Madhiyazhagan et al. (2015) reported the synthesis of crystalline spherical Ag-NPs with FCC geometery, ranging from 43 to79 nm in size using the aqueous extract of the seaweed *Sargassum muticum*. The synthesis of silver nanospheres was confirmed through visual assessment as the colour of the solution turned from yellowish light brown to dark brown after the addition of 1 mM $AgNO_3$ to 5% (w/v) algal extract at 95 °C. Initially no SPR peaks were observed however after 120 min of incubation, a characteristic SPR band of Ag-NPs at 420 nm was reported and the peak steadily increased over time indicating the saturation of the peak along with complete reduction of $AgNO_3$ (Madhiyazhagan et al., 2015) (Table 9).

5.3. Algae-mediated synthesis of other nanomaterials

As discussed in the previous sections, different types of algal species were reported to synthesize gold and silver NPs. Synthesis of various other NPs such as ZnO-NPs, TiO_2, CdS, Pt, Pd, Fe_3O_4 have also been reported (Table 10). Lengke et al. (2006b) for the first time developed an alternative method to abiotic chemical methods for the synthesis of platinum NPs and platinum (II) organics from *Plectonema boryanum UTEX 485*. They investigated synthesis at temperatures ranging from 25 to 180 °C, and the optimal temperature was found to be 29 °C. The resulting NPs were spherical, connected with bead-like organic moieties released from dead cyanobacterial cells. However, the size could not be systematically studied as the variation in temperature and time was huge. Crystallization and re-crystallization were affected by temperature, at lower temperature amorphous behaviour was observed contrary to the crystalline structure at higher temperature (180 °C) (Lengke et al., 2006b). *Phormidium* was found to be a suitable candidate for the extracellular synthesis of copper NPs. The reduction of cationic copper was believed to be done by a 25 kDa metal chelating protein moiety in aerobic conditions at neutral pH and room temperature. The role of proteins in the stabilization of NPs was confirmed by SDS- PAGE and FT-IR (Rahman et al., 2009). The aqueous cellular extract of diazotrophic cyanobacterial strain *Anabaena* L31 was exercised for the synthesis of ZnO-NPs conjugated with shinorine, water-soluble UV-B absorbent. A sharp decline in the surface charge of the conjugate from +30.25 mV to 3.75 mV resulted from the changes in the surface functionalities after conjugation formation (Singh et al., 2014a, 2014b, Pathak et al., 2019).

Aqueous extract from *Sargassum plagiophyllum* was reported successfully for the fabrication of AgCl-NPs (Dhas et al., 2014) (Table 10). Advanced characterization techniques like UV-Vis, FT-IR, FE-SEM, HR-TEM and XRD were employed to confirm the formation of AgCl-NPs which could be used as antimicrobial agents (Dhas et al., 2014). While screening a candidate for the synthesis of ZnO-NPs, *Sargassum myriocystum* was found to be suitable and process optimization was done for its synthesis (Azizi et al., 2014). To optimize parameters resulting in the synthesis of 36 nm sized ZnO-NPs extracellularly, pH, temperature, concentration of seaweed extract and metal concentration were studied. *Sargassum muticum* was also reported to biosynthesize hexagonal ZnO-NPs with an average size of 4 nm (Azizi et al., 2014). *Sargassum muticum* is so far the only algal species whose aqueous extract could manoeuvre cubic Fe_3O_4 NPs at room temperature. Apart from XRD, FT-IR, FE-SEM, ED-XRF and TEM, vibrating sample magnetometer (VSM) was studied to check the magnetic behaviour. FT-IR revealed sulphated polysaccharides were efficient stabilizers and bioreductants (Mahdavi et al., 2013).

A rapid and simple method for complete reduction of Pd (II) ions to Pd NPs by aqueous extract *Chlorella vulgaris* was demonstrated by Arsiya et al. (2017). Gradual colour change of the solution from yellow to dark brown indicated the formation of Pd-NPs. The reaction was completed in 10 min as the characteristic peak of Pd (II) ions at 410 and 420 nm disappeared. Furthermore, the formation of Pd-NPs was confirmed by SPR peak range at 370-440 nm. Polyol and amide groups of the extract were assumed to be responsible for the reduction and stabilization as strong and intense peaks were observed at 1051 cm^{-1} (Carbohydrate v(C-O-C) of polysaccharides, Nucleic Acid (and other phosphate-containing compounds), 1641 cm^{-1} (amide or C=C

Table 10
Algae mediated synthesis of other nanomaterials (NMs).

Microalgae	NP	Size	Application/Activitys	Characterization	Bioreductant and capping agent	Reference
Cyanobacteria						
Plectonema boryanum UTEX 485	Pt	30 nm–0.3 μm, spherical	First study as an alternative method to abiotic chemical methods	SEM,TEM, XPS	Polysaccharides have abundant uronic acid subunits, which, through their carboxyl groups	(Lengke et al., 2006b)
Plectonema boryanum UTEX 485	Pd	> 30 nm, spherical, fcc	First viable alternative method	SEM, TEM, XPS, XRD	Organic materials	(Lengke et al., 2007b)
Spirulina platensis	Ag/Au bimetallic	17–25 nm, fcc,	Single cell protein as nanobiofactories	UV-Vis, FT-IR, XRD, HR-TEM	Polypeptide/proteins	(Govindaraju et al., 2008)
Anabaena flos-aquae	β-FeOOH	-	-	XRD, HR-TEM, SEM-EDS	Intracellular	(Brayner et al., 2009)
Calothrix pulvinata	β-FeOOH	-	-	XRD, HR-TEM, SEM-EDS	Intracellular	(Brayner et al., 2009)
Phormidium cyanobacterium	CuO	10–40 nm, quasi-spheres, crystalline	Proteins induced under metal stress play a dual role of hydrolysis of precursor salt to CONPs and stabilizing agent, as particle solution is stable at room temperature for more than a week	UV-Vis, TEM, SEM,EDAX, XRD, FT-IR, SDS-PAGE	Extracellular, 25 kDa protein fraction as capping agent	(Rahman et al., 2009)
Phormidium tenue NTDM05	CdS	5.1 ± 0.2 nm, spherical	Biolabelling	FT-IR. EDAX, TEM, UV-Vis	C-phycoerythrin, thiol groups partial capping along with biological molecules	(MubarakAli et al., 2012)
Anabaena strain L31	ZnO	80 nm, hexagonal	Environmental-friendly sunscreen filters	UV-Vis, XRD, SEM, TEM, FT-IR, SAED, DLS	Phycobiliproteins	(Singh et al., 2014a, 2014b)
Brown						
Sargassum muticum	Fe_3O_4	18 ± 4 nm, cubic shape	High functional bioactivity	UV-Vis, EDXRF, XRD, FESEM, VSM,FT-IR, TEM	Sulphated polysaccharides in the reduction process and the stabilization, extracellular synthesis	(Mahdavi et al., 2013)
Sargassum myriocystum	ZnO	36 nm, spherical, triangle, radial, hexagonal, rod, rectangle size	Natural nanomedicine against microbial infection.	UV–visible, DLS, AFM, SEM, EDX, TEM, XRD, FT-IR	Fucoidan water soluble pigments	(Nagarajan and Arumugam, 2013)
Sargassum plagiophyllum	AgCl	18–42 nm, spherical	Antibacterial properties	UV-Vis, FT-IR, EDAX, HR-TEM, FESEM,XRD	Role of C=C in the reduction	(Dhas et al., 2014)
Bifurcaria bifurcata	CuO	5 to 45 nm, spherical	Antibacterial	UV-Vis, FT-IR, XRD, TEM	Water-soluble compounds such as diterpenoids	(Abboud et al., 2014)
Sargassum ilicifolium	Pd	60–80 nm, spherical		SEM, UV-Vis		(Prasad and Padmesh, 2014)
Sargassum bovinum	Pd	5–10 nm, monodispersed, octahedral	Catalytic performance by electrochemical reduction of hydrogen peroxide (H_2O_2)	UV–Vis, TEM, XRD, EDX, FT-IR	Sulphated polysaccharides	(Momeni and Nabipour, 2015)
Sargassum muticum	ZnO	3–57 nm, hexagonal wurtzite structures	One pot method for synthesis	UV-Vis, XRD, FESEM	Sulfate and hydroxyl moieties of polysaccharide	(Azizi et al., 2014)
Sargassum muticum	ZnO	3–57 nm, hexagonal wurtzite structures	Antiangiogenic and antiapoptotic effects on Human liver cancer cell line (HepG2).	UV-Vis, XRD, FESEM	Sulfate and hydroxyl moieties of polysaccharide	(Sanaeimehr et al., 2018)
Green						
Klebsormidium flaccidum	β-FeOOH	-	-	XRD, HR-TEM, SEM-EDS	Intracellular	(Brayner et al., 2009)
Chlorella vulgaris	Pd	7 nm, spherical	Photosynthetically driven metal transformation	TEM, SEM, ICP-OES, XPS	NADPH	(Eroglu et al., 2012)
Chlamydomonas reinhardtii	Ag/Au bimetallic	10–20 nm, spherical	Impact of metals salts on cell viability and characteristics of the NPs	UV-Vis, TEM	Extracellular matrix	(Dahoumane et al., 2014a, 2014b)
Chlorococcum sp. MM11	Fe	20–50 nm, spherical	Remediation of toxic Cr(VI)	UV-Vis, TEM, DLS, FT-IR, EDAX	Carbonyl and amine bonds from polysaccharides and glycoproteins present in the algal cell wall	(Subramaniyam et al., 2015)

(*continued on next page*)

Table 10 (*continued*)

Microalgae	NP	Size	Application/Activitys	Characterization	Bioreductant and capping agent	Reference
Scenedesmus-24	CdS	120–175 nm, oval shape	Environmental remediation-based application	FT-IR, XRD, TEM	Hydroxly group, N-H bond of amino group	(Jena et al., 2015)
Chlorella vulgaris	Pd	5–20 nm, spherical, monodisperse, crystalline	Easy and fast bioprocess	UV-Vis, FT-IR, XRD, TEM	Polyol and amide groups	(Arsiya et al., 2017)
Red						
Gracilaria edulis	ZnO	66–95 nm, rod shaped	Anticancerous against PC3 cell lines	UV-Vis, EDX, FT-IR, FESEM, XRD	Quinines	(Priyadharshini et al., 2014)
Gracilaria	Ag/Au bimetallic	22–30 nm, spherical	Gram + ve *S. aureus* Gram –ve *K. pneumoniae*	UV-Vis, HR-SEM	-	(Ramakritinan et al., 2013)

stretching vibrations of aromatic rings), 2922 (C − H stretching of polyols) and 3417 cm^{-1} (O − H group of polyols) in the FT-IR spectrum (Arsiya et al., 2017).

5.4. Algae-mediated synthesis of bimetallic nanoparticles

Bimetallic NPs are composed of two different metals which combine in different ratios to show novel properties derived from the constituting metals. These NMs have drawn more interest than monometallic NMs due to the presence of an extra degree of freedom. Extracellular interaction of single-cell proteins of *Spirulina platensis* with aqueous $AgNO_3$ and $HAuCl_4$ was examined for the biosynthesis of Ag-NPs, Au- NPs and Ag-Au core shell NPs. The interaction of cyanobacterial biomass and the metal precursor solutions ($AgNO_3$ and $HAuCl_4$ each at 10^{-3} M) solely or in combination for 120 h at 37 °C led to significant chromatic changes due to the excitation of surface plasmon vibrations in the metal NPs. The visual change in the colour of the reaction mixture to yellowish brown (Ag-NPs), ruby red (Au-NPs) and purple to brown (Ag-Au bimetallic) was noticed. SPR λ_{max} bands were observed at 424, 530 for Ag-NPs, Au-NPs. However, for bimetallic NPs absorption peaks were observed at 509, 486 and 464 nm for 75:25, 50:50 and 25:75 (Au:Ag) mol concentrations, respectively. The gradual shift from 530 to 424 nm was commensurate with the increased mole fraction of silver. The size of the NPs observed for Ag-NPs was 7-16 nm, Au-NPs was 6-10 nm and for bimetallic Au-Ag NPs it was 17-25 nm (Govindaraju et al., 2008; Pathak et al., 2019).

Similarly, green alga *Chlamydomonas reinhardtii* has also been reported to synthesize bimetallic Ag-Au NPs intracellularly. Aqueous mixtures of $AgNO_3$ and $HAuCl_4{\cdot}H_2O$ in different ratios (Ag:Au::1:0, 3:1, 1:1, 1:3, 0:1, 0:2) was introduced to the culture broth at room temperature (22 °C) under controlled light and dark exposure of 8 h dark/16 h day light. The creation of NPs starts within the cell soon after the introduction of metal salts. It occurs in three stages, initially the noble metals get internalized and reduced to NPs. Then the NPs get entrapped in the extracellular matrix to achieve colloidal stability and later the NPs are released into the culture medium from the extracellular matrix. The NPs recovered had a round shape with a narrow size distribution. SPR bands were reported ranging between 420 nm (Ag) and 555 nm (Au) in a linear proportion to the stoichiometric ratio at which these two metals were added to the culture (Dahoumane et al., 2014a).

Ramakritinan et al. (2013) employed *Gracilaria* spp. to form Ag-NPs, Au-NPs and even bimetallic Ag-Au nanoalloys. The reduction of metal solutions to corresponding NPs and bimetallic nanoalloys was validated by a change in colour *i.e* for Ag-NPs (transparent to dark brown), Au-NPs (ruby red) and Ag-Au bimetallic NPs (pale pink). The corresponding λ_{max} peaks at 419 nm for Ag, 536 nm for Au, 504 nm for Ag/Au (1,1), 526 nm for Ag/Au (1,3) and 501 nm for Ag/Au (3,1) corroborated their synthesis. However, it was confirmed by SEM analysis that all the NPs formed were colloidal in nature.

6. Applications of metallic nanoparticles

Metallic NPs fabricated from various algal sources used a multidisciplinary approach resulting from the investigational use of NPs in biological systems (Iravani et al., 2014). They can compete with the conventional medicines and have been reported to have antibacterial (Sharma et al., 2015a), anticancerous (Govindaraju et al., 2015) and antifungal activities (Azizi et al., 2013). Apart from medicinal applications, the metal NPs have extensive applicability in electronics, optics, cosmetics, coatings (Singh et al., 2014a, 2014b), food packaging, sensing devices, space industries, therapeutics, bioremediation (Iravani et al., 2014), environmental health (Husain et al., 2019), mechanics, light emitters, nonlinear optical devices, chemical industries (Khan et al., 2017), and photo-electrochemical applications (Mukherji et al., 2012; Makarov et al., 2014) (Tables 2-10).

6.1. Antimicrobial activity

NPs have drawn increasing interest from every branch of medicine for their ability to deliver drugs in the optimum dosage range often resulting in increased therapeutic efficiency of the drugs, weakened side effects and improved patient compliance (Khan et al., 2017). Au-NPs fabricated from diverse seaweeds have multifaceted roles in the medical industry as antibacterial agents against both Gram +ve (Rajathi et al., 2012; Venkatesan et al., 2014) and Gram -ve bacterial pathogens (Rajeshkumar et al., 2013b; Venkatesan et al., 2014), as antifungal against *Fusarium dimerum* and *Humiclo insulans* (Varun et al., 2014) and antitumor activity against lung and liver cells *in vitro via* activation of cell death (Singh et al., 2014a, 2014b). The small size of NPs disrupts the membrane functions of cells (permeability or respiration) by adhering to its surface and consequently penetrating the cell and further, damaging the DNA (Vijayan et al., 2016).

Au-NPs synthesized from *Spirulina platensis* exhibited strong antibacterial activity against Gram +ve bacteria *(Bacillus subtilis* and *Staphylococcus aureus)* where vancomycin was taken as a positive control. Protein functionalized Au-NPs managed to penetrate through the thick peptidoglycan layer and damaged the cell (Suganya et al., 2015). The use of brown alga *(Turbinaria conoides)* has been reported for the synthesis of Au-NPs exhibiting maximum antibacterial activity against *Streptococcus* spp. The opportune bacteria *B. subtilis* has a minimum range and pneumonia fever causing bacteria *Klebsiella pneumoniae* has a medium range of inhibition (Rajeshkumar et al., 2013b). Au-NPs synthesized using *Stoechospermum marginatum* were evaluated for their antibacterial effects against *Enterobacter faecalis* and it was higher than that of the positive control tetracycline, and the minimum zone of inhibition was recorded against *K. pneumonia*. However, no inhibition was found against *Escherichia coli* (Rajathi et al., 2012). On the basis of the nature of the extract derived from *Galaxaura elongate* (powder, ethanol and ethanol free extract), different types of Au-NPs were synthesized. The corresponding Au-NPs fabricated were evaluated for their antibacterial activities. Maximum inhibition was observed for Au-NPs from ethanolic extract against *E. coli*, *K. pneumoniae* and MRSA (Methicillin-resistant *Staphylococcus aureus*) followed by Au-NPs from free ethanolic extract which only exhibited high activity against MRSA. However, Au-NPs from powder of *G. elongata* were found to be effective against *E. coli* and *K. pneumonia* (Abdel-Raouf et al., 2017). Extracellularly synthesized Ag-NPs from brown marine weed, *Sargassum wightii* were tested for bacteria isolated from silkworm *Bombyx mori* L. Excellent zone of inhibition was observed in all the test species of bacteria (*S. aureus, Bacillus rhizoids*, *E. coli* and *Pseudomonas aeruginosa)* (Govindaraju et al., 2009).

Ethanolic extract of *Acanthophora specifera* acted as both capping and reducing agent in tailoring the cubic shaped Ag-NPs of 33-81 nm effective against a wide range of microbes including Gram +ve (*S. aureus* and *B. subtillis)*, Gram -ve (*Salmonella* sp. and *E. coli*) and yeast strain *Candida albicans* suggesting it may be a proficient antimicrobial agent (Ibraheem et al., 2016). The synthesized Ag-NPs from cellular metabolites of *Microcoleus* sp acted as a strong antibacterial agent against *E.coli, Proteus vulgaris, Salmonella typhi, Vibrio cholerae, B. subtilis, S. aureus, Streptococcus* and *Corynebacterium* (Sudha et al., 2013). Fucoidan, water-soluble pigments in aqueous cell extracts were identified to be responsible for capping and reduction. The resulting ZnO-NPs were highly stable up to 6 months and were effective antibacterial agents against Gram +ve and Gram -ve bacteria (Nagarajan and Arumugam, 2013). Biocompatible Ag-NPs, biosynthesized from *Gracilaria corticata* have an effective antifungal activity against ubiquitous fungi and are opportunistic pathogens of immunocompromised hosts i.e. *Candida albicans* and *Candida glabrata*. Spherical, stable Ag-NPs of 18-46 nm range were obtained at 60 °C within 20 min (Kumar et al., 2013b). Synthesis of Ag-NPs using the aqueous extract of red seaweed *Gelidiella acerosa* as the reducing agent exhibited antifungal property against *Humicola insolens* (MTCC 4520), *Fusarium dimerum* (MTCC 6583), *Mucor indicus* (MTCC 3318), and *Trichoderma reesei* (MTCC 3929) (Vivek et al., 2011; LewisOscar et al., 2016). In another report, the effect of the algal (*Sargassum longifolium*) mediated Ag-NPs against the pathogenic fungi *Aspergillus fumigatus*, *C. albicans*, and *Fusarium* sp. was determined (Rajeshkumar et al., 2014; LewisOscar et al., 2016).

6.2. Antifouling agents

Several studies have revealed that "nano-functionalized materials" inhibit bacterial adhesion and biofilm formation on surfaces by coating techniques (Beyth et al., 2008, Roe et al., 2008) and impregnation or embedding NMs (Lellouche et al., 2009). Targeting novel receptors involved in biofilm formation is the best strategy to control problems caused by the biofilm in marine environments (Vijayan et al., 2016). Vijayan et al. (2014) did a comparative study of biosynthesized Ag-NPs and Au-NPs from *Turbinaria conoides*. Ag-NPs were found to be efficient in controlling biofilm formation in *E. coli* followed by *Salmonella* sp., *Serratia liquefaciens,* and *Aeromonas hydrophila,* whereas Au-NPs were almost ineffective. Also, spherical (2-17 nm) Ag-NPs were lethal to brine shrimp *Artemia salina* with LC_{50} value of 88.914 μL mL^{-1}, which affirms it as a potent anti-microfouling agent (Vijayan et al., 2014). A similar study was performed by Kumar et al. (2012a) in synthesizing Ag-NPs from *Sargassum ilicifolium* with size range 33-40 nm and evaluated its cytotoxicity in *Artemia salina* (Kumar et al., 2012a) (Table 9). Krishnan et al. (2015) suggested that the 'coat' made of phytagel and apcomin zinc chrome paint glazed with Ag-NPs synthesized from *Turbinaria ornata* can prevent microflora and macroflora. The synthesized Ag-NPs restricted the growth of 15 biofilm isolates with maximum inhibition in *E. coli* (71.9%) and a minimum in *Micrococcus* sp. (40%) due to the secretion of extracellular polymeric substances (EPS) from Gram +ve bacteria. These silver based NPs can initiate a new quest of green antifouling compounds as the cytotoxic study revealed 100% mortality for *Balanu samphitrite* larvae and 56.6% for *Artemia marina* at 250 μg ml^{-1} and demonstrated lower toxicity to non-target species (Krishnan et al., 2015).

6.3. Bioremediation

It has been found that nanomaterials provide a wonderful platform for remediating pollution caused by various industrial effluents. In a study done by Ramakrishna et al. (2016), aqueous extracts of brown algae (*Turbinaria conoides* and *Sargassum tenerrimum*) were used as a reducing agent for Au-NPs synthesis. Biosynthesized Au-NPs showed efficient catalytic activity for the reduction of aromatic nitro compounds (4-nitrophenol and p-nitroaniline) and organic dye molecules (Rhodamine B and Sulforhodamine 101). *T. conoides* exhibited greater catalytic potential than *S. tenerrimum.* The Ag-NPs fabricated from *Ulva lactuca* actively degraded methyl orange photocatalytically under visible light illumination using silver as a nanocatalyst (Kumar et al., 2013a). Murugan et al. (2015) highlighted that *Ulva lactuca* mediated synthesis of stable Ag-NPs can be employed at low dosages to actively reduce populations of chloroquine-resistant *Plasmodium falciparum*. The smoke repellents based on *Ulva lactuca* may be cheaper and safer than the permethrin coils available in the market (Murugan et al., 2015). Ag-NPs synthesized from *Microchaete* NCCU-342 exhibited appreciable dye decolorization ability of azo dye methyl red as compared to cyanobacterial extract. Ag-NPs exhibited excellent photocatalytic activity against dye molecules and can be used in remediating pollution due to dyes and also in water purification systems (Husain et al., 2019). Intracellular synthesis of cadmium sulphide NPs was demonstrated in lipid-producing green alga *Scenedesmus*-24 (Table 10). The adsorption and adsorption kinetics of Cd (II) followed Langmuir isotherm pattern and Lagergren's pseudo-second-order model respectively, collectively signifying a chemisorbed monolayer of cadmium ions irreversibly bound on the algal biomass. The high retention of cadmium by the alga substantiates *Scenedesmus*-24 as a model microalga for bioremediation (Jena et al., 2015).

6.4. Other applications

The aqueous cellular extract of diazotrophic cyanobacterial strain *Anabaena* L31 was exercised for the synthesis of ZnO-NPs conjugated with shinorine, water-soluble UV-B absorbent. A sharp decline in the surface charge of the conjugate from +30.25 mV to 3.75 mV resulted from the changes in the surface functionalities after conjugate formation. The resulting conjugate reduced the ROS generation by up to 75%, which makes it a competent non-toxic sunscreen agent of biological origin (Singh et al., 2014a, 2014b). *Lemanea fluviatilis*, an edible freshwater epilithic red alga was used to biosynthesize Au-NPs, which showed remarkable antioxidant activity of the Au-NPs in the DPPH (2,2-diphenyl-1-picrylhydrazyl) assay (Sharma et al., 2014b). Catalytic performance of the biosynthetic Pd-NPs from *Sargassum bovinum* was investigated for electrochemical reduction of hydrogen peroxide (H_2O_2) (Momeni and Nabipour, 2015). Pd-NPs modified carbon ionic liquid electrode (Pd-NPs/CILE) was developed which gave a fast response time, high sensitivity and selectivity, and a low detection limit of H_2O_2, making it a promising electrochemical sensing platform.

7. Conclusion

Scientific breakthroughs have employed several algal systems for the synthesis of metal and metal oxide NPs. Low cultivation cost, less production time and eco-friendly synthesis minimize the use of hazardous chemicals that makes algae an alternative platform for the synthesis of NPs. Cyanobacterial strains such as *Spirulina* spp. and *Microcoleus* spp. have been explored to synthesize Ag-NPs with broad spectrum antibacterial activities against Gram +ve and Gram -ve bacteria. Au-NPs and Ag-NPs from members of Chlorophyceae such as *Chlorella* and *Ulva* show therapeutic potential against bacteria, fungi, protozoa and many cancerous cell lines. These are also being utilized in photocatalytic purification and remediation of polluted air and water, respectively. In addition, microalga *Scendesmus* is known for Cd retention and can be considered for the synthesis of Cd-NPs playing an important role in bioremediation. Among all algae, *Sargassum* spp. could be used to fabricate diverse kinds of NMs including Au-NPs, Ag-NPs, ZnO-NPs and TiO_2, opening a new scientific era for clinical diagnostics, therapeutic agents, fertilizers, biosensors, food packaging, cosmetics, paint, and biofilms. Different parameters (pH, temperature, concentration, and time), which decide shape and morphology of the NPs need to be optimized for specific products. Nevertheless, finite knowledge of synthesis mechanisms limits the use of a diverse range of algal species. Development of clean, bio-compatible, non-toxic and eco-friendly methods for the synthesis of the NPs is required (Gnanasangeetha and SaralaThambavani, 2013). Besides valuable implications, the issues related to environmental hazards generated due to heavy metals need to be considered to limit the serious affect NPs may have on the environment. Limitations ranging from variability of NP features due to the biological variability and different methodologies adopted to exploit these resources have impeded the path to quality control and market entrance. Emerging advanced characterization techniques would facilitate comparative and controlled performance of NPs, which will encourage judicious selection of algae-based NPs. Based on emerging reports presented in this review, in the future, a remarkable boom may be witnessed in the biosynthesis of algae-based NMs that will be likely to have enormous potential in pharmaceutics, agriculture, cosmetics and medicine.

Author contributions

PK and DG outlined the paper, and major contributions to the text for specific sections were written by PK. AK helped in data compilation. PK and DG contributed equally with general comments and editing the entire manuscript.

Declaration of Competing Interests

The authors have declared that no competing interests exist.

Acknowledgments

The authors are thankful to Director, Thapar Institute of Engineering and Technology, Patiala, Punjab, India.

References

Abboud, Y., Saffaj, T., Chagraoui, A., El Bouari, A., Brouzi, K., Tanane, O., Ihssane, B., 2014. Biosynthesis, characterization and antimicrobial activity of copper oxide nanoparticles (CONPs) produced using brown alga extract (*Bifurcaria bifurcata*). Appl. Nanosci. 4, 571–576.

Abdel-Raouf, N., Al-Enazi, N.M., Ibraheem, I.B., 2017. Green biosynthesis of gold nanoparticles using *Galaxaura elongata* and characterization of their antibacterial activity. Arab. J. Chem. 10, S3029–S3039.

Aboelfetoh, E.F., El-Shenody, R.A., Ghobara, M.M., 2017. Eco-friendly synthesis of silver nanoparticles using green algae (*Caulerpa serrulata*): reaction optimization, catalytic and antibacterial activities. Environ. Monit. Assess. 189 (7), 349.

Agnihotri, S., Mukherji, S., Mukherji, S., 2014. Size-controlled silver nanoparticles synthesized over the range 5–100 nm using the same protocol and their antibacterial efficacy. RSC Adv. 4, 3974–3983.

Ali, D.M., Sasikala, M., Gunasekaran, M., Thajuddin, N., 2011. Biosynthesis and characterization of silver nanoparticles using marine cyanobacterium, *Oscillatoria willei* NTDM01. Dig. J. Nanomater 6, 285–290.

Amendola, V., Meneghetti, M., 2009. Laser ablation synthesis in solution and size manipulation of noble metal nanoparticles. Phys. Chem. Chem. Phys. 11 (20), 3805–3821.

Annamalai, J., Nallamuthu, T., 2016. Green synthesis of silver nanoparticles: characterization and determination of antibacterial potency. Appl. Nanosci. 6, 259–265.

Anshup, Venkataraman J.S., Subramaniam, C., Kumar, R.R., Priya, S., Kumar, T.S., Omkumar, R.V., John, A., Pradeep, T., 2005. Growth of gold nanoparticles in human cells. Langmuir 21, 11562–11567.

Apolinário, A., Quitério, P., Sousa, C.T., Proença, M.P., Azevedo, J., Susano, M., Moraes, S., Lopes, P., Ventura, J., Araújo, J.P., 2014. Bottom-up nanofabrication using self-organized porous templates. J. Phys. Conf. Ser. 534, 012001.

de Aragao, A.P., de Oliveira, T.M., Quelemes, P.V., Perfeito, M.L.G., Araujo, M.C., Santiago, J.D.A.S., Cardoso, V.S., Quaresma, P., de Almeida, J.R.D.S., da Silva, D.A., 2016. Green synthesis of silver nanoparticles using the seaweed *Gracilaria birdiae* and their antibacterial activity. Arab. J. Chem. https://doi.org/10.1016/j.arabjc.2016.04.014.

Arbain, R., Othman, M., Palaniandy, S., 2011. Preparation of iron oxide nanoparticles by mechanical milling. Miner. Eng. 24 (1), 1–9.

Arsiya, F., Sayadi, M.H., Sobhani, S., 2017. Green synthesis of palladium nanoparticles using *Chlorella vulgaris*. Mater. Lett. 186, 113–115.

Asmathunisha, N., Kathiresan, K., 2013. A review on biosynthesis of nanoparticles by marine organisms. Colloids Surf. B: Biointerfaces 103, 283–287.

Aziz, N., Faraz, M., Pandey, R., Shakir, M., Fatma, T., Varma, A., Barman, I., Prasad, R., 2015. Facile algae-derived route to biogenic silver nanoparticles: synthesis, antibacterial, and photocatalytic properties. Langmuir 31, 11605–11612.

Azizi, S., Namvar, F., Mahdavi, M., Ahmad, M., Mohamad, R., 2013. Biosynthesis of silver nanoparticles using brown marine macroalga, *Sargassum Muticum* aqueous extract. Materials 6, 5942–5950.

Azizi, S., Ahmad, M.B., Namvar, F., Mohamad, R., 2014. Green biosynthesis and characterization of zinc oxide nanoparticles using brown marine macroalga *Sargassum muticum* aqueous extract. Mater. Lett. 116, 275–277.

Baker, S., Harini, B.P., Rakshith, D., Satish, S., 2013. Marine microbes: Invisible nanofactories. J. Pharm. Res. 6, 383–388.

Barsanti, L., Gualtieri, P., 2014. Algae: Anatomy, Biochemistry, and Biotechnology. CRC Press, Second Edition.

Barwal, I., Ranjan, P., Kateriya, S., Yadav, S.C., 2011. Cellular oxido-reductive proteins of *Chlamydomonas reinhardtii* control the biosynthesis of silver nanoparticles. J. Nanobiotechnol. 9, 56.

Baskar, B.B., 2013. Biosynthesis of silver nanoparticles using *Kappa phycus* species. Int. J. Res. Pharm. Sci. 3, 55–63.

Beyth, N., Houri-Haddad, Y., Baraness-Hadar, L., Yudovin-Farber, I., Domb, A.J., Weiss, E.I., 2008. Surface antimicrobial activity and biocompatibility of incorporated polyethylenimine nanoparticles. Biomaterials 29 (31), 4157–4163.

Bhaviripudi, S., Jia, X., Dresselhaus, M.S., Kong, J., 2010. Role of kinetic factors in chemical vapor deposition synthesis of uniform large area graphene using copper catalyst. Nano Lett. 10 (10), 4128–4133.

Bhimba, B.V., Kumari, P.R., 2014. Phytosynthesis of silver nanoparticles from the extracts of seaweed *Ulva lactuca* and its antimicrobial activity. Int. J. Pharm. Bio. Sci. 5, 666–677.

Brayner, R., Yéprémian, C., Djediat, C., Coradin, T., Herbst, F., Livage, J., Fiévet, F., Couté, A., 2009. Photosynthetic microorganism-mediated synthesis of akaganeite (beta-FeOOH) nanorods. Langmuir 25, 10062–10067.

Castro, L., Blázquez, M.L., Muñoz, J.A., González, F., Ballester, A., 2013. Biological synthesis of metallic nanoparticles using algae. IET Nanobiotechnol. 7, 109–116.

Chakraborty, N., Banerjee, A., Lahiri, S., Panda, A., Ghosh, A.N., Pal, R., 2009.

Biorecovery of gold using cyanobacteria and an eukaryotic alga with special reference to nanogold formation – a novel phenomenon. J. Appl. Phycol. 21, 145.
Chen, F., Jiang, Y. (Eds.), 2013. Algae and Their Biotechnological Potential. Springer Science & Business Media.
Cheng, W., Zhang, W., Hu, L., Ding, W., Wu, F., Li, J., 2016. Etching synthesis of iron oxide nanoparticles for adsorption of arsenic from water. RSC Adv. 6 (19), 15900–15910.
Chisti, Y., 2007. Biodiesel from microalgae. Biotechnol. Adv. 25, 294–306.
Chisti, Y., 2008. Biodiesel from microalgae beats bioethanol. Trends Biotechnol. 26, 126–131.
Chisti, Y., Moo-Young, M., 1986. Disruption of microbial cells for intracellular products. Enzym. Microb. Technol. 8, 194–204.
D'Amato, R., Falconieri, M., Gagliardi, S., Popovici, E., Serra, E., Terranova, G., Borsella, E., 2013. Synthesis of ceramic nanoparticles by laser pyrolysis: From research to applications. J. Anal. Appl. Pyrolysis 104, 461–469.
Dahoumane, S.A., Djediat, C., Yéprémian, C., Couté, A., Fiévet, F., Coradin, T., Brayner, R., 2012a. Recycling and adaptation of *Klebsormidium flaccidum* microalgae for the sustained production of gold nanoparticles. Biotechnol. Bioeng. 109, 284–288.
Dahoumane, S.A., Djediat, C., Yéprémian, C., Couté, A., Fiévet, F., Coradin, T., Brayner, R., 2012b. Species selection for the design of gold nanobioreactor by photosynthetic organisms. J. Nanopart. Res. 14, 883.
Dahoumane, S.A., Wijesekera, K., Filipe, C.D., Brennan, J.D., 2014a. Stoichiometrically controlled production of bimetallic Gold-Silver alloy colloids using micro-alga cultures. J. Colloid Interface Sci. 416, 67–72.
Dahoumane, S.A., Yéprémian, C., Djédiat, C., Couté, A., Fiévet, F., Coradin, T., Brayner, R., 2014b. A global approach of the mechanism involved in the biosynthesis of gold colloids using micro-algae. J. Nanopart. Res. 16, 2607.
Dahoumane, S.A., Wujcik, E.K., Jeffryes, C., 2016. Noble metal, oxide and chalcogenide-based nanomaterials from scalable phototrophic culture systems. Enzym. Microb. Technol. 95, 13–27.
Devi, J.S., Bhimba, B.V., 2012. Anticancer activity of silver nanoparticles synthesized by the seaweed *Ulva lactuca* invitro. Sci. Rep. 1, 242.
Devi, J.S., Bhimba, B.V., Ratnam, K., 2012. In vitro anticancer activity of silver nanoparticles synthesized using the extract of *Gelidiella* sp. Int J Pharm Pharm Sci 4, 710–715.
Devi, J.S., Bhimba, B.V., Peter, D.M., 2013. Production of biogenic silver nanoparticles using *Sargassum longifolium* and its applications. Indian J. Mar. Sci. 42, 125–130.
Dhanalakshmi, P.K., Azeez, R., Rekha, R., Poonkodi, S., Nallamuthu, T., 2012. Synthesis of silver nanoparticles using green and brown seaweeds. Phykos 42, 39–45.
Dhas, T.S., Kumar, V.G., Abraham, L.S., Karthick, V., Govindaraju, K., 2012. *Sargassum myriocystum* mediated biosynthesis of gold nanoparticles. Spectrochim. Acta A Mol. Biomol. Spectrosc. 99, 97–101.
Dhas, T.S., Kumar, V.G., Karthick, V., Angel, K.J., Govindaraju, K., 2014. Facile synthesis of silver chloride nanoparticles using marine alga and its antibacterial efficacy. Spectrochim. Acta A Mol. Biomol. Spectrosc. 120, 416–420.
El-Rafie, H.M., El-Rafie, M., Zahran, M.K., 2013. Green synthesis of silver nanoparticles using polysaccharides extracted from marine macro algae. Carbohydr. Polym. 96, 403–410.
El-Said, W.A., Cho, H.Y., Yea, C.H., Choi, J.W., 2014. Synthesis of metal nanoparticles inside living human cells based on the intracellular formation process. Adv. Mater. 26 (6), 910–918.
Elumalai, S., Santhose, B.I., Devika, R., Revathy, S., 2013. Collection, isolation, identification, and biosynthesis of silver nanoparticles using microalga *Chlorella pyrenoidosa*. Nanomech. Sci. Technol. Int. J. 4, 59–66.
Eroglu, E., Chen, X., Bradshaw, M., Agarwal, V., Zou, J., Stewart, S.G., Duan, X., Lamb, R.N., Smith, S.M., Raston, C.L., Iyer, K.S., 2012. Biogenic production of palladium nanocrystals using microalgae and their immobilization on chitosan nanofibers for catalytic applications. RSC Adv. 3, 1009–1012.
Fawcett, D., Verduin, J.J., Shah, M., Sharma, S.B., Poinern, G.E.J., 2017. A review of current research into the biogenic synthesis of metal and metal oxide nanoparticles via marine algae and seagrasses. J. Nanosci. 2017.
Focsan, M., Ardelean, I.I., Craciun, C., Astilean, S. 2011. Interplay between gold nanoparticle biosynthesis and metabolic activity of cyanobacterium *Synechocystis* sp. PCC 6803. Nanotechnology, 22(48), 485101.
Ganesan, V., Aruna Devi, J., Astalakshmi, A., Nima, P., Thangaraja, A., 2013. Eco-friendly synthesis of silver nanoparticles using a sea weed, *Kappaphycus Alvarezii* (Doty) Doty ex P.C.Silva. Int. J. Eng. Adv. Technol. 2, 559–563.
Ghodake, G., Lee, D.S., 2011. Biological synthesis of gold nanoparticles using the aqueous extract of the brown algae *Laminaria japonica*. J. Nanoelectron. Optoelectron. 6 (3), 268–271.
Ghorbani, H.R., 2014. A review of methods for synthesis of Al nanoparticles. Orient. J. Chem. 30 (4), 1941–1949.
Gnanasangeetha, D., SaralaThambavani, D., 2013. One pot synthesis of zinc oxide nanoparticles via chemical and green method. Res. J. Mater. Sci. 1, 1–8.
González-Ballesteros, N., Prado-López, S., Rodríguez-González, J.B., Lastra, M., Rodríguez-Argüelles, M.C., 2017. Green synthesis of gold nanoparticles using brown algae *Cystoseira baccata:* Its activity in colon cancer cells. Colloids Surf. B: Biointerfaces 153, 190–198.
Govindaraju, K., Basha, S.K., Kumar, V.G., Singaravelu, G., 2008. Silver, gold and bimetallic nanoparticles production using single-cell protein (*Spirulina platensis*) Geitler. J. Mater. Sci. 43 (15), 5115–5122.
Govindaraju, K., Kiruthiga, V., Kumar, V.G., Singaravelu, G., 2009. Extracellular synthesis of silver nanoparticles by a marine alga, *Sargassum wightii Grevilli* and their antibacterial effects. J. Nanosci. Nanotechnol. 9, 5497–5501.
Govindaraju, K., Krishnamoorthy, K., Alsagaby, S.A., Singaravelu, G., Premanathan, M., 2015. Green synthesis of silver nanoparticles for selective toxicity towards cancer cells. IET Nanobiotechnol. 9, 325–330.
Grima, E.M., Belarbi, E.H., Fernández, F.A., Medina, A.R., Chisti, Y., 2003. Recovery of microalgal biomass and metabolites: process options and economics. Biotechnol. Adv. 20, 491–515.
Gurentsov, E.V., Eremin, A.V., Schulz, C., 2007. Formation of carbon nanoparticles by the condensation of supersaturated atomic vapor obtained by the laser photolysis of C_3O_2. Kinet. Catal. 48, 194–203.
Guzmán, M.G., Dille, J., Godet, S., 2009. Synthesis of silver nanoparticles by chemical reduction method and their antibacterial activity. World Acad. Sci. Eng. Technol. 43, 357–364.
Hatakeyama, H., Akita, H., Harashima, H., 2011. A multifunctional envelope type nano device (MEND) for gene delivery to tumours based on the EPR effect: a strategy for overcoming the PEG dilemma. Adv. Drug Deliv. Rev. 63, 152–160.
Hulkoti, N.I., Taranath, T.C., 2014. Biosynthesis of nanoparticles using microbes—a review. Colloids Surf. B: Biointerfaces 121, 474–483.
Husain, S., Sardar, M., Fatma, T., 2015. Screening of cyanobacterial extracts for synthesis of silver nanoparticles. World J. Microbiol. Biotechnol. 31 (8), 1279–1283.
Husain, S., Afreen, S., Yasin, D., Afzal, B., Fatma, T., 2019. Cyanobacteria as a bioreactor for synthesis of silver nanoparticles-an effect of different reaction conditions on the size of nanoparticles and their dye decolorization ability. J. Microbiol. Methods 162, 77–82.
Ibraheem, I.B.M., Abd-Elaziz, B.E.E., Saad, W.F., Fathy, W.A., 2016. Green biosynthesis of silver nanoparticles using marine Red Algae *Acanthophora specifera* and its antimicrobial activity. J. Nanomed. Nanotech. 7, 1–4.
Ibrahim, H.M., 2015. Green synthesis and characterization of silver nanoparticles using banana peel extract and their antimicrobial activity against representative microorganisms. J. Radiat. Res. Appl. Sci. 8, 265–275.
Ingham, B., 2015. X-ray scattering characterisation of nanoparticles. Crystallogr. Rev. 21, 229–303.
Iravani, S., 2011. Green synthesis of metal nanoparticles using plants. Green Chem. 13, 2638–2650.
Iravani, S., Korbekandi, H., Mirmohammadi, S.V., Zolfaghari, B., 2014. Synthesis of silver nanoparticles: chemical, physical and biological methods. Res Pharm. Sci. 9, 385–406.
Jeffryes, C., Agathos, S.N., Rorrer, G., 2015. Biogenic nanomaterials from photosynthetic microorganisms. Curr. Opin. Biotechnol. 33, 23–31.
Jena, J., Pradhan, N., Dash, B.P., Sukla, L.B., Panda, P.K., 2013. Biosynthesis and characterization of silver nanoparticles using microalga *Chlorococcum humicola* and its antibacterial activity. Int. J. Nanomater. Biostruct. 3, 1–8.
Jena, J., Pradhan, N., Nayak, R.R., Dash, B.P., Sukla, L.B., Panda, P.K., Mishra, B.K., 2014. Microalga *Scenedesmus* sp.: a potential low-cost green machine for silver nanoparticle synthesis. J. Microbiol. Biotechnol. 24, 522–533.
Jena, J., Pradhan, N., Aishvarya, V., Nayak, R.R., Dash, B.P., Sukla, L.B., Panda, P.K., Mishra, B.K., 2015. Biological sequestration and retention of cadmium as CdS nanoparticles by the microalga *Scenedesmus*-24. J. Appl. Phycol. 27, 2251–2260.
Kalabegishvili, T.L., Kirkesali, E.I., Rcheulishvili, A.N., Ginturi, E.N., Murusidze, I.G., Pataraya, D.T., Gurielidze, M.A., Tsertsvadze, G.I., Gabunia, V.N., Lomidze, L.G., Gvarjaladze, D.N., 2012. Synthesis of gold nanoparticles by some strains of *Arthrobacter* genera. Proc. Inst. Mech. Eng. Part L J. Mat. Des. Appl. 7, 1–7.
Kanimozhi, S., Johnson, A., Kala, M., Shibila, P.C., Revathy, I., 2015. Extracellular synthesis of silver nanoparticles from a marine alga, *Sargassum polycystum* C. Agardh and their biopotentials. World J. Pharm. Pharm. Sci. 4, 1388–1400.
Kannan, R.R.R., Arumugam, R., Ramya, D., Manivannan, K., Anantharaman, P., 2013a. Green synthesis of silver nanoparticles using marine macroalga *Chaetomorpha linum*. Appl. Nanosci. 3, 229–233.
Kannan, R.R.R., Stirk, W.A., Van Staden, J., 2013b. Synthesis of silver nanoparticles using the seaweed *Codium capitatum* P.C. Silva (Chlorophyceae). S. Afr. J. Bot. 86, 1–4.
Karthikeyan, P., Mohan, D., Abishek, G., Priya, R., 2015. Synthesis of silver nanoparticles using Phytoplankton and its characteristics. Int. J. Fish Aquac. Stu. 2, 398–401.
Kathiraven, T., Sundaramanickam, A., Shanmugam, N., Balasubramanian, T., 2015. Green synthesis of silver nanoparticles using marine algae *Caulerpa racemosa* and their antibacterial activity against some human pathogens. Appl. Nanosci. 5, 499–504.
Keat, C.L., Aziz, A., Eid, A.M., Elmarzugi, N.A., 2015. Biosynthesis of nanoparticles and silver nanoparticles. Bioresour. Bioprocess 2, 47.
Khalil, M.M., Ismail, E.H., El-Baghdady, K.Z., Mohamed, D., 2014. Green synthesis of silver nanoparticles using olive leaf extract and its antibacterial activity. Arab. J. Chem. 7, 1131–1139.
Khan, I., Saeed, K., Khan, I., 2017. Nanoparticles: properties, applications and toxicities. Arab. J. Chem. https://doi.org/10.1016/j.arabjc.2017.05.011.
Krishnan, M., Sivanandham, V., Hans-Uwe, D., Murugaiah, S.G., Seeni, P., Gopalan, S., Rathinam, A.J., 2015. Antifouling assessments on biogenic nanoparticles: a field study from polluted offshore platform. Mar. Pollut. Bull. 101, 816–825.
Kumar, P., Selvi, S.S., Praba, A.L., Selvaraj, M., 2012a. Antibacterial activity and in-vitro cytotoxicity assay against brine shrimp using silver nanoparticles synthesized from *Sargassum ilicifolium*. Dig. J. Nanomater Biostruct. 7, 1447–1455.
Kumar, P., Senthamilselvi, S., Lakshmipraba, A., Premkumar, K., Muthukumaran, R., Visvanathan, P., Ganeshkumar, R.S., Govindaraju, M., 2012b. Efficacy of bio-synthesized silver nanoparticles using *Acanthophora spicifera* to encumber biofilm formation. Dig. J. Nanomater Biostruct. 7, 511–522.
Kumar, P., Govindaraju, M., Senthamilselvi, S., Premkumar, K., 2013a. Photocatalytic degradation of methyl orange dye using silver (Ag) nanoparticles synthesized from *Ulva lactuca*. Colloids Surf. B: Biointerfaces 103, 658–661.
Kumar, P., Selvi, S.S., Govindaraju, M., 2013b. Seaweed-mediated biosynthesis of silver nanoparticles using *Gracilaria corticata* for its antifungal activity against *Candida* spp. Appl. Nanosci. 3, 495–500.

Lellouche, J., Kahana, E., Elias, S., Gedanken, A., Banin, E., 2009. Antibiofilm activity of nanosized magnesium fluoride. Biomaterials 30 (30), 5969–5978.
Lengke, M.F., Fleet, M.E., Southam, G., 2006a. Morphology of gold nanoparticles synthesized by filamentous cyanobacteria from gold(I)-thiosulfate and gold(III)–chloride complexes. Langmuir. 22, 2780–2787.
Lengke, M.F., Fleet, M.E., Southam, G., 2006b. Synthesis of platinum nanoparticles by reaction of filamentous cyanobacteria with platinum (IV)-chloride complex. Langmuir. 22, 7318–7323.
Lengke, M.F., Ravel, B., Fleet, M.E., Wanger, G., 2006c. Mechanisms of gold bioaccumulation by filamentous cyanobacteria from gold (III)− chloride complex. Sci. Technol. China 40, 6304–6309.
Lengke, M.F., Fleet, M.E., Southam, G., 2007a. Biosynthesis of silver nanoparticles by filamentous cyanobacteria from a silver(I) nitrate complex. Langmuir. 23, 2694–2699.
Lengke, M.F., Fleet, M.E., Southam, G., 2007b. Synthesis of palladium nanoparticles by reaction of filamentous cyanobacterial biomass with a palladium(II) chloride complex. Langmuir. 23, 8982–8987.
LewisOscar, F., Vismaya, S., Arunkumar, M., Thajuddin, N., Dhanasekaran, D., Nithya, C., 2016. Algal nanoparticles: synthesis and biotechnological potentials. In: Algae-Organisms for Imminent Biotechnology. IntechOpen.
Li, X., Xu, H., Chen, Z.S., Chen, G., 2011. Biosynthesis of nanoparticles by microorganisms and their applications. J. Nanomater. 2011, 1–16.
Li, X., Schirmer, K., Bernard, L., Sigg, L., Pillai, S., Behra, R., 2015a. Silver nanoparticle toxicity and association with the alga *Euglena gracilis*. Environment. Sci. Nano. 2, 594–602.
Li, Y., Tang, X., Song, W., Zhu, L., Liu, X., Yan, X., Jin, C., Ren, Q., 2015b. Biosynthesis of silver nanoparticles using *Euglena gracilis, Euglena intermedia and their extract*. IET Nanobiotechnol. 9, 19–26.
Liu, B., Xie, J., Lee, J.Y., Ting, Y.P., Chen, J.P., 2005. Optimization of high-yield biological synthesis of single-crystalline gold nanoplates. J. Phys. Chem. B 109, 15256–15263.
Luangpipat, T., Beattie, I.R., Chisti, Y., Haverkamp, R.G., 2011. Gold nanoparticles produced in a microalga. J. Nanopart. Res. 13, 6439–6445.
Madhiyazhagan, P., Murugan, K., Kumar, A.N., Nataraj, T., Dinesh, D., Panneerselvam, C., Subramaniam, J., Kumar, P.M., Suresh, U., Roni, M., Nicoletti, M., 2015. *Sargassum muticum*-synthesized silver nanoparticles: an effective control tool against mosquito vectors and bacterial pathogens. Parasitol. Res. 114 (11), 4305–4317.
Mahdavi, M., Namvar, F., Ahmad, M.B., Mohamad, R., 2013. Green biosynthesis and characterization of magnetic iron oxide (Fe_3O_4) nanoparticles using seaweed (*Sargassum muticum*) aqueous extract. Molecules. 18, 5954–5964.
Mahdieh, M., Zolanvari, A., Azimee, A.S., Mahdieh, M., 2012. Green biosynthesis of silver nanoparticles by *Spirulina platensis*. Scientia Iranica. 19, 926–929.
Makarov, V.V., Love, A.J., Sinitsyna, O.V., 2014. "Green" nanotechnologies: synthesis of metal nanoparticles using plants. Acta Nat. 6, 35–44.
Mata, Y.N., Torres, E., Blazquez, M.L., Ballester, A., González, F.M.J.A., Munoz, J.A., 2009. Gold (III) biosorption and bioreduction with the brown alga *Fucus vesiculosus*. J. Hazard. Mater. 166, 612–618.
Menon, S., Rajeshkumar, S., Kumar, V., 2017. A review on biogenic synthesis of gold nanoparticles, characterization, and its applications. Resource-Efficient Technol. 3 (4), 516–527.
Michalak, I., Chojnacka, K., 2015. Algae as production systems of bioactive compounds. Eng. Life Sci. 15, 160–176.
Mohandass, C., Vijayaraj, A.S., Rajasabapathy, R., Satheeshbabu, S., Rao, S.V., Shiva, C., De-Mello, I., 2013. biosynthesis of silver nanoparticles from marine seaweed *Sargassum cinereum* and their antibacterial activity. J. Invest Dermatol. 78, 206–209.
Mohseniazar, M., Barin, M., Zarredar, H., Alizadeh, S., Shanehbandi, D., 2011. Potential of microalgae and *lactobacilli* in biosynthesis of silver nanoparticles. Bioimpacts. 1, 149–152.
Momeni, S., Nabipour, I., 2015. A simple green synthesis of palladium nanoparticles with Sargassum alga and their electrocatalytic activities towards hydrogen peroxide. App. Biochem. Biotechnol. 176 (7), 1937–1949.
MubarakAli, D., Gopinath, V., Rameshbabu, N., Thajuddin, N., 2012. Synthesis and characterization of CdS nanoparticles using C-phycoerythrin from the marine cyanobacteria. Mater. Lett. 74, 8–11.
MubarakAli, D., Arunkumar, J., Nag, K.H., SheikSyedIshack, K.A., Baldev, E., Pandiaraj, D., Thajuddin, N., 2013. Gold nanoparticles from Pro and eukaryotic photosynthetic microorganisms-Comparative studies on synthesis and its application on biolabelling. Colloid Surfaces B 103, 166–173.
Mukherjee, P., Senapati, S., Mandal, D., Ahmad, A., Khan, M.I., Kumar, R., Sastry, M., 2002. Extracellular synthesis of gold nanoparticles by the fungus *Fusarium oxysporum*. Chembiochem. 3, 461–463.
Mukherji, S., Ruparelia, J., Agnihotri, S., 2012. Antimicrobial activity of silver and copper nanoparticles: variation in sensitivity across various strains of bacteria and fungi. Nano-antimicrobials. 225–251.
Murugan, K., Samidoss, C.M., Panneerselvam, C., Higuchi, A., Roni, M., Suresh, U., Chandramohan, B., Subramaniam, J., Madhiyazhagan, P., Dinesh, D., Rajaganesh, R., 2015. Seaweed-synthesized silver nanoparticles: an eco-friendly tool in the fight against *Plasmodium falciparum* and its vector *Anopheles stephensi*? Parasitol. Res. 114, 4087–4097.
Murugesan, S., Elumalai, M., Dhamotharan, R., 2011. Green synthesis of silver nano particles from marine alga *Gracilaria edulis*. Biosci. Biotech. Res. Comm. 4, 105–110.
Nagarajan, S., Arumugam, Kuppusamy K., 2013. Extracellular synthesis of zinc oxide nanoparticle using seaweeds of gulf of Mannar, India. J. Nanobiotechnol. 11, 39.
Namvar, F., Azizi, S., Ahmad, M.B., Shameli, K., Mohamad, R., Mahdavi, M., Tahir, P.M., 2015. Green synthesis and characterization of gold nanoparticles using the marine macroalgae *Sargassum muticum*. Res. Chem. Intermed. 41, 5723–5730.
Nath, D., Banerjee, P., 2013. Green nanotechnology–a new hope for medical biology. Environ. Toxicol. Pharmacol. 36, 997–1104.
Naveena, B.E., Prakash, S., 2013. Biological synthesis of gold nanoparticles using marine algae *Gracilaria corticata* and its application as a potent antimicrobial and antioxidant agent. Asian J. Pharm. Clin. Res. 6, 179–182.
Oza, G., Pandey, S., Mewada, A., Kalita, G., Sharon, M., Phata, J., Ambernath, W., Sharon, M., 2012. Facile biosynthesis of gold nanoparticles exploiting optimum pH and temperature of fresh water algae *Chlorella pyrenoidusa*. Adv. Appl. Sci. Res. 3, 1405.
Parial, D., Pal, R., 2014. Green synthesis of gold nanoparticles using cyanobacteria and their characterization. Indian J. Appl. Res. 4, 69–72.
Parial, D., Pal, R., 2015. Biosynthesis of monodisperse gold nanoparticles by green alga *Rhizoclonium* and associated biochemical changes. J. Appl. Phycol. 27, 975–984.
Parial, D., Patra, H.K., Dasgupta, A.K.R., Pal, R., 2012a. Screening of different algae for green synthesis of gold nanoparticles. Eur. J. Phycol. 47, 22–29.
Parial, D., Patra, H.K., Roychoudhury, P., Dasgupta, A.K., Pal, R., 2012b. Gold nanorod production by cyanobacteria—a green chemistry approach. J. Appl. Phycol. 24, 55–60.
Patel, V., Berthold, D., Puranik, P., Gantar, M., 2015. Screening of cyanobacteria and microalgae for their ability to synthesize silver nanoparticles with antibacterial activity. Biotechnol. Rep. 5, 112–119.
Pathak, J., Ahmed, H., Singh, D.K., Pandey, A., Singh, S.P., Sinha, R.P., 2019. Recent developments in green synthesis of metal nanoparticles utilizing cyanobacterial cell factories. In: Nanomaterials in Plants, Algae and Microorganisms. Academic Press, pp. 237–265.
Pinjarkar, H., Gaikwad, S., Ingle, A.P., Gade, A., Rai, M., 2016. Phycofabrication of silver nanoparticles and their antibacterial activity against human pathogens. Adv. Mater. Lett. 7, 1010–1014.
Poinern, G.E.J., 2014. A Laboratory Course in Nanoscience and Nanotechnology. CRC Press.
Prasad, T.N.V.K.V., Elumalai, E.K., 2013. Marine algae mediated synthesis of silver nanopaticles using *Scaberia agardhii Greville*. J. Biol. Sci. 13, 566–569.
Prasad, B., Padmesh, T., 2014. Seaweed (*Sargassum ilicifolium*) assisted green synthesis of palladium nanoparticles. Int. J. Sci. Eng. Res. 5, 229–231.
Prasad, T.N.V.K.V., Kambala, V.S.R., Naidu, R., 2013. Phyconanotechnology: synthesis of silver nanoparticles using brown marine algae *Cystophora moniliformis* and their characterisation. J. Appl. Phycol. 25, 177–182.
Prasad, R., Pandey, R., Barman, I., 2016. Engineering tailored nanoparticles with microbes: quo vadis? Wiley Interdiscip. Rev. Nanomed. Nanobiotechnol. 8 (2), 316–330.
Priyadharshini, R.I., Prasannaraj, G., Geetha, N., 2014. Microwave-mediated extracellular synthesis of metallic silver and zinc oxide nanoparticles using macro-algae (*Gracilaria edulis*) extracts and its anticancer activity against human PC3 cell lines. Appl. Biochem. Biotechnol. 174, 2777–2790.
Quester, K., Avalos-Borja, M., Castro-Longoria, E., 2013. Biosynthesis and microscopic study of metallic nanoparticles. Micron 54, 1–27.
Rahdar, A., 2013. Study of different capping agent effect on the structural and optical properties of Mn doped ZnS nanostructures. World Appl. Programm. 3, 56–60.
Rahimi, Z., Yousefzadi, M., Noori, A., 2014. Green synthesis of silver nanoparticles using *Ulva flexousa* from the Persian Gulf, Iran. J. Persian Gulf. 5, 9–16.
Rahman, A., Ismail, A., Jumbianti, D., Magdalena, S., Sudrajat, H., 2009. Synthesis of copper oxide nano particles by using *Phormidium cyanobacterium*. Indones J. Chem. 9, 355–360.
Rajasulochana, P., Krishnamoorthy, P., Dhamotharan, R., 2012. Potential application of *Kappaphycus alvarezii* in agricultural and pharmaceutical industry. J. Chem. Pharm. Res. 4, 33–37.
Rajathi, A.A.F., Parthiban, C., Kumar, V.G., Anantharaman, P., 2012. Biosynthesis of antibacterial gold nanoparticles using brown alga, *Stoechospermum marginatum* (kützing). Spectrochim. Acta A Mol. Biomol. Spectrosc. 99, 166–173.
Rajesh, S., Raja, D.P., Rathi, J.M., Sahayaraj, K., 2012. Biosynthesis of silver nanoparticles using *Ulva fasciata* (Delile) ethyl acetate extract and its activity against *Xanthomonas campestris* pv. *malvacearum*. J. Biopest. 5, 119–128.
Rajeshkumar, S., Kannan, C., Annadurai, G., 2012a. Green synthesis of silver nanoparticles using marine brown algae *Turbinaria conoides* and its antibacterial activity. Int. J. Pharm. Bio Sci. 3, 502–510.
Rajeshkumar, S., Kannan, C., Annadurai, G., 2012b. Synthesis and characterization of antimicrobial silver nanoparticles using marine brown seaweed *Padina tetrastromatica*. Drug Invent. Today 4, 511–513.
Rajeshkumar, S., Malarkodi, C., Gnanajobitha, G., Paulkumar, K., Vanaja, M., Kannan, C., Annadurai, G., 2013a. Seaweed-mediated synthesis of gold nanoparticles using *Turbinaria conoides* and its characterization. J. Nanostruct. Chem. 3, 44.
Rajeshkumar, S., Malarkodi, C., Vanaja, M., Gnanajobitha, G., Paulkumar, K., Kannan, C., Annadurai, G., 2013b. Antibacterial activity of algae mediated synthesis of gold nanoparticles from *Turbinaria conoides*. Der. Pharma Chem. 5, 224–229.
Rajeshkumar, S., Malarkodi, C., Paulkumar, K., Vanaja, M., Gnanajobitha, G., Annadurai, G., 2014. Algae mediated green fabrication of silver nanoparticles and examination of its antifungal activity against clinical pathogens. Int. J. Met. 2014, 1–8.
Ramakrishna, M., Babu, D.R., Gengan, R.M., Chandra, S., Rao, G.N., 2016. Green synthesis of gold nanoparticles using marine algae and evaluation of their catalytic activity. J. Nanostruct. Chem. 6, 1–13.
Ramakritinan, C.M., Kaarunya, E., Shankar, S., Kumaraguru, A.K., 2013. Antibacterial effects of Ag, Au and bimetallic (Ag-Au) nanoparticles synthesized from red algae. In: Solid State Phenomena. 201. Trans Tech Publications, pp. 211–230.
Roe, D., Karandikar, B., Bonn-Savage, N., Gibbins, B., Roullet, J.B., 2008. Antimicrobial surface functionalization of plastic catheters by silver nanoparticles. J. Antimicrob. Chemother. 61 (4), 869–876.
Rösken, L.M., Cappel, F., Körsten, S., Fischer, C.B., Schönleber, A., van Smaalen, S.,

Geimer, S., Beresko, C., Ankerhold, G., Wehner, S., 2016. Time-dependent growth of crystalline Au0-nanoparticles in cyanobacteria as self-reproducing bioreactors: 2. *Anabaena cylindrica*. Beilstein J. Nanotechnol. 7 (1), 312–327.
Roychoudhury, P., Pal, R., 2014. *Spirogyra submaxima*–a green alga for nanogold production. J. Algal Biomass Utln. 5, 15–19.
Sahayaraj, K., Rajesh, S., Rathi, J.M., 2012. Silver nanoparticles biosynthesis using marine alga *Padina pavonica* (linn.) and its microbicidal activity. Dig. J. Nanomater Biostruct. 7, 1557–1567.
Sahoo, P.C., Kausar, F., Lee, J.H., Han, J.I., 2014. Facile fabrication of silver nanoparticle embedded $CaCO_3$ microspheres via microalgae-templated CO_2 biomineralization: application in antimicrobial paint application. RSC Adv. 4, 32562–32569.
Sajidha, Parveen K., Lakshmi, D., 2016. Biosynthesis of silver nanoparticles using red algae, *Amphiroa fragilissima* and its antibacterial potential against Gram positive and Gram negative bacteria. Int. J. Curr. Sci. 19, 93–100.
Salari, Z., Danafar, F., Dabaghi, S., Ataei, S.A., 2016. Sustainable synthesis of silver nanoparticles using macroalgae *Spirogyra varians* and analysis of their antibacterial activity. J Saudi Chem. Soc. 20, 459–464.
Sanaeimehr, Z., Javadi, I., Namvar, F., 2018. Antiangiogenic and antiapoptotic effects of green-synthesized zinc oxide nanoparticles using *Sargassum muticum* algae extraction. Cancer Nanotechnol. 9 (1), 3.
Sangeetha, N., Saravanan, K., 2014. Biogenic silver nanoparticles using marine seaweed (*Ulva lactuca*) and evaluation of its antibacterial activity. J. Nanosci. Nanotechnol. 2, 99–102.
Sangeetha, G., Rajeshwari, S., Venckatesh, R., 2011. Green synthesis of zinc oxide nanoparticles by *aloe barbadensis* miller leaf extract: Structure and optical properties. Mater. Res. Bull. 46 (12), 2560–2566.
Sastry, M., Ahmad, A., Khan, M.I., Kumar, R., 2003. Biosynthesis of metal nanoparticles using fungi and actinomycete. Curr. Sci. 85, 162–170.
Satapathy, S., Shukla, S.P., Sandeep, K.P., Singh, A.R., Sharma, N., 2015. Evaluation of the performance of an algal bioreactor for silver nanoparticle production. J. Appl. Phycol. 27, 285–291.
Schröfel, A., Kratošová, G., Bohunická, M., Dobročka, E., Vávra, I., 2011. Biosynthesis of gold nanoparticles using diatoms—silica-gold and EPS-gold bionanocomposite formation. J. Nanopart. Res. 13, 3207–3216.
Sekine, N., Chou, C.-H., Kwan, W.L., Yang, Y., 2009. ZnO nano-ridge structure and its application in inverted polymer solar cell. Org. Electron. 10, 1473–1477.
Senapati, S., Syed, A., Moeez, S., Kumar, A., Ahmad, A., 2012. Intracellular synthesis of gold nanoparticles using alga *Tetraselmis kochinensis*. Mater. Lett. 79, 116–118.
Shabnam, N., Pardha-Saradhi, P., 2013. Photosynthetic electron transport system promotes synthesis of Au-nanoparticles. PLoS One 8, e71123.
Shah, M., Fawcett, D., Sharma, S., Tripathy, S., Poinern, G., 2015. Green synthesis of metallic nanoparticles via biological entities. Materials. 8, 7278–7308.
Shakibaie, M., Forootanfar, H., Mollazadeh-Moghaddam, K., Bagherzadeh, Z., Nafissi-Varcheh, N., Shahverdi, A.R., Faramarzi, M.A., 2010. Green synthesis of gold nanoparticles by the marine microalga *Tetraselmis suecica*. Biotechnol. Appl. Biochem. 57, 71–75.
Sharma, D., Sharma, S., Kaith, B.S., Rajput, J., Kaur, M., 2011. Synthesis of ZnO nanoparticles using surfactant free in-air and microwave method. Appl. Surf. Sci. 257, 9661–9672.
Sharma, B., Purkayastha, D.D., Hazra, S., Gogoi, L., Bhattacharjee, C.R., Ghosh, N.N., Rout, J., 2014a. Biosynthesis of gold nanoparticles using a freshwater green alga, *Prasiola crispa*. Mater Lett. 116, 94–97.
Sharma, B., Purkayastha, D.D., Hazra, S., 2014b. Biosynthesis of fluorescent gold nanoparticles using an edible freshwater red alga, *Lemanea fluviatilis* (L.) C. Ag. and antioxidant activity of biomatrix loaded nanoparticles. Bioprocess Biosyst. Eng. 37, 2559–2565.
Sharma, D., Kanchi, S., Bisetty, K., 2015a. Biogenice synthesis of nanoparticles: a review. Arab. J. Chem. https://doi.org/10.1016/j.arabjc.2015.11.002.
Sharma, G., Jasuja, N.D., Kumar, M., Ali, M.I., 2015b. Biological Synthesis of Silver Nanoparticles by Cell-Free Extract of *Spirulina platensis*. J. Nanotechnol. 2015. https://doi.org/10.1155/2015/132675.
Sharma, A., Sharma, S., Sharma, K., Chetri, S.P., Vashishtha, A., Singh, P., Kumar, R., Rathi, B., Agrawal, V., 2016. Algae as crucial organisms in advancing nanotechnology: a systematic review. J. Appl. Phycol. 28, 1759–1774.
Shedbalkar, U., Singh, R., Wadhwani, S., Gaidhani, S., Chopade, B.A., 2014. Microbial synthesis of gold nanoparticles: current status and future prospects. Adv. Colloid Interf. Sci. 209, 40–48.
Shiny, P.J., Mukherjee, A., Chandrasekaran, N., 2013. Marine algae mediated synthesis of the silver nanoparticles and its antibacterial efficiency. Int J Pharm Pharm Sci 5, 239–241.
Shukla, A.K., Iravani, S., 2017. Metallic nanoparticles: green synthesis and spectroscopic characterization. Environ. Chem. Lett. 15 (2), 223–231.
Shukla, M.K., Singh, R.P., Reddy, C.R.K., Jha, B., 2012. Synthesis and characterization of agar-based silver nanoparticles and nanocomposite film with antibacterial applications. Bioresour. Technol. 107, 295–300.
Sicard, C., Brayner, R., Margueritat, J., Hémadi, M., Couté, A., Yéprémian, C., Djediat, C., Aubard, J., Fiévet, F., Livage, J., Coradin, T., 2010. Nano- gold biosynthesis by silica -encapsulated micro-algae: a "living" bio-hybrid material. J. Mater. Chem. 20, 9342–9347.
Siddiqui, M.N., Redhwi, H.H., Achilias, D.S., Kosmidou, E., Vakalopoulou, E., Ioannidou, M.D., 2017. Green synthesis of silver nanoparticles and study of their antimicrobial properties. J. Polym. Environ. 1–11.
Singaravelu, G., Arockiamary, J.S., Kumar, V.G., Govindaraju, K., 2007. A novel extracellular synthesis of monodisperse gold nanoparticles using marine alga, *Sargassum wightii Greville*. Colloids Surf. B: Biointerfaces 57, 97–101.
Singh, M., Kalaivani, R., Manikandan, S., Sangeetha, N., Kumaraguru, A.K., 2013. Facile green synthesis of variable metallic gold nanoparticle using *Padina gymnospora*, a brown marine macroalga. Appl. Nanosci. 3, 145–151.
Singh, G., Babele, P.K., Kumar, A., Srivastava, A., Sinha, R.P., Tyagi, M.B., 2014a. Synthesis of ZnO nanoparticles using the cell extract of the cyanobacterium, *Anabaena* strain L31 and its conjugation with UV-B absorbing compound shinorine. J. Photochem. Photobiol. B 138, 55–62.
Singh, M., Kumar, M., Manikandan, S., Chandrasekaran, N., Mukherjee, A., Kumaraguru, A.K., 2014b. Drug delivery system for controlled cancer therapy using physico-chemically stabilized bioconjugated gold nanoparticles synthesized from marine macroalgae, *Padina Gymnospora*. J. Nanomed. Nanotechol. S5, 1–7.
Sinha, S., Pan, I., Chanda, P., Sen, S.K., 2009. Nanoparticles fabrication using ambient biological resources. J. Appl. Biosci. 19, 1113–1130.
Sinha, S.N., Paul, D., Halder, N., Sengupta, D., Patra, S.K., 2015. Green synthesis of silver nanoparticles using fresh water green alga *Pithophora oedogonia* (Mont.) Wittrock and evaluation of their antibacterial activity. Appl. Nanosci. 5, 703–709.
Subramaniyam, V., Subashchandrabose, S.R., Thavamani, P., Megharaj, M., Chen, Z., Naidu, R., 2015. *Chlorococcum* sp. MM11—a novel phyco-nanofactory for the synthesis of iron nanoparticles. J. Appl. Phycol. 27, 1861–1869.
Sudha, S.S., Amanickam, K., Rengaramanujam, J., 2013. Microalgae mediated synthesis of silver nanoparticles and their antibacterial activity against pathogenic bacteria. Indian J. Exp. Biol. 51, 393–399.
Suganya, K.U., Govindaraju, K., Kumar, V.G., Dhas, T.S., Karthick, V., Singaravelu, G., Elanchezhiyan, M., 2015. Blue green alga mediated synthesis of gold nanoparticles and its antibacterial efficacy against Gram positive organisms. Mater. Sci. Eng. C 47, 351–356.
Suriya, J., Bharathi Raja, S., Sekar, V., Rajasekaran, R., 2012. Biosynthesis of silver nanoparticles and its antibacterial activity using seaweed *Urospora* sp. Afr. J. Biotechnol. 11, 12192–12198.
Tanaka, Y., 2018. Synthesis of nanosize particles in thermal plasmas. In: Handbook of Thermal Science and Engineering, pp. 2791–2828.
Thakkar, K.N., Mhatre, S.S., Parikh, R.Y., 2010. Biological synthesis of metallic nanoparticles. Nanomedicine. 6, 257–262.
Thangaraju, N., Venkatalakshmi, R.P., Chinnasamy, A., Kannaiyan, P., 2012. Synthesis of silver nanoparticles and the antibacterial and anticancer activities of the crude extract of *Sargassum polycystum* C. Agardh Nano Biomed. Eng. 4, 89–94.
Ting, Y.P., Teo, W.K., Soh, C.Y., 1995. Gold uptake by *Chlorella vulgaris*. J. Appl. Phycol. 7, 97–100.
Tsibakhashvili, N.Y., Kirkesali, E.I., Pataraya, D.T., Gurielidze, M.A., Kalabegishvili, T.L., Gvarjaladze, D.N., Tsertsvadze, G.I., Frontasyeva, M.V., Zinicovscaia, I.I., Wakstein, M.S., Khakhanov, S.N., 2011. Microbial synthesis of silver nanoparticles by *Streptomyces glaucus* and *Spirulina platensis*. Adv. Sci. Lett. 4, 1–10.
Türk, M., Erkey, C., 2018. Synthesis of supported nanoparticles in supercritical fluids by supercritical fluid reactive deposition: current state, further perspectives and needs. J. Supercrit Fluids 134, 176–183.
Ullah, H., Khan, I., Yamani, Z.H., Qurashi, A., 2017. Sonochemical-driven ultrafast facile synthesis of SnO_2nanoparticles: growth mechanism structural electrical and hydrogen gas sensing proper-ties. Ultrason. Sonochem. 34, 484–490.
Varun, S., Sudha, S., Kumar, P.S., 2014. Biosynthesis of gold nanoparticles from aqueous extract of *Dictyota Bartayresiana* and their antifungal activity. Indian J. Adv. Chem. Sci. 2, 190–193.
Velammal, S.P., Devi, T.A., Amaladhas, T.P., 2016. Antioxidant, antimicrobial and cytotoxic activities of silver and gold nanoparticles synthesized using *Plumbago zeylanica* bark. J. Nanostructure Chem. 6, 247–260.
Venkatesan, J., Manivasagan, P., Kim, S.K., Kirthi, A.V., Marimuthu, S., Rahuman, A.A., 2014. Marine algae-mediated synthesis of gold nanoparticles using a novel *Ecklonia cava*. Bioprocess Biosyst. Eng. 37, 1591–1597.
Verma, V.C., Kharwar, R.N., Gange, A.C., 2010. Biosynthesis of antimicrobial silver nanoparticles by the endophytic fungus *Aspergillus clavatus*. Nanomedicine. 5, 33–40.
Vijayan, S.R., Santhiyagu, P., Singamuthu, M., Kumari Ahila, N., Jayaraman, R., Ethiraj, K., 2014. Synthesis and characterization of silver and gold nanoparticles using aqueous extract of seaweed, *Turbinaria conoides*, and their antimicrofouling activity. Sci. World J. 2014, 938272.
Vijayan, S.R., Santhiyagu, P., Ramasamy, R., Arivalagan, P., Kumar, G., Ethiraj, K., Ramaswamy, B.R., 2016. Seaweeds: a resource for marine bionanotechnology. Enzym. Microb. Technol. 95, 45–57.
Vijayaraghavan, K., Mahadevan, A., Sathishkumar, M., Pavagadhi, S., Balasubramanian, R., 2011. Biosynthesis of Au (0) from Au (III) via biosorption and bioreduction using brown marine alga *Turbinaria conoides*. Chem. Eng. J. 167 (1), 223–227.
Vivek, M., Kumar, P.S., Steffi, S., Sudha, S., 2011. Biogenic silver nanoparticles by *Gelidiella acerosa* extract and their antifungal effects. Avicenna J. Med. Biotechnol. 3, 143–148.
Xie, J., Lee, J.Y., Wang, D.I.C., Ting, Y.P., 2007a. Silver nanoplates: from biological to biomimetic synthesis. ACS Nano 1, 429–439.
Xie, J., Lee, J.Y., Wang, D., Ting, Y.P., 2007b. Identification of active biomolecules in the high-yield synthesis of single-crystalline gold nanoplates in algal solutions. Small. 3, 672–682.
Yousefzadi, M., Rahimi, Z., Ghafori, V., 2014. The green synthesis, characterization and antimicrobial activities of silver nanoparticles synthesized from green alga *Enteromorpha flexuosa* (wulfen) J. Agardh. Mater Lett. 137, 1–4.
Zinicovscaia, I., 2012. Use of bacteria and microalgae in synthesis of nanoparticles. Chem. J. Mold. 7, 32–38.

Inorganic Chemistry Communications 142 (2022) 109676

Contents lists available at ScienceDirect

Inorganic Chemistry Communications

journal homepage: www.elsevier.com/locate/inoche

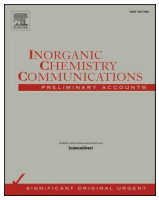

Short communication

Photocatalytic degradation of textile dyes using phycosynthesised ZnO nanoparticles

Prerna [a], Harshit Agarwal [b,c], Dinesh Goyal [a,*]

[a] Department of Biotechnology, Thapar Institute of Engineering and Technology, (Deemed University), Patiala 147 004, Punjab, India
[b] Department of Physics, Banaras Hindu University, Varanasi, Uttar Pradesh, India
[c] Laboratory of Crystallography, University of Bayreuth, Bayreuth, Germany

ARTICLE INFO

Keywords:
Co-precipitation method
Anabaena variabilis ARM 441
Zinc oxide
UV driven photocatalysis
Brilliant Green

ABSTRACT

Phycosynthesis of ZnO nanoparticles (ZnO NPs) using a single-step process, from biomolecules present in the cyanobacterial extracts of *Anabaena variabilis* ARM 441 was carried out and analysed for photocatalytic degradation of textile dyes. Bioactive components of algal extracts identified by GC–MS and NMR (13C and 1H NMR) spectroscopy, reveals 21 different compounds, among which n-hexadecanoic acid and 13 tetradecenal had properties of reducing and capping agent required in the synthesis of ZnO NPs. Microscopic investigation of particle size and zeta potential confirmed the formation of hexagonal ZnO NPs with an average size of 33.31 nm. The EDX and XPS analyses established the chemical composition and high purity of ZnO NPs. The rietveld refinement studies of X-ray diffraction studies elucidated crystalline and wurtzite phase of ZnO NPs. Pore size (11.551 nm), surface area (38.718 m^2/g) and pore volume (0.1633 cc/g) were studied by BET analysis. The photocatalytic degradation of brilliant green (BG) and indigo carmine (IC) dyes in aqueous solution by ZnO NPs was 98.07% and 80.8% for BG and IC, respectively, which followed first-order kinetics, suggesting that ZnO NPs are capable of degrading harmful and toxic chemical dyes that persists in the environment.

1. Introduction

Nanotechnology has allured tremendous attention due to parallel augmentation in the experimental techniques for the development of sustainable materials and resources. It is a diverse and contemporary field of research, stimulating the development of nanoscale systems and analyzing their assets *via* size, shape, and morphology. Nanoparticles bridge the gap between bulk materials and atomic or molecular structures [1]. Generally, nanomaterials possess a high surface area to volume ratio with improved surface functionalization, making nanoparticles exhibit pharmacological activity, thermal conductivity, optoelectronic property, chemical steadiness, and catalytic reactivity [2,3]. Such widespread applications of nanomaterials have opened novel frontiers in innovating protocols for the synthesis of nanoparticles. The existing physicochemical methods are inconvenient to use and are often complicated as they involve toxic reducing and stabilizing agents, non-biodegradable organic and inorganic chemicals, have high-energy consumption and relatively low yield [4,5]. Additionally, the resulting nanomaterials retain the capping of hazardous chemical reagents involved in the conventional synthetic process, resulting in diminished therapeutical application of nanoparticles [2]. Thus, a crucial need for the development of green strategies has emerged. A wide array of plants, bacteria, fungi, lichens, virus, algae etc. have been employed for the synthesis of nanoparticles as a bio-compatible alternative which is a harmless and environment-friendly approach [1,6]. The extracts of these bio-moieties have a cocktail of natural compounds such as phenolics, terpenoids, flavonones, amines, amides, proteins, pigments, alkaloids etc., which assists in both metal reduction and their stabilization at ambient temperature with controlled pH for desired size, shape and composition of nanoparticles [7]. Noteworthy, such green approaches have limited negatives such as high cost, the release of toxic by-products and are less cumbersome as compared to physicochemical processes [8]. Additional advantages include large-scale, cost-effective nanoparticles free from noxious chemicals (impurities) and easy accessibility of raw materials from natural surroundings. Although greener technologies would not be an alternative to physico-chemical methods, lesser damage to the ecosystem could be definitely assured. The existing literature on green approaches for the synthesis of nanoparticles using phyto-ingredients is voluminous. Different plant species such as *Aloe vera* [9], *Mentha spicata* [10], *Garcinia mangostana* [11], *Hylocereus polyrhizus*

* Corresponding author.
E-mail address: dgoyal@thapar.edu (D. Goyal).

https://doi.org/10.1016/j.inoche.2022.109676
Received 16 April 2022; Received in revised form 3 June 2022; Accepted 10 June 2022
Available online 15 June 2022

[12] *Nasturtium officinale* [13], *Hibiscus rosa-sinensis* [14] fungal species such as *Aspergillus niger* [15] etc. have been used. Algae, the largest photoautotrophic group of microorganisms, are the storehouse of secondary metabolites, pigments, and proteins. Algae belonging to different classes such as *Cyanophyceae, Chlorophyceae, Phaeophyceae,* and *Rhodophyceae* have been widely exploited for intracellular and extracellular synthesis of metallic nanoparticles (Ag, Au, Pt, Ni, etc.) and metal oxide nanoparticles (CuO, ZnO, MnO_2, TiO_2, Fe_3O_4, etc.)[16]. However, in contrast to other microorganisms, very few algae have been screened for their ability to promote the biogenic synthesis of ZnO NPs.

ZnO is essentially a multifaceted semiconductor with some exciting characteristic properties such as non-toxicity, wide band gap (~3.37 eV), excitation energy (60 meV) [11], high electron mobility, broad absorption range, high thermal and chemical stability, large binding energy, excellent transparency in the visible range, photostability, oxidation resistivity, high piezoelectric features, biocompatibility and biodegradability [3]. ZnO NPs are exceptionally advantageous, as they have exhibited outstanding performances in various fields such as cosmetics, food packaging, anti-corrosives, sensors, electronics, communication, environmental remediation, and medicinal therapeutics and photo-catalysis [17]. Brilliant green (BG) (4-{[4-(diethylamino) phenyl](phenyl)methylidene}-N,N-diethylcyclohexa -2,5-dien-1-iminium) is triphenylmethane based cationic dye [18] which has insightful applications as a biological stain [19], as a dermatological agent, as a veterinary medicine, an additive to poultry feed to inhibit propagation of mould, intestinal parasites and fungus [20]. It has extensive usage in the leather, textile and paper industry [21]. Time bound exposure of hazardous BG dye causes gastrointestinal and respiratory tract irritation in humans. Rarely, exposure of this perilous dye to skin may lead to dermatitis [22]. Indigo carmine (IC) (3,3′-dioxo-2,2′-bisindolyden-5,5′-disulfonic acid sodium salt) is an anionic dye belonging to the highly toxic indigoid class of dye [23]. It is widely used as a colorant in the textile industry and as an additive in pharmaceutical capsules and food items [24]. It has widespread application in the health industry [25]; however, prolonged consumption of IC tainted water can cause mild to severe hypertension, cardiovascular and respiratory disorders [26]. It may have deleterious carcinogenic impact on reproductive, developmental, and neuronal health [27]. Moreover, the presence of hazardous dye molecules like BG and IC in the industrial effluent streams which mixes with river and domestic water sources leads to a polluted water ecosystem [17,28]. Hence, effective treatment of these dye polluted aqueous streams by a simple, effective and low-cost methodology is needed [29,30].

Anabaena variabilis ARM 441 was chosen because it grows luxuriantly in paddy fields and it can be easily cultivated in inorganic media [31]. The present investigation was focused to explore the role of aqueous cellular extract of diazotrophic cyanobacterium *A. variabilis* ARM 441 in the fabrication of ZnO NPs [32]. Bioactive components present in aqueous extracts of *A. variabilis* ARM 441 were assessed by Gas chromatography-mass spectrometry (GC–MS), proton nuclear magnetic resonance (^{1}H NMR), ^{13}C nuclear magnetic resonance (^{13}C NMR), and FTIR spectroscopic analysis and were employed for the fabrication of ZnO NPs by using zinc acetate as a precursor by the co-precipitation method. Systematic characterizations of prepared ZnO NPs were performed through different analytical techniques. Microstructural analysis of ZnO NPs was carried out and used for photocatalytic degradation of brilliant green and indigo carmine dyes.

2. Material and methods

2.1. Chemicals and reagents

Zinc acetate dihydrate (Zn $(CH_3COO)_2{\cdot}2H_2O$)) (99.9%) was purchased from Merck EMSURE®, Germany. Both the dyes brilliant green ($C_{27}H_{33}N_2.HO_4S$) and indigo carmine ($C_{16}H_8N_2Na_2O_8S_2$) were purchased from Sigma Aldrich, USA. All the experiments were performed using analytical grade water with a resistivity of 18.2 MΩ cm from a Millipore Milli-Q Gradient filtration system (Millipore, USA). Unless otherwise stated, all other reagents and chemicals were of analytical grade and obtained from HiMedia Pvt. Ltd., India.

2.2. Preparation of cyanobacterial cell extracts

Anabaena variabilis ARM 441 was procured from the Centre for Conservation and Utilisation of Blue-Green Algae (CCUBGA), Indian Agricultural Research Institute (IARI), New Delhi (India). *A. variabilis* ARM 441 was cultivated for 21 days in Erlenmeyer flasks (5 L), stirred daily with continuous white light illumination (3000 Lux) at 28 °C. After 21 days, during the late logarithmic phase, biomass was filtered with Whatman's filter no. 1, thoroughly washed with milli-Q water to remove adhering medium debris, and shade dried. Dried algal biomass was powdered using a sterile mortar and pestle and stored in airtight vials at room temperature. 3 g of dried biomass was taken in 100 ml of milli-Q water in the Soxhlet apparatus for continuous solvent extraction, using water solvent at 90–95 °C for approximately 3 h to prepare algal extract (Fig. 1) [33]. A gradual development of green colour was noticed. The extract was allowed to cool at room temperature and filtered with Whatman's filter no. 1 to eliminate the biomass residues, leaving the dark green solution. The final extract was stored in glass vials at 4 °C for further analysis.

2.3. GC–MS analysis, ^{1}H NMR, and ^{13}C NMR spectroscopy of extract

The aqueous extract of *A. variabilis* ARM 441 was concentrated using a rotary evaporator for GC–MS analysis, ^{1}H NMR, and ^{13}C NMR spectroscopy to detect the bioactive compounds of interest [34]. The compounds obtained from *A. variabilis* ARM 441 were analyzed as per standard protocol using a Thermo Scientific TSQ 800 GC–MS. The extract components were identified by comparing the retention time and fragmentation pattern with mass spectra of the NIST database. The relative percentage of compounds was expressed along with peak area normalization, ^{1}H NMR and ^{13}C NMR were carried out using FT NMR Spectrometer model advance II (Bruker) at 400 MHz with a 5 mm inverse probe.

2.4. Phycosynthesis of ZnO NPs

Bioactive components from cell extracts of *A. variabilis* ARM 441 were utilized as reducing and a capping agent for the fabrication of ZnO NPs (Fig. 1). Initially, the dark green extract prepared from *A. variabilis* ARM 441 was diluted by 1:5 (v/v) to obtain a stock solution by addition of milli-Q water. Thereafter, 10 ml of $Zn(CH_3COO)_2$ (0.2 M) solution was added drop by drop to 90 ml of cyanobacterial stock solution in a round bottom flask. The mixture was maintained at 80 °C using a silicone oil bath, continuously stirred at 500 rpm on a magnetic stirrer for 6 h until the colour changed from dark green to cloudy light green. After cooling at room temperature, the pellet was collected by centrifugation at 8000 rpm for 10 min, and the supernatant was discarded. Further, the pellet was washed twice with milli-Q water followed by ethanol (99.9%) to remove the impurities and dried in a vacuum oven at 100 °C for 12 h. The dried powder was uniformly ground, sieved, and stored for subsequent analyses.

2.5. Analytical characterizations

2.5.1. UV–Visible spectroscopy

After visual identification, to affirm the complete reduction of zinc acetate to ZnO NPs was confirmed by UV Spectrophotometer containing UV Win Software. The absorption maxima were determined by scanning the sample in a quartz cuvette from 200 to 800 nm where the cuvette path length was set 1 cm [35].

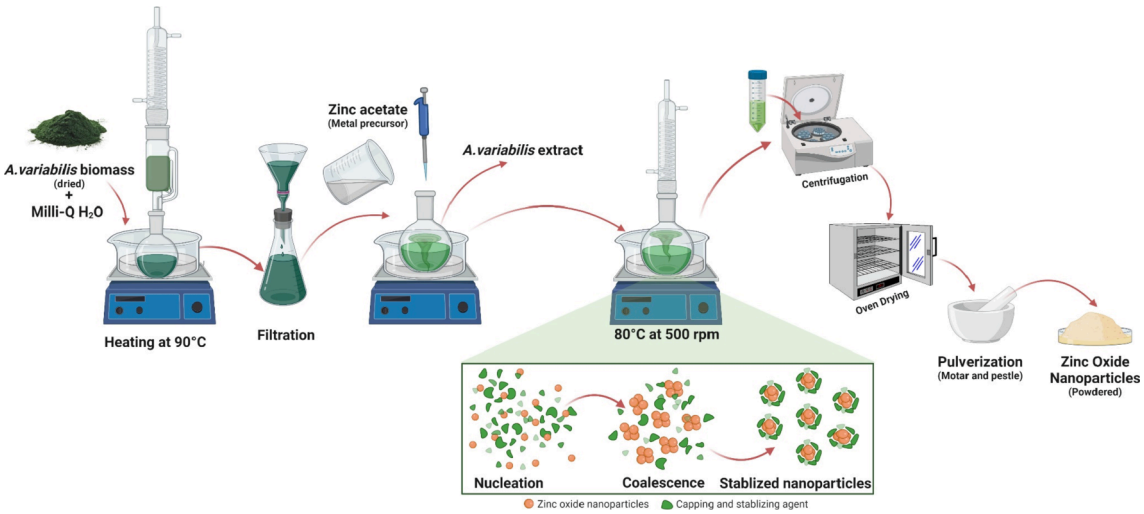

Fig. 1. Schematic flow illustrating the preparation of *A. variabilis* ARM441 extract and formation-mechanism of the ZnO nanoparticles.

2.5.2. Particle size, polydispersity index (PDI), and zeta potential

The stability of nanoparticles was evaluated by zeta potential whereas PDI estimates homogeneity of the sample. The average hydrodynamic size, PDI and zeta potential of synthesized ZnO NPs was determined using a Malvern Zen 3600 particle sizer, with the principle of dynamic light scattering. 1 mg of ZnO NPs powder was added to 1 ml of milli-Q water and sonicated for 20 min [36].

2.5.3. Fourier transform spectroscopy (FT-IR) analysis

Functional groups on the surface were identified using a PerkinElmer's FTIR. *A. variabilis* ARM 441 extract and ZnO NPs were triturated with pure KBr (Sigma Aldrich) and pressed in a mechanical press to generate pellets [37]. These pellets were analyzed along with pure KBr pellets at the background, and FT-IR spectrum was recorded in 4000–400 cm^{-1} to ascertain the possible secondary metabolites responsible for capping and stabilizing nanoparticles [38].

2.5.4. Brunauer–Emmett–Teller (BET)

Estimation of pore diameter, surface area, and porosity of ZnO NPs were characterized under liquid nitrogen temperature using Quanta Chrome Nova-1000 surface analyzer instrument. It involves multilayer adsorption–desorption of N_2 as a function of relative pressure. After degassing the samples at 150 °C for 2 h in N_2, final measurements were carried out. BET and de Boer t-plot methods were used to determine surface area and pore volume [39].

2.5.5. X-ray powder diffraction (XRD) analysis

XRD analysis of as-synthesized ZnO NPs was carried out in reflection geometry with PANalytical X'Pert PRO diffractometer using Cu Kα radiation (1.5406 Å) for an angle (2θ) range of 20°- 80° with step size 0.02 and counting time 5 s per step operating at 10 kV and 30 mA for identification of structure and crystalline phase. The crystallite size was calculated from XRD peaks by Debye Schererr equation $D = k\lambda/\beta\cos\theta$ where D is the crystallite size, λ is the wavelength for Cu Kα, β is full width half maxima (FWHM), θ is Bragg's diffraction angle, and k is constant (0.9). XRD data was analyzed by reitveild refinement by using crystallographic computing software Jana 2006 [40]. The phase composition was confirmed using the JCPDS PDF database (release 2011) [41].

2.5.6. X-ray photoelectron spectroscopy (XPS)

The atomic concentration and binding energy of synthesized ZnO NPs has been analyzed using the X-ray Photoelectron Spectroscopy PHI 5000 VersaProbe III (Physical Electronics). The binding energy was corrected for the charge shift using the C1s peak of graphitic carbon (BE ¼ 284.6 eV) as a reference. XPS measurement was performed with a step size of 0.2 eV. Spectra were processed and fitted by Origin 9.0 software using Gaussian–Lorentzian curve profile and Shirley baseline [42].

2.5.7. Field emission scanning electron microscopy (FE-SEM) and energy-dispersive X-ray spectroscopy (EDX), High-resolution transmission electron microscopy (HR-TEM), and Selected area diffraction (SAED) analysis

Size, morphology, and size distribution were analyzed using FE-SEM and elemental analysis was done using EDX. Powdered sample was used for FE-SEM at an accelerating voltage of 15 kV on MIRA3 TESCAN-XMU (Czech Republic). One drop of sonicated ZnO NPs in ethanol (99.9%) was dropped over the copper grid (200 mesh) and dried for surface analysis [43]. The micrographs and SAED pattern of as-synthesized ZnO NPs was recorded on high-resolution transmission electron microscope Jeol, JEM2100 at 200 kV. The microstructural analysis for obtained results from SEM and TEM was determined with ImageJ software.

2.6. Photocatalytic degradation of brilliant green and indigo carmine

The photocatalytic efficiency of as-synthesized ZnO NPs was estimated by the photodegradation of BG and IC dyes. The impact of major parameters (pH, dye concentration, catalyst dosage and time) affecting the dye degradation was evaluated individually. The ZnO NPs and dye mixture was stirred in the dark for 20 min to achieve the adsorption–desorption equilibrium and eliminate the adsorption errors. However, negligible chemisorption on the catalyst surface was observed. Each mixture was placed inside two 15 W low-pressure mercury lamps (LP Hg lamps, Cole-Parmer) with monochromatic emission at 253.7 nm. The fluency rate of the lamp was calculated to be 1.3 W/cm^2 photoreactor and exposed to UV light with continuous stirring. All the photochemical experiments were done in triplicates and at 40–45 °C. Milli-Q water was used in the preparation of sample solutions. Over desired time intervals (0–130 min) about 5 ml solution was collected and centrifuges to separate the catalyst. The absorption spectra for the supernatant were analysed using UV–Visible spectrophotometer in the 200–800 nm range. The degradation efficiency (%) was calculated by the following reference (Eq. (1)).

$$\text{Degradation efficiency } (\%) = \frac{(C_0 - C)}{C_0} \times 100 \quad (1)$$

where C_0 and C are the initial concentration (t = 0) and concentration at a given time interval of each dye at λ_{max}, respectively. LC-MS was conducted to study the photodegradation by products.

3. Results and discussion

3.1. Biosynthesis of ZnO NPs

A.variabilis ARM 441 mediated synthesis of ZnO NPs was achieved using a co-precipitation method. In the present study, the development of cloudy green colour in the reaction mixture confirmed the fabrication of ZnO NPs, which might be attributed to the interaction of functional groups of bioactive moieties of the cyanobacterial extract with zinc acetate to reduce it into Zn^0 ions, thus stabilizing ZnO NPs.

The gradual change in colour during the reaction between zinc acetate and aqueous extract of *A.variabilis* ARM 441 indicated the phycoreduction of zinc acetate to ZnO NPs as reported by [44]. The absorbance band edge of synthesized ZnO NPs was approximately 356 nm as shown in Fig. 2 (a), which coincides with the findings of Agarwal and Shanmugam (2019) [45]. The optical absorption seems to be enhanced in the 325–375 nm region. This indicates the blue shift in the absorption energies of ZnO NPs which are the manifestations of quantum size confinement in ZnO NPs. The broad band observed for ZnO NPs indicated the formation of varied sizes and shapes of the nanoparticles (Fig. 2(a)). However, the dynamic absorption peak within 200–250 nm suggests the presence of secondary metabolites such as fatty acids, polyphenols which might have been responsible for reduction of Zn $(CH_3COO)_2$ to ZnO NPs. The band gap energy of phycosynthesized ZnO NPs was calculated by Wood's Tauc relation (Eq. (2)),

$$[h\upsilon\alpha = c(h\upsilon - E_g)^n] \quad (2)$$

where α is absorption coefficient, c is constant, hυ is the photon energy, and E_g is band gap. The parameter 'n' varies with type of electronic transitions i.e. n = 2, 1/2, 2/3 or 3 for the direct-allowed, indirect-allowed, direct-forbidden, and indirect-forbidden transitions, respectively. As ZnO is a direct bandgap material, value of n = 2. Fig. 2(a)

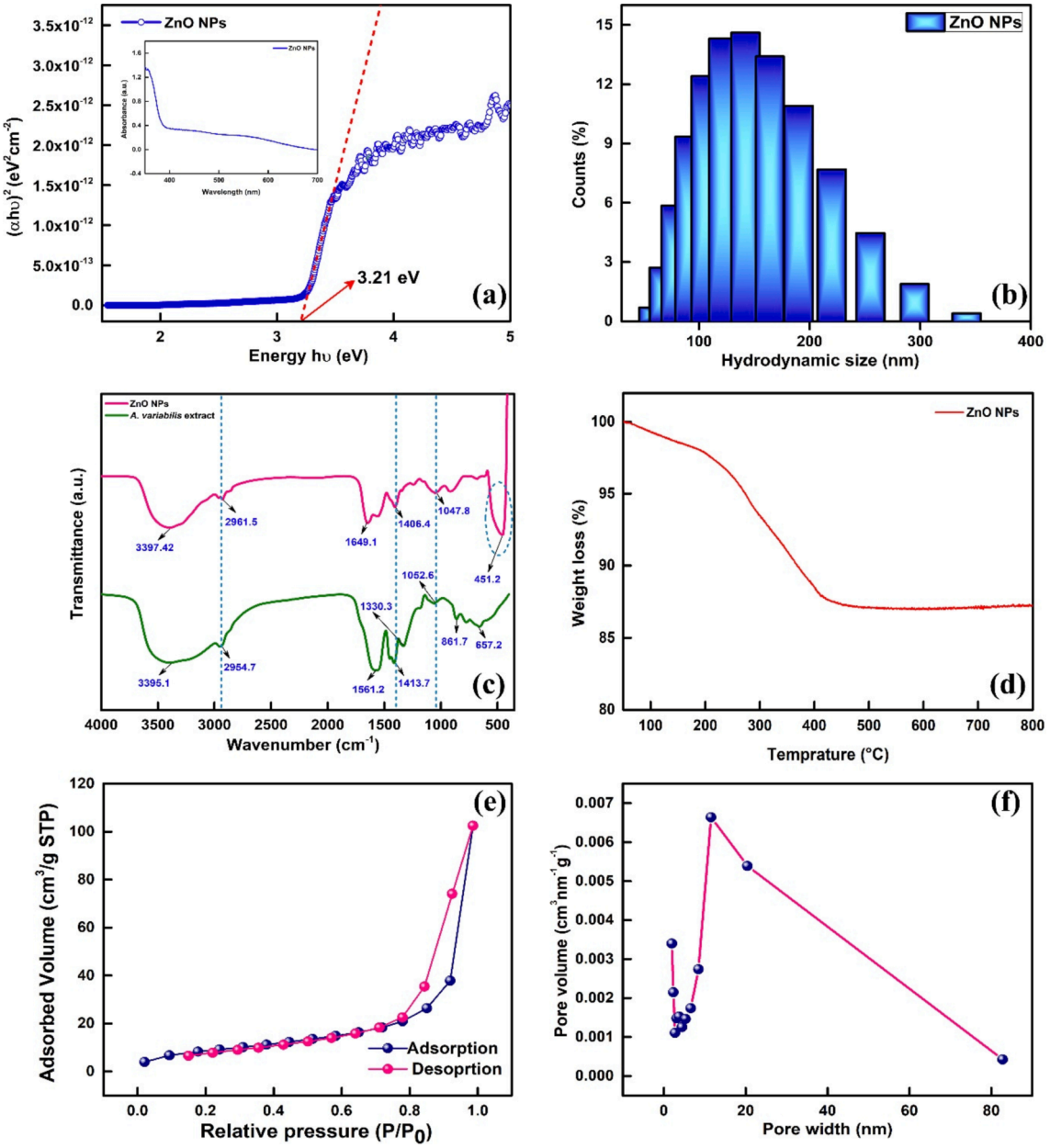

Fig. 2. (a) Plot of $(\alpha h\upsilon)^2$ vs hυ inset UV–vis spectra of the ZnO NPs synthesized using *A.variabilis* ARM 441 extract (b) Particle size distribution (DLS histogram) of the ZnO NPs synthesized using *A.variabilis* ARM 441 extract (c) FTIR spectra of *A.variabilis* ARM 441 extract and ZnO NPs; (d) TG thermogram (e) Nitrogen adsorption-desorption isotherm (f) Pore size distribution curve.

shows obtained data replotted between hυ v/s $(\alpha h\upsilon)^2$ by using origin 9.0 and the band gap was obtained by the extrapolation of a linear regression on X-axis. It is 3.21 eV which is similar to the previous reports [43]. The enhanced radiative absorptions in 325–375 nm region and broadening of the corresponding adsorption region (3.21 eV) could be due to the discrete inter-band absorptions between the energy state of conduction band and valence band.

3.2. Characterization methods

3.2.1. Particle size, polydispersity index (PDI), and zeta potential

Particle size, polydispersity index (PDI), and Zeta potential of the ZnO NPs were done using a Malvern Zeta sizer. Before analysis, sample (5 mg) was diluted (1:1, w/v) using 5 ml of milli-Q water and sonicated for 15 min. The peak of the graph (Fig. 2(b)) depicted 138.23 nm hydrodynamic size. Further, the PDI value was observed to be 0.753, which anticipated the presence of polydispersed ZnO NPs. The hydrodynamic size of as-synthesized ZnO NPs was relatively higher in contrast to solid-state. The phytochemicals and ions or molecules involved in the synthesis of ZnO NPs add extra hydrate layers, thus, higher hydrodynamic size in aqueous environment [46,47]. Also, as an additional aid to a certain degree was agglomeration, as reported [48,49].

The Zeta potential of phycosynthesized ZnO NPs can be affected by the bio-moieties present in *A.variabilis* ARM 441 extract [37]. On the contrary, nanoparticles' stability and biological activity can be derived from the surface charge. In this study, phycosynthesized ZnO NPs had a negative charge of −9.32 mV. The negative charge on ZnO NPs' surface was attributed to the presence of negative charge on long-chain fatty acid and aldehydes. This result indicated the presence of n-hexadecanoic acid and 13-tetradecenal on the surface of ZnO NPs. Several other reports are demonstrating comparable negative zeta potential for biogenic metallic nanoparticles [50]. Additionally, the current work's magnitude of zeta potential advocates the high stability of ZnO NPs suspension [37].

3.2.2. Fourier transform spectroscopy (FT-IR) analysis

FTIR study was performed to recognize the active biomolecules present in the *A. variabilis* extract involved in ZnO synthesis (Fig. 2(c)). A broad peak at 3395 cm^{-1} is an indication of O-H hydrogen bonds of alkaloids and steroids, which is in good correlation with the ZnO peak at 3397.42 cm^{-1}. Absorption peaks at 2961.5 cm^{-1} and 2954.7 cm^{-1} correspond to the alkyl (methyl) group's- C-H vibration in ZnO NPs *A. variabilis* extract, respectively. Prominent peaks of proteins were observed in *A. variabilis* extract for C═O stretching (amide I) and C—N stretching and N—H deformation (amide II) at 1561.2 cm^{-1}. The weak stretching of peaks at 1413.7 cm^{-1}, 1047.8 cm^{-1}, and 1413.7 cm^{-1}, 1052.6 cm^{-1} revealed the presence of C═O and C—O—C stretching in ZnO NPs and *A. variabilis* ARM 441 extract, respectively [3]. The spectrum of ZnO NPs showed a significant peak at 1649.9 cm^{-1}, which was characteristic stretching of fatty acid and carboxylic O-H bending vibration of fatty acid [51–53]. A distinct high intensity band was observed at 451.2 $cm^{-}1$, resulting from the presence of the oxygen and zinc bands while this peak was not observed in cyanobacterial extract. It is reported that secondary metabolites present in *A. variabilis* ARM 441 could be responsible for the reduction of zinc acetate dihydrate into ZnO NPs. Thus, it can be inferred that the nanoparticle is synthesized and stabilized by replacing acidic protons with methyl and hydroxyl groups [47]. Moreover, the less intense peaks that appeared at 861.7 cm^{-1} and 657.2 cm^{-1} were attributed to C—Cl and C≡C group of alkyl halides, and alkynes found in cyanobacterial extract, confirmed the incorporation of synthesis ZnO NPs. The primary molecules responsible for the stabilization are fatty acids, which have been validated with the findings of GC–MS and NMR.

3.2.3. Thermal behaviour

The synthesis of ZnO NPs was maneuvered *via* moderate thermal treatment and stability of the product with temperature variations is an important aspect of analysis. Thermogravimetric analysis (TGA) was employed to as-synthesized ZnO NPs at the temperature range of 25–800 °C (Fig. 2(d)). The ZnO NPs showed a minimal (1%) decrease in weight at 100 °C due to residual moisture ascribed to the dehydration phenomenon. A substantial continuous weight loss of about (~12%) was observed at above 200 °C due to the organic moieties of the cyanobacterial extract. After 442 °C, the extract is completely decomposed as a capping agent on ZnO NPs [54]. However, ZnO itself is stable at much higher temperatures than the studied range [55]. The weight loss was attributed majorly due to the decomposition of bioactive compounds. Predominant reduction of Zn $(CH_3COO)_2$ to Zn^{2+} by biomoieties occurred in the initial phase of synthesis with low formation levels of *A. variabilis*/Zn^{2+} complex which is further reduced to ZnO NPs [30]. Thus, secondary metabolites and other bioactive components in the extract of *A. variabilis* ARM 441 were significantly present over synthesized ZnO NPs, and confirmed through this analysis as well [56].

3.2.4. Nitrogen adsorption–desorption isotherms analysis (BET analysis)

Nitrogen adsorption and desorption experiments were performed to investigate the surface characteristics such as surface area and porous nature of synthesized ZnO NPs mediated *via A. variabilis* ARM 441. The results revealed a typical type IV isotherm attended by a type H3 hysteresis loop which authenticates mesoporous dominance (Fig. 2(e)) [57]. The pore size distribution is shown in Fig. 2(f), with an average pore diameter 11.551 nm, surface area was 38.718 m^2/g with pore volume 0.1633 cc/g. The average diameter was found to be smaller, with a greater surface area expectation. As the diameter decreases, surface area increases; hence the as-synthesized nanoparticles can be utilized as a catalyst involving adsorption and desorption of reactants [57]. A decrease in pore diameter of ZnO NPs can be another reason for its enlarged active sites [13,58].

3.2.5. Crystallinity study

XRD is the primary tool for characterizing synthesized ZnO NPs. It was performed to analyse the structural properties of pulverized ZnO NPs. The diffraction patterns obtained *via* phycosynthesis were indexed as hexagonal wurtzite structure according to ICDS data (JCPDS 01-079-2205) as shown in Fig. 3 (a). The fabricated nanoparticles were pure and crystalline in nature as no evidence of peak related to any foreign moiety or bulk remnant was observed. Subsequently, narrow and sharp diffraction peaks at 2θ and indexed with planes at 31.79° (1 0 0), 34.45° (0 0 2), 36.28° (1 0 1), 47.56° (1 0 2), 56.62° (1 1 0), 62.89° (1 0 3), 67.97° (1 1 2), 69.09° (2 0 1) provide the evidence for the synthesis of single-phase wurtzite crystal structure [59]. Further, the XRD pattern was refined and analyzed employing Rietveld whole profile fitting method based on refinement technique with the help of the Jana (2006) in Fig. 3 (b,c and d) and Table 1.

3.2.6. Structural and chemical nature

To validate the wurtzite structure and chemical purity of *A.variabilis* ARM 441 mediated ZnO NPs, XPS analysis was performed. Fig. 4 (a) shows the survey spectrum indicating the presence of Zn, O along with adventitious carbon [60]. The sample was chemically pure and devoid of any contaminants. High-resolution XPS spectra of the elements Zn and O are shown in Fig. 4 (b) and (c) respectively. The Zn 2p spectrum was deconvoluted (Fig. 4 (b)) and displayed a strong spin–orbit coupling doublet at 1022.39 eV and 1045.57 eV corresponding to core levels Zn $2p_{3/2}$ and Zn $2p_{1/2}$ respectively with binding energy 23.18 eV. Sharp peaks of Zn $2p_{3/2}$ were observed; thus it confirmed that the Zn element exists in the form of Zn^{2+} [61].

In the case of O1s, an asymmetric peak was observed in Fig. 4 (c). XPS line was fitted by Gauss profile functions including linear background [62]. O1s emission was composed of two contributions, with significant peaks centered at 531.77 and 533.17 eV. As per the literature, these peaks can be ascribed to Zn-OH bonding and to the presence

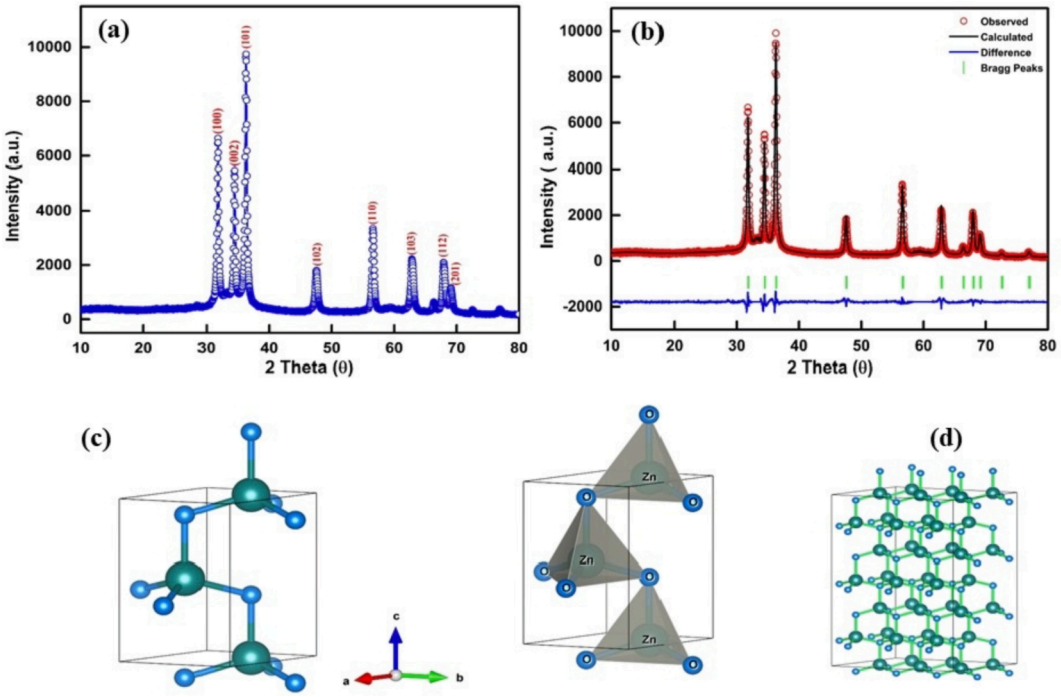

Fig. 3. (a) Crystallographic (XRD) pattern (b) Reitveild refinement (c,d) Wurzite hexagonal structure of ZnO NPs.

Table 1
Refined Parameters and Phase Data.

Cell parameters	a = b = 3.2488 Å; c = 5.2054 Å α = β = 90; γ = 120
Space group	$P6_3mc$ (186)
R-factor	R_{wp} = 5.60 %, R_{exp} = 6.83% GOF = 1.61
Damping factor	0.1000
Volume	47.58 $Å^3$

of C═O bonding originating from surface defects and chemisorbed oxygen, respectively [42,63]. Also, Zn 2p and O1s regions are consistent with stoichiometric ZnO. To pre-conclude, it can be deduced that Zn atoms in ZnO NPs crystal are in oxidation state 2p. The results show that the ratio O/Zn is slightly lower than unity, confirming that the synthesized powders are pure ZnO as confirmed by XRD results. In view of the XPS and EDX results, no impurities were found in their detection limits.

3.2.7. *Microstructural features*

Fig. 5 represents the microscopic analysis of synthesized ZnO NPs. FE-SEM micrographs illustrate that nanoparticles are of various shapes and sizes, primarily polygonal and spherical (Fig. 5 (a,b)). Aggregation was also visible. The drop-off in size was noticeable, which can be due to the entrapment of extract over ZnO NPs. The entrapment of extract played a vital role in remodeling hexagonal shape to spherical nanoparticles in SEM images and EDX analysis was also done as shown in Fig. 5 (c). Three peaks were observed between 1.1, 8.5 and 9.5 keV, characteristic of elemental zinc which certifies the formation of high purity ZnO NPs [64,65]. Apart from zinc (42.89%), a finite percentage of oxygen (57.11%) was also detected [66]. These results undoubtedly imply that even after several washings some residual portion of the extract was carried over the surface of ZnO NPs which establishes the strong bonding of bioactive molecules with ZnO NPs [64]. Reports have suggested that the use of different zinc salt precursors influences the morphological, textural and optical properties of ZnO NPs. As reported by Mayekar et al 2014 [67], ZnO NPs fabricated from zinc acetate possessed highest purity, whereas ZnO NPs fabricated from other zinc salts show similar crystallite size with different shapes. Additionally, it was predicted that acetate ions provide shielding effect during the synthesis preventing nanoparticle fusion during growth [68].

Further, HR-TEM images clearly illustrated the presence of faded but clear boundaries of extracts over the particles (Fig. 6 (a)) [58]. Hence, capping action of phytochemicals of cyanobacterial extract can be associated with reducing the size by preventing them from growing further and changing the shape during the crystallization process. The average particle size calculated from HR-TEM was 33.31 nm (Fig. 6 (b)). The interplanar adjacent planes were 0.256 nm, which corresponds to the inter-planar separation of 002 face-centered cubic ZnO NPs (Fig. 6 (b)). SAED pattern of ZnO NPs was also studied. In Fig. 6(c), the presence of bright rings suggested the crystalline nature of fabricated ZnO NPs. The hexagonal wurtzite phase of ZnO NPs was evident from the concentric rings assigned to (1 0 0), (0 0 2), (1 0 1), (1 0 2), (1 1 0), (1 0 3), (1 1 2), (2 0 1) [69]. These findings agree well with the estimated calculations of XRD.

3.3. *Determination of A. variabilis ARM 441 bio-active compounds content*

3.3.1. *GC–MS analysis of extract from A.variabilis ARM 441*

Chromatogram of *A.variabilis* ARM 441 extract shows a number of peaks of bioactive compounds with variable retention times (Fig. 7). The major components present in the cyanobacterial extract of *A.variabilis* ARM 441, along with the molecular formula, molecular weight, retention time, and peak area, are presented in Table 2. The principle bioactive compounds (21) present in the extract include 13-tetradecenal (33.19 %), chloromethyl 5-chloroundecanoate (19.91%), n-hexadecanoic acid (12.83%), 4-hydroxy-4-methyl-2-pentanone (9.39%), octadecanoic acid (5.69%), 2-chloroethyl linoleate (3.09%), tetradecanoic acid, 10,13-dimethyl-, methyl ester (2.15%) hexadecanoic acid, 2-hydroxy-1-(hydroxymethyl) ethyl ester (1.86%), ricinoleic acid (0.81%), phytol (0.44%)[70,71] Thus, potential candidates for capping agents could be fatty acids, palmitic acid, and phytol along with protein moieties and some other ancillary phytochemicals. The abundant presence of n-hexadecanoic acid and 13-tetradecenal in cyanobacterial cell extract act as a coating and provide stability to ZnO NPs [70–72].

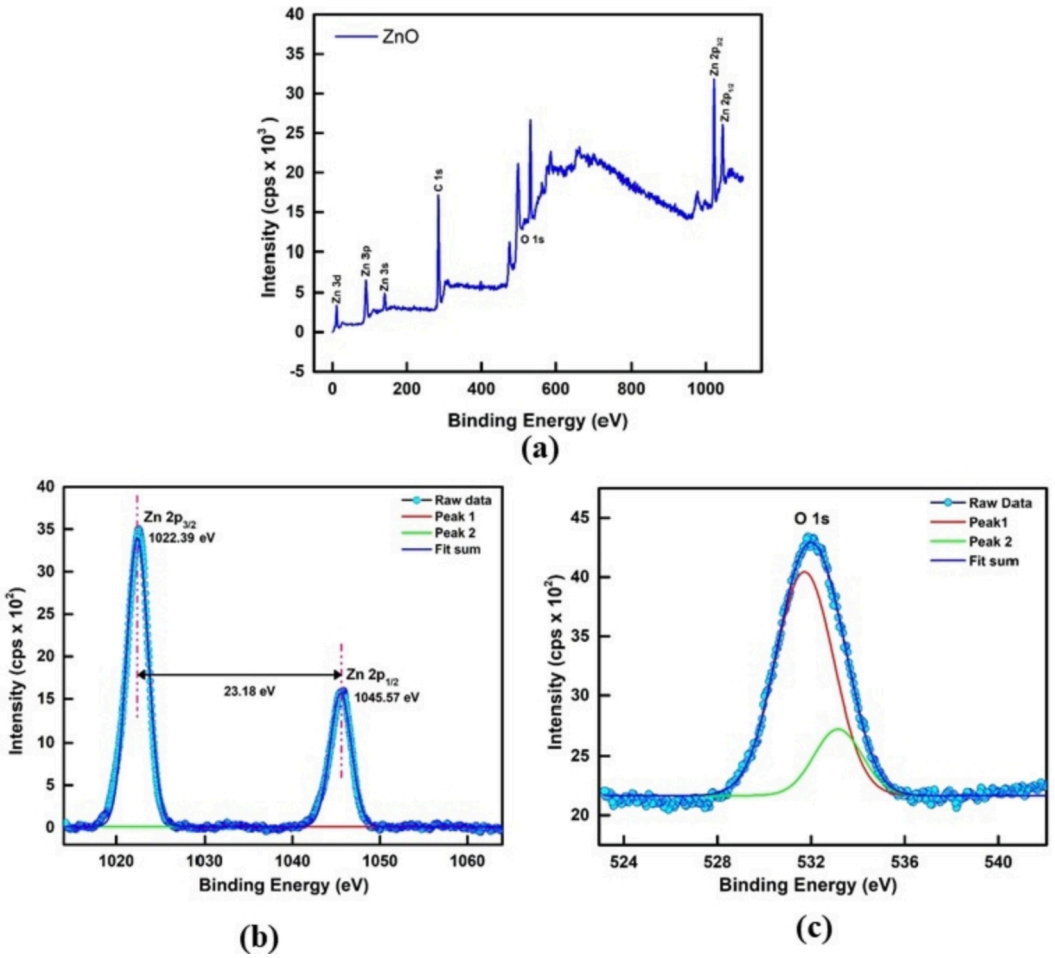

Fig. 4. (a) XPS survey scan; Deconvolution spectra of (b) Zn 2p (c) O1s.

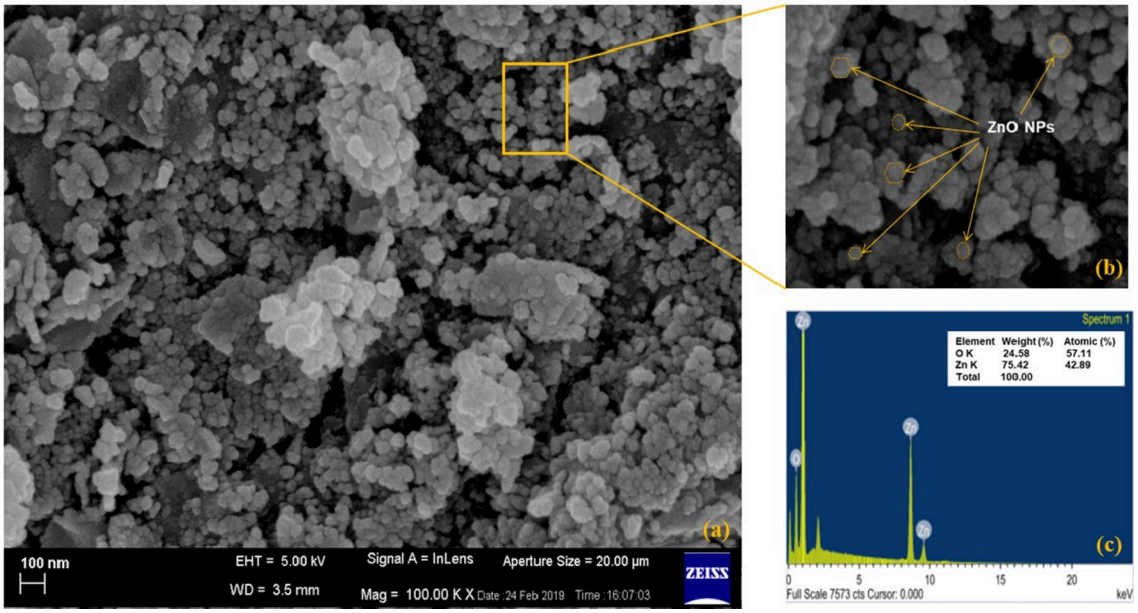

Fig. 5. Micrographs of as-prepared ZnO NPs (a, b) FESEM image (c) EDX Spectra (Unlabelled peak is of gold).

3.3.2. ^{1}H and ^{13}C NMR spectroscopic analysis A. variabilis ARM 441 extract

NMR spectroscopy is suitable for metabolite profiling and analysis as it provides an overview of all the metabolites and detects diverse groups of secondary metabolites [73,74]. ^{1}H and ^{13}C NMR spectroscopic investigations were done to determine the components present in the *A.*

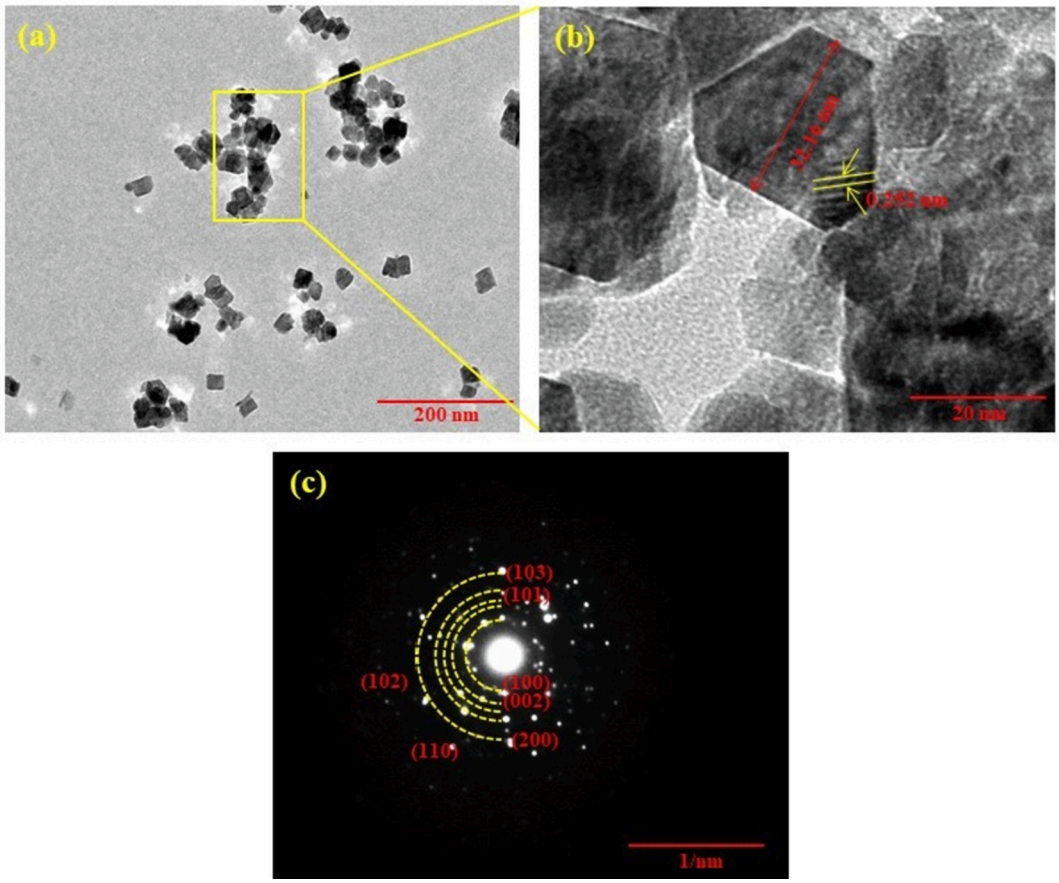

Fig. 6. (a,b)HRTEM image; (c) SAED pattern.

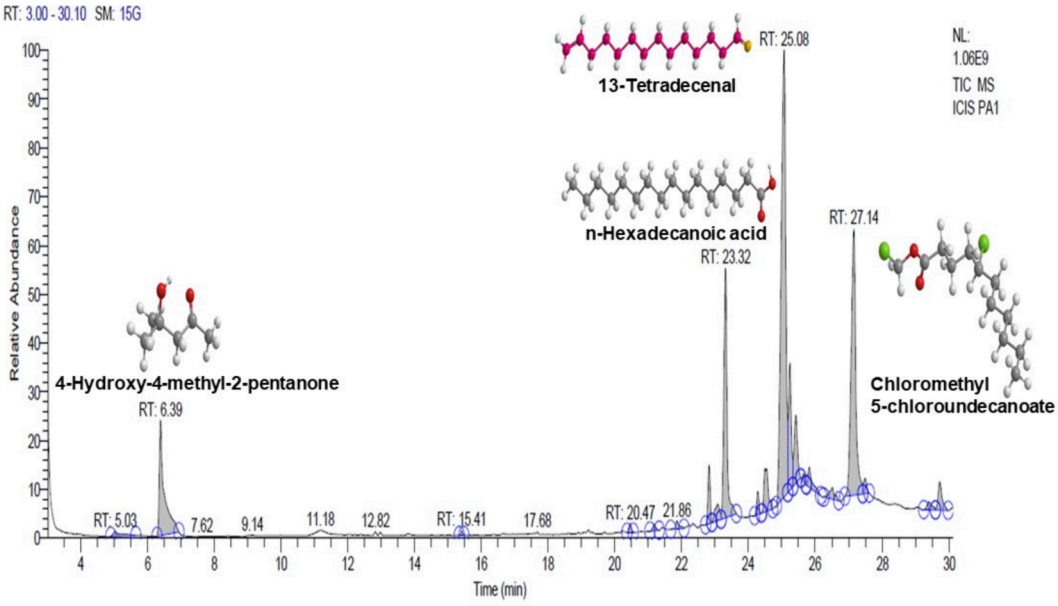

Fig. 7. GCMS of *A.varaibilis* ARM 441 extract.

variabilis ARM 441 cyanobacterial extract (S1). The ^{1}H NMR spectral data show chemical shift values ranging between $\delta = 0$ to 9.0, as displayed in Table 3. The chemical shift values δ 0.83, 0.85, 0.91, 0.93, 0.94 signify 1° alkanes; δ 1.21, 1.22, 1.31 represent 2° alkanes and δ 1.48 correspond to 3° alkanes whereas δ 1.78, 1.80, 1.91, 1.96, 2.02, 2.04, 2.05, 2.16, 2.18, 2.19 indicate the presence of alkenes and δ 2.31 imply for alkynes. The chemical shifts δ 3.89, 3.90, 3.91, 3.93 represent alkyl chloride and δ 2.53, 3.60, 3.62, 3.64 correspond to acids and esters[34]. Finally, the peaks arising from δ 3.06, 3.13, 3.20 indicate alcohols, δ 5.32, 5.33 signify the presence of 2-furanoyl group and δ 8.36 as aldehyde/ketone components, according to the standard chart [74].

The chemical shifts for ^{13}C NMR ranged between $\delta = 0$ to 200.0, as

Table 2
Bioactive compounds of *A. variabilis* ARM 441 extract identified through GC–MS analysis.

Peak No.	Retention time (RT)	Area%	Compound Name	Molecular Formula	Compound nature
1	5.03	0.61	4-Methyl-3-penten-2-one	$C_6H_{10}O$	Mesityl oxide
2	6.39	9.39	4-Hydroxy-4-methyl-2-pentanone	$C_6H_{12}O_2$	Diacetone alcohol
3	15.41	0.15	Dodecamethyl-cyclohexasiloxane	$C_{12}H_{36}O_6Si_6$	
4	20.47	0.26	Dodecane, 2,7,10-trimethyl-	$C_{15}H_{32}$	Sesquiterpene
5	21.18	0.33	Tetradecanoic acid	$C_{14}H_{28}O_2$	Myristic acid, Fatty acid
6	21.86	0.44	Phytol, acetate	$C_{22}H_{42}O_2$	Diterpene
7	22.83	2.15	Tetradecanoic acid, 10,13-dimethyl-, methyl ester	$C_{17}H_{34}O_2$	
8	23.08	1.32	cis,cis,*cis*-7,10,13-Hexadecatrienal	$C_{16}H_{26}O$	
9	23.32	12.83	n-Hexadecanoic acid	$C_{16}H_{32}O_2$	Palmitic acid
10	24.29	0.86	13-Hexyloxacyclotridec-10-en-2-one	$C_{18}H_{32}O_2$	
11	24.50	3.09	2-Chloroethyl linoleate	$C_{20}H_{35}ClO_2$	Fatty acid
12	25.08	33.19	13-Tetradecenal	$C_{14}H_{26}O$	Volatile steroid
13	25.25	5.69	Octadecanoic acid	$C_{18}H_{36}O_2$	Oleic acid
14	25.42	3.79	*cis*-7,*cis*-11-Hexadecadien-1-yl acetate	$C_{18}H_{32}O_2$	Alkyl Chalcogenides
15	25.66	0.29	17-Octadecynoic acid	$C_{18}H_{32}O_2$	Long-chain fatty alcohols
16	25.84	1.36	(R)-(-)-14-Methyl-8-hexadecyn-1-ol	$C_{17}H_{32}O$	Long-chain fatty alcohols
17	26.50	0.99	Methyl 12-hydroxy-9-octadecenoate	$C_{19}H_{36}O_3$	Fatty acid methyl ester
18	27.14	19.91	Chloromethyl 5-chloroundecanoate	$C_{12}H_{22}Cl_2O_2$	
19	27.47	0.81	Ricinoleic acid	$C_{18}H_{34}O_3$	Fatty acid
20	29.39	0.68	cis, 6-Octadecenoic acid, trimethylsilyl ester	$C_{21}H_{42}O_2Si$	Oleic acid
21	29.72	1.86	Hexadecanoic acid, 2-hydroxy-1-(hydroxymethyl)ethyl ester	$C_{19}H_{38}O_4$	Palmitic acid

Table 3
Characteristic peaks of *A. variabilis* ARM 441 extract identified through of ^{1}H and ^{13}C NMR.

Compound	^{1}H NMR chemical shift values	^{13}C NMR chemical shift values
Alkane		
1°	0.83, 0.85, 0.91, 0.93, 0.94	14.1, 14.0, 16.9, 20.2, 20.9
2°	1.21, 1.22, 1.31, 1.31	21.3, 22.3, 24.7, 25.2
3°	1.48	31.5, 34.0
Alkene	1.78, 1.80, 1.91, 1.96, 2.02, 2.04, 2.05, 2.16, 2.18, 2.19	125.7, 127.1, 127.7, 128.1, 128.2, 128.4, 129.7, 130.0, 131.6
Alkyne	2.31	72.6
Alkyl chloride	3.89, 3.90, 3.91, 3.93	48.7, 49.9, 63.0, 63.2
Acid/Ester	2.53, 3.60, 3.62, 3.64	172.5, 174.8
Alcohol	3.06, 3.13, 3.20	
Aldehyde/ Ketone	8.36	177.8
2-Furanoyl group	5.32, 5.33	66.8, 70.6, 172.6, 174.9

shown in Fig. S2 & Table 2. The ^{13}C spectrum showed resonance at δ 14.0, 14.1, 16.9, 20.2, 20.9 representing 1° alkanes; δ 21.3, 22.3, 24.7, 25.2 corresponding to 2° alkanes and δ 31.5, 34.0 signifying 3° alkanes whereas δ 125.7, 127.1, 127.7, 128.1, 128.2, 128.4, 129.7, 130.0, 131.6 indicate the presence of alkenes and δ 72.6 represent alkynes. The chemical shifts δ 48.7, 49.9, 63.0, 63.2 represent alkyl chloride and δ 172.5, 174.8 signify acids and esters. Finally, the peaks arising from δ 66.8, 70.6, 172.6, and 174.9 indicate the presence of the 2-furanoyl group and δ 177.8 as aldehyde/ketone components affirming the ^{1}H NMR spectral data[75]. Vinotha et al., 2019 [34] point out that the potential of NMR-based metabolomics is indiscriminating classes of compounds that may contribute to nanoparticles' surface stabilization. The obtained ^{1}H and ^{13}C NMR spectral analysis further corroborates with the GC–MS spectroscopic data.

3.4. Mechanism of synthesis of ZnO nanoparticles

In the present study, *A.variabilis* ARM 441 aqueous extract as a new, safe and inexpensive source was selected to manufacture ZnO NPs. The unique consortia of secondary metabolites present in algal extracts are commonly utilized as a native stabilizing and capping agent[64]. Recent studies have revealed that n-hexadecanoic acid has a potential role in synthesizing various nanoparticles [2,3] whereas using this algal extract for the effective synthesis of ZnO NPs is still being undiscovered. *A. variabilis* ARM 441 extract contains an abundance of phytochemical compounds that play vital roles of reducing and stabilizing agents for obtaining a good yield of ZnO NPs. Amongst all, 13-tetradecenal and n-hexadecanoic acid make up about 46% of *A.variabilis* ARM 441 aqueous crude extract with a percentage of 33.19% and 12.83% respectively. Therefore, it is assumed that 13-tetradecenal and n-hexadecanoic acid primarily lead the process of reducing Zn^{2+} ions to stable Zn atoms. The probable chemical equations for synthesis of *A.variabilis* /ZnO NPs as shown in Eqs. (3) and (4). Fig. 8 illustrates a plausible mechanism of interaction of Zn^{2+} ions and the main components of *A.variabilis* ARM 441 extract.

$$A.variabilis + H_2O_{(L)} + Zn^{2+} \rightarrow \left[A.variabilis/Zn^{2+}\right] \quad (3)$$

$$\left[A.variabilis/Zn^{2+}\right] + O_2 \rightarrow [A.variabilis/ZnO\,NPs] + CO_{2(g)} \quad (4)$$

This illustrates, excess of negatively charged atoms present in the extract donate their electrons and stabilize positively charged Zn^{2+} complex ions. As a result, the Zn^{2+} complex ions get converted to ZnO NPs [76,77].

3.5. Photocatalytic activity of ZnO NPs

Semiconductors like ZnO under the illumination of UV light absorb photons of energy equal or higher than the band gap energy, electrons and holes are created on the surface of a photocatalyst and generate highly reactive species which lead to the degradation of dyes [16,78]. Photocatalytic efficiency of a catalyst is dependent on several factors, such as crystallinity, phase composition, particle size, morphology, band gap, surface area and surface hydroxyl density, etc[30]. The photocatalytic behavior of *A.variabilis* ARM 441 synthesized ZnO NPs was estimated by the photodegradation of Brilliant green (BG) and Indigo caramine (IC) under UV illumination. A comparative study was performed to test the photocatalytic efficiency of ZnO NPs over cationic and anionic dyes. Various operational parameters such as dye concentration, pH, catalyst dosage, and time were studied for both BG and IC (S3). Fig. 9 (a) and (b) illustrate the absorption spectra of BG (λ_{max} = 625 nm) and IC (λ_{max} = 610 nm) during UV illumination for 130 min. The absorption peak of BG and IC decreased noticeably with progression of reaction time, hence the decreased relative concentration (C/C_0) of BG and IC (Fig. 10 (a)). After 130 min of exposure of BG to UV light, about 98.07 % of BG dye was degraded with a rate constant min (Table 4). Photodegradation was also visible by the gradual disappearance of BG's

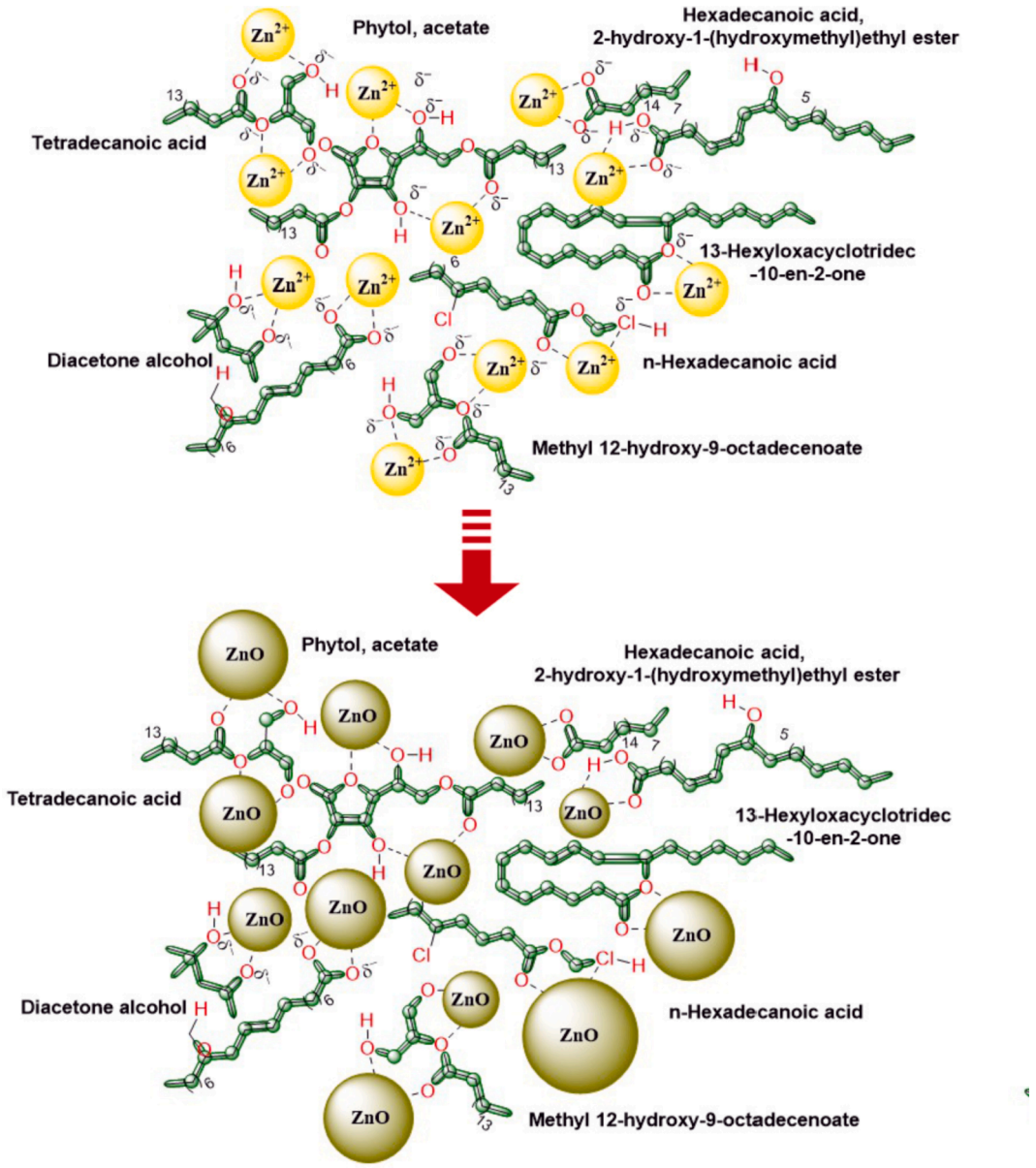

Fig. 8. Schematic diagram of interaction of Zn^{2+} ions with main compounds found in *A.variabilis* ARM 441 to produce ZnO-NPs.

bluish green colour to a colourless solution, indicating the complete removal of chromophore in BG molecules, which was further analysed the by-products by LC-MS analysis. The photodegradation of BG dye followed first order kinetics with catalytic dosage (50 mg/100 ml), dye concentration (30 mM); pH (7). However, in the case of IC, after the exposure of 130 min, about 80.8% of the dye was degraded and it also followed first order kinetics with catalytic dosage (50 mg/100 ml), dye concentration (30 mM), and pH (5) (Fig. 10 (b)).

Concerning the interference of absorbance with photodegradation the control set of experiments (Fig. S5 (a)) were conducted in the absence of UV light with ZnO NPs. No significant changes in the concentration of dyes was observed after attaining the adsorption–desorption equilibrium. Additionally, another control test for the photocatalytic degradation of the respective dyes in the absence of ZnO NPs was performed and the results were not significantly different (Fig S5 (b)), which confirms the high photostability of dyes under the presence of UV light. Further, the decolouration reusability experiments for BG and IC were performed and the results are shown in Fig S6. The figure clearly illustrates the decline in degradation efficiency. It was observed that after 5 cycles, the degradation efficiency of ZnO NPs for BG and IC was 88% and 69% respectively. The stable crystal structure of ZnO NPs is mainly what makes catalytic reusability work well [78]. A comparetive literature search with current experimental data is represented in Table 5, which reveals that the photocatalytic efficiency of our phycosynthesized ZnO NPs is significant.

3.6. Mechanism of photodegradation

Photodegradation of dyes under UV illumination is governed by simultaneous photooxidation followed by photosensitization. In photooxidation, photoelectron-hole pairs are generated in the conduction and valence band, which pair with free oxygen and water molecules of the solution to generate hydroxyl radicals and superoxide anions. $OH^{\bullet}$ generated is the potential oxidizing agent that assists the degradation of dyes (Eqs. (5)–(12)) [21,78,81].

$$ZnO + h\upsilon \rightarrow ZnO\left(e^{-}_{C.B.} + h^{+}_{V.B}\right) \quad (5)$$

$$e^{-}_{C.B.} + O_2 \rightarrow \cdot O^{-}_{2} \quad (6)$$

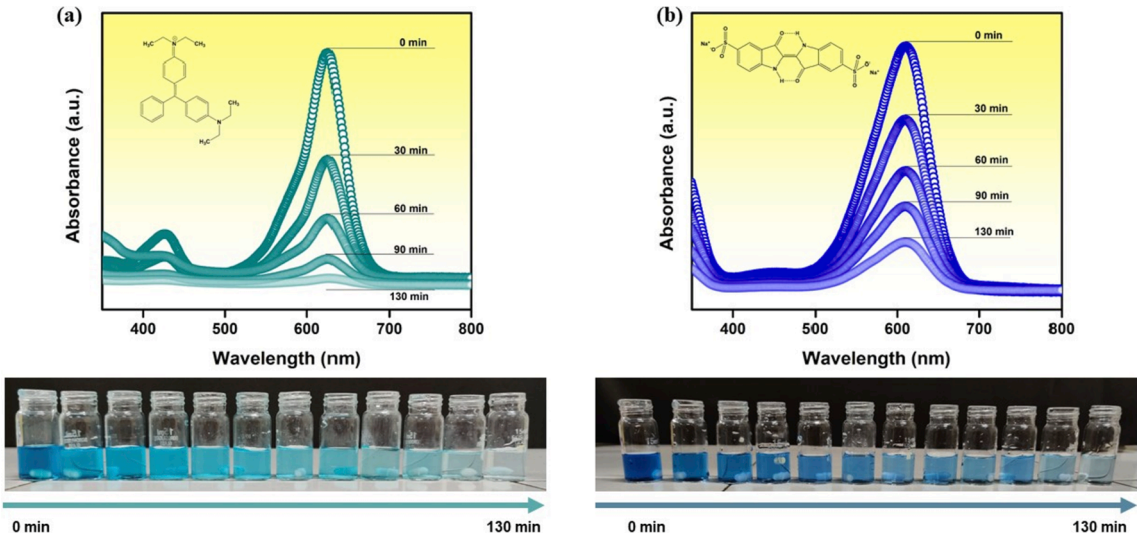

Fig. 9. Time dependent photocatalytic degradation studies by ZnO NPs (a) Absorption spectra of BG dye samples (b) Absorption spectra of IC dye samples.

$$h^{+}_{V.B} + OH^{-} \rightarrow \cdot OH^{-} \quad (7)$$

$$h^{+}_{V.B} + H_2O \rightarrow H^{+} + OH^{-} \quad (8)$$

$$\cdot O^{-}_{2} + H^{+} \rightarrow \cdot HO_2 \quad (9)$$

$$BG + \cdot OH^{-} \rightarrow Degradation\ \ Product \quad (10)$$

$$BG + h^{+}_{V.B} \rightarrow Oxidation\ \ Product \quad (11)$$

$$BG + e^{-}_{C.B.} \rightarrow Reduction\ \ Product \quad (12)$$

Simultaneously, the photosensitization mechanism, adsorbed dye molecules (BG), are excited by energy from UV irradiation. This leads to the formation of dye radicals (BG*) by jumping electrons to the conduction band of ZnO NPs and further producing extra oxygen radicals (O^{-}_{2}) (Eq. (13)–(16)) [19,21,81].

$$BG + h\upsilon \rightarrow BG^{*} \quad (13)$$

$$BG + ZnO \rightarrow \cdot BG^{+} + ZnO\left(e^{-}_{C.B.}\right) \quad (14)$$

$$ZnO\left(e^{-}_{C.B.}\right) + O_2 \rightarrow \cdot O^{-}_{2} + ZnO \quad (15)$$

$$\cdot BG^{+} \rightarrow Degradation\ \ Products \quad \text{.....(16)}$$

As brilliant green is a cationic dye, its excited dye radicals interact with the hydroxyl radicals and oxide radicals to generate degraded products (Eq. (17)–(24)) [82].

$$\cdot BG^{+} + OH^{-} \rightarrow BG + HO\cdot \quad (17)$$

$$BG + 2HO\cdot \rightarrow H_2O + Oxidation\ \ products \quad (18)$$

$$\cdot O^{-}_{2} + H^{+} \rightarrow \cdot HO_2 \quad (19)$$

$$\cdot HO_2 + H^{+} + e^{-}_{C.B.} \rightarrow H_2O_2 \quad (20)$$

$$H_2O_2 + e^{-}_{C.B.} \rightarrow HO\cdot + HO^{-} \quad (21)$$

$$\cdot BG^{+} + \cdot O^{-}_{2} \rightarrow Degradation\ \ Products \quad (22)$$

$$\cdot BG^{+} + \cdot HO_2 \rightarrow Degradation\ \ Products \quad (23)$$

$$\cdot BG^{+} + HO\cdot \rightarrow Degradation\ \ Products \quad (24)$$

The abundant production of oxidizing radicals during the process was highly beneficial for decolourization of BG [11,82]. Further, the degradation products were studied *via* LC-MS analysis and identified by interpretation of their *m/z* value (where *m* is molecular weight of the intermediates in the mass spectra and *z* is charge number) [83]. Fig. 11 (a) represents the mass spectrum of standard BG dye and its characteristic peak was identified at 386.50 *m/z* and Fig. 11 (b, c) depict their mass spectrum in presence of ZnO NPs under UV irradiation after 60 min and 130 min respectively. Various by-products (BP) of lower masses (*m/z*) at different degradation stages were observed (Fig. 11 (b, c)) and their plausible fragmentation pattern is illustrated in Fig. 12.

Initial de-ethylation of BG either by direct photolysis or ˙OH have contributed to the independent formation of BP1 with *m/z* 357.23. The removal of the $HO^{\cdot}_{2}$ group from peroxy radical and then upon subsequent reaction with H_2O can lead to the generation of degradation product BP1, an enol (ethenol) [84]. This ethenol can undergo keto-enol tautomerism forming acetaldehyde. These de-ethylated byproducts were also reported by Rehman et al [84]. Another degradation product BP9 (*m/z* 399.36) was formed, and its hydroxylation can lead to the formation of BP10 with *m/z* 415.34 [84]. Direct photolysis of BP9 can form BP4 *m/z* 254.18; following the same mechanistic pathway BP10 can lead to production of BP5 (*m/z* 270.13). Such types of hydroxylation byproducts have been reported in literature [85–87]. The addition of ˙OH net resulted in the formation of intermediate by product BP4 with *m/z* 254.13 [84]. Hydroxylation of BP4, possibly at the aromatic ring, could lead to the formation of BP5, *m/z* 270.13 whereas its de-ethylation can lead to the formation of degradation product BP6, *m/z* 226.12 [84,86]. There is the elimination of the $–NCH_2CH_3$ group, followed by the insertion of H^{+}, forming BP2 with *m/z* 347.21. The OH group added to BP2 and easily oxidized to –CO and forming benzophenone (BP3) as the oxidizing agent [88]. Due to presence of excess ˙OH, and subsequent addition to BP3 intermediate degradation products were obtained followed by an internal cycle process resulting in formation of BP7 (*m/z* 149.12) identified as phthalic anhydride. Subsequently, decarboxylation process followed by addition of ˙OH led to formation of BP8. Further, the opening of the aromatic rings occurred and aliphatic compounds were converted into oxalic acid, which ultimately oxidized into CO_2 and H_2O. After that, further degradation and abstraction of H-atom from the resulting intermediates causes *m/z* to dip further into the lowest value of 60.

The final solution consisted of smaller hydrocarbons and other organic residues. It was evident that photodegradation was more efficient and selective for cationic dye brilliant green compared to anionic indigo caramine because of the electrostatic interaction between the dye molecules and photocatalyst. ZnO NPs were negatively charged (Zeta potential = −9.32 mV) in a neutral solution which elucidated the

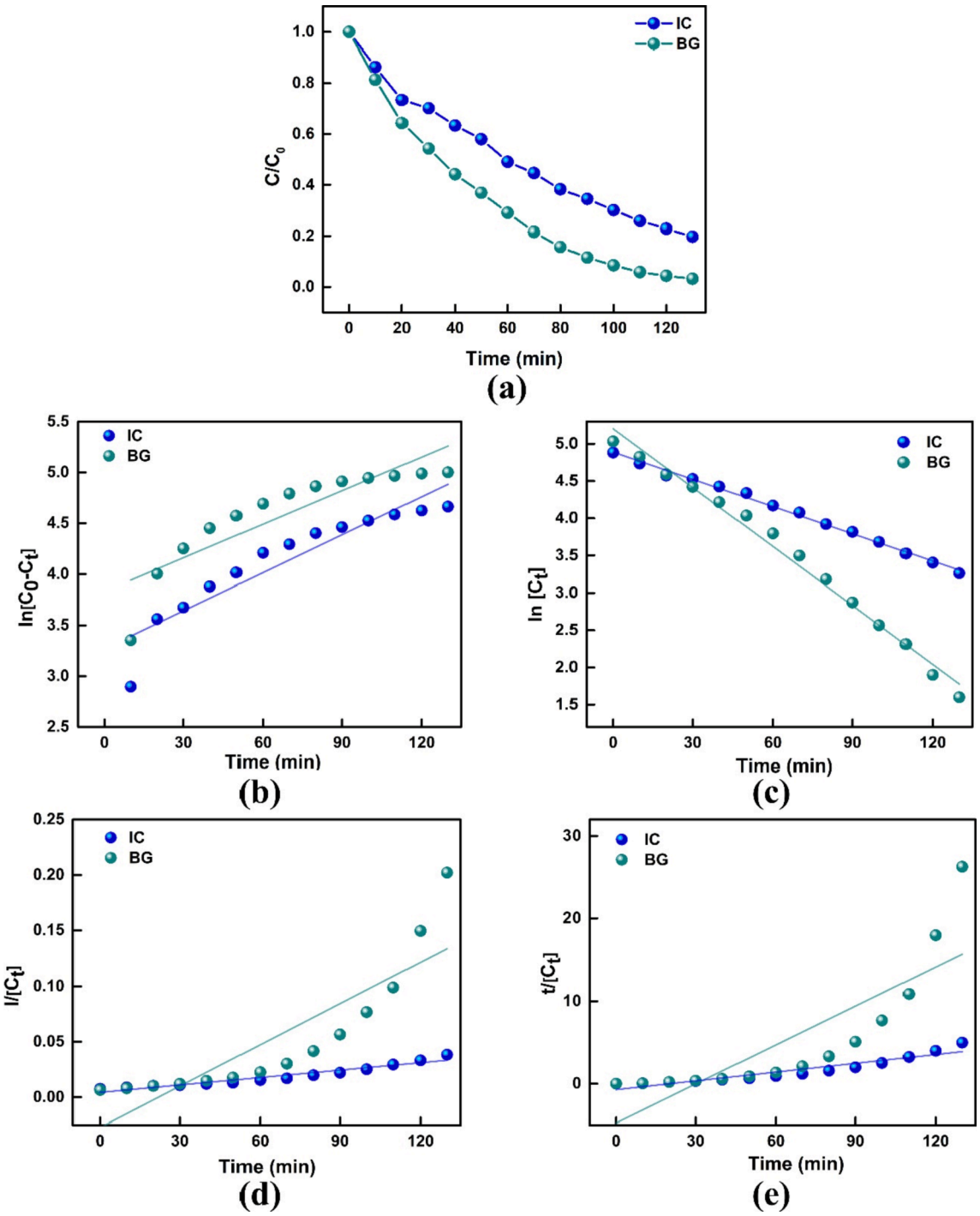

Fig. 10. Plots of BG and IC dyes (a) Time dependent degradation (b) First order kinetics (c) Pseudo first order kinetics (d) Second order kinetics (e) Pseudo second order.

Table 4
Kinetic parameters for degradation of BG and IC *via* ZnO NPs under UV- illumination.

		Brilliant Green		**Indigo Carmine**	
Model	Equation	Rate constant, k	R^2 values	Rate constant, k	R^2 values
First order	$lnC = lnC_0 - kt$	26.4×10^{-3} min^{-1}	0.98743	12.1×10^{-3} min^{-1}	0.99499
Pseudo-first order	$ln[C - C_0] = lnC - kt$	10.9×10^{-3} min^{-1}	0.75623	12.4×10^{-3} min^{-1}	0.85349
Second order	$\frac{1}{C} = \frac{1}{C_0} + kt$	1.2×10^{-3} $mg^{-1}L^{-1}min^{-1}$	0.73602	2.2×10^{-4} $mg^{-1}L^{-1}min^{-1}$	0.92604
Pseudo-second order	$\frac{t}{C} = \frac{t}{C_0} - \frac{1}{kC_0^2}$	5.2×10^{-3} $mg^{-1}L^{-1}min^{-1}$	0.66775	1.7×10^{-3} $mg^{-1}L^{-1}min^{-1}$	0.88115

Table 5
Comparison of photocatalytic performance of phycosynthesized ZnO NPs with other green synthesized ZnO nanomaterials on degradation of different chemical dyes.

Nanomaterial	Green source	Dye	Irradiation source	Degradation time (min)	Degradation efficiency (%)	Reference
ZnO	*Hylocereus polyrhizus*	Methylene Blue	Sunlight	120	95.0	[12]
ZnO	*Carissa edulis*	Congo Red	Photo-reactor	130	97.0	[77]
ZnO	*Calotropis procera*	Methyl Orange	UV light	100	81.0	[78]
ZnO	*Ulva lactuca*	Methylene Blue	Sunlight	120	90.4	[79]
ZnO	*Coriandrum sativum*	Reactive Yellow 186	Sunlight	130	93.4	[80]
ZnO	*Anabaena variabilis* ARM 441	Brilliant Green	UV light	130	98.1	Current study

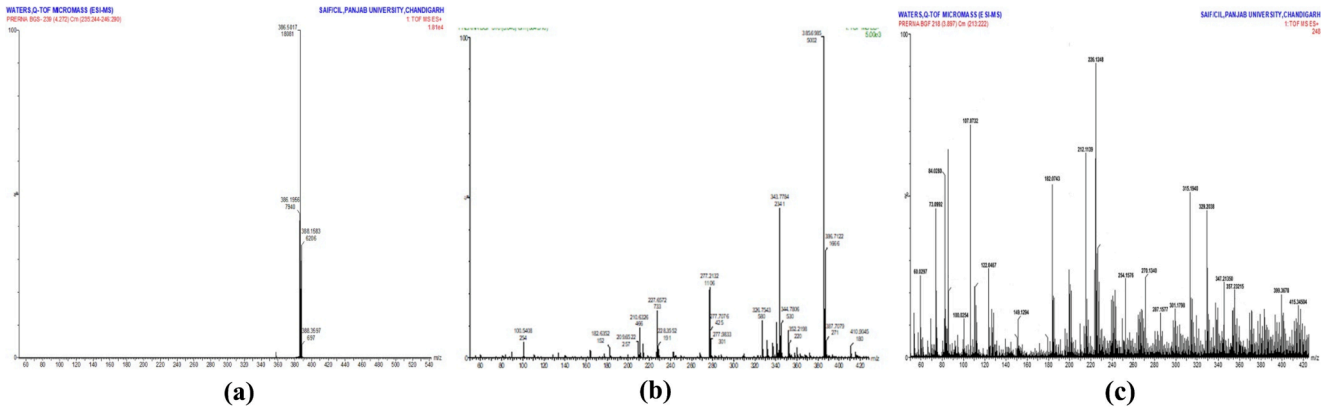

Fig. 11. Mass spectra of BG Dye (a) Before irradiation (b) after UV irradiation in the presence of ZnO NPs for 60 and 130 min, respectively.

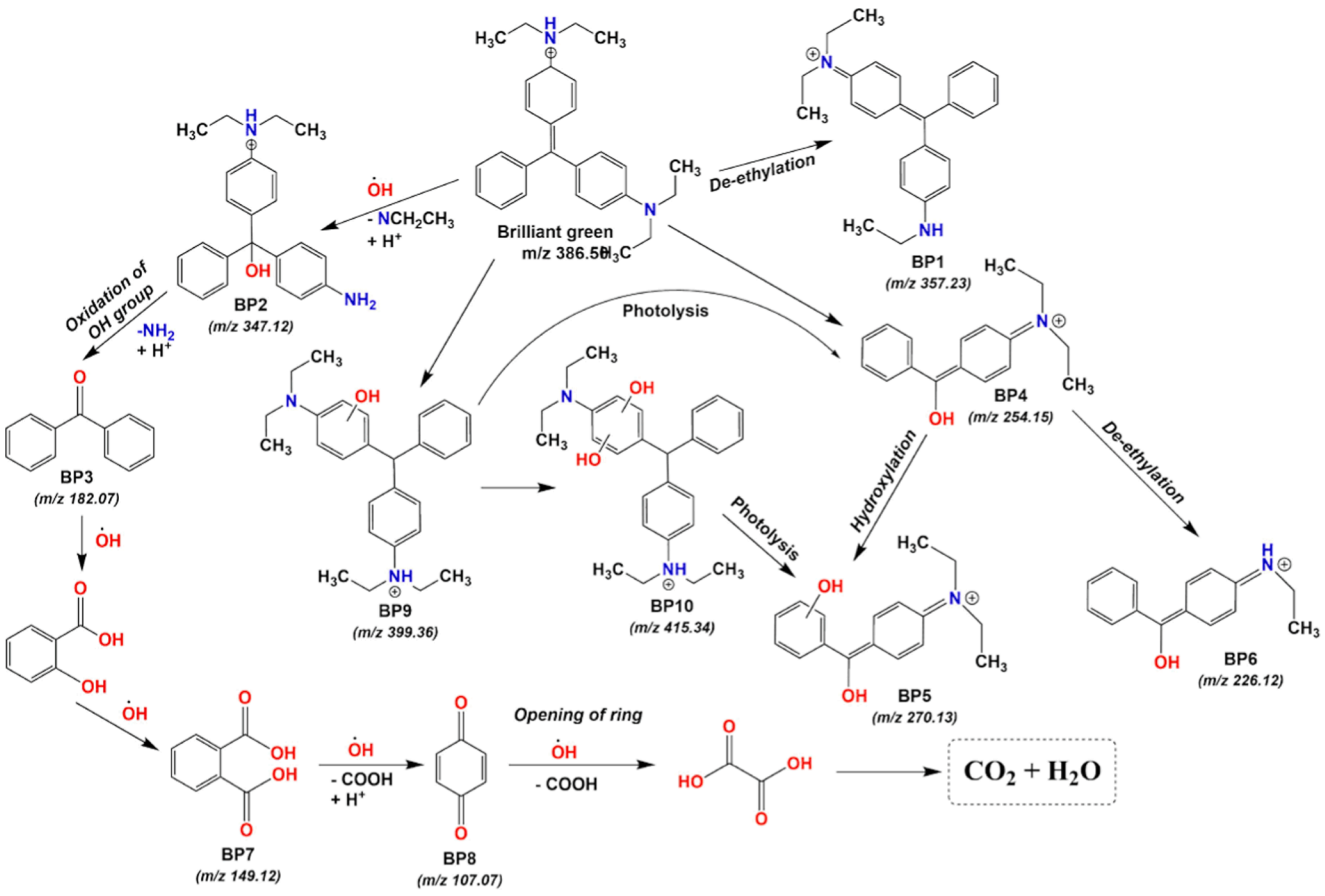

Fig. 12. Detailed photocatalytic degradation mechanism of BG dye by ZnO NPs under UV irradiations.

selectivity for cationic dyes.

4. Conclusion

ZnO NPs were fabricated successfully by co-precipitation method using an aqueous extract of *A. variabilis* ARM 441 witho,ut utilizing any additional solvent, catalyst or template. The mechanism behind the green synthesis of this nanomaterial was deciphered in which the antioxidants of the cyanobacterial extract formed coordinated complexes with Zn^{2+} and nanoscale particles of ZnO. Characterization revealed the property of biosynthesized ZnO NPs, which includes crystalline of nanoscale dimension (33.31 nm) possessing hexagonal wurtzite phase, exhibiting promising optical properties. The heterogeneous morphology and sizes were due to the method employed and the calcination temperature, where it was difficult to control the size and shape of the particles. BET analysis confirms the formation of highly porous nanoparticles. The photocatalytic degradation studies revealed amphoteric and rapid photocatalytic activity of ZnO NPs and exhibited excellent degradation of cationic dye BG as compared to anionic IC dye. The optimal dosage of 0.05 g/100 ml was identified to remove the maximum amount of BG dye molecules at 30 mM dye concentration. The photodegradation followed first order kinetic model with rate constant 26.4×10^{-3} min^{-1} with $R^2 = 0.98743$. The results compiled that the ZnO NPs degraded both cationic as well as anionic dyes in acidic as well as neutral conditions. The ability of as-prepared ZnO NPs to produce an extensive amount of reactive radicals (such as superoxides, hydroxides and peroxides) owing to their large surface area makes it an eligible photocatalyst. Biosynthesized ZnO NPs showed evidence to act as an effective photocatalyst, which is appropriate for industrial wastewater treatment, especially to degrade harmful and toxic pollutants that persist in aquatic environment.

CRediT authorship contribution statement

Prerna: Methodology, Validation, Formal analysis, Investigation, Writing – original draft, Visualization. **Harshit Agarwal:** Methodology, Resources, Writing – review & editing, Visualization, Supervision. **Dinesh Goyal:** Conceptualization, Resources.

Declaration of Competing Interest

The authors declare that they have no known competing financial interests or personal relationships that could have appeared to influence the work reported in this paper.

Acknowledgements

The authors would like to thank the Director, Thapar Institute of Engineering & Technology (Deemed to be University), Patiala for infrastructural support. The authors wish to thank Head, Department of Physics, Banaras Hindu University, for having provided the necessary analytical facilities to carry out this work.

Appendix A. Supplementary material

Supplementary data to this article can be found online at https://doi.org/10.1016/j.inoche.2022.109676.

References

[1] P. Khanna, A. Kaur, D. Goyal, J. Microbiol. Methods 163 (2019), 105656.
[2] D. Borah, N. Das, N. Das, A. Bhattacharjee, P. Sarmah, K. Ghosh, M. Chandel, J. Rout, P. Pandey, N.N. Ghosh, C.R. Bhattacharjee, Appl. Organomet. Chem. 34 (5) (2020) 852.
[3] M. Ebadi, M.R. Zolfaghari, S.S. Aghaei, M. Zargar, M. Shafiei, H.S. Zahiri, K. A. Noghabi, RSC Adv. 9 (41) (2019) 23508–23525.
[4] Y. He, F. Wei, Z. Ma, H. Zhang, Q. Yang, B. Yao, Z. Huang, J. Li, C. Zeng, Q. Zhang, RSC Adv. 7 (63) (2017) 39842–39851.
[5] J. Huang, L. Lin, D. Sun, H. Chen, D. Yang, Q. Li, Chem. Soc. Rev. 44 (17) (2015) 6330–6374.
[6] V. Patel, D. Berthold, P. Puranik, M. Gantar, Biotechnol. Reports 5 (Supplement C) (2015) 112–119.
[7] N. Asmathunisha, K. Kathiresan, Colloids Surf. B Biointerfaces 103 (Supplement C) (2013) 283–287.
[8] S. Azizi,, M.B. Ahmad,, F. Namvar,, R. Mohamad, Mater. Lett. 116(Supplement C) (2014) 275–277.
[9] G. Sangeetha, S. Rajeshwari, R. Venckatesh, Mater. Res. Bull. 46 (12) (2011) 2560–2566.
[10] A. Abdelkhalek, A.A. Al-Askar, NATO Adv. Sci. Inst. Ser. E Appl. Sci. 10 (15) (2020) 5054.
[11] M. Aminuzzaman, L.P. Ying, W.-S. Goh, A. Watanabe, Bull. Mater. Sci. (2018), https://doi.org/10.1007/s12034-018-1568-4.
[12] M. Aminuzzaman, P.S. Ng, W.-S. Goh, S. Ogawa, A. Watanabe, Synth. React. Inorg. Met.-Org. Nano-Met. Chem. 49 (11) (2019) 401–411.
[13] A. Bayrami, E. Ghorbani, S. Rahim Pouran, A. Habibi-Yangjeh, A. Khataee, M. Bayrami, Ultrason. Sonochem. 58 (2019), 104613.
[14] H.-Y. Chai, S.-M. Lam, J.-C. Sin, Mater. Lett. 242 (2019) 103–106.
[15] V.N. Kalpana, B.A.S. Kataru, N. Sravani, T. Vigneshwari, A. Panneerselvam, V. Devi Rajeswari, OpenNano 3 (2018) 48–55.
[16] D. Suresh, P.C. Nethravathi, H. Udayabhanu, H. Rajanaika, S.C.S. Nagabhushana, Mater. Sci. Semicond. Process. 31 (2015) 446–454.
[17] A.K. Chauhan, N. Kataria, V.K. Garg, Chemosphere 247 (2020), 125803.
[18] D.J. Alderman, J. Fish Dis. (1985) 289–298, https://doi.org/10.1111/j.1365-2761.1985.tb00945.x.
[19] M. Zhang, L. Chang, Y. Zhao, Z. Yu, Arab. J. Sci. Eng. 44 (1) (2019) 111–121.
[20] A. Demirbas, J. Hazard. Mater. 167 (1–3) (2009) 1–9.
[21] D. Bhattacharya, D. Ghoshal, D. Mondal, B.K. Paul, N. Bose, S. Das, M. Basu, Results Phys. 12 (2019) 1850–1858.
[22] G. A.,, A.A. J.,, G. A.,, S. V. M.,, T. M.,, M.A. Riswan Ahamed,, R.S. Azarudeen, J. Hazard. Mater. 373 (2019) 493–503.
[23] S. Ryali, P.D. Sanasi, J. Chin. Chem. Soc. 65 (12) (2018) 1423–1430.
[24] U.R. Lakshmi, V.C. Srivastava, I.D. Mall, D.H. Lataye, J. Environ. Manage. 90 (2) (2009) 710–720.
[25] N. Almoisheer, F.A. Alseroury, R. Kumar, M. Aslam, M.A. Barakat, RSC Adv. 9 (1) (2018) 560–568.
[26] A.K. Subramani, K. Byrappa, S. Ananda, K.M. Lokanatha Rai, C. Ranganathaiah, M. Yoshimura, Bull. Mater. Sci. (2007) 37–41, https://doi.org/10.1007/s12034-007-0007-8.
[27] M.G. Yazdi, M. Ivanic, A. Mohamed, A. Uheida, RSC Adv. 8 (43) (2018) 24588–24598.
[28] S.A. Ali, I.Y. Yaagoob, M.A.J. Mazumder, H.A. Al-Muallem, J. Hazard. Mater. 369 (2019) 642–654.
[29] M. Aminuzzaman, C.-Y. Chong, W.-S. Goh, Y.-K. Phang, T. Lai-Hock, S.-Y. Chee, M. Akhtaruzzaman, S. Ogawa, A. Watanabe, J. Cluster Sci. 32 (4) (2021) 949–958.
[30] K. Rambabu, G. Bharath, F. Banat, P.L. Show, J. Hazard. Mater. 402 (2021), 123560.
[31] D. Chittora, M. Meena, T. Barupal, P. Swapnil, Biochem. Biophys. Rep. 22 (2020), 100737.
[32] A. Malek Shahkouhi, E. Motamedian, PLoS ONE 15 (1) (2020), e0227977.
[33] S.A. Khan, F. Noreen, S. Kanwal, A. Iqbal, G. Hussain, Mater. Sci. Eng. C Mater. Biol. Appl. 82 (2018) 46–59.
[34] V. Vinotha, A. Iswarya, R. Thaya, M. Govindarajan, N.S. Alharbi, S. Kadaikunnan, J.M. Khaled, M.N. Al-Anbr, B. Vaseeharan, J. Photochem. Photobiol. B 197 (2019), 111541.
[35] A.K. Dutta, S.K. Maji, B. Adhikary, Mater. Res. Bull. 49 (2014) 28–34.
[36] S. Thakur, S. Singh, B. Pal, J. Nanostruct. Chem. (2021), https://doi.org/10.1007/s40097-021-00412-x.
[37] K.M. Ezealisiji, X. Siwe-Noundou, B. Maduelosi, N. Nwachukwu, R.W.M. Krause, International Nano Letters 9 (2) (2019) 99–107.
[38] N. Akhtar, D. Goyal, A. Goyal, Energy Convers. Manage. 141 (2017) 133–144.
[39] R. Kaur, D. Goyal, S. Agnihotri, Carbohydr. Polym. 262 (2021), 117906.
[40] H. Agarwal, J.A. Alonso, Á. Muñoz, R.J. Choudhary, O.N. Srivastava, M.A. Shaz, J. Alloys Compd. 845 (2020), 156355.
[41] H. Agarwal, J.A. Alonso, Á. Muñoz, R.J. Choudhary, O.N. Srivastava, M.A. Shaz, J. Phys. Condens. Matter 33 (2021) 26, https://doi.org/10.1088/1361-648X/abfc14.
[42] A. Diallo, B.D. Ngom, E. Park, M. Maaza, J. Alloys Compd. 646 (2015) 425–430.
[43] L.P. Brazuna, T.G. Tabuti, A. de Paula Silva, D.B. Tada, M.J. Politi, R. Bacani, E. R. Triboni, New J. Chem. 43 (48) (2019) 18988–18995.
[44] M. Naseer, U. Aslam, B. Khalid, B. Chen, Sci. Rep. 10 (1) (2020) 9055.
[45] H. Agarwal, V.K. Shanmugam, J. Drug Deliv. Sci. Technol. 54 (2019), 101291.
[46] L. Telgmann, M.T.K. Nguyen, L. Shen, V. Yargeau, H. Hintelmann, C.D. Metcalfe, Anal. Bioanal. Chem. 408 (19) (2016) 5169–5177.
[47] W.R. Rolim,, M.T. Pelegrino,, B. de Araújo Lima,, L.S. Ferraz,, F.N. Costa,, J.S. Bernardes,, T. Rodigues,, M. Brocchi,, A.B. Seabra, Appl. Surf. Sci. 463 (2019) 66–74.
[48] V. Ahluwalia, S. Elumalai, V. Kumar, S. Kumar, R.S. Sangwan, Microb. Pathog. 114 (2018) 402–408.
[49] L.F.T.F. Santos, C.R.G. Torres, T.M.F. Caneppele, A.C. Magalhães, A.B. Borges, Acta Odontol. Scand. 74 (2) (2016) 121–126.
[50] A. Sudha, J. Jeyakanthan, P. Srinivasan, Resour.-Effic. Technol. 3 (4) (2017) 506–515.

[51] R. Sankar, P. Manikandan, V. Malarvizhi, T. Fathima, K.S. Shivashangari, V. Ravikumar, Spectrochim. Acta A Mol. Biomol. Spectrosc. 121 (2014) 746–750.
[52] J.A. Carballo, A.L. Johnson, S.G. Sedgwick, R.S. Cha, Cell 132 (5) (2008) 758–770.
[53] P. Sharma, S. Pant, V. Dave, K. Tak, V. Sadhu, K.R. Reddy, J. Microbiol. Methods 160 (2019) 107–116.
[54] K. Rambabu, B. Fawzi, G.S. Nirmala, S. Velu, P. Monash, G. Arthanareeswaran, et al., Desalination Water Treat. 156 (2019) 267–277.
[55] M. Khatami, H.Q. Alijani, H. Heli, I. Sharifi, Ceram. Int. 44 (13) (2018) 15596–15602.
[56] K. Vimala, S. Sundarraj, M. Paulpandi, S. Vengatesan, S. Kannan, Process Biochem. 49 (1) (2014) 160–172.
[57] A.V. Anupama, W. Keune, B. Sahoo, J. Magn. Magn. Mater. 439 (2017) 156–166.
[58] A. Bayrami, S. Alioghli, S. Rahim Pouran, A. Habibi-Yangjeh, A. Khataee, S. Ramesh, Ultrason. Sonochem. 55 (2019) 57–66.
[59] P.E.J. Saloga, A.F. Thünemann, Langmuir 35 (38) (2019) 12469–12482.
[60] I.G. Morozov, O.V. Belousova, D. Ortega, M.-K. Mafina, M.V. Kuznetcov, J. Alloys Compd. 633 (2015) 237–245.
[61] J. Liqiang, W. Dejun, W. Baiqi, L. Shudan, X. Baifu, F. Honggang, S. Jiazhong, J. Mol. Catal. A Chem. 244 (1) (2006) 193–200.
[62] F. Säuberlich, J. Fritsche, R. Hunger, A. Klein, Thin Solid Films 431–432 (2003) 378–381.
[63] K. Steffy, G. Shanthi, A.S. Maroky, S. Selvakumar, J. Infect. Public Health 11 (4) (2018) 463–471.
[64] A. Król, V. Railean-Plugaru, P. Pomastowski, B. Buszewski, Phytochem. Lett. 31 (2019) 170–180.
[65] M. Fakhar-e-Alam, S. Rahim, M. Atif, M. Hammad Aziz, M. Imran Malick, S.S. Z. Zaidi, R. Suleman, A. Majid, Laser Phys. Lett. (2014), 039501, https://doi.org/10.1088/1612-2011/11/3/039501.
[66] M.G. Demissie, F.K. Sabir, G.D. Edossa, B.A. Gonfa, J. Chem. Chem. Eng. 2020 (2020), https://doi.org/10.1155/2020/7459042.
[67] Mayekar,, Dhar,, Radha, Int. J. Res. Adv. Eng. (n.d.).
[68] Pourrahimi,, Liu,, Pallon,, Andersson, RSC Adv. (n.d.).
[69] S. Gao, W. Yang, J. Xiao, B. Li, Q. Li, J. Mater. Sci. Technol. 35 (4) (2019) 610–614.
[70] P.R. Gandhi, C. Jayaseelan, R.R. Mary, D. Mathivanan, S.R. Suseem, Exp. Parasitol. 181 (2017) 47–56.
[71] S. Gurusamy, M.R. Kulanthaisamy, D.G. Hari, A. Veleeswaran, B. Thulasinathan, J. B. Muthuramalingam, R. Balasubramani, S.W. Chang, M.V. Arasu, N.A. Al-Dhabi, A. Selvaraj, A. Alagarsamy, J. Photochem. Photobiol. B 193 (2019) 118–130.
[72] P.E. Gnanakani,, P. Santhanam,, K. Premkumar,, K.E. Kumar,, M.D. Dhanaraju, Asian Pacific J. Cancer Prevention (2019) 2353–64. 10.31557/apjcp.2019.20.8.2353.
[73] K. Ayouni, M. Berboucha-Rahmani, H.K. Kim, D. Atmani, R. Verpoorte, Y.H. Choi, Ind. Crops Prod. 88 (2016) 65–77.
[74] R.M. Silverstein,, F.X. Webster,, D.J. Kiemle,, D.L. Bryce, (2014).
[75] R.M. Silverstein, G.C. Bassler, J. Chem. Educ. (1962).
[76] S.N.A. Mohamad Sukri, K. Shameli, M. Mei-Theng Wong, S.-Y. Teow, J. Chew, N. A. Ismail, J. Mol. Struct. 1189 (2019) 57–65.
[77] G. Indramahalakshmi, Asian J. Phys. Chem. Sci. (2017) 1–7, https://doi.org/10.9734/ajopacs/2017/35917.
[78] Udayabhanu, G. Nagaraju, H. Nagabhushana, D. Suresh, C. Anupama, G.K. Raghu, S.C. Sharma, Ceram. Int. 43(15) (2017) 11656–11667.
[79] J. Fowsiya, G. Madhumitha, N.A. Al-Dhabi, M.V. Arasu, J. Photochem. Photobiol. B 162 (2016) 395–401.
[80] V.V. Gawade, N.L. Gavade, H.M. Shinde, S.B. Babar, A.N. Kadam, K.M. Garadkar, J. Mater. Sci.: Mater. Electron. 28 (18) (2017) 14033–14039.
[81] F. Zhang, J. Zhao, T. Shen, H. Hidaka, E. Pelizzetti, N. Serpone, Appl. Catal. B 15 (1) (1998) 147–156.
[82] N. Shanmugam, T. Sathya, G. Viruthagiri, C. Kalyanasundaram, R. Gobi, S. Ragupathy, Appl. Surf. Sci. 360 (2016) 283–290.
[83] C. Qi, H. Chen, C. Xu, Z. Xu, H. Chen, S. Yang, S. Li, H. He, C. Sun, Chemosphere 260 (2020), 127681.
[84] F. Rehman, M. Sayed, J.A. Khan, N.S. Shah, J. Hazard. Mater. (2018).
[85] L.A. Shah, A. Haleem, M. Sayed, M. Siddiq, J. Environ. Chem. Eng. 4 (3) (2016) 3492–3497.
[86] L.A. Shah, T. Malik, M. Siddiq, A. Haleem, M. Sayed, A. Naeem, J. Environ. Chem. Eng. 7 (5) (2019), 103291.
[87] W. He, Y. Ding, J. Tu, C. Que, Z. Yang, J. Xu, Org. Biomol. Chem. 16 (10) (2018) 1659–1666.
[88] F.L. Migliorini, J.R. Steter, R.S. Rocha, M.R.V. Lanza, M.R. Baldan, N.G. Ferreira, Diam. Relat. Mater. 65 (2016) 5–12.